Carbonate U-Pb dating via LA-ICPMS : insights into chronostratigraphy in lacustrine settings

Damaris Montano

Damaris Montano. Carbonate U-Pb dating via LA-ICPMS : insights into chronostratigraphy in lacustrine settings. Earth Sciences. Sorbonne Université, 2021. English. NNT : 2021SORUS545 . tel-03828503

HAL Id: tel-03828503
https://theses.hal.science/tel-03828503v1

Submitted on 25 Oct 2022

Sorbonne Université

Ecole doctorale 398

Carbonate U-Pb dating via LA-ICPMS: insights into chronostratigraphy in lacustrine settings

PhD Thesis in Geology

Presented on 09 December 2021

Members of the Jury:

PhD director:	
Dr. Marta GASPARRINI	University of Milan
PhD supervision:	
Dr. Sébastien ROHAIS	IFP Energies nouvelles
Prof. Axel GERDES	Goethe Universität, Frankfurt am Main
Reviewers:	
Prof. David CHEW	Trinity College Dublin
Prof. Anneleen FOUBERT	University of Fribourg
Examiners:	
Prof. Massimo TIEPOLO	University of Milan
Dr. Andrea ORTENZI	ENI, E&P division
Prof. Pierpaolo ZUDDAS	Sorbonne University of Paris
Invited:	
Dr. Richard Albert	Goethe Universität, Frankfurt am Main

Candidate:

Damaris MONTANO

From Boltzmann to quantum theory, from Einstein to loop quantum gravity, our understanding of time has been undergoing radical transformations. Time flows at different speeds in different places, the past and the future differ far less than we might think and the very notion of the present evaporates in the vast universe.

Carlo Rovelli, ‘*The order of Time’*

ACKNOWLEDGMENTS

The journey toward this PhD dissertation has been a life-changing experience for me and it would have not been the same without the support that I received from many people.

First of all, I would like to acknowledge IFP Energies nouvelles to have founded this PhD project and Goethe University of Frankfurt to allow me access to their labs.

I express my sincere gratitude to my thesis director Marta Gasparrini for her presence, dedication, guidance and constant feedback. I will always keep your advices with me.

A special thanks goes to my supervisor Sébastien Rohais, for his scientific support and kindness especially in the long period of isolation.

I unknowledge my supervisor Axel Gerdes whose expertise, scientific enthusiasm and smiles accompanied me along this journey. Many thanks to Richard Albert, for his advices and ability to explain very complex concepts in the easiest way. Thanks to the other members of the Petrology and Geochemistry department of Goethe University, for the valuable scientific exchange and support during data acquisition and to Giovanna Della Porta from Milan university who has been always available since the times of my Master degree.

I would like to thank the members of the monitoring committee, Guillaume Morin and Julien Mercadier, and the members of the PhD jury, David Chew, Anneleen Foubert, Massimo Tiepolo, Andrea Ortenzi and Pierpaolo Zuddas, that accepted to evaluate this thesis and provide their valuable scientific apport.

These years would have not been the same without the presence of my dearest friends that continue to be part of my life no matter distance nor life-choices. Thank you guys.

I would also like to say a heartfelt thanks to you, mum and dad, for the unconditional love and the constant presence. You have been and will always be my rock.

More than a thanks goes to my brother. There are many things that could be said about us Gio, but my favourite one is that I would not be me without you. Our brotherhood is priceless.

And finally, a huge thanks to Walter who has been by my side throughout these long years apart. I probably would not have had the courage to embark on this journey without you. You believed in me, encouraged me, suffered with me, were always there for me. This new life together, is our reward.

ABSTRACT

Lacustrine deposits are extensively investigated because they play a pivotal role as environmental recorders and host valuable economic resources. However, chronostratigraphic reconstructions in these settings are usually hampered by the scarcity of data required to establish the depositional age of the system. The prime objective of this PhD project was examining benefits and limitations of carbonate U-Pb (LA-ICPMS) dating (LAcarb) as new chronostratigraphic tool for lacustrine deposits. The second objective was to investigate the dating potential, in terms of dating success and time resolution, of various carbonate types and mineralogies with the aim to better organize future LAcarb based research. To achieve these goals, depositional (microbialites, ooids, oncoids) and early diagenetic carbonate phases of known absolute age were collected from two lacustrine settings: the Ries Crater basin (Miocene, SW Germany) and the Yacoraite formation (Fm.) from the Salta rift basin (Cretaceous-Paleogene, NW Argentina).

A sedimentologic and diagenetic study based on petrography and Oxygen (O) and Carbon (C) stable isotope analysis allowed to select carbonate phases that most possibly preserved the pristine U-Pb geochemical composition and consequently inform on the timing of deposition. In the Ries Crater basin, LAcarb provided accurate ages that allowed chronostratigraphic correlations at a time resolution of the 3rd order stratigraphic sequence (0.5–5Ma). In the framework of the Yacoraite Fm., two depositional age depth model were obtained along a stratigraphic section. One derived from zircon (ash layer) geochronology (maximum depositional age depth model; MDA depth model) and the other from LAcarb (minimum depositional age depth model; MIDA depth model). The two models remarkably overlap and describe the same sedimentation rate dynamic with a time resolution between 0.9 and 2% (2σ). The revised depositional age of the Yacoraite Fm. was then integrated in a chronostratigraphic model merging biostratigraphic, chemostratigraphy and magnetostratigraphy data from literature. Accordingly, the KPg limit was interpreted to be located in the Yacoraite Fm. whereas the two Paleocene-Eocene hyperthermals (Paleocene-Eocene Thermal Maximum, PETM; early Eocene Climate Optimum, EECO) were identified in the two overlying formations.

A statistical analysis was achieved based on the ages of 80 carbonate phases from the Yacoraite Fm. Microbialites provided the lowest dating success (41% ages consistent with the MDA depth model) and age precision (2σ < 10%) in contrast with lacustrine cements that yielded the highest dating success (64% ages consistent with MDA depth model) and age precision (2σ < 3%). Furthermore, calcitic phases usually provided more precise ages than dolomitic phases.

The better comprehension of potentialities and limitations of LAcarb acquired in this PhD allowed to propose a workflow to build a robust depositional age depth model in lacustrine settings. Three possible perspective scenarios were introduced: 1) the study of the Ries Crater basin as analogue of paleolakes on Mars; 2) the use of LAcarb to select pristine carbonates for chronostratigraphic studies; and 3) basin scale chronostratigraphic correlations in the Yacoraite Fm.

Keywords: Carbonate U-Pb dating, LA-ICPMS, chronostratigraphy, dating potential, lacustrine deposits, Ries Crater, Yacoraite Fm.

Résumé

Les dépôts lacustres font l'objet d'études approfondies car ils sont propices à l’enregistrement des modifications de nombreux facteurs environnementaux (changement climatique, modification du couvert végétal…), et également car ils renferment des ressources en matière première de toute première importance. Cependant, les reconstructions chronostratigraphiques dans ces contextes sont généralement entravées par la rareté des données permettant d’établir l'âge des dépôts de manière continue. L'objectif principal de ce projet de thèse est d'examiner les avantages et les limites de la datation au carbonate U-Pb (LA-ICPMS) (méthode LAcarb) comme un nouvel outil chronostratigraphique pour les dépôts lacustres. Le deuxième objectif est d'étudier plus précisément le potentiel de datation de la méthode en analysant sa capacité à établir un âge avec résolution temporelle pertinente en fonction des différents types de carbonates et de minéralogies. Pour atteindre ces objectifs, plusieurs phases carbonatées (microbialites, ooides, oncoides) et ciments diagenétiques ont été collectés dans deux exemples lacustres fossiles ayant un âge absolu relativement bien établit: le Miocène du bassin du cratère Ries (SW Allemagne) et la formation Yacoraite (Crétacé-Paléogène) du bassin de Salta (NW de l'Argentine). Une étude sédimentologique et diagenétique s’appuyant sur des analyses pétrographiques et des isotopes stables de l’oxygène (O) de du carbone (C), a permis de sélectionner les phases carbonatées les plus précoces. Ce travail a été réalisé afin de maximiser les chances d’avoir préservé la composition géochimique originelle en U-Pb des fluides en présence lors du dépôt. Dans le bassin du cratère Ries, la méthode LAcarb a fourni des âges précis qui ont permis des corrélations chronostratigraphiques à une résolution temporelle de l’ordre de la séquence stratigraphique du 3e ordre (0,5 à 5 Ma). Dans le cadre de la formation Yacoraite, deux modèles d'âge ont été obtenus le long d'une coupe stratigraphique de référence. L'un est dérivé de la géochronologie des zircons extraits des dépôts de cendre volcaniques intercalés dans la formation Yacoraite (modèle d'âge maximum des dépôts; MDA). Le second est dérivé de la méthode LAcarb (modèle d'âge minimum des dépôts; MIDA). Les deux modèles se superposent remarquablement et permettent de décrire une même dynamique des taux de sédimentation avec une résolution temporelle d'environ 0,9 à 2% (2σ). L'âge des dépôts révisé pour la formation Yacoraite a ensuite été intégré dans un modèle chronostratigraphique combinant les données biostratigraphiques, chemiostratigraphiques et magnétostratigraphiques issues de la littérature. La localisation de la limite Crétacé-Paléogène (KPg) a bien été confortée dans la formation Yacoraite. De plus, la révision des âges de la partie sommitale de la formation Yacoraite a également permis de valider la localisation des deux phases hyperthermiques du Paléocène-Éocène (Paleocene-Eocene Thermal Maximum: PETM, et l'optimum climatique de l'Eocène; EECO) dans les deux formations sus-jacentes.

Une analyse statistique a ensuite été réalisée sur la base des âges de 80 phases carbonatées de la formation Yacoraite. Les microbialites ont fourni les plus faibles succès en potentiel de datation (41 % d'âges cohérents avec le modèle MDA) ainsi que les plus basses précisions concernant l'âge (2σ <10 %). A l'inverse, les ciments lacustres ont été couronnés des meilleurs potentiels de datation (64 % d'âges cohérents avec le modèle MDA) avec des âges de meilleure précision. De plus, les phases dominées par la calcite ont généralement fourni des âges plus précis que les phases dolomitiques. Les avancées concernant les potentialités et les limites associées à la méthode LAcarb ont ainsi permis de proposer au travers de cette thèse une méthode complète pour construire un modèle d'âge robuste des dépôts en milieu lacustre. Les perspectives de ces travaux sont multiples, avec par exemple, une application sur d'autres sous-bassins sédimentaires de la formation Yacoraite pour mieux comprendre la segmentation des grands systèmes lacustres crétacés, ou l'influence de l'hydrologie locale sur le potentiel de datation, ou encore des études plus avancées sur l'étude des proxys pouvant servir à restaurer les conditions hydrologiques et paléo-environnementales des lacs.

Mots-clés: Datation au carbonate U-Pb, LA-ICPMS, chronostratigraphie, potentiel de datation, dépôts lacustres, Ries Crater, Yacoraite Fm.

Table of Content

CHAPTER 2. CHRONOSTRATIGRAPHY VIA ZIRCON AND CARBONATE DATING

CHAPTER 9 CONCLUSIONS AND PERSPECTIVES

1 INTRODUCTION

1.1 The importance of lacustrine carbonate dating

Sedimentary rocks record the passage of time on the Earth through their lithologic, magnetic and geochemical features and paleontological content. Layered sedimentary successions are most like massive books to be leafed through to unravel the story of our planet. ‘By extending the principle of Uniformitarism of James Hutton (Hutton, 1788) it derives that *the past is the key to the future (Doe, 1983).* Investigating what happened in the past allows to predict future geologic trends such as the behavior of natural systems in response to climate/environmental changes and catastrophic events (e.g. meteorite impacts, volcanism and earthquakes; Font & Bond, 2021; Shuman, 2021). This is of prime importance when considering the present day anthropogenic impact on climate and ecosystems (e.g. Fawzy et al., 2020). In addition, the study of the past geologic history is essential to understand the driving forces for life evolution and extinction (e.g. Raup & Sapkoski, 1982; Nakashima et al., 2018; Chatterjee, 2021; Màngano & Buatois, 2021) and it is required for the discovery and quantification of sub-surface resources of economic interest (e.g. ores, coal, geothermal resources, hydrocarbons; O’Brien et al., 2011). It derives that establishing the absolute age of sedimentary rocks represents the key to investigate the past history of the Earth.

This PhD project focuses on a new promising tool to establish the absolute age of carbonate rocks: *in situ* U-Pb carbonate dating via laser ablation inductively coupled plasma mass spectrometer (LA-ICPMS), which is also named LAcarb (Rasbury et al., 2021). Benefits and limitations of LAcarb have been investigated in the context of lacustrine sedimentary systems of Cretaceous to Miocene age.

Lacustrine carbonates have been under the spotlight over the past decade because they play a pivotal role as environmental recorders (e.g. Keltz & Talbot, 1990; Leng & Marshall, 2004; Elias, 2021), yielding the most complete time-continuous record of terrestrial climate changes. They were investigated to gather insights on various ‘extreme’ events such as hypertermals (e.g. Scholz et al., 2007; Matys Grygar et al., 2017), glacial–deglacial climate variations (e.g. Noronha-D'Mello et al., 2021; Li et al., 2021) and extinctions (e.g. Rohais et al., 2019). They are also studied for their economic value (e.g. Herrero & Escavy, 2010) since they constitute both source and reservoir rocks of hydrocarbons (e.g. pre-salt petroleum system; Fernandez et al., 2020), host industrial minerals and rocks (Katz, 2001) and valuable elements. Finally, lacustrine marginal carbonates from meteorite impact basins are currently investigated as analogues for palaeolakes on Mars (e.g. Horgan et al., 2020) which are major targets for future landed investigations and sample return (e.g. Bosac et al., 2021; Carr, 2021; Scheller et al., 2021; Svensson et al., 2021).

A commonly used statement among scientists who study lacustrine basins is that “lakes are not small oceans”. Lakes differ from oceans in several significant ways and the chronostratigraphic tools commonly used to investigate marine settings do not necessarily apply in lacustrine systems (e.g. Bohacs et al. 2000). In this scenario, carbonate absolute dating via LAcarb may represent the game changer for lacustrine chronostratigraphy.

Carbonate minerals were considered undatable since the pioneering work of Smith & Farquar (1989) on Phanerozoic sediments. In successive decades, the application of the U-Pb geochronometer to carbonates remained a niche geochronological tool, limited by the low spatial resolution of available techniques and by the analytical challenges in handling low amounts of U and Pb heterogeneously incorporated in carbonates (Rasbury & Cole, 2009). Technical advances on LA-ICPMS analysis have largely increased the success rate of carbonate dating and opened up a wide range of applications. Previous authors provided the timing for brittle deformation (Roberts & Walker, 2016; Ring & Gerdes, 2016; Goodfellow et al., 2017; Hansman et al., 2018; Parrish et al., 2018; Beaudoin et al., 2018; Nuriel et al., 2017, 2019; Smeraglia et al., 2019; Smeraglia et al., 2021), hydrocarbon migration (Mangenot et al., 2018; Holdsworth et al., 2019, 2020), ore mineralisation (Burisch et al., 2017, 2018; Kreissl et al., 2018), hydrothermal and deep-crustal fluid flow (Drake et al., 2017, 2019, 2020; Mazurek et al., 2018; Walter et al., 2018; Incerpi et al., 2019; MacDonald et al., 2019; Cruset et al., 2020; Mottram et al., 2020; Roberts et al., 2020a, 2020b, 2021; Bilau et al., 2021), ocean crust alteration (Coogan et al., 2016) and thermal evolution and fluid/rock interaction in sedimentary basins (Li et al., 2014; Pagel et al., 2018; Mangenot et al., 2018; Godeau et al., 2018; Lawson et al., 2018).

However, one of the most intriguing implications of LAcarb is the use as chronostratigraphic tool in hardly datable depositional settings such as lacustrine and more broadly continental systems. Encouraging results are shown by previous authors that provided depositional ages consistent with those obtained by other radiometric techniques for meteoric cements in speleothems (Hopley et al., 2019; Scardia et al., 2019 ; Woodhead & Petrus, 2019; Nicholson et al., 2020) and hardgrounds (Methner et al., 2016; Liivamägi et al., 2018; Scardia et al., 2019; Kurumada et al., 2020; Brigaud et al. 2021), lacustrine tufa, micrites and associated cements (Drost et al., 2018; Frisch et al. 2019; Parrish et al., 2019; Hoareau et al., 2021; Rasbury et al., 2021), marine cements (Meinhold et al., 2020; Hoareau et al., 2021) and bioclasts (Drost et al., 2018).

Nevertheless, given the relatively recent application to carbonates (Li et al., 2014), at today benefits and limitations of LAcarb as chronostratigraphic tools are not fully understood (e.g. Roberts et al., 2020a) and deserve further investigation. An important issue is represented by the carbonate dating potential. It is well accepted that not all carbonates are datable and their dating potential is strongly connected to their initial U-Pb isotope composition which in turn may vary among different carbonates and paleoenvironments (e.g. Rasbury & Cole, 2009). The pristine isotope composition can be also easily disturbed during syn- and post-depositional diagenetic processes causing age reset and degradation (e.g. Rasbury & Cole, 2009). Despite several decades of studies primarily driven by the field of nuclear waste storage/characterization and environmental hazard (e.g. Suzuki et al., 2016; Neiva et al., 2019; Romanchuk et al., 2020), the behavior of U and Pb incorporation during carbonate precipitation till remains unclear. This limits the successful application of LAcarb in various fields of geoscience and does not allow focusing on specific carbonates that are more suitable to be dated.

1.2 Aims, workflow and thesis outline

The PhD project was held at and funded by IFP Energies nouvelles in collaboration with the Earth Sciences department of the University of Milan (Italy) and the Frankfurt Isotope & Element Research Centre (FIERCE) at Goethe Universität Frankfurt (Germany) and has the following aims:

1) to assess the accuracy and precision of the LAcarb chronometer on lacustrine carbonates of known age based on other absolute radiometric constraints;

2) to evaluate the suitability of LAcarb as chronostratigraphic tool to build robust depositional age depth models in lacustrine settings;

3) to investigate the dating potential of different lacustrine and early diagenetic carbonates;

4) to provide a protocol to use LAcarb as a succesfull tool for chronostratigraphic reconstructions.

The Nördlinger Ries Crater basin (Miocene, SW Germany) and the Yacoraite formation (Fm.) (Cretaceous-Paleogene, NW Argentina) were investigated for these purposes. They were chosen because include various depositional (microbialite, oncoids, ooids) and early diagenetic (lacustrine and meteoric cements) carbonates with different mineralogies (calcitic and dolomitic). The burial diagenetic overprint was limitedenhancing the probability to investigate carbonates preserving the pristine isotope composition. Moreover, these two areas have been extensively investigated in the past (e.g. Arp et al., 2017,2019a,b; Rohais et al., 2012, 2014, 2019; Deschamps et al., 2020 and references therehin) allowing to work in a well-framed geochronological, sedimentologic, geochemical and palaeoenvironmental context.

The Ries Crater basin was used as a pilot project to test the use of LAcarb as chronostratigraphic tool for depositional and early diagenetic carbonates from cool water spring mounds and algal bioherms of Miocene age. The analyses performed gave accurate and precise results, with ages consistent with those proposed by previous authors. The accuracy and precision of LAcarb data demonstrated for lacustrine carbonates of the Ries Crater, paved the ground for the investigation of older Cretaceous-Paleogene carbonates from the Yacoraite Fm.

The Yacoraite Fm. from the Salta rift basin represents the main object of the PhD project. This formation was the subject of the JIP COMPAS, a Joint Industrial Project supported by 13 companies and carried out by IFP Energies nouvelles in the period 2012-2015 (Rohais et al., 2012, 2014; 2019; Deschamps et al., 2020). The Yacoraite Fm. is the ideal geological object for the aims of the present research because it consists of a lacustrine sedimentary succession of known age as it is interbedded with volcanic ashes and exposed in outcrops allowing continuous sampling along vertical sections. A sampling campaign was accomplished in June-July 2018 in the Salta province (Argentine) to collect samples from two vertical sections of the basin. The depositional age of the Yacoraite Fm. was obtained from volcanic ash layers by zircon U-Pb (LA-ICPMS) geochronology. Prior to LAcarb dating, carbonates were analysed for petrography (optical and CL petrography) and geochemistry C-O stable isotopes) to select depositional and early diagenetic carbonate phases that most possibly preserve their pristine isotope compositions. The dataset acquired was used to evaluate the dating potential of different carbonate types and mineralogies and better understand the main driving factors for U-Pb incorporation in carbonates from lacustrine settings.

The PhD thesis is organized as follows.

- Chapter 2. General principles of chronostratigraphy, U-Pb absolute dating of zircon grains and carbonates, mechanisms for U-Pb sequestration in carbonates and the most commonly used techniques for carbonate dating.
- Chapter 3. Methods used for sample characterization and U-Pb dating (e.g. petrography, geochemistry and isotope geochronology).
- Chapter 4. Application of LAcarb to the Ries Crater basin. Results are included in a scientific article published on Earth and Planetary Science Letters (Montano et al., 2021).
- Chapter 5. The Yacoraite Fm., from geological settings to field work and sample acquisition.

- Chapter 6. Application of LAcarb to the Yacoraite Fm. with developments of two depositional age depth models based on zircon and carbonate dating. Results are included in a scientific article (Montano et al., in revision). The data showed implications for the recognition of the KPg limit and of the Paleocene-Eocene hyperthermals (Chapter 6.2).
- Chapter 7. Dating potential statistical analysis based on 80 carbonate phases from the Yacoraite Fm. Section 7.1 includes a preliminary paragenetic analysis. In Chapter 7.2 the impact of early and late diagenesis on the dating potential is discussed. Chapter 7.3 includes a statistical analysis of the dating success and age precision for different carbonate types (microbialite, ooids, oncoids, cements) and mineralogies (Chapter 7.3).
- Chapter 8. A workflow to build a robust depositional age depth model via LAcarb in lacustrine sedimentary section is proposed (Chapter 7.4).
- Chapter 9. Main achievements of the PhD project (Chapter 8.1) and potential future perspectives (Chapter 8.2).

A detailed workflow of the PhD project is shown in figure 1.

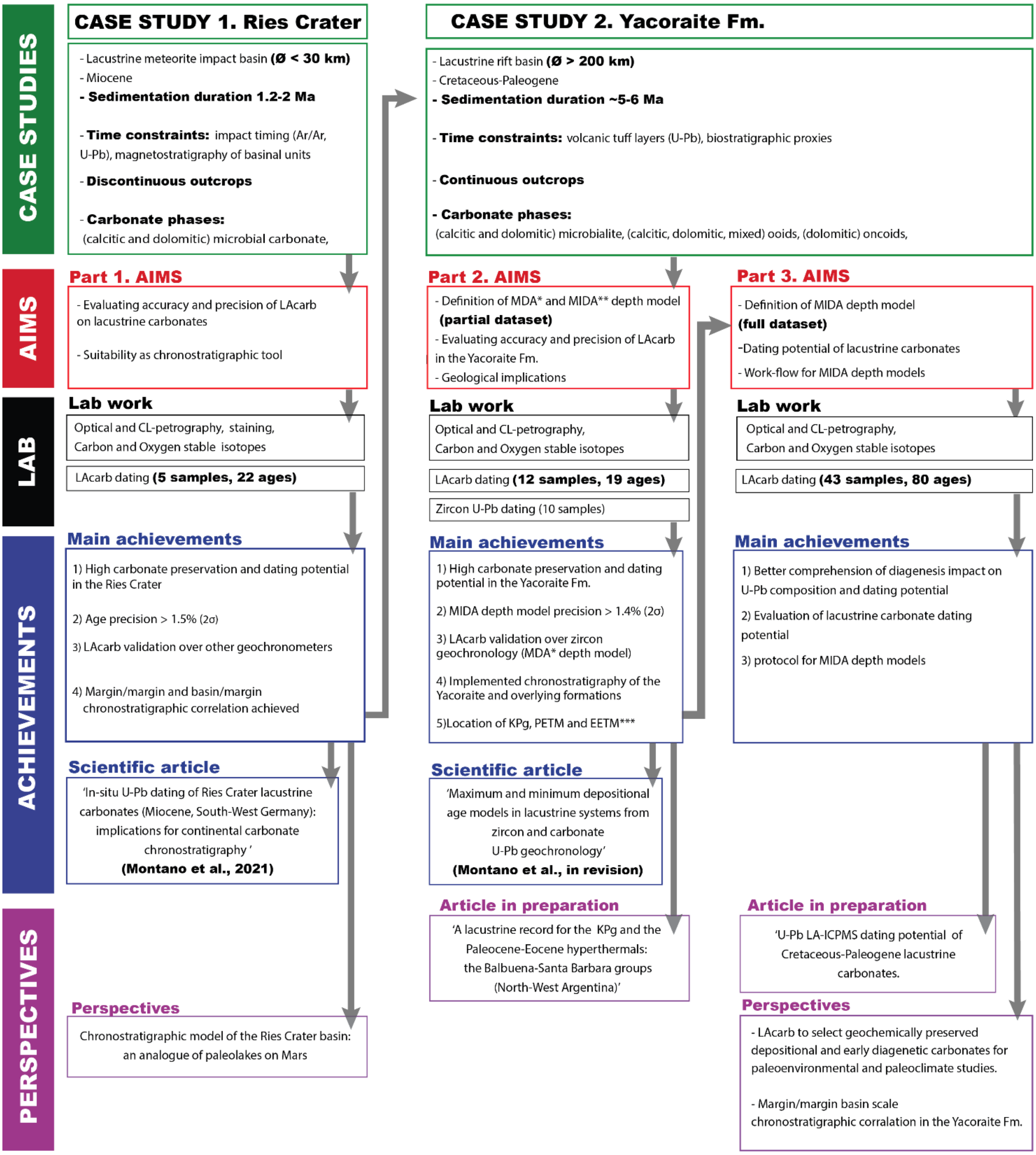

CASE STUDY 1. Ries Crater

- Lacustrine meteorite impact basin **(Ø < 30 km)**
- Miocene
- **Sedimentation duration 1.2-2 Ma**

- **Time constraints:** impact timing (Ar/Ar, U-Pb), magnetostratigraphy of basinal units
- **Discontinuous outcrops**
- **Carbonate phases:** (calcitic and dolomitic) microbial carbonate,

Part 1. AIMS

- Evaluating accuracy and precision of LAcarb on lacustrine carbonates
- Suitability as chronostratigraphic tool

Lab work

Optical and CL-petrography, staining, Carbon and Oxygen stable isotopes

LAcarb dating **(5 samples, 22 ages)**

Main achievements

1) High carbonate preservation and dating potential in the Ries Crater

2) Age precision > 1.5% (2σ)

3) LAcarb validation over other geochronometers

4) Margin/margin and basin/margin chronostratigraphic correlation achieved

Scientific article

'In-situ U-Pb dating of Ries Crater lacustrine carbonates (Miocene, South-West Germany): implications for continental carbonate chronostratigraphy'
(Montano et al., 2021)

Perspectives

Chronostratigraphic model of the Ries Crater basin: an analogue of paleolakes on Mars

CASE STUDY 2. Yacoraite Fm.

- Lacustrine rift basin **(Ø > 200 km)**
- Cretaceous-Paleogene
- **Sedimentation duration ~5-6 Ma**

- **Time constraints:** volcanic tuff layers (U-Pb), biostratigraphic proxies
- **Continuous outcrops**
- **Carbonate phases:** (calcitic, dolomitic) microbialite, (calcitic, dolomitic, mixed) ooids, (dolomitic) oncoids,

Part 2. AIMS

- Definition of MDA* and MIDA** depth model **(partial dataset)**
- Evaluating accuracy and precision of LAcarb in the Yacoraite Fm.
- Geological implications

Lab work

Optical and CL-petrography, Carbon and Oxygen stable isotopes

LAcarb dating **(12 samples, 19 ages)**

Zircon U-Pb dating (10 samples)

Main achievements

1) High carbonate preservation and dating potential in the Yacoraite Fm.

2) MIDA depth model precision > 1.4% (2σ)

3) LAcarb validation over zircon geochronology (MDA* depth model)

4) Implemented chronostratigraphy of the Yacoraite and overlying formations

5)Location of KPg, PETM and EETM***

Scientific article

'Maximum and minimum depositional age models in lacustrine systems from zircon and carbonate U-Pb geochronology'
(Montano et al., in revision)

Article in preparation

'A lacustrine record for the KPg and the Paleocene-Eocene hyperthermals: the Balbuena-Santa Barbara groups (North-West Argentina)'

Part 3. AIMS

- Definition of MIDA depth model **(full dataset)**
-Dating potential of lacustrine carbonates
- Work-flow for MIDA depth models

Lab work

Optical and CL-petrography, Carbon and Oxygen stable isotopes

LAcarb dating **(43 samples, 80 ages)**

Main achievements

1) Better comprehension of diagenesis impact on U-Pb composition and dating potential

2) Evaluation of lacustrine carbonate dating potential

3) protocol for MIDA depth models

Article in preparation

'U-Pb LA-ICPMS dating potential of Cretaceous-Paleogene lacustrine carbonates.

Perspectives

- LAcarb to select geochemically preserved depositional and early diagenetic carbonates for paleoenvironmental and paleoclimate studies.
- Margin/margin basin scale chronostratigraphic corralation in the Yacoraite Fm.

Figure 1. PhD project workflow.

2 CHRONOSTRATIGRAPHY VIA ZIRCON AND CARBONATE DATING

This chapter aims at providing to the reader background information regarding the use of zircon and carbonate dating for the chronostratigraphy of lacustrine systems. Chapter 2.1 describes the challenges in performing accurate chronostratigraphic studies in lacustrine settings, if compared to marine systems and, in this respect, discuss the importance of radiometric dating (tephrachronology) in the framework of lacustrine systems. Section 2.2 includes the principles for zircon and carbonate absolute. A specific focus is given to the present-day knowledge about the mechanisms for U-Pb incorporation in carbonates, relevant for the comprehension of carbonate dating. In Chapter 2.3 discuss the pro and cons of the two most commonly used techniques for dating (ID-TIMS vs LA-ICPMS).

2.1 Insights for marine and lacustrine chronostratigraphy

Chronostratigraphy is an interdisciplinary branch of geology that aims at subdividing and correlating rock strata according to their age and thus it is required for establishing the relative and absolute time relationship between sedimentary successions regionally and worldwide (e.g. Cohen et al., 2018; Lucas, 2018). It includes disciplines such as sedimentology, biostratigraphy, chemostratigraphy,

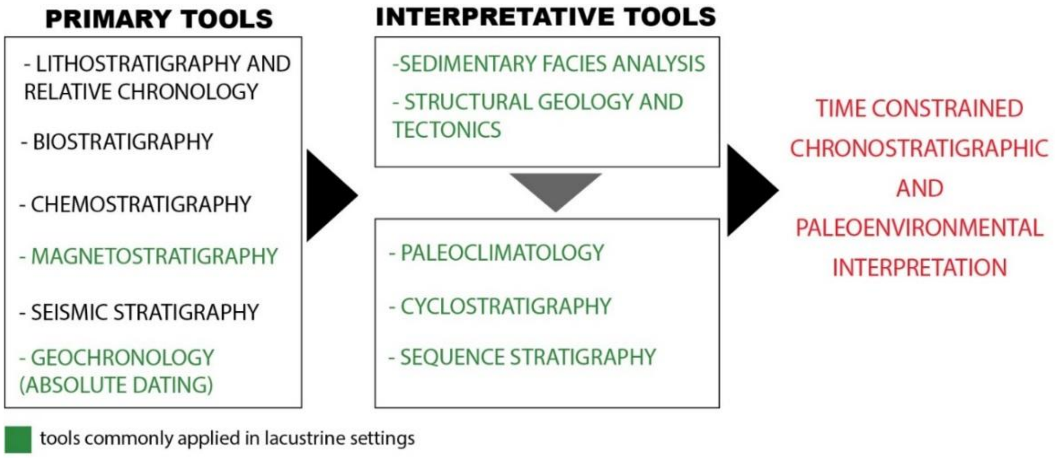

Figure 2. Schematic overview the principal chronostratigraphic tools. Interpretative tools are based on primary tool data integration and interpretation.

magnetostratigraphy, cyclostratigraphy, seismic stratigraphy, sequence stratigraphy, and geochronology (Fig. 2).

In marine settings integrated chronostratigraphic studies can faithfully rely on various tools. Marine lithostratigraphic facies have high lateral continuity allowing fast chronostratigraphic correlations usually based on marker beds (i.e. a bed of rock strata that are readily distinguishable by reason of physical characteristics and are traceable over large horizontal distances). Biostratigraphy is extensively applied due to common presence of index taxa (i.e. guide fossils that lived for short time periods and over wide geographic areas) and biozones (i.e. fossil assemblages) of short time duration and well known absolute age. The most known examples are the planktonic foraminifera and ammonites that evolved quickly during Cretaceous allowing high biostratigraphic resolution (e.g. Lehmann, 2015; Lucas, 2021).

Chemostratigraphy (i.e. the study of environmental chemical variations recorded by sedimentary rocks) is largely employed in marine systems because the ratios between specific isotopes (e.g. $^{87}Sr/^{86}Sr$, $^{13}C/^{12}C$ and $^{18}O/^{16}O$) in sea water is mostly homogeneous at any one time but fluctuated over geological time. The resultant ‘seawater curves’ of isotope variation can be used as relative dating tools for marine sediments (e.g. Burke et al., 1982; Veizer et al., 1999; McArthur et al., 2020). Chemostratigraphy also relies on the occurrence of specific isotope compositions in sediments, fairly related to past events (e.g. Sial et al., 2015). To mention some, the $\delta^{13}C$, Iridium, Osmium and Sulfur anomalies are currently used to locate the boundary between Cretaceous and Paleogene which corresponds to one the five major extinction events on the Earth (e.g. Schoene et al., 2019). Magnetostratigraphy is used to correlate the record of the polarity reversals of the Earth's magnetic field recorded in sediments with the geomagnetic polarity time scale (GPTS) provided with numerical (geochronology and astrochronology) age constraints (e.g. Opdyke & Channel, 1996; Langereis et al. 2010) whereas cyclostratigraphy uses astronomical cycles of known periodicities (e.g. Milankovic cycles; Milankovic, 1920, 1941) to interpret repetitive patterns in the sedimentary record (e.g. Gilbert, 1895; Einsele & Ricken, 1991; Hilgen et al., 2004). This is based on the fact the orbital cycles have a direct control on the climate and thus influence sea level, sedimentary features, stacking pattern, biological content and geochemical composition. Finally, sequence stratigraphy coupled with seismic stratigraphy are powerful tools for the study of marine sedimentary succession allowing the recognition of the relationship between strata architecture and changes of sediment supply and relative sea level (e.g. Catuneanu et al., 2009). All the primary and interpretative tools previously listed (Fig. 2) yields to high resolution, well time constrained, chronostratigraphic reconstructions in marine settings. This is usually not the case of non-marine, and especially lacustrine, carbonate systems.

Non-marine carbonates are carbonate rock deposits located in continental settings and consist mainly of karst and cave deposits, hot and cool spring and stream carbonates, calcrete and marginal, lacustrine-palustrine carbonates (e.g. De Boever et al., 2017; Fig. 3).

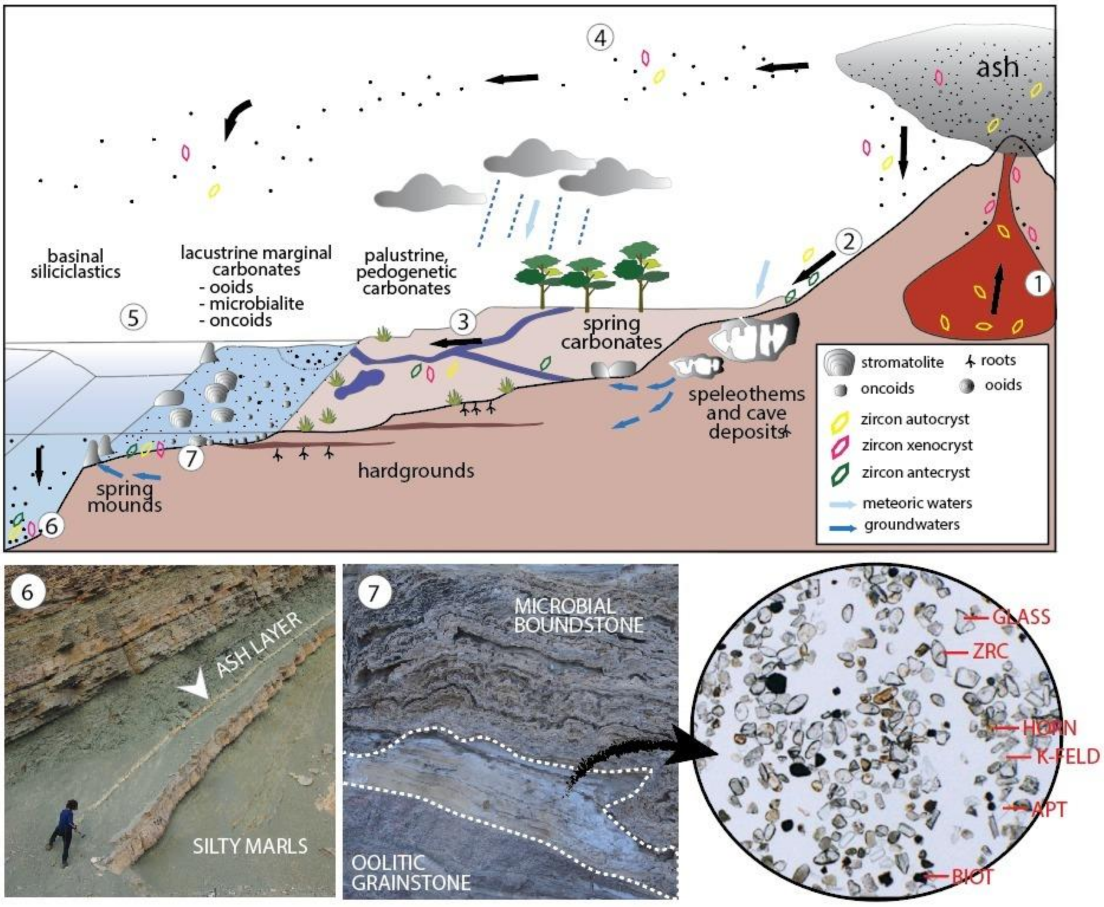

Figure 3 Non marine carbonates depositional profile and mechanisms for volcanic ash transport and sedimentation in continental lacustrine settings. (Modified after De Boever et al., 2017). Volcanic ashes, including zircon grains, are ejected during the magmatic eruption. Zircon autocrysts form during or shortly before the magmatic eruption whereas older zircon xenocrysts are assimilated during magma migration (1). Autocrysts and xenocrysts are transported by streams where they are mixed with zircon antecrysts (path 1-> 2-> 3-> 5). Zircon grains are also transported by the wind for long distances (path 1-> 4-> 5). Volcanic ashes are then deposited within the sediments as showed in pictures 6 and 7. In the circle, photomicrograph of the heavy minerals included in a volcanic ash layers from the Yacoraite Fm. RC=zircon, HORN=horneblend, K-feld = Potassium feldspars; APT=apatite, BIOT= biotite.

Among non-marine carbonates, lacustrine carbonate deposits attract the highest attention due to their economic value and for their importance in palaeoenvironmental studies (Bohacs et al., 2000). However, they are some of the most complex systems to investigate for chronostratigraphic reconstructions.

Lakes are dynamic systems mainly controlled by climate and tectonic processes (e.g. Flügel, 2010). This induces frequent high-amplitude changes in water level together with high and variable sediment accumulation rate (e.g. Enos et al., 1991; Einsele, 2001) resulting in a high lateral lithofacies variation that makes lithology effectively useless for chronostratigraphic reconstructions (e.g. Bohacs et al. 2000; Deschamps et al., 2020). Moreover, they usually lack biozones of short duration and palynomorphs are not easily recovered, limiting the use of biostratigraphy to vertebrate fossils. Concerning the lacustrine water chemical composition, closed lakes are basin with relatively low volume a low water exchange. This in turns implies a site specific geochemistry (e.g. Talbot et al., 1990; Della Porta, 2015) that hinders correlations with the 'seawater curves' of isotope variation (e.g. Burke et al., 1982; Veizer et al., 1999; McArthur et al., 2020).

A variety of approaches have been employed in an effort to overcome these limitations, such as seismic stratigraphy, magnetic-reversal stratigraphy, cyclostratigraphy, astrochronology and sequence stratigraphy (e.g. Bohacs, 2000; Fig. 2). Each of these approaches carries intrinsic advantages and limitations. Seismic stratigraphy generally lacks the resolution required to capture fine details of a rapidly evolving lake. Magnetostratigraphy instead has been largely applied in lakes due to their usually higher sedimentation rates and lack of bioturbation if compared to marine deposits. This allowing preservation of the initial magnetization signal (Opdyke & Channel, 1996). Cyclostratigraphy, astrochronology and sequence stratigraphy can also be applied due to the influence of climate cycles on the sedimentary architecture. However, all these tools do not provide by themselves any absolute age constraints.

Among the absolute dating tools, tephrachronology is of great importance in lacustrine settings (e.g. Lowe, 2011). It uses tephra (i.e. volcanic ashes from a single eruption) to create a chronological framework in which chemo- magneto- cyclo- stratigraphic data can be placed. Ash layers are key beds for chronostratigraphy. Ashes settle almost instantaneously over wide areas and include minerals (e.g. zircon, hornblende, K-feldspar, biotite, quartz) formed (almost) coevally with the volcanic eruption (Fig. 3) and that can be dated with high accuracy with various radiometric methods. To mention some, fission tracks analysis (on zircon and glass), Argon isotopes dating (K/Ar and ^{40}Ar/^{39}Ar variant; Deino et al., 2010; Cassata et al., 2010), U-series dating (U-Th/He and U-Pb; Weiman et al., 2018; Ducassou et al., 2019) and ^{14}C for ash layers deposits younger than 60 Ka

(Alloway et al., 2007). This permits physical and chronologic correlations between far and contrasting sediment environments. Detrital zircon grains may be also found dispersed in sediments (e.g. Rossignol et al., 2019). The use of these minerals to establish the depositional age of the system is defined ‘detrital zircon geochronology’ and is becoming very popular in chronostratigraphic studies (Finzel & Rosenblume, 2021). Tephrachronology and detrital zircon geochronology are more successful in lacustrine carbonate settings if compared to marine deposits due to the low clastic sediment flux that increase the relative proportion of zircon grains deposited from volcanic ash falls. However, tephra do not always occur interbedded within depositional sequences and thus most non marine and especially lacustrine settings often completely lack absolute time constraints for deposition.

2.2 U-Pb chronometer: general principles

Since the pioneering work of Holmes (1911), the use of the Uranium-Lead (U-Pb) isotope chronometer has come a long way, becoming one of the most powerful dating technique in the geologic toolbox. It allowed to provide crucial time constraints for the formation of the solar system and of the Earth (e.g. Patterson et al., 1953; Connelly & Bizzaro, 2017). In the last decades, development of high-precision dating methods and the sophistication of sampling techniques opened up a wide range of applications in the Earth sciences. Minerals such as zircon, apatite, monazite are dated to provide high precision temporal constraints to the geologic timescale (e.g. Gradstein et al., 2004), for provenance studies in sedimentary settings (source to sink, e.g. Resentini et al., 2020), to reconstruct the timing of magmtic and metamorphic processes and for thermochronology studies (e.g. Kirkland et al., 2018). In this section, specific attention is given to the application of the U-Pb chronometer for the chronostratigraphy of carbonate and siliciclastic depositional systems via zircon and carbonate geochronology.

The U-Pb isotope chronometer is based on the natural decay processes of the U radioactive isotopes (i.e. radionuclides) initially incorporated in the mineral to be dated (Fig. 4). In nature the most common U radionuclides are ^{238}U and ^{235}U. Over time, ^{238}U and ^{235}U (i.e. father isotopes) decay exponentially in ^{206}Pb and ^{207}Pb stable products (i.e. daughter isotopes) at a rate described by a parameter known as the half-life, which are 4,47 billion years for the ^{238}U-^{206}Pb and 0,703 billion

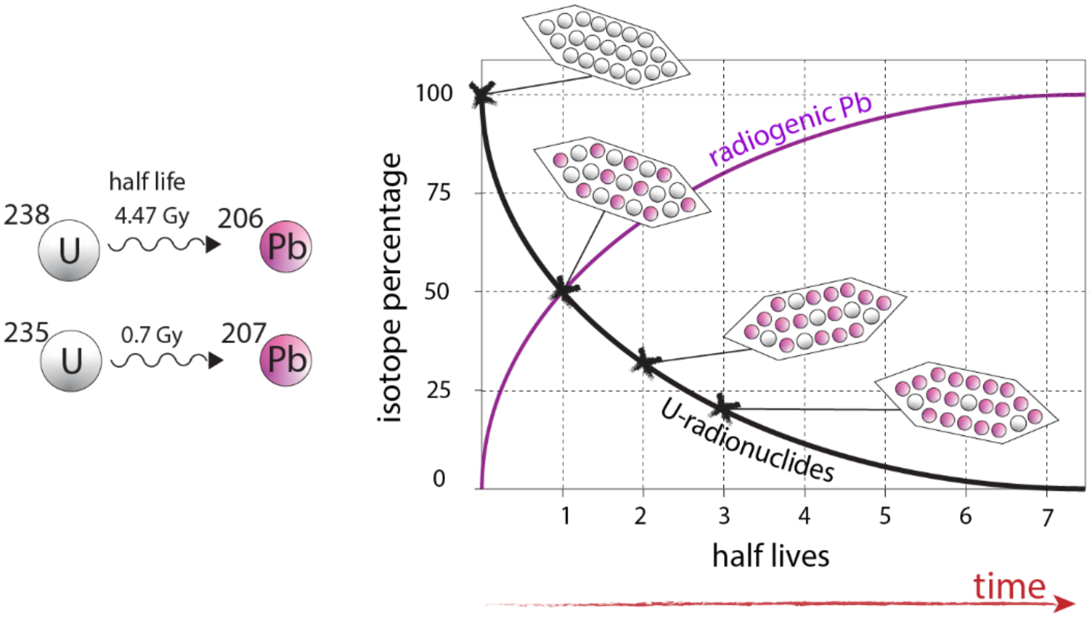

Figure 4. ^{238}U and ^{235}U are the 2 long half-life radionuclides of the Uranium used for U-Pb geochronology. They decay in radiogenic Pb (^{206}Pb and ^{207}Pb) according to 2 independent decay chains with associated half-lives. The half-life is the time necessary to transform half of the radionuclides in radiogenic Pb. The decay rate is exponential.

years for the ^{235}U-^{207}Pb decay chains. After one half-life has elapsed, half of the atoms of the father isotopes will have decayed into the daughter isotope (Fig. 4).

The two U- decays systems are represented by the Bateman equations (Bateman, 1910; Eq. 2.1 and 2.2):

$$^{206}Pb = {}^{206}Pb_0 + {}^{238}U\,(e^{\lambda_{238}t} - 1) \qquad \textbf{2.1}$$

$$^{207}Pb = {}^{207}Pb_0 + {}^{235}U\,(e^{\lambda_{235}t} - 1) \qquad \textbf{2.2}$$

where the subscript *0* refers to the initial concentration of that isotope or concentration of non-radiogenic Pb (i.e. common Pb), λ is the decay constant precisely determined by alpha-counting experiments and t is the time elapsed from initial crystallization to the present.

Mass spectrometric techniques employed to date, allow to collect more precisely the isotope ratios rather than the concentration of the single isotopes. Thus a reference stable isotope has to be used for normalization as a denominator of the decay equations. The ^{204}Pb is the only stable isotope of Pb and it is usually a common choice as a reference isotope.

By normalizing the equations 2.1 and 2.2 it results that

$$\frac{^{206}\boldsymbol{Pb}}{^{204}\boldsymbol{Pb}} = \left(\frac{^{206}\boldsymbol{Pb}}{^{204}\boldsymbol{Pb}}\right)_{\mathbf{0}} + \left(\frac{^{238}\boldsymbol{U}}{^{204}\boldsymbol{Pb}}\right)\left(\boldsymbol{e}^{\lambda_{238}\boldsymbol{t}} - \mathbf{1}\right) \qquad \mathbf{2.3}$$

$$\frac{^{207}\boldsymbol{Pb}}{^{204}\boldsymbol{Pb}} = \left(\frac{^{207}\boldsymbol{Pb}}{^{204}\boldsymbol{Pb}}\right)_{\mathbf{0}} + \left(\frac{^{235}\boldsymbol{U}}{^{204}\boldsymbol{Pb}}\right)\left(\boldsymbol{e}^{\lambda_{235}\boldsymbol{t}} - \mathbf{1}\right) \qquad \mathbf{2.4}$$

The following equation is obtained by dividing the equation 2.4 over the equation 2.3.

$$\frac{\left(\frac{^{207}\boldsymbol{Pb}}{^{204}\boldsymbol{Pb}}\right) - \left(\frac{^{207}\boldsymbol{Pb}}{^{204}\boldsymbol{Pb}}\right)_{\mathbf{0}}}{\left(\frac{^{206}\boldsymbol{Pb}}{^{204}\boldsymbol{Pb}}\right) - \left(\frac{^{206}\boldsymbol{Pb}}{^{204}\boldsymbol{Pb}}\right)_{\mathbf{0}}} = \left(\frac{^{235}\boldsymbol{U}}{^{238}\boldsymbol{U}}\right)\frac{\left(\boldsymbol{e}^{\lambda_{235}\boldsymbol{t}} - \mathbf{1}\right)}{\left(\boldsymbol{e}^{\lambda_{238}\boldsymbol{t}} - \mathbf{1}\right)} = \left(\frac{^{207}\boldsymbol{Pb}}{^{206}\boldsymbol{Pb}}\right)^{*} \qquad \mathbf{2.5}$$

Equation 2.5 is very useful because allows to avoid measuring ^{235}U concentration. ^{235}U has a natural smaller abundance and a shorter half-life if compared to ^{238}U, it derives that most of the primordial ^{235}U in the Earth has decayed. At present-day the ^{235}U/^{238}U ratio (in equation 2.8) is assumed to be a known constant in terrestrial and meteoritic systems and equal to 137.818 ± 0.045 (Hiess et al., 2012). Although its value, together with those of the decay constants, are still a matter of debate in the geochronological community (Craig et al., 2020). The only unknown in these equation remains the common Pb which represents the amount of Pb that do not derive from the decay of U.

There are several equations allowing the calculation of the common Pb composition and different diagrams have been used as convenient ways of displaying the isotope composition. In the following paragraphs the use of the Wetherill Concordia plot for zircon dating and of the Tera-Wasserburg Concordia diagram for carbonates dating are discussed.

Both approaches require introducing the Concordia curve. Here follows a general explanation of what the Concordia curve represents and how it is defined.

The Concordia curve (Wetherill, 1956) is a parametric curve that define the evolution of the radiogenic Pb ratios through time. In a closed system, the composition of a mineral that initially did not incorporate any Pb will plot directly on the Concordia curve in a position that provides the concordant age of the sample. On a simplified dual decay model with no common Pb incorporated, the equations 2.1 and 2.2 would be:

$$\boldsymbol{{}^{206}Pb} \;=\; \boldsymbol{{}^{238}U}\,(\boldsymbol{e^{\lambda_{238}t}} - \mathbf{1}) \qquad \mathbf{2.6}$$

$$\boldsymbol{{}^{207}Pb} \;=\; \boldsymbol{{}^{235}U}\,(\boldsymbol{e^{\lambda_{235}t}} - \mathbf{1}) \qquad \mathbf{2.7}$$

Since the two decay system develop in parallel within a given mineral, they should produce the same age (i.e. concordant age). Thus, the equations 2.6 and 2.7 can be combined in a diagram where the composition of a mineral at any given time is given by the coordinates X,Y

$$\boldsymbol{X_{axis}} \;=\; \left(\frac{\boldsymbol{{}^{207}Pb*}}{\boldsymbol{{}^{235}U}}\right) = \left(\boldsymbol{e^{\lambda_{235}t}} - \mathbf{1}\right) \qquad \mathbf{2.8}$$

$$\boldsymbol{Y_{axis}} \;=\; \left(\frac{\boldsymbol{{}^{206}Pb*}}{\boldsymbol{{}^{238}U}}\right) = \left(\boldsymbol{e^{\lambda_{238}t}} - \mathbf{1}\right) \qquad \mathbf{2.9}$$

The Concordia curve is obtained by plotting all the (X,Y) points in which the time (t) is equivalent in equations 2.6 and 2.7 (Fig 5).

The simultaneous use of the two decay chains is the most important value of the U-Pb chronometer because it provides a powerful internal quality check of the age obtained. If a mineral composition does not plot on the Concordia curve, the sample incorporated non radiogenic Pb or the isotope system was disturbed over time (opening system behavior).

It is worth mentioning that none of the U parent isotopes decays directly to Pb, but instead follows a sequence of alpha and beta decays that create a series of intermediate daughter isotopes and always lead to the same stable isotope of Pb (Bateman, 1910). In the ^{235}U/^{207}Pb and ^{238}U/^{206}Pb decay chains, the decay constants of all the intermediate daughter isotopes are order of magnitude higher than those of the parent radionuclide. This means that after a sufficient amount of time the activity (i.e. the product of the decay constant and concentration of an isotope) of all intermediate daughters is equal. This condition is defined ‘secular equilibrium’. Intermediate daughter isotope such as ^{230}Th are used to date young materials (<250 Ka) and may constitute a factor of discordance to be corrected (intermediate daughter product disequilibrium; Schoene et al., 2014).

In high U-bearing minerals such as zircon and monazite, most of Pb occurring is radiogenic and the eventual Pb initially incorporate can be neglected and occasionally corrected. Minerals such as apatites or carbonates may instead incorporate high amounts of Pb at the time of crystallization. For these types of minerals dating is done with a different approach: the isochron dating approach.

2.3 Zircon geochronology and chronostratigraphy

The U-Pb chronometer is commonly applied to date high U-bearing minerals such as zircon grains, because upon crystallization they incorporate amounts of U at the site of Zirconium ion (Zr) and virtually no Pb. This means that most of the Pb occurring in zircon grains has a radiogenic origin.

One of the most commonly used graphical representations for the U-Pb isotope composition of a zircon is the Wetherill Concordia plot (Wetherill, 1956; Fig. 5) which presents ^{206}Pb/^{238}U and ^{207}Pb/^{235}U isotope ratios on the x and y-axes, respectively. If no opening behavior occurred and the eventual common Pb was corrected, a single data point falling on the Concordia is sufficient to define

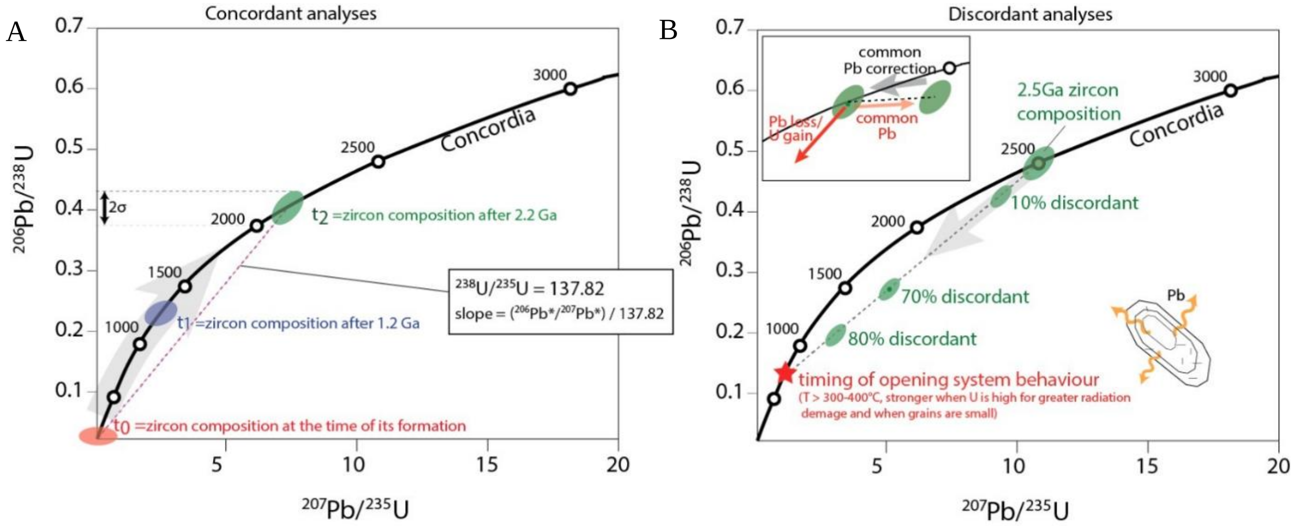

Figure 5. Synthetic examples of Wetherill Concordia diagrams. To the left. Concordant zircon composition from the timing of its crystallization (red spot) 2.2 Ga ago. To the right. Discordant analyses on zircon grains due to opening system behaviour or presence of initial non radiogenic Pb (common Pb).

an age. However, some geologic processes (e.g. metamorphism, fracturing and fluid migration) may cause U and Pb loss/gain in zircon and thus ages will not plot directly on the Concordia curve (Fig. 5B). Such minerals may also incorporate low amounts of Pb that can be generally corrected.

One approach is the common Pb correction based on Stacey & Krammers (1975) model of the Pb isotope composition of the Earth over time. The modeled isotope ratios values are substituted in the equation 2.5. On the Wetherill diagram, this would visually result in a shift of the data point to a position on the Concordia curve (Fig. 5B). There are various approaches to correct for common Pb and discordance. Further information is in the review Schoene et al. (2014).

Zircon U-Pb geochronology is commonly applied to date sedimentation of carbonate and siliciclastic rocks. This is done by dating zircon rich deposits such as volcanoclastic sediments (e.g. ash layers) interbedded within the sedimentary pile or by dating small quantities of zircon grains dispersed in sediments (i.e. detrital zircon geochronology). Zircon grains included in these deposits may be autocrysts (i.e. zircon grains belonging to the youngest magma pulse), antecrysts (i.e. zircon belonging to older magma pulses) and xenocrysts (i.e. zircon grains incorporated during magma transit) (Miller et al., 2007; Figure 3). Thus, zircon-based chronostratigraphy produces maximum depositional ages (MDA) which are well known proxies for the true depositional age (TDA) of the system (e.g. Wotzlaw et al., 2014; Rossignol et al., 2019). Two prerequisetes must be fulfilled in order to obtain the best assessment for the TDA of the host-rock. 1) The dated minerals must have crystallized during or shortly before the volcanic eruption (i.e. autocrysts); and 2) volcanic activity and sedimentation must be coeval (Rossignol et al., 2019).

To obtain the MDA of the host deposits, the youngest population of statistically meaningful, equivalent and concordant zircon grain ages have to be selected because, according to the law of inclusions, deposition must postdate the youngest constituent (Dickinson & Gehrels, 2009). Although various approaches exist to select the youngest population of zircon grains (e.g. Vermeesh et al., 2021), due to the sampling bias it is possible that the youngest population is not found in the ash layer/sediments. Various strategies are applied to overcome these limitations. One is the high-n sampling strategy which requires to sample at least 60-300 zircon grains to limit sampling bias (Sharman & Malkowski, 2020). Another reliable method consists of systematically comparing the MDA obtained from a set of samples along a stratigraphic section. If MDA become younger going upward in the section, this may suggest that the MDA provide the age of sedimentation. Moreover, prior to dating, reworking processes need to be carefully evaluated and zircon grains with magmatic composition need to be preferentially targeted.

2.4 Carbonate geochronology and U-Pb incorporation

Carbonates are low to intermediate U-bearing minerals (10 ppb to 100 ppm; Weyer et al., 2008; Nuriel et al., 2021; Fig. 6) that incorporate variable amounts of Pb at the time of crystallization (i.e. common Pb) resulting in a potentially high variability of the parent/daughter isotope ratio, usually expressed as µ (i.e. $^{238}U/^{204}Pb$). Carbonate ages obtained from the two decays chains are hardly concordant and their composition will plot out of the Concordia curve.

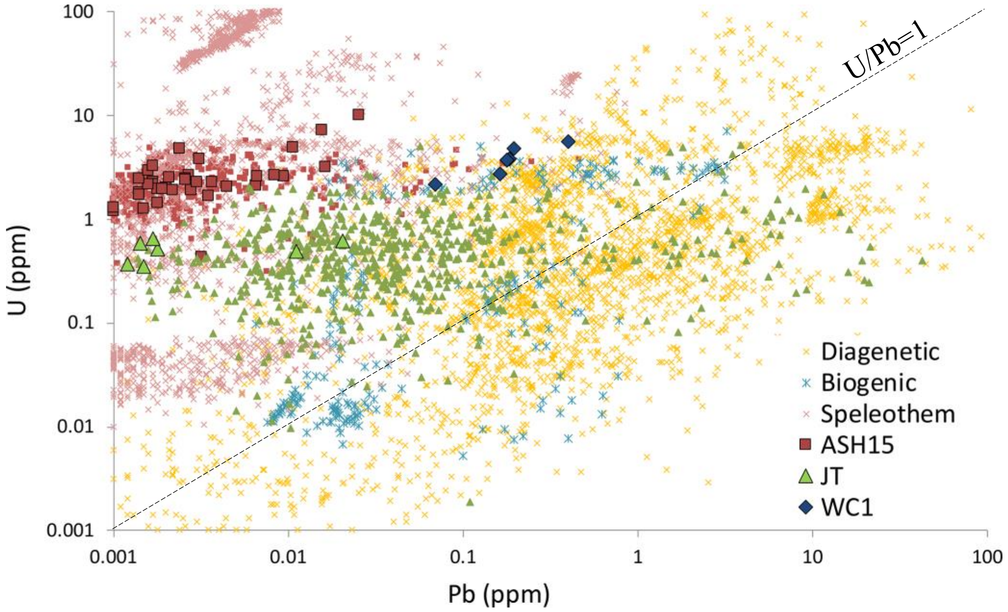

Figure 6 Uranium (U) and total lead (Pb, including common and radiogenic) contents of various carbonate materials based on a compilation from Nuriel et al. (2021). ASH-15D, JT and WC 1 are currently used carbonate reference materials (RM).

The amount of common Pb is evaluated with the isochron method (Moorbath et al.,1987; Jahn & Cuvellier, 1994) requiring to perform multiple analyses on the same carbonate phase. If coeval carbonate minerals evolved from the same inherited Pb composition (e.g. multiple analyses on the same carbonate), they will form a straight line with age significance on a plot within $^{20x}Pb/^{204}Pb$ vs $^{23x}U/^{204}Pb$ space. The regression line of the data points is named isochron and consist of a mixed line between a total common Pb composition (i.e y-intercept) and a total radiogenic composition (x-intercept) (Fig. 7). Carbonate U-Pb isotope composition is usually plotted on a 3D Tera-Wasserburg Concordia diagram (TW diagram; Tera & Wasserburg, 1972a; 1972b) that include both decay chains (Fig. 7) and it is the inverse of the Concordia diagram (Equations 2.8, 2.9). The TW Concordia diagram presents the $^{238}U/^{206}Pb$ ratio on the x-axis and the $^{207}Pb/^{206}Pb$ on the y-axis and also contains the Concordia curve previously discussed. Here, a single U-Pb datapoint composition will plot with the following coordinates:

$$\boldsymbol{X_{axis}} = \left(\frac{^{238}\boldsymbol{U}}{^{206}\boldsymbol{Pb}*}\right) = \frac{\mathbf{1}}{(\boldsymbol{e}^{\lambda_{238}t} - \mathbf{1}\,)} \qquad \mathbf{2.10}$$

$$\boldsymbol{Y_{axis}} = \left(\frac{^{207}\boldsymbol{Pb}*}{^{206}\boldsymbol{Pb}*}\right) = \boldsymbol{k}\,\frac{(\boldsymbol{e}^{\lambda_{235}t} - \mathbf{1}\,)}{(\boldsymbol{e}^{\lambda_{238}t} - \mathbf{1}\,)} \qquad \mathbf{2.11}$$

where k is the present-day U ratio (^{235}U/^{238}U = 1/137.88). The Concordia curve is obtained by considering the same t in the equations 2.10 and 2.11.

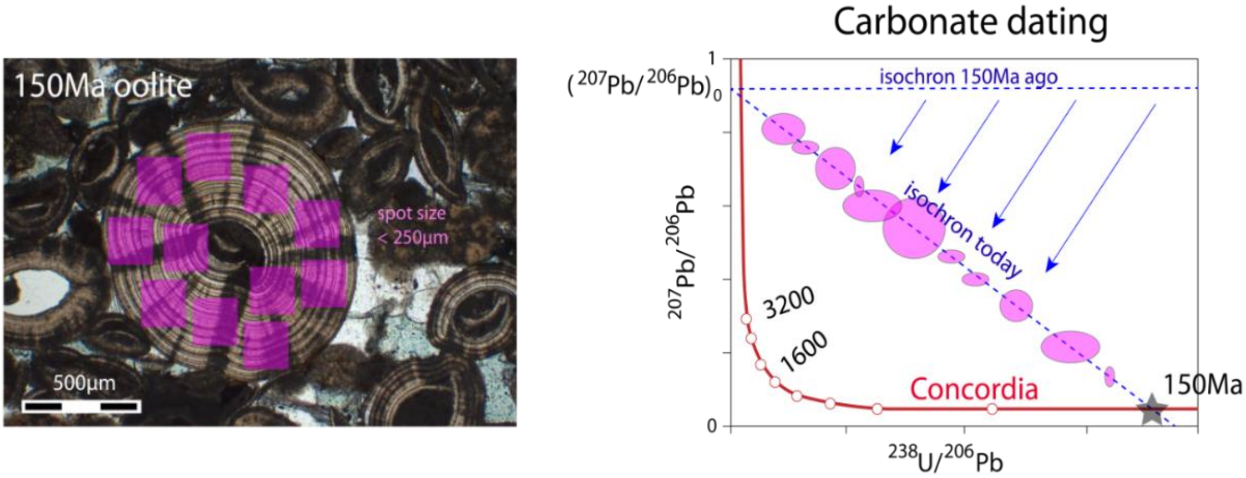

Figure 7. U-Pb geochronology on carbonates and associated Tera-Wasserburg (TW) Concordia diagrams. To the left. Petrographic image of an oolitic grainstone. The purple squares represent the size of the ablation pits. To the right. Tera Wasserburg Concordia diagram. Each purple ellipse represents a single analysis and relative ^{238}U/^{206}Pb and ^{207}Pb /^{206}Pb isotope ratio values. The major and minor axis of the ellipses indicate the uncertainties of the two measured ratios. In ideal conditions at crystallization time the U/Pb isotope ratios are heterogeneous and Pb/Pb ratio is homogeneous resulting in a horizontal regression line (the isochron, dotted blue line). As time passes and radioactive U decays in radiogenic Pb, the regression line will increase its slope and intersect the Concordia curve in a position which indicates the age of the sample. The upper intercept between the regression line and the y-axis is the initial ^{207}Pb /^{206}Pb composition of the mineral.

The initial composition of a carbonate (at t_0) will plot on a TW Concordia diagram as a set of data points aligned along a horizontal regression line. Over time, U isotopes of each data point decay in Pb in a predictable way resulting in a progressive decrease of the slope of the regression line. The age of the carbonate formation is obtained by the lower intercept between the regression line and the Concordia curve. For this reason, it is named 'lower intercept age'.

In order to produce a robust and meaningful age from a carbonate sample, few prerequisites must be fulfilled: a) the initial ^{207}Pb/^{206}Pb composition has to be homogeneous; b) there must be a sufficient spread of the µ ratio and preferentially high µ values; c) the isotope system has to remain closed (Fig. 8). Each of these three conditions is necessary, though not sufficient for a carbonate to be successfully dated. The first two prerequisites are linked to the behavior of U and its daughter isotopes in aqueous systems and their sequestration in carbonates. The complexity of carbonate systems may easily result in Pb isotope heterogeneity or in homogeneous ^{238}U/^{206}Pb, both hindering successful dating. Another fundamental factor to consider is the impact of diagenesis that may modify the pristine isotope composition and thus age.

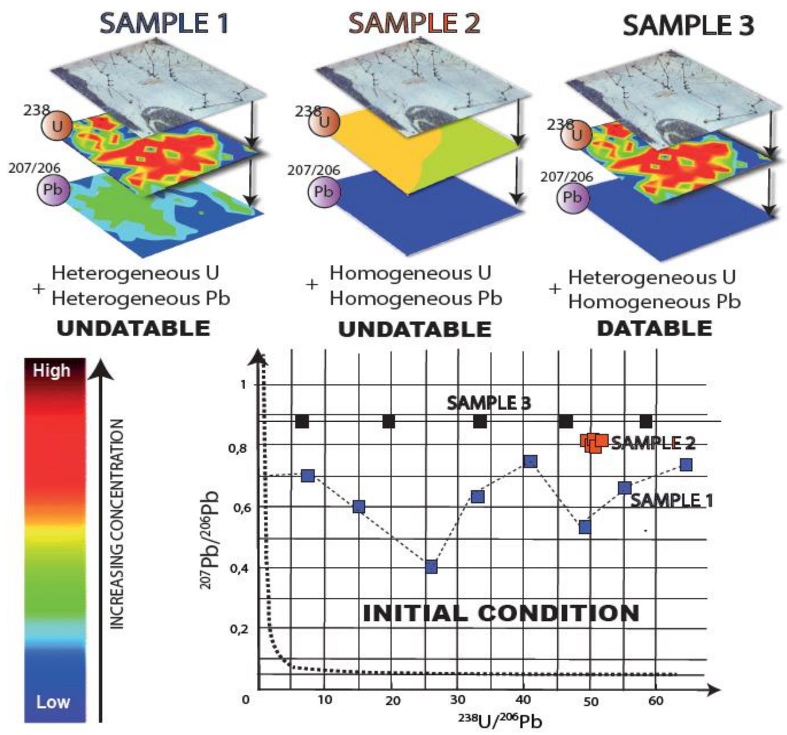

Figure 8. Initial concentration of the U and Pb isotopes which makes the sample suitable to be dated. Three end-members are shown. Sample 1 and sample 2 represent the initial conditions unsuitable for dating where both U and Pb are heterogeneous or homogeneous. Sample 3 represents the ideal initial conditions for dating: when U is heterogeneous and Pb is homogeneous the sample is datable. Below, the hypothetical U-Pb analysis on these 3 samples are shown in a Tera-Wasserburg Concordia diagram where the Concordia curve is represented by the dotted line. From Mangenot, 2017.

The mechanisms for U and Pb incorporation and disturbance in carbonates during deposition and diagenesis are not well understood because they do not rely on thermodynamically determined partition coefficients, but on a large number of phenomenological variables. These include trace element availability, calcite growth rate, temperature, pH, Eh, pCO_2 and the Ca^{2+}/CO_3^{2-} ratio in solution, ionic size, and U complexation (Roberts et al., 2021). The complexity of this phenomenon results in an unpredictable U-Pb isotope concentration. In fact, carbonates formed by the same fluid are generally characterized by different U and Pb concentration. For example, coeval marine carbonates from the present day Bahamas bank showed highly variable average concentrations of U (~0.03 in mollusks shells and ~3.5 ppm in ooids, Chung & Swart, 1990; Romaniello et al., 2013).

Specific initial composition of carbonates is required to produce robust U-Pb ages (Fig. 8) and while the spread of U-Pb ratio matters for dating, it is usually the U concentration that limits the dating potential (Rasbury et al., 2021). At today the promising circumstances for U heterogeneous sequestration and Pb rejection in carbonates are not fully understood this hindering to evaluate the dating potential of different carbonates and precipitation conditions and limiting the interpretation of the derived U-Pb ages. In the last years, geochronology-focused studies about the U incorporation in carbonates flourished (e.g. Rasbury & Cole, 2009; Kelly et al., 2003, Roberts et al., 2021; Miyajima et al., 2020). This chapter is a state of the art of the present knowledge of the mechanisms for U-Pb sequestration in carbonates.

Pb and U are known to be syn-genetically incorporated in carbonate lattice substituting for the Ca^{2+} ion or adsorbed as inner sphere complexes which means that are bind to the calcite surface through covalent bonding (Fig. 9).

Pb^{2+} cation is relatively insoluble and particle reactive and in natural fluids it is found at very low levels (ppt–ppb) providing high Ca/Pb ratio. Despite the slightly larger radius of Pb^{2+} relative to Ca^{2+} (Shannon, 1976; Rouff et al., 2004), it shows affinity for calcite substituting Ca^{2+} in the crystal lattice and mostly occur as an inner sphere complex (Rasbury & Cole, 2009).

The incorporation of U in carbonates is instead a complex process, less understood. The speciation of U in the fluid is strictly linked to low-temperature redox conditions of the fluid whereas the solubility depends mainly on Eh and Ph (e.g. Klinkhammer & Palmer, 1991; Seder-Colomina et al., 2018). U has then two commonly identified redox states: U^{+4} (more common in reducing environments) and U^{+6} (more common in oxic environments such as soils, surface waters, oxidized seawater and groundwater). U^{4+} has an ionic radius similar to Ca^{2+} (0.89 Å in six-fold coordination;

Shannon,1976) and thus should be ideally incorporated into carbonates. However, U^{4+} is mostly insoluble in natural systems and it is usually sequestered by other minerals precipitating in reducing environments (e.g. uraninite). No lab experiment at low temperature have demonstrated the incorporation of U^{+4} in carbonate, however: 1) patterns of elevated U concentration are known to occur in natural carbonates with reduced U (e.g. Klinkhammer & Palmer, 1991; Sturchio et al., 1998; Cole et al., 2004); 2) progressively higher U concentrations found down core in the Bahamas deposits where other geochemical parameters (Mo, V, Cr and Co) suggested higher reducing conditions (Wray et al., 2018); and 3) particularly high U concentrations were detected in cements precipitated in deep anoxic groundwaters (Drake et al., 2018). Thus, reducing conditions should generally promote the incorporation of U in carbonates. A possible explanation for U^{4+} incorporation is provided by Rasbury et al. (2021). Based on the high concentration found is lacustrine tufa mounds of the Barstow Fm. and Mono lake carbonates, they hypothesized that U^{+4} could have been complexed with some oxyanion (e.g. phosphate, bicarbonate) in the lake bottom waters and then incorporated during carbonate formation. Conclusively, it appears that U^{4+} is the most stable specie of U in carbonates (Roberts et al., 2021).

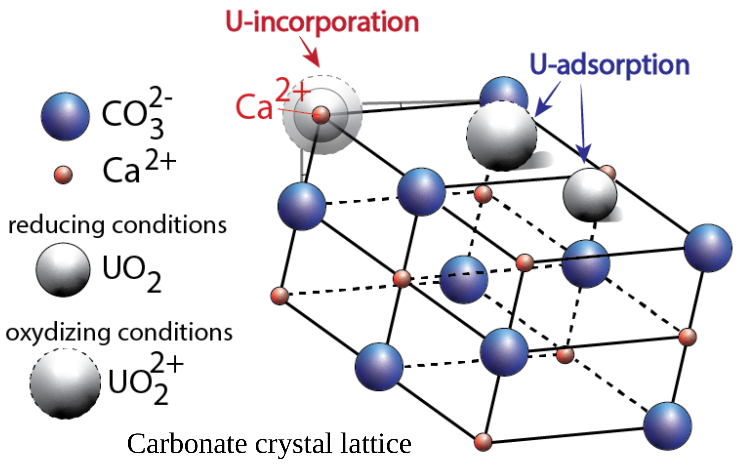

Figure 9. In natural aqueous systems U occurs in two oxidation states: U^{+4} and U^{+6}. U^{+4} (in reducing environments) forms UO_2. U^{+6} (in oxidizing environments) forms Uranyl (UO_2^{2+}) ion. These two compounds can be adsorbed on the carbonate crystal lattice surface or be syn-genetically incorporated at the site of Ca^{2+} ions, inducing a lattice distortion. Uranyl ion is larger than UO_2 and Ca^{2+} sites and for this reason it has lower affinity with carbonates.

In oxic conditions U^{+6} exists in the form of uranyl complex (UO_2^{2+}) (Langmuir, 1978) and it is more soluble if compared to U^{+4}. Uranyl ion is larger than UO_2 and Ca^{2+} sites. Thus, due to the larger size and higher solubility in natural fluids, its occurrence in carbonates was a long-standing problem. Kelly et al. (2003) and Reeder et al., (2001) demonstrated that Uranyl can be syn-genetically incorporated in carbonates at the site of Ca^{2+} ions inducing a lattice distortion and be long-term sequestrated (Kelly et al., 2003; 2006).

Uranyl and U-rich minerals (e.g. uraninite) formed in reducing conditions can also be adsorbed to the crystal lattice surface (Carroll et al., 1992, Geipel et al., 1997, Elzinga et al., 2004, Rihs et al., 2004). This adsorption process is influenced by the speciation of U^{+4}, the Ca concentration in the fluid, the Ph and the biogeochemical processes (i.e. the presence of organic matter and its interaction with iron and manganese oxids). In particular, when Ph > 7 the % of U^{+4} adsorpted via inner sphere complex strongly decreases whereas more acidic Ph promote adsorption (e.g. Elzinga et al., 2004).

Different carbonate pseudomorphs are also characterized by different U concentrations. Using modern settings and a laboratory understanding of trace element incorporation, it is known that U incorporation is higher in aragonite > high Mg calcite> calcite (Chung & Swart, 1990; Reeder et al., 2001). This is possibly due to a size mismatch between U and Mg which is greater than the one with Ca (Rasbury & Cole, 2021). No experimental study is available for the incorporation of U in dolomites. However, due to the similar structures it is expected that dolomite incorporates similar U concentrations than high Mg calcites (e.g. Rasbury et al., 2021).

Organic matter (OM) degradation and bacterial activity play a pivotal role in the incorporation of U with processes of direct enzymatic reduction, biosorption, biomineralisation and bioaccumulation (e.g. McManus et al, 2006; Weyer et al., 2008; Tribovillard et al., 2011). The major effect is given by the induced changes of redox conditions. Since deposition, the degradation of the OM in sediments progressively reduces the levels of O (higher reducing conditions down-core) and increases CO_2 (promotes carbonate precipitation). The higher reducing conditions of the pore fluid induce a reduction of U^{+6} to U^{+4} thus promoting the sequestration of U into carbonates.

Alkalinity may also be a factor influencing U incorporation as it has been demonstrated that alkalinity is responsible for the elevated actinide group concentration in carbonates (e.g. Anderson et al., 1982; Simpson et al., 1982).

Although it is not clear how the interaction between these factors affects U sequestration in carbonates, it was underlined that specific carbonate types are characterized by high and heterogeneous U concentrations and lower and homogeneous Pb concentration (Rasbury & Cole, 2009 and Roberts et al., 2021). These are speleothems (e.g. Woodhead et al., 2006; Woodhead & Petrus, 2019), hardgrounds, aragonitic carbonates or generally carbonate that have an aragonite precursor (Roberts et al., 2020a; Nuriel et al. 2021; Fig. 6).

2.5 Dating techniques. ID-TIMS and LA-ICPMS

Until the last decade, most carbonates were considered undatable due to the low/undetectable concentration of U and Pb isotopes (Chapter 2.4) and the low special resolution of available sampling techniques. Progressive analytical advances are allowing to date carbonate phases which were previously considered impossible to date. Initially, sampling was performed via isotope dilution (ID) and the Thermal ionization mass spectrometer (TIMS) was employed to measure isotope ratios (i.e. ID-TIMS U-Pb carbonate geochronology). ID-TIMS is known to produce the most accurate assessment for the age of a sample (e.g. Roberts et al., 2020a) and do not require a solid reference material. However, it has few disadvantages:

1) sampling requires a clean laboratory facility and a long analytical time with relative high costs,
2) aliquots of the material need to be sampled by drilling or eventually micro-drilling (Fig.10). Moreover, low U-bearing minerals require a high volume of material to be samples. This hinders to date poorly voluminous carbonate phases (e.g. fringes of cement), increase the risk of mixing adjacent carbonates and homogenizes the small scale isotope ratios heterogeneity (i.e. averaging effect, Roberts et al., 2020a) possibly degrading the accuracy of the final ages (e.g. Moorbath et al., 1987; Li et el., 2014),
3) in order to target carbonate phases with promising isotope composition and limit the costs, prior to date it is desirable to map the isotope concentration with other techniques (e.g Drost et al., 2018).

For these reasons, ID-TIMS is usually employed to precisely date voluminous carbonates phases and thus it is of prime importance to accurately estimate the age of the reference material (RM). This is essential for successful dating and interlaboratory comparison.

The Laser ablation inductively coupled plasma mass spectrometer (LA-ICPMS) has become a central analytical technique for carbonate dating because it has several advantages if compared to ID-TIMS based geochronology.

1) A clean laboratory facility is not necessary and sample preparation is minimal.
2) LA-ICPMS has high spatial resolution. Sampling is performed directly on this section or slab via Laser ablation. Ablation spots usually have diameter around 100-200 µm. The carbonate material required to produce one aliquot (i.e. one data point) is of about 5µg against 5-20mg for solution based analyses (Axel Gerdes, pers. Comm) (Fig. 10)

3) It is possible to perform a pre-screening of a large number of samples in order to choose those suitable for geochronology in a relative short period of time and for little cost, without necessarily involving other mapping techniques.
4) U and Pb isotope detection limit is down to 0.1-0.4ppb, which is ideal for low U-bearing minerals such as carbonates.

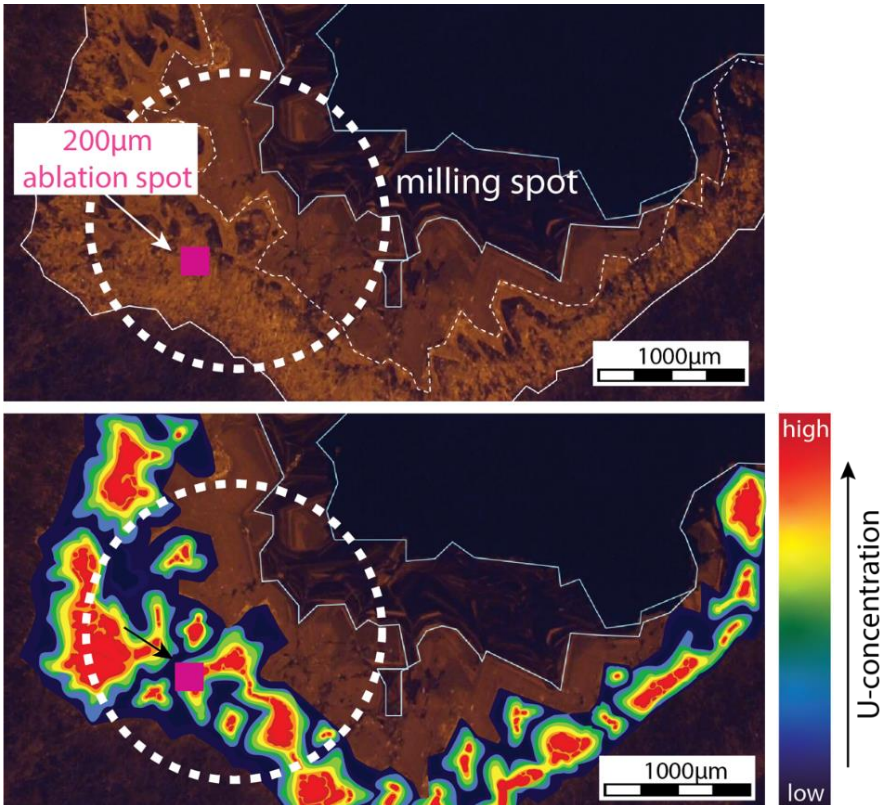

Figure 10. ID-TIMS vs LA-ICP-MS. The first image is a Cathodoluminescence (CL) view of a carbonate sample where 4 different carbonate phases occur. Each phase precipitated in a specific time. The sampling through milling required for ID-TIMS analysis is not capable to isolate the carbonate phases, causing mixing of the 4 age domains and relative U-Pb isotope compositions. The ablation pit (pink square, 200 µm by side) used in the LA-ICP-MS method allow to limit mixing among phases. Conceptual model.

Age produced by LA-ICPMS are known to be less precise than those produced by ID-TIMS (Li et al., 2014; Roberts et al., 2020a). Indeed, LA-ICPMS has an about 10-20 lower analytical precision for each analyses (Axel Gerdes pers. Comm.). Nowadays, it has been demonstrated that ID-TIMS dating does not always lead to an improvement in accuracy on the regressed ages because the averaging effect may limit targeting the spread of isotope ratios (Roberts et al., 2020a). This results specifically important in carbonate samples with high µ variability. In order to accommodate the lower precision of LAcarb ages, high-n (i.e. n=number of analyses on which the regression line is produced) are recommended when dating by LA-ICPMS. At least 20-30 analyses are considered sufficient to produce robust LAcarb ages (Beaudoin et al., 2018; Godeau et al., 2018; Yokoyama et al., 2018) although the appropriate number is strongly sample-specific and depends on the variability of the initial isotope content (Guillong et al., in revision).

One another limitation of the LAcarb compared to the ID-TIMS dating is the need to normalize the carbonate isotope composition to the one of a matrix-matched carbonate reference material. A matrix-

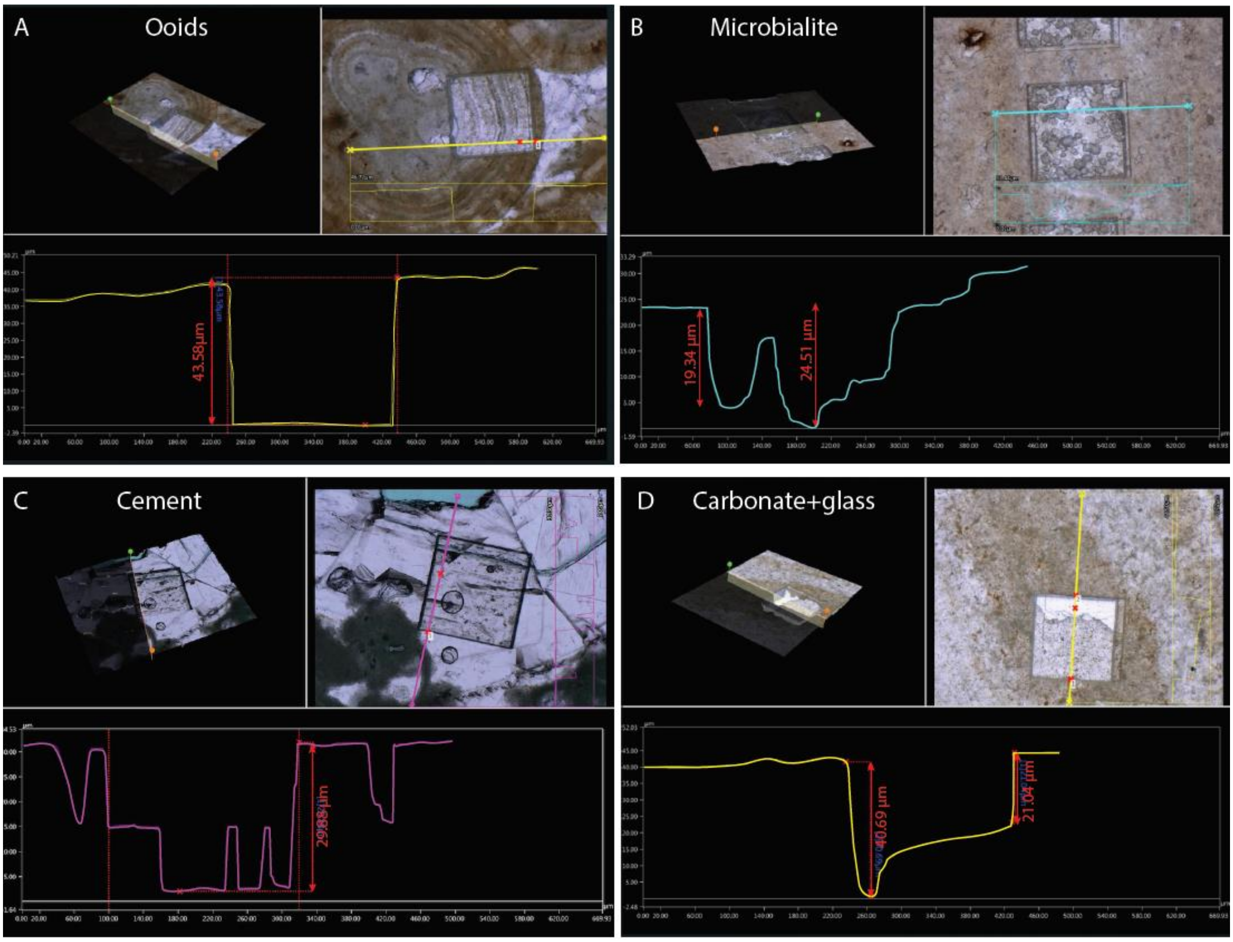

Figure 11. Profiles and depth of ablation craters (square ablation spot of 193µm) in different carbonate types. The depth and profile of the crater depth induces a bias in the volume of material ablated, this possibly affecting the final age results. A) Regular crater in calcitic ooid. B) Irregular crater in calcitic microbialite reflecting internal heterogeneity. C) Irregular profile in a calcitic cement. This type profile may be caused by the different optical properties at the contact between calcite crystals. D) Ablation crater that reaches the thin section glass. In correspondence with the glass the crater is deeper due to the different optical properties. Images and graphics were produced with the Digital Microscope VHX-6000 in the department of Petrology and Geochemistry of Goethe Universität of Frankfurt am Main.

matched reference material (RM) is required because optical and chemical properties of the sample to be dated induce changes in ablation speed (and volume of ablated material) as well as processes of inter and intra element isotope fractionation at the laser pit site and into the plasma (e.g. Eggins et al., 1998). This results in a bias between real isotope composition and the measured. Other factors may be involved. These are the shape and size of the ablation pit, the carbonate mineralogy (Elias et al., 2021; Nuriel et al., 2021) and the fluency chosen. Nuriel et al. (2019) noted differences between the use of coarse-grained sparry RM to fine-grained polycrystalline RM, with the latter being skewed towards older ages by several percent. In this respect, figure 11 shows the different ablation profiles obtained with the same analytical conditions from various materials. To move toward better precision and accuracy of LAcarb it will be necessary to have a range of well characterised reference materials that cover variable carbonate mineralogy (e.g. aragonite, dolomite, calcite), as well as internal morphology and texture.

An ideal matrix-matched RM is usually characterized by homogeneous isotope composition and/or ratios. As extensively discussed in the previous sections such conditions are hardly meet in natural carbonates and since the processes for U-Pb incorporation in carbonates are not fully understood, producing a synthetic RM with homogeneous composition is not an easy task. Recently, few synthetic calcite carbonate standards were proposed and are currently tested as secondary RM (e.g. Miyajima et al., 2020). In the absence of a homogeneous synthetic carbonate RM, Chew et al. (2014) proposed for LAcarb the use of a natural carbonate sample characterized by a most possibly concordant age (i.e. all age data points fall on the Concordia curve) or by an isotopically heterogeneous composition which falls along a mixing line between initial common Pb and radiogenic components (Fig. 12).

The U content of this type of RM has to be not excessive to match signal counts between the reference material and un-knowns material analysed (Roberts et al., 2017) and ideally it should have a radiogenic Pb composition > 98% (i.e. its composition plots nearby the Concordia curve; Fig. 12A). Young carbonates are not good candidates because they contain more common Pb than radiogenic. Indeed, a sufficient amount of time is necessary for the radiogenic Pb to dominate the Pb isotope composition and make the common Pb amount almost negligible (Roberts et al., 2017). Available natural carbonate RMs for LAcarb are WC1 (Roberts et al., 2020a; Fig. 12A), ASH-15D (Mason et al., 2013; Nuriel et al., 2021; Fig. 12B), JT (Looser et al., 2020; Guillong et al., 2020); AHX-1a (Cheng et al., 2020) plus few others which are currently tested in different facilities. However, none of these standards is ‘perfect’. For example, WC-1 is the most used RM. It has a natural 2–3% excess scatter about the regression line (e.g. the ellipses on the Tera-Wasserburg diagram are not well aligned) and variable amounts of common Pb (>2%) that can be minimized by data treatment.

Reference materials with poor scatter around the U/Pb regression line are therefore a pre-requisite for improving LAcarb dating.

Details on the LA-ICPMS method for carbonate adopted by three major laboratories taking a similar approach are provided in Roberts & Walker (2016) and Drake et al. (2017) for the British Geological Survey laboratory (Nottingham, UK); Ring & Gerdes (2016) and Methner et al. (2016) for Goethe-Universität (Frankfurt, Germany), and Nuriel et al., (2017, 2019, 2021) for University of California Santa Barbara (Santa Barbara, USA).

Other techniques of data acquisition, such are the SIMS (U-Pb dating) are now emerging and are currently refined to be suitable for carbonates dating. An exhaustive review of pro and cons for each dating technique is provided by Kylander-Clark (2020) and Hoareau et al. (2021).

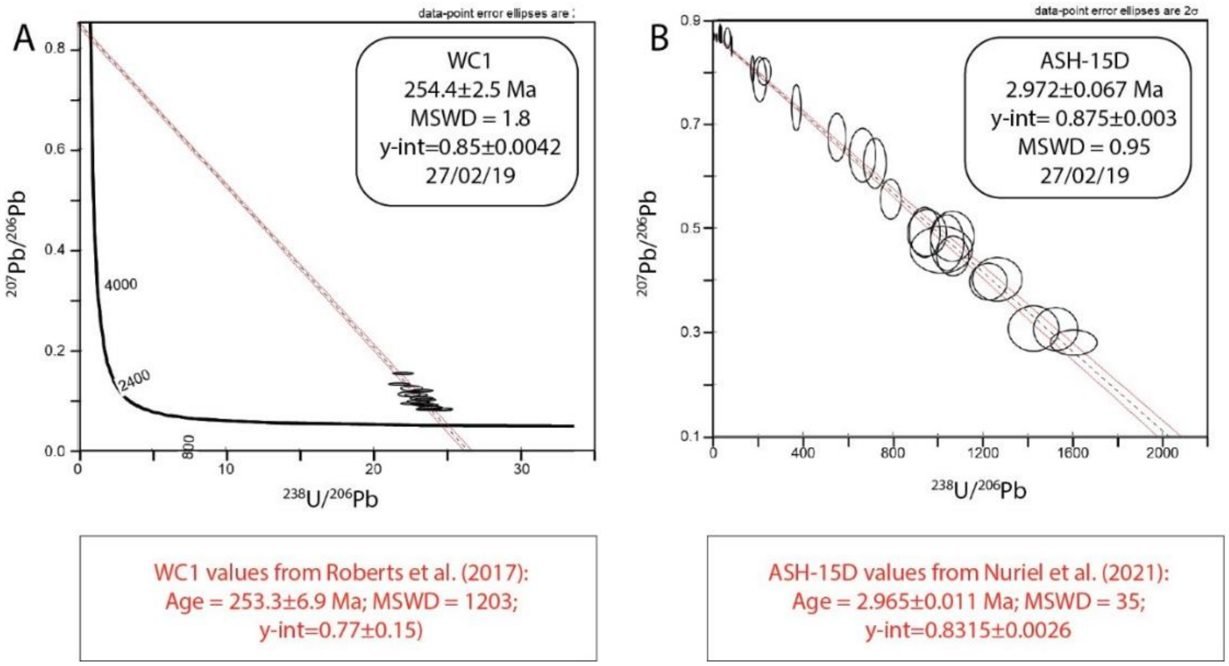

WC1 values from Roberts et al. (2017):
Age = 253.3±6.9 Ma; MSWD = 1203;
y-int=0.77±0.15)

ASH-15D values from Nuriel et al. (2021):
Age = 2.965±0.011 Ma; MSWD = 35;
y-int=0.8315±0.0026

Figure 12. Tera-Wasserburg Concordia diagrams obtained by LA-ICPMS for WC1 and ASH15D carbonate reference materials. A) WC1 reference material has > 98% radiogenic Pb composition. Isotope ratio data-points are almost on the Concordia curve (black curve). B) ASH15D reference material has high µ ratio heterogeneity and radiogenic Pb composition < 80%. The isotope ratio data points fall on a mixed line between a total common Pb composition (upper y-intercept) and a total radiogenic composition (intercept with the Concordia curve, not reported).

3 METHODS

3.1 Zircon (ash layer) analysis: from sampling to dating

Volcanic ash samples (2-4 kg for each sample) were prepared for petrographic analysis and isotope dating in the Institute of Geosciences Johann-Wolfgang-Goethe University Frankfurt (Germany) (Fig. 13). Samples were fragmented with high voltage discharge using a SelFrag Lab system. Mud was removed via multiple cycles of washing and decantation in a Becher. Powders were then dried overnight at 200°C and sieved for a fraction < 280 µm using disposable Nylon sieves. Heavy grains were then separated through manual panning. Up to 182 zircon grains were randomly handpicked for each ash layer sample to get a representative selection of the overall zircon populations and to minimize sampling bias. Zircon grain were grouped according to the size, embedded in epoxy resin mounts, ground down to about half their thickness and then polished.

Zircon petrography was achieved under binocular and was followed by Scanning Electron Microscope (SEM) analysis. Cathodoluminescence (CL) and back scattered electron (BSE) images

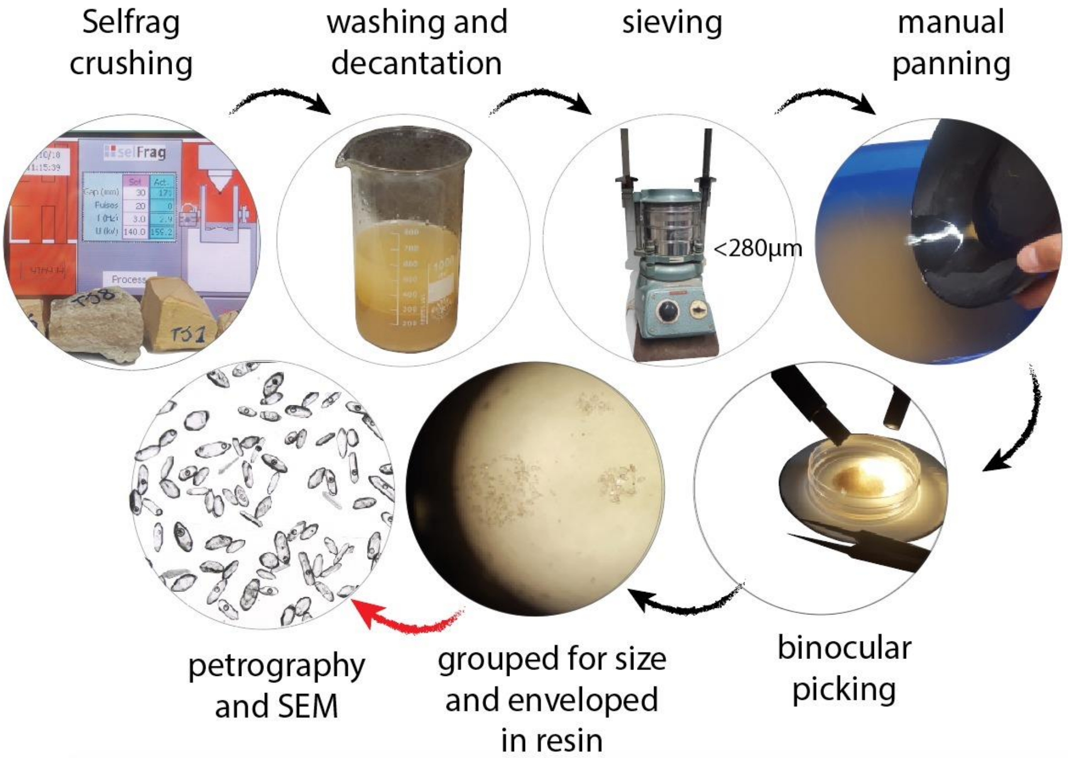

Figure 13 Procedure of zircon grains separation from volcanic ash, from Self rag crushing to petrography and SEM.

were acquired using a JEOL JSM-6490 SEM. Zircon grains of magmatic origin. (prismatic habitus and oscillatory zoning; Corfu, 2012) were then selected for analysis to maximize the chances to determine the youngest zircon crystallization event.

Zircon grains from the ash layers sampled were analysed for U, Th and Pb isotope by LA-ICPMS at FIERCE (Frankfurt Element and Isotope Research Centre), Goethe University Frankfurt following the methods described by Gerdes & Zeh (2006, 2009). Further details are in Montano et al. (in revision, Section 6.1).

3.2 Carbonate petrography, geochemistry and LAcarb

Thin sections (50-60µm thick) were prepared for each carbonate sampled both at IFPEN laboratories (Rueil Malmaison, France) and at the Thin Section Lab (Toul, France). Manual hand-polishing was performed on half of these sections.

The sections were analysed under optical and cathodoluminescence (CL) microscopy in order to characterize the different depositional facies and identify various depositional and diagenetic carbonate phases. Additionally, petrography aimed at selecting carbonate phases that showed no major evidence of post-depositional diagenetic modification. Conventional optical petrography was performed using a Nikon ECLIPSE LV100 POL polarized light microscope and allowed observations under plane- and cross-polarized light (PPL and XPL). Cathodoluminescence (CL) microscopy was accomplished with a cold CL apparatus (8200 Mk5 CITL). The electron beam worked under vacuum (< 0.1 mbar) with acceleration voltage of 10 kV, and current of 250 µA. All thin sections were partially stained with a solution of 10 % diluted HCl, Alizarin Red-S and potassium ferricyanide (Dickson, 1966). Calcite cement habitus and dolomite textures were described based on Flügel (2004) and Sibley & Gregg (1987) classification, respectively.

The C-O stable isotope signature was obtained from the different carbonate phases occurring in the samples because bulk analysis was considered unsuitable for the purpose of this study. Carbonate powders were carefully extracted from polished rock slabs by means of a dental drill (Dremel 225, drill tip size of 0.8mm) under a binocular microscope or directly from thin sections by a software-controlled MicroMill device (New wave research; drill tip size 75µm). Analyses were achieved at the Geozentrum Nordbayern (Germany) by Prof. Micheal Joachimski. Powders were reacted with 100% phosphoric acid at 70◦C using a Gasbench II connected to a ThermoFisher Delta V Plus mass spectrometer and analysed for C and O stable isotopes The $\delta^{13}C$ and $\delta^{18}O$ values for carbonates are reported in ‰ relative to Vienna Pee Dee Belemnite (V-PDB) standard. Reproducibility and accuracy were monitored by replicate analysis of laboratory standards NBS19 and IAEA-CO9. Reproducibility for $\delta^{13}C$ and $\delta^{18}O$ values measured on the studied carbonates was ±0.04x and ±0.03y (1 std.dev), respectively. Oxygen isotope values reported for dolomite, were not corrected with the phosphoric acid fractionation.

The workflow followed for LAcarb dating samples preparation is in figure 14.

3.2.1 U-Pb Carbonate geochronology via LAcarb

Sample preparation and LA-ICPMS device. Thin sections were resized with a diamond blade to reach the size of 2.7 x 2.1 cm in order maximize the number of samples for each analytical session. Then they were cleaned in an ultrasonic bath with ethanol for 5 minutes, dried with sterile paper and inserted in the instrument holder (Figures 14 and 15). In order to have a natural light vision and better discriminate the carbonate phases during the LA-ICPMS analysis, each holder was scanned with a Resolution of 1200dpi. The image acquired was shown during the LA-session in parallel with the fast CCD-camera image (Figures 15 and 16).

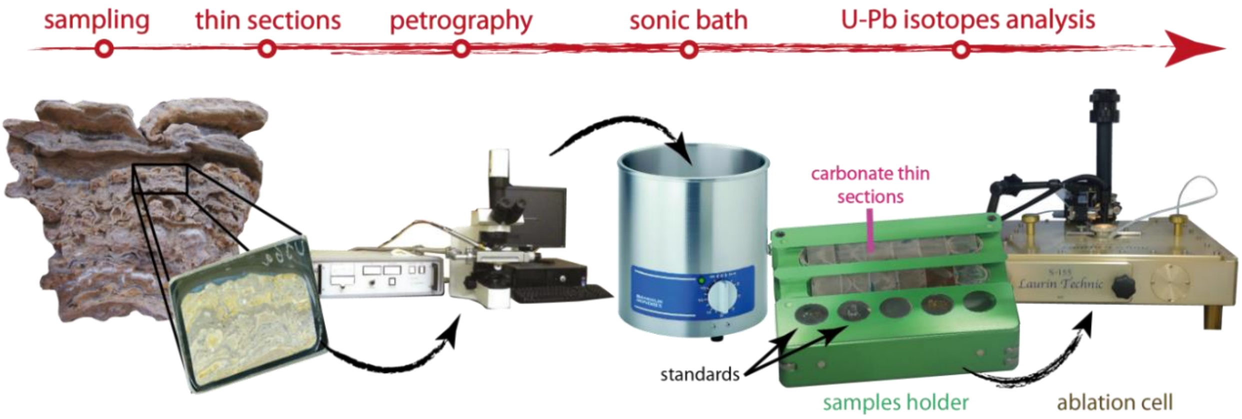

Figure 14. From sampling to U-Pb carbonate analysis. 60µm thick thin sections are prepared and analysed by optical and cathodoluminescence microscopy in order to select the syn-sedimentary phases which do not show evidence of later diagenetic overprint (e.g. recrystallization). Thin sections are cleaned in a sonic bath of ethanol (5% mol/L) for 5 minutes, dried in a sterile paper and inserted in the samples holder together with the 4 standards (cylindrical wafers): 2 NIST glass and 2 carbonates. The holder is inserted in the ablation cell (Laurin Technic, Australia).

Carbonate thin sections were analysed in 8 U-Pb analytical sessions at FIERCE, Goethe University Frankfurt (Germany). Analyses were carried out with a Laser Ablation Inductively coupled plasma mass spectrometer (LA-ICPMS) consisting in a Thermo Scientific Element 2 Xr sector field ICP-MS coupled to a Resolution S-155 (Resonetics) 193 nm ArF Excimer laser (CompexPro 102, Coherent) equipped with a two-volume ablation cell (Laurin Technic, Australia) (Fig. 17).

The ablation is performed in-situ (directly on samples) in a helium atmosphere (300 ml/min). Being carbonates very low to intermediate U-bearing minerals and also soft materials, a squared ablation spot of 143-213µm in side was chosen. LA-ICPMS device laser can reach 30µm in side, but a sufficient amount of material needs to be ablated in order to keep the U-signal high and thus higher diameters are recommended for carbonate dating. The laser beam (8 Hz frequency and fluency of about 2 J/cm^2) impacts the sample surface inducing thermal vaporisation and atom ionization in a process called 'laser ablation'. The aerosol produced–is transported into the ICP-MS device by a constant flux of argon (Ar, 1 L/min) and nitrogen (N_2; 8 ml/min) (i.e. carrier gas) and introduced into an argon plasma torch that dissociate the molecules (i.e. atomization) and ionize the elements. The excited ions are pass through the skimmer cone to reach the detector for elemental and isotopic analysis. Ions are deflected according to their mass/charge ratio and measured. The ^{206}Pb and ^{238}U detection limits for this device are ~ 0.1 and 0.04 ppb, respectively. Raw data were corrected off-line using the Isoplot (Ludwig, 2012) supported Microsoft Excel-based spreadsheet (Gerdes and Zeh, 2006; 2009).

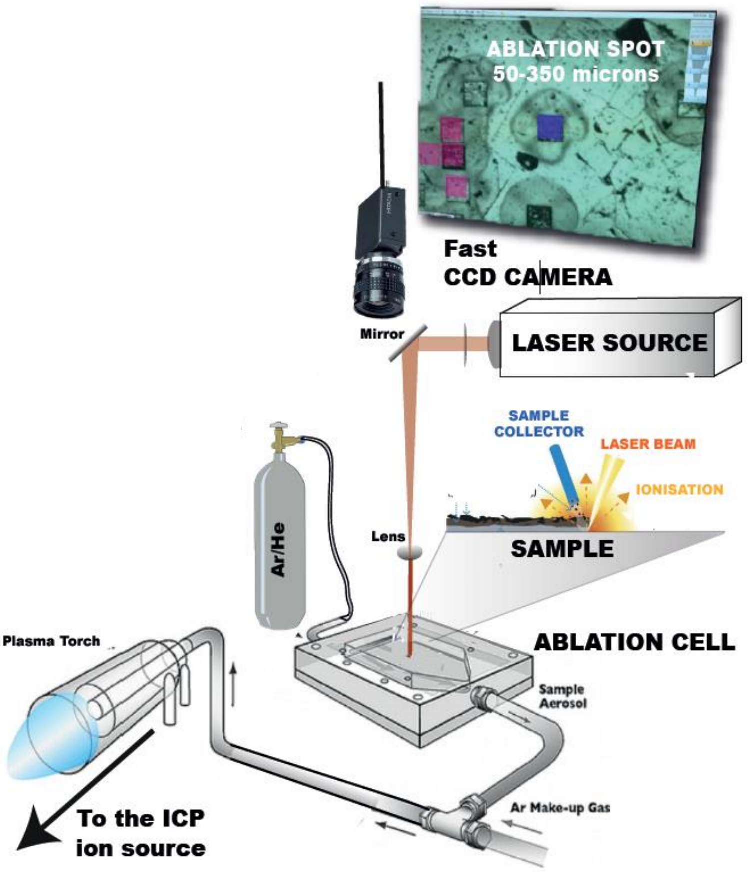

Figure 15 Schematic representation of a LA-ICP set-up. From Mangenot, 2017.

Reference materials. In this study two Soda lime glass NIST-SRM (614 and 612) and two carbonates (WC-1 and ASH-15D) were considered as RMs. Soda lime glass NIST-SRM are Standard Reference Material (SRMs) coming from the National Institute of Standards & Technology (U.S. Department of Commerce) and consist of 35x3mm wafer of silica glass characterized by a nominal trace elements composition. Nist 612 (https://www-s.nist.gov/srmors/certificates/612.pdf) was used for the apparatus calibration whereas fractionation of $^{206}Pb/^{238}U$, $^{207}Pb/^{206}Pb$ ratios and their drift were corrected based on repeated analyses of soda-lime glass NIST-SRM 614 (http://www3.nd.edu/~asimonet/ENGV60500/SRM_NIST_614.pdf; U=0.823±0.002 ppm, Th=0.748±0.006 ppm, Pb=2.32±0.04 ppm).

The LA-ICP-MS method for carbonates follows a typical sample-standard bracketing approach that uses a matrix-matched reference material (RM) with known and highly reproducible U-Pb age to normalize the values measured (i.e. values of the unknown). WC-1 vein calcite was dated by ID-TIMS at 254.4±6.4 Ma (Roberts et al., 2017). Speleothem ASH-15D was dated by ID-TIMS at 2.965 ± 0.011 Ma (2σ, Nuriel et al. 2021) and used as calibrator (or secondary RM). RM cylinders are inserted in the holder together with the samples. A sequence of 6 analyses on RMs (2 on Nist glass 614, 2 on WC-1 and 2 on ASH-15D) were achieved periodically in the analytical session.

LA-ICPMS calibration. Several parameters are adjusted during the calibration which is performed via continuous ablation through linear pathways on the SRM-NIST glass 620 characterized by a nominal concentration of U, Th and Pb isotopes. These are: (1) oxides formation (<1% by keeping stable plasma conditions); (2) the concentrations of the carrier gas (N_2, He and Ar); (3) the cooling gas parameters; (4) the lenses orientation; (5) the torch orientation/plasma position and radiofrequencies (Rf); (6) the plasma auxiliary gas (Ar); and (8) the magnet field.

Spot selection (pre-screening). Each carbonate phase investigated was manually screened to identify areas which ensure high and variable U/Pb and $^{207}Pb/^{206}Pb$ ratios and possibly high dating potential in the final result (Fig. 18). In order to increase sensitivity and reduce downhole fractionation, large square holes (143-213µm) have been chosen. During the pre-screening, the operator can visualize on a screen the amount of ^{238}U, ^{206}Pb expressed in counts per second (cps) to have a general idea of the U and Pb concentrations in the sample and discard those with very high and homogeneous Pb composition. For each LA session, 400-500 spots (including those on the standards) were selected.

After spot selection the analytical session is launched overnight (12 hours) in a fully-automated mode. Each analysis lasts for ~1.1 min and consists of 3 secs pre-ablation (to remove surface contamination), 20 sec of pre-ablation-washout, 20 sec of background acquisition, 20 sec of sample ablation and 5 sec of washout to remove the ablated and avoid any contamination between different spots. For each spot, during the 42-45 sec of data acquisition, the discrete signal of ^{206}Pb, ^{207}Pb, ^{208}Pb, ^{232}Th and ^{238}U is detected by peak jumping in pulse counting and analogue mode, with a total integration time of 0.1 s for all five isotopes, resulting in 420-479 mass scans.

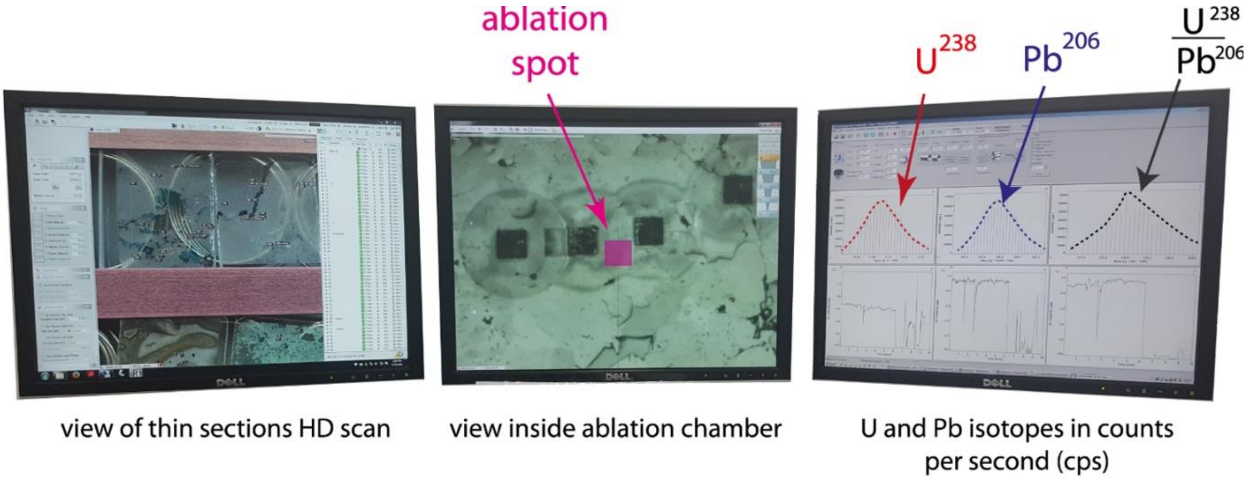

Figure 16. In situ pre-screening stage. The left screen: HD 1200dpi scan view of the samples holder. Central screen: live view of a blocky calcite inside the ablation chamber. Black squares are pre-ablations (with the classic crown of the material ablated around) in position where common Pb was very high (discarded). The pink square indicates a position selected for the further analyses. Right screen: diagrams having on the x-axis the atomic mass and on the y-axis the counts per second of the atomic masses (i.e. ^{238}U, ^{206}Pb). The present configuration is from the pink spot selected.

Data processing. Raw data were corrected offline using an in-house Microsoft Excel spread-sheet program (Gerdes & Zeh, 2009) modified by Axel Gerdes and Richard Albert (Goethe University, Frankfurt em Main) to fit for carbonates.

The data correction consists of several steps and starts with the treatment of the RM data. Subsequently corrections are propagated into the unknowns (analyses on samples to be dated).

The instrumental mass bias (i.e. the instrumental drift over time) and is calculated by estimating the drift of the machine in respect to the primary RM NIST 614 (e.g. Jarvis & Williams, 1993). This drift is modeled by a polynomial curve which is used for normalization. After applying the normalization factor, a scatter around the nominal value of the RM remains and represent the 'excess of scatter' source of uncertainty (Fig. 17A).

The excess of scatter is the percentage by which all primary RM internal uncertainties have to be increased (see Horstwood et al., 2016). These corrections are propagated to the sequence of unknowns. Corrections need to be also applied to each analysis. Usually the isotope ratios for each analysis has a systematic drift toward lower values due to the downhole fractionation (Eggins et al., 1998) (Fig. 17B) which has to be corrected by the intercept method.

The matrix offset represent the inter-element fractionation due to the optical properties and chemical composition of the material analysed. If after correcting for the machine drift the age obtained from WC-1 RM is not consistent with the known age, an internal standard normalized fractionation factor is extrapolated (with MSWD of WC1 age = 1; Horstwood et al., 2016) and multiplied to all the ^{206}Pb/^{238}Pb isotope ratios of the sequence to increase their uncertainties. Carbonates have heterogeneous compositions and thus values measured during the single ablation (data point signal) are not constant. The signal for each ablation spot is given by 420-479 mass scans (i.e. total mass scan, including background acquisition) that are

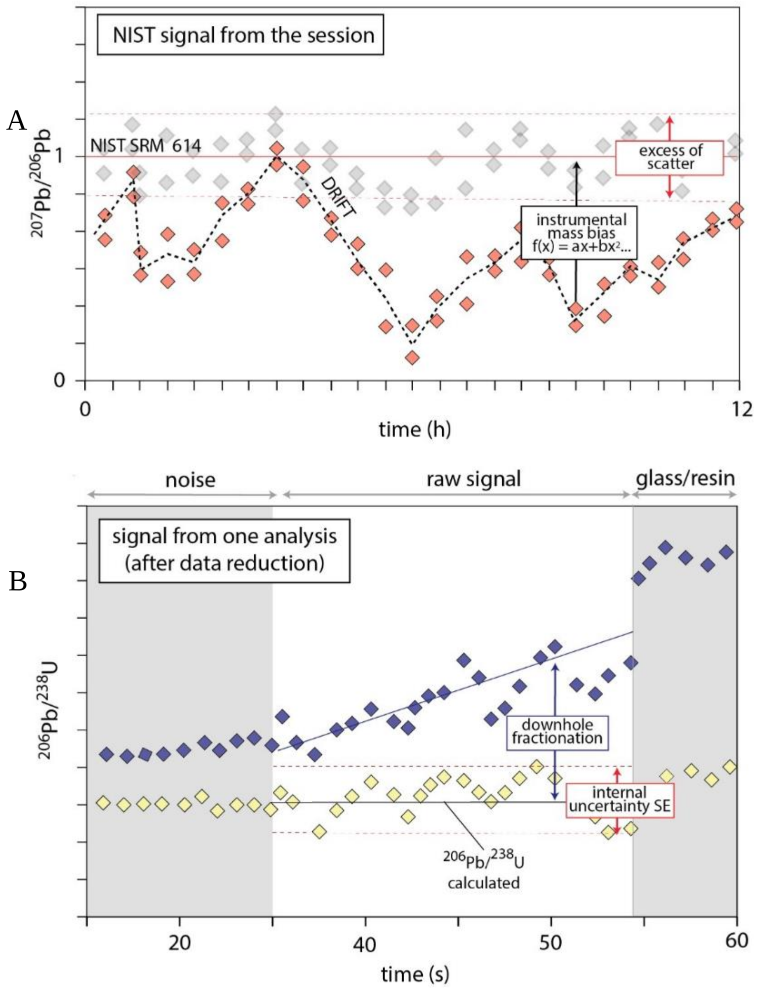

Figure 17. Synthetic examples of data treatment. Vertical scale is exaggerated. A) Data of the standards (entire session). In red the raw signal from NIST SRM 614 representing the behaviour of the LA-ICPMS during the analytical session (12h). The signal is normalized to the known value of the glass with a polynomial equation. The remaining scatter around the 'true value' (grey symbols) represents the 'excess of scatter' B) Treatment of each measurement. In blue the raw data obtained from a single measurement with the noise (or background) in the first seconds and the signal from the glass in the last seconds of ablation. The shift of ^{206}Pb/^{238}U is due to the downhole fractionation. The internal uncertainty (SD) of each data point is the scatter remaining after downhole fractionation correction.

reduced to ~60 by automatized averaging data reduction. The signal scatter around the mean value represents the internal uncertainty of each data point (SE, Fig. 17B). The background or blank noise (measured after 'wash out') is subtracted to obtain a baseline-subtracted intensity. This adding another source of uncertainty. Finally, the signal of each data point is manually corrected for outliers (i.e. out of the $\pm 2\sigma$ SD of the regression line) and possible mixing between different age domains.

Uncertainty propagation. The uncertainty of the age is proportional to the U-Pb data-points scatter and spread along the linear regression. A poorly constrained regression line (i.e. data scatter, low spread of the isotope ratios) implies a higher uncertainty of the slope and of the $Y_{(x=0)}$ intercept, and thus of the age. The best fit of the regression line is quantified by the Mean Squared of the Weighted Deviates (MSWD; Wendt, & Carl, 1991). If the assigned errors are the only cause of scatter, the MSWD will tend to be = 1. Values of MSWD << 1 generally indicate either overestimated analytical errors or unrecognized error-correlations whereas MSWD >> 1 indicate either underestimated analytical errors or the presence of non-analytical scatter (Ludwig, 2012). In other words, MSWD appreciably different from 1 suggest that the system was disturbed after carbonate formation and multiple age domains are mixed. This is the so-called either 'geological scatter', carbonate opening system behaviour or U-Pb system disturbance. Taken into account the complexity of carbonate geochronological datasets, Brooks et al. (1972) suggest a cutoff of 2.5 for the MSWD. This rule is still followed and considered in this study. High data scatter due to isotope system disturbance usually produce dates with MSWD > 2.5 and are considered errorochrons or, in other words, dates without geologic meaning. The MSWD values depend also on the uncertainty of each data point (i.e. ellipses diameters) and their distribution along the regression line. Analyses via dilution techniques (Chapter 2.5) produce data points with smaller uncertainty and thus MSWD may be > 2.5 not necessarily implying a mixing between age populations.

In the present study the ratio data point uncertainty is given by the quadratic addition of all sources of uncertainty (random uncertainties) as in the equation 2.13

$$\boldsymbol{2\sigma = 2\sqrt{\ (\varepsilon_a)^2 + SE^2 + (\varepsilon_b)^2 + (\varepsilon_c)^2 +\ CS^2}} \qquad \mathbf{2.13}$$

where $\mathcal{E}_a$ = excess of scatter, SE = internal uncertainty $\mathcal{E}_b$ = excess of variance and $\mathcal{E}_c$= background uncertainty and the counting statistical uncertainty (CS).

The couting statistical uncertainty (CS) informs on the reliability of each measurement. It is expressed with the eq. 2.14

$$\boldsymbol{CS} = \frac{\sqrt{\boldsymbol{I}\frac{\boldsymbol{DT}}{\boldsymbol{1000}}}}{\sqrt{\boldsymbol{N}}}\left(\frac{\boldsymbol{1000}}{\boldsymbol{DT}}\right) \qquad \textbf{2.14}$$

where I = signal intensity I (high signal when concentration is high), DT = dwell time and N = number of measurements for each DT.

According to Horstwood et al. (2016) the random uncertainties has to be propagated with systematic uncertainty (i.e. limiting uncertainties below which the final uncertainty cannot be quoted or reduced by increasing the number of data point of the decay constant). Here the decay constant uncertainty and the long term excess of variance (see below) were propagated into the dataset. This resulting in the final internal uncertainty of the data point.

Common Pb correction was only done in few samples from the Ries Crater basin providing very high U-Pb ratio and low common Pb (see details in Montano et al., 2021; Chapter 4.1).

Results are plotted in Tera-Wasserburg Concordia plots (Tera & Wasserburg, 1972a, b) using Isoplot 4.15 which is a Visual Basic Add-in for Microsoft *Excel*®, produced by the Berkeley Geochronology Center (Ludwig, 2012). Ages were calculated as the intersection of the regression line of the isotope values (isochron) with the Concordia curve. Regression lines were constrained with at least 30 ablation spots (N) for each of the investigated carbonate phases, except few cases. The final uncertainty of the age is given by the error envelope of the regression line and it is named $2\sigma_i$ (internal uncertainty of the age).

In the framework of this PhD project there was the opportunity to analyse the secondary reference material speleothem calcite ASH-15D (Mason et al., 2016; Nuriel et al., 2021) as an unknown during six analytical sessions between 2017 and 2019 (Montano et al., 2021, Chapter 4.1) (Fig. 18). This is done to verify the reproducibility and accuracy of the applied method and compare the results from the different analytical sessions. The ages obtained yielded a weighted average age of 2.961 ±0.037 Ma (MSWD =1.4), consistent within uncertainty with the ID-TIMS age of ASH-15D (2.965 ±0.011 Ma, 2σ; Nuriel et al., 2020). The 'long term excess of variance Ɛ'' obtained from ASH-15D data is 1.45% (2σ; Fig. 20) and was added by quadratic addition to the uncertainties of each lower intercept age of the analysed carbonates. A 0.34% long term excess of variance for the ^{207}Pb/^{206}Pb y-intercept of the regression line was obtained from the ASH-15D data (weighted mean of 0.8737 ±0.0014 and MSWD =2 without excess of scatter and 0.8737 ±0.0016 and MSWD =1 with excess of scatter of

0.34%) and was also added by quadratic addition to the y-intercept uncertainty of each analysis (i.e. on the ^{207}Pb/^{206}Pb initial ratio).

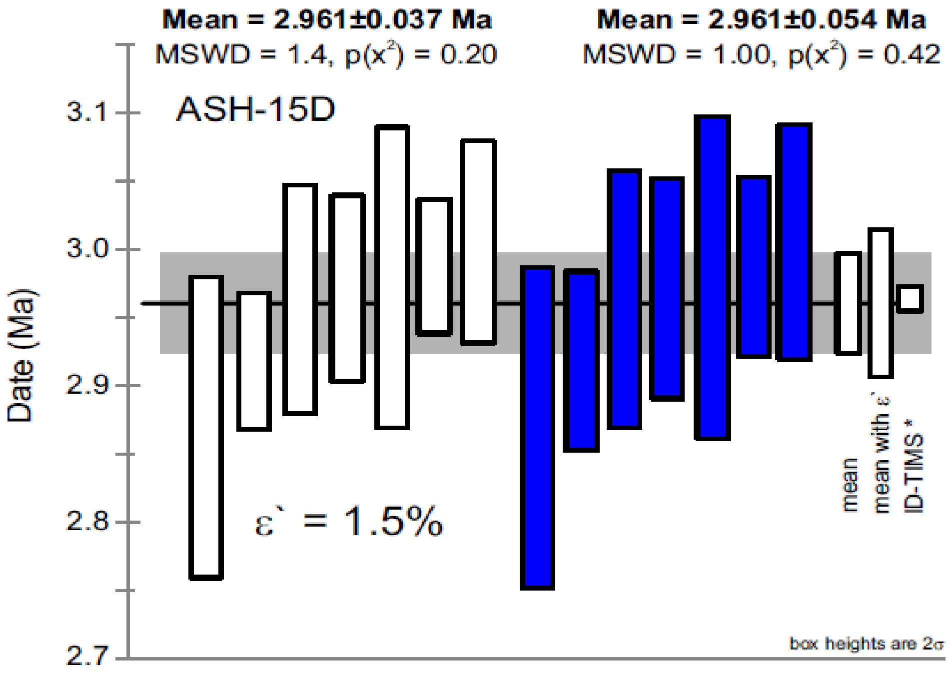

Figure 18. Sorted intercept ages with 2σ uncertainty for ASH-15D (white; $n_w = 7$, MSWD = 1.4) analysed over a period of about 3 years (2016 to 2019) used to estimate the long-term excess of variance (ε`) of 1.5%. Data to the right (blue) includes the excess of variance propagated by quadratic addition. Also presented is the super-population mean with ε` and reference age from ID-TIMS (Nuriel et al., 2021).

After this estimation, the internal uncertainties $2\sigma_i$ of all ages obtained in this project were propagated with Ɛ` = 1.5% (value calculated is 1.45%, 2σ). This resulting in a final expanded uncertainty expressed by the equation 2.15.

$$2\sigma_{exp} = \sqrt{(2\sigma_i{}^2 + (\varepsilon')^2} \tag{2.15}$$

4 THE MIOCENE RIES CRATER BASIN

The study of the Ries Crater basin aimed at investigating lacustrine carbonates of Miocene age to test the suitability of LAcarb as chronostratigraphic tool in these settings. The Ries Crater marginal carbonates provided high dating success and U-Pb ages consistent with those reported by previous authors for the lacustrine sedimentation (Rocholl et al., 2011; 2017; Schmieder et al., 2018) and with a precision down 1.5% (2σ). A scientific article has been published on Earth and Planetary Science Letters (Montano et al., 2021; Chapter 4.1).

The results obtained allowed stratigraphic correlation between marginal facies and between marginal facies a basinal siliciclastic units at the resolution of the third order stratigraphic sequence (0.5-5 Ma). Therefore, they assessed for the success of LAcarb as chronostratigraphic tool in lacustrine settings and allowed to address further research on another lacustrine succession: the Yacoraite Fm.

Discussion about the perspectives of the results achieved in this study, are in Chapter 9.2.

4.1 In-situ U-Pb dating of Ries Crater lacustrine carbonates (Miocene, South-West Germany): Implications for continental carbonate chronostratigraphy

4.1.1 Abstract

The Nördlinger Ries Crater lacustrine basin (South-West Germany), formed by a meteorite impact in the Miocene (Langhian; ∼14.9Ma), offers a well-established geological framework to understand the strengths and limitations of U-Pb LA-ICPMS (*in situ* Laser Ablation-Inductively Coupled Plasma Mass Spectrometry) geochronology as chronostratigraphic tool for lacustrine (and more broadly continental) carbonates. The post-impact deposits include siliciclastic basinal facies at the lake centre and carbonate facies at the lake margins, coevally deposited in a time window of >1.2 and <2Ma. Depositional and diagenetic carbonate phases (micrites and calcite cements) were investigated from three marginal carbonate facies (Hainsfarth bioherm, Adlersberg bioherm and Wallerstein mound). Petrography combined with C and O stable isotope analyses indicate that most depositional and early diagenetic carbonates preserved pristine geochemical compositions and thus the U-Pb system should reflect the timing of original precipitation. In total, 22 U-Pb ages were obtained on 10 different carbonate phases from five samples. The reproducibility and accuracy of the U-Pb (LA-ICPMS) method were estimated to be down to 1.5% based on repeated analyses of a secondary standard (speleothem calcite ASH-15d) and propagated to the obtained ages. Micrites from the Hainsfarth, Adlersberg and Wallerstein facies yielded ages of 13.90 ± 0.25, 14.14 ± 0.20 and 14.33 ± 0.27Ma, respectively, which overlap within uncertainties, and are consistent with the weighted average age of 14.30 ±0.20Ma obtained from all the preserved depositional and early diagenetic phases. Data indicate that sedimentation started shortly after the impact and persisted for >1.2 and <2Ma, in agreement with previous constraints from literature, therefore validating the accuracy of the applied method. Later calcite cements were dated at 13.2 ±1.1 (n_w=2), 10.2 ±2.7 and 9.51 ±0.77Ma, implying multiple post-depositional fluid events. This study demonstrates the great potential of the U-Pb method for chronostratigraphy in continental systems, where correlations between time-equivalent lateral facies are often out of reach. In Miocene deposits the method yields a time resolution within the 3rd order depositional sequences (0.5–5Ma).

Keywords: U-Pb dating, Laser Ablation, lacustrine carbonates, chronostratigraphy, Miocene.

4.1.2 Introduction

The application of carbonate U-Pb geochronology was initially limited mainly due to the difficulty in identifying carbonate samples with high and variable U/Pb isotope ratios, together with the analytical challenge in handling low amounts of U and Pb (usually <1ppm) heterogeneously incorporated in carbonates (Rasbury & Cole, 2009). Analytical advances on in-situ U-Pb geochronology via Laser Ablation-Inductively Coupled Plasma Mass Spectrometry (LA-ICPMS) have greatly facilitated direct dating of carbonates (e.g. Roberts et al., 2017; 2020a; Guillong et al., 2020).

Recent studies have focussed on a wide spectrum of applications within the geosciences, including the assessment of tectonic events and fracturing (e.g. Hansman et al., 2018; Nuriel et al., 2019), the thermal evolution of sedimentary basins (e.g. Mangenot et al., 2018; MacDonald et al., 2019) and the fluid-rock interactions (e.g. Li et al., 2014; Godeau et al., 2018). Geochronology applied to stratigraphic reconstructions requires dating tools able to produce precise ages. Previous studies showed that carbonate geochronology via U-Pb (LA-ICPMS) often produces ages that exceed 2-3% precision (2σ) (Roberts et al., 2020a), making the technique not always suitable for stratigraphic applications. The U-Pb (LA-ICPMS) geochronology has been used to determine carbonate depositional ages by dating speleothems and palaeosoils (e.g. Scardia et al., 2019; Kurumada et al., 2020) and only a few studies have reported U-Pb ages for lacustrine carbonates (e.g. Cole et al., 2005; Frisch et al., 2019). Furthermore, at our knowledge, no study has attempted chronostratigraphic reconstructions in continental carbonates deposited in time windows of < 5Ma.

Dating lacustrine carbonates is relevant for a variety of applications. In particular, these deposits may assist palaeoenvironmental and palaeoclimatic studies since they potentially record the lake geochemical evolution through time. Moreover, they represent potential sources and reservoirs for hydrocarbons and are targets for petroleum exploration (e.g. Bohacs et al., 2000; Rohais et al., 2019). Lacustrine marginal carbonates include coated grain and skeletal carbonate sands, as well as carbonate build-ups, located along the lake shoreline and often organized in discontinuous bodies (e.g. Della Porta, 2015 and references therein). They are characterized by high facies heterogeneity and commonly lack biostratigraphic markers, which hinders chronostratigraphic correlations among time-equivalent lateral facies (e.g. Deschamps et al., 2020). Furthermore, the site-specific geochemistry of continental fluids does not permit the use of proxies, such as $\delta^{18}O$, $\delta^{13}C$ and $^{87}Sr/^{86}Sr$, conventionally applied to indirectly date marine carbonates (Veizer et al., 1999). Consequently, at present, constraining the relative and absolute ages of lacustrine marginal carbonates and performing basin-scale correlations remain a challenge.

The Miocene Nördlinger Ries Crater in South-West Germany is one of the most precisely dated meteorite impact basins on Earth. The impact timing was constrained by the U-Pb and Ar-Ar geochronometers (Schwarz et al., 2020 and references therein). The post-impact lacustrine deposits include siliciclastic basinal facies and carbonate marginal facies (Füchtbauer et al., 1977; Jankowski, 1977). The onset of lacustrine sedimentation is thought to have occurred shortly after the impact (Buchner and Schmieder, 2009; Stöffler et al., 2013) and a magnetostratigraphy dataset is available for the basinal facies (Pohl, 1977; Pohl et al., 2010).

Different depositional and diagenetic carbonate phases (i.e. micrites and calcite cements) from three marginal facies of the Ries Crater basin were investigated with conventional petrography and carbon (C) and oxygen (O) stable isotope analyses prior to U-Pb geochronology. This was aimed at identifying phases not affected by later diagenetic modifications, which could have reset the carbonate U-Pb system (Li et al., 2014; Mangenot et al., 2018).

This study aims to assess: (1) the reliability of the U-Pb (LA-ICPMS) method to obtain geologically consistent (accurate) and precise ages from lacustrine carbonates of known stratigraphic age (Miocene) deposited in a time window of <2 Ma; and (2) the suitability of this method for chronostratigraphy and diagenesis studies in continental sedimentary settings.

4.1.3 Geological and geochronological setting

The Nördlinger Ries lacustrine basin is a circular, flat depression of ~26km in diameter located in South-West Germany (Fig. 19) that formed due to a meteorite impact (Shoemaker and Chao, 1961). The impact structure comprises a central crater, an inner ring, a megablock zone and a tectonic crater rim (Füchtbauer et al., 1977) (Fig. 19).

In this study, it is assumed that the meteorite impact occurred at ~14.9Ma (Langhian, Miocene) in line with most ages published in the last decade: 14.92±0.02Ma (Rocholl et al., 2018), 14.808±0.038 Ma (Schmieder et al. 2018a), 14.89±0.34 and 14.75±0.22Ma (Schwarz et al., 2020) (see details in Supplementary data; Section 4.1.9).

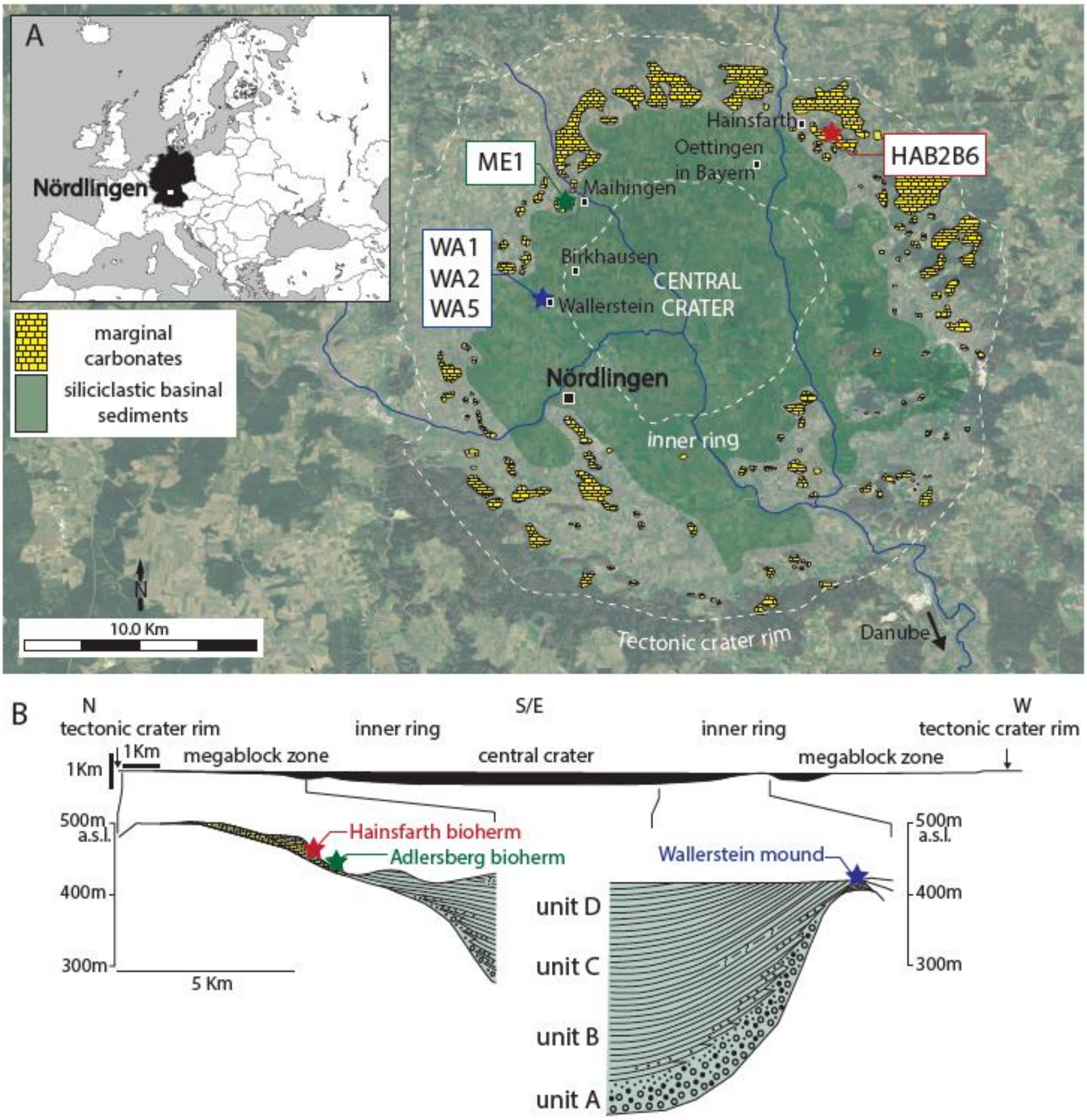

Figure 19. Geographic and geological setting of the study area. A) In the insert, the location of the Ries Crater impact lake in South-West Germany (centred at 48° 52′ 5.3" N, 10° 33 ′ 32" E). The Google Earth satellite image illustrates the main structural elements of the impact zone and the location of basinal and marginal deposits. The provenance of the investigated samples (HAB2B6, ME1, WA1, WA2 and WA5) is also reported. B) Simplified North–South cross-section of the Ries Crater (modified after Arp et al., 2013a). On the left, the location of the studied carbonate marginal facies (Hainsfarth bioherm, Adlersberg bioherm, and Wallerstein mound) is indicated by stars. On the right are reported the basinal A-B-C-D lithostratigraphic units that correspond respectively to the basal, the laminite, the marlstone and the claystone members (after Füchtbauer et al., 1977; Jankowski, 1977).

Shortly after the impact a fluvial system established within the crater (Jankowski, 1981; Buchner and Schmieder, 2009; Stöffler et al., 2013). River waters, along with post-impact springs circulated in the basin forming the Ries Crater lake. By the end of the Miocene the basin was filled by up to 350m of lacustrine sediments (Bolten & Müller, 1969; Arp et al., 2017).

The Ries post-impact sedimentary succession was investigated through outcrop surveys and borehole core drillings (Füchtbauer et al., 1977; Jankowski, 1977; Arp et al., 2013a, b; 2017; 2019a) and comprises a basinal succession at the lake centre and marginal facies on the lake margins (Fig. 19).

The basinal succession was subdivided into four lithostratigraphic units (Füchtbauer et al., 1977; Jankowski, 1977) from base to top (Fig. 19): basal Member (unit A) mainly consisting of sandstones reworked from suevite (Stöffler et al., 2013); laminite Member (unit B); marlstone Member (unit C); and claystone Member (unit D), partially eroded during Plio-Pleistocene time.

Four main facies characterize the basin margins (Arp, 1995 and references therein) (Fig. 19): algal bioherms, sub-lacustrine spring mounds, carbonate sands and fluvio-deltaic conglomerates. Algal bioherms (i.e. Staudiberg, Hainsfarth and Adlersberg; Arp, 1995) are mainly built by inverted cones of Cladophorites green algae, encrusted by micrite (Riding, 1979; Arp, 1995; Della Porta, 2015). Spring mounds are associated with post-impact hydrothermal springs (e.g. Erbisberg mound; Arp et al., 2013b) or ambient temperature springs (e.g. the Wallerstein mound; Pache et al., 2001) discharging into the lake, and consist of mounds and pinnacles made of porous crystalline, micritic laminated and clotted peloidal carbonate fabrics (Arp, 1995; Pache et al., 2001).

A precise time estimate for the duration of lacustrine sedimentation remains hard to define because the uppermost deposits of basinal unit D have been eroded during Plio-Pleistocene time (Füchtbauer et al., 1977). Based on rhythmic laminations and magnetostratigraphic data from basinal sediments, Füchtbauer et al. (1977) and Pohl (1977) proposed that the entire (preserved and eroded) lacustrine succession was deposited over a time window of 0.3 to 2Ma, whereas more recently, Arp et al. (2017) reported a duration of 2Ma. Additionally, based on sedimentation rates of basinal units, Jankowski (1981) suggested that the currently preserved lacustrine deposits formed over a time interval of up to 1.2Ma. In conclusion, according to the existing literature constraints, the four (A-B-C-D) basinal units were deposited in a time window of >1.2 and <2Ma. Further age constraints on the deposition of the basinal units derive from magnetostratigraphy data (Pohl, 1977; Pohl et al., 2010), using an approach previously presented by Arp et al. (2013b). In this contribution the meteorite impact was assigned to the top of C5Bn.1r reverse chron in line with the interpretation of Rocholl et al. (2017, 2018). As a consequence, unit A is considered to be deposited during the C5Bn.1n normal chron, the transition from unit B to unit C is within the C5Adr chron and the onset of unit D deposition was assigned to the boundary between C5ACr and C5ACn chrons (see details in Supplementary data; Section 4.1.9).

4.1.4 Material and methods

Investigated samples. Five microbial boundstone samples from the marginal facies of the Ries Crater were collected from three locations (Fig. 1 9and Table 1). The HAB2B6 sample (Hainsfarth bioherm facies) and the ME1 sample (Adlersberg bioherm facies) come from the Hainsfarth quarry and the Mellerberg locality, respectively (see Arp, 1995). The WA1, WA2 and WA5 samples (Wallerstein mound build-up facies) were collected at the base of the Wallerstein Castle (see Pache et al., 2001). Although the sample stratigraphic height along the Wallerstein mound is unknown, based on the petrographic description of Pache et al. (2001), WA1 and WA2 can be ascribed to the basal part of the mound, and WA5 to the central part.

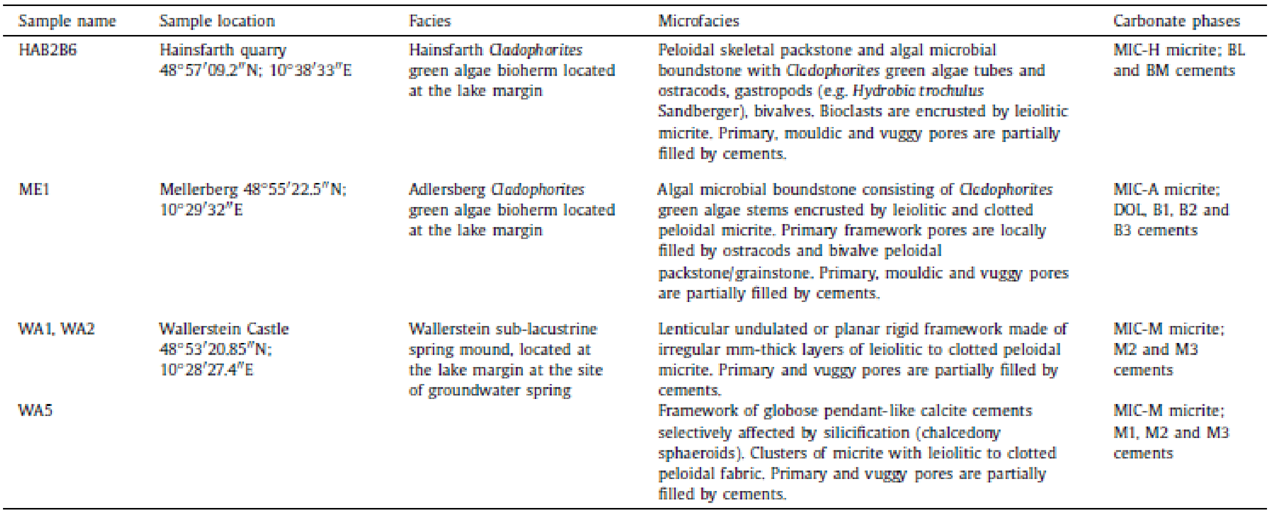

Sample name	Sample location	Facies	Microfacies	Carbonate phases
HAB2B6	Hainsfarth quarry 48°57′09.2″N; 10°38′33″E	Hainsfarth *Cladophorites* green algae bioherm located at the lake margin	Peloidal skeletal packstone and algal microbial boundstone with *Cladophorites* green algae tubes and ostracods, gastropods (e.g. *Hydrobic trochulus* Sandberger), bivalves. Bioclasts are encrusted by leiolitic micrite. Primary, mouldic and vuggy pores are partially filled by cements.	MIC-H micrite; BL and BM cements
ME1	Mellerberg 48°55′22.5″N; 10°29′32″E	Adlersberg *Cladophorites* green algae bioherm located at the lake margin	Algal microbial boundstone consisting of *Cladophorites* green algae stems encrusted by leiolitic and clotted peloidal micrite. Primary framework pores are locally filled by ostracods and bivalve peloidal packstone/grainstone. Primary, mouldic and vuggy pores are partially filled by cements.	MIC-A micrite; DOL, B1, B2 and B3 cements
WA1, WA2	Wallerstein Castle 48°53′20.85″N; 10°28′27.4″E	Wallerstein sub-lacustrine spring mound, located at the lake margin at the site of groundwater spring	Lenticular undulated or planar rigid framework made of irregular mm-thick layers of leiolitic to clotted peloidal micrite. Primary and vuggy pores are partially filled by cements.	MIC-M micrite; M2 and M3 cements
WA5			Framework of globose pendant-like calcite cements selectively affected by silicification (chalcedony sphaeroids). Clusters of micrite with leiolitic to clotted peloidal fabric. Primary and vuggy pores are partially filled by cements.	MIC-M micrite; M1, M2 and M3 cements

Table 1. Location, facies description and depositional environment of the five samples investigated. Macro- and microscopic facies are based on previous studies by Riding (1979), Arp (1995) and Della Porta (2015). The carbonate phases occurring in each sample are also reported (see details in Table 2).

Petrographic analysis. Eight polished thin sections (50-60µm thick) were prepared in order to identify the different depositional and diagenetic carbonate phases (Table 2). Conventional optical petrography was performed using a Nikon ECLIPSE LV100POL polarized light microscope and allowed observations under plane- and cross-polarized light (PPL and XPL). Cathodoluminescence (CL) microscopy was accomplished with a cold CL 8200 Mk5 CITL instrument. The electron beam worked under vacuum (<0.1 mbar) with acceleration voltage of 10kV, and current of 250µA. All thin sections were partially stained with a solution of 10% diluted HCl, Alizarin red-S and potassium ferricyanide (Dickson, 1966).

C and O stable isotope analysis. Forty-one powder samples from 10 carbonate phases were carefully extracted from polished rock slabs and thin sections by means of a dental drill or a software-controlled MicroMill device. Powders were reacted with 100% phosphoric acid at 70°C using a Gasbench II connected to a ThermoFisher Delta V Plus mass spectrometer and analysed for C and O stable isotopes at Geozentrum Nordbayern (Germany). $\delta^{13}C$ and $\delta^{18}O$ values for carbonates are reported in ‰ relative to the Vienna Pee Dee Belemnite (V-PDB) standard.

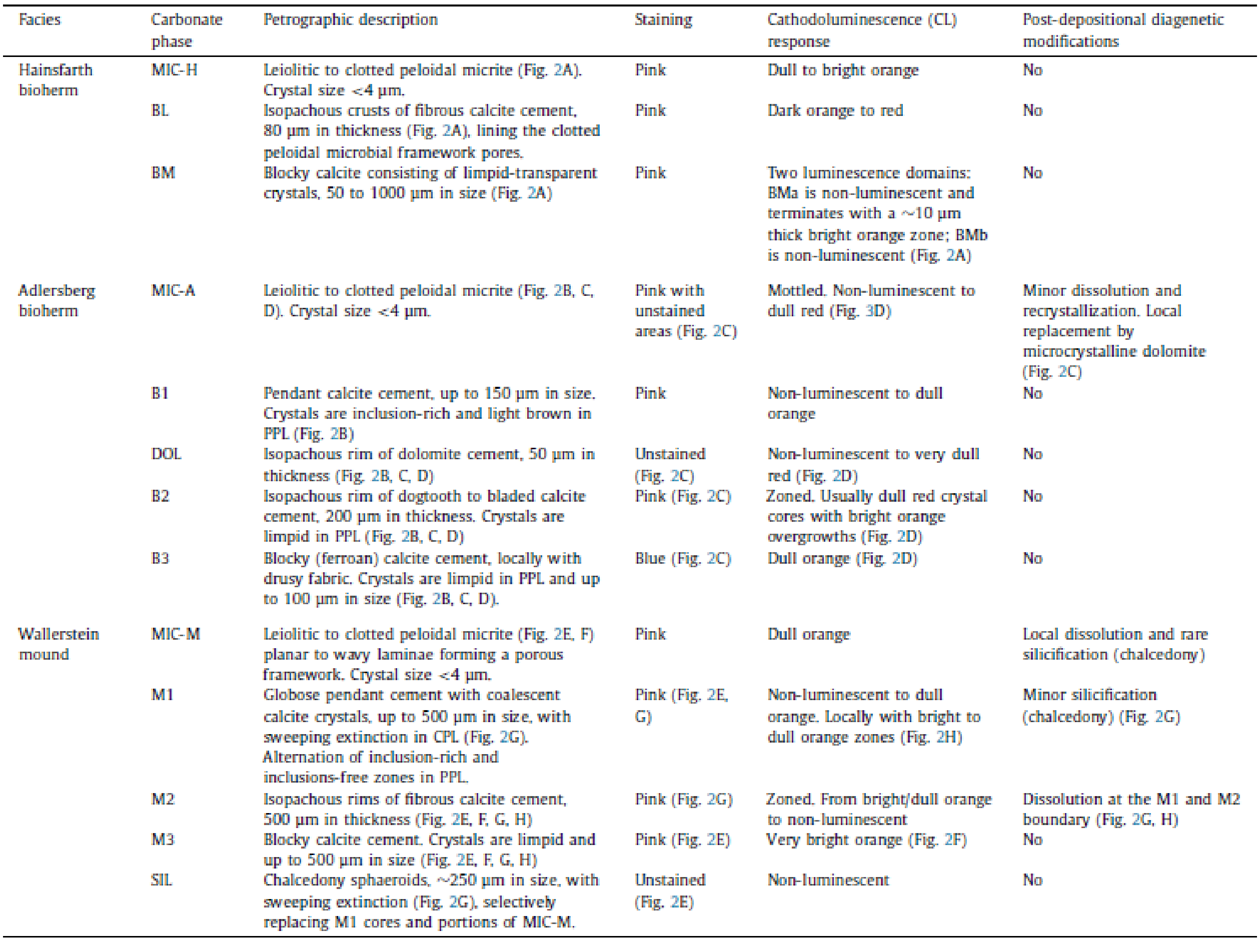

Facies	Carbonate phase	Petrographic description	Staining	Cathodoluminescence (CL) response	Post-depositional diagenetic modifications
Hainsfarth bioherm	MIC-H	Leiolitic to clotted peloidal micrite (Fig. 2A). Crystal size <4 µm.	Pink	Dull to bright orange	No
	BL	Isopachous crusts of fibrous calcite cement, 80 µm in thickness (Fig. 2A), lining the clotted peloidal microbial framework pores.	Pink	Dark orange to red	No
	BM	Blocky calcite consisting of limpid-transparent crystals, 50 to 1000 µm in size (Fig. 2A)	Pink	Two luminescence domains: BMa is non-luminescent and terminates with a ~10 µm thick bright orange zone; BMb is non-luminescent (Fig. 2A)	No
Adlersberg bioherm	MIC-A	Leiolitic to clotted peloidal micrite (Fig. 2B, C, D). Crystal size <4 µm.	Pink with unstained areas (Fig. 2C)	Mottled. Non-luminescent to dull red (Fig. 3D)	Minor dissolution and recrystallization. Local replacement by microcrystalline dolomite (Fig. 2C)
	B1	Pendant calcite cement, up to 150 µm in size. Crystals are inclusion-rich and light brown in PPL (Fig. 2B)	Pink	Non-luminescent to dull orange	No
	DOL	Isopachous rim of dolomite cement, 50 µm in thickness (Fig. 2B, C, D)	Unstained (Fig. 2C)	Non-luminescent to very dull red (Fig. 2D)	No
	B2	Isopachous rim of dogtooth to bladed calcite cement, 200 µm in thickness. Crystals are limpid in PPL (Fig. 2B, C, D)	Pink (Fig. 2C)	Zoned. Usually dull red crystal cores with bright orange overgrowths (Fig. 2D)	No
	B3	Blocky (ferroan) calcite cement, locally with drusy fabric. Crystals are limpid in PPL and up to 100 µm in size (Fig. 2B, C, D).	Blue (Fig. 2C)	Dull orange (Fig. 2D)	No
Wallerstein mound	MIC-M	Leiolitic to clotted peloidal micrite (Fig. 2E, F) planar to wavy laminae forming a porous framework. Crystal size <4 µm.	Pink	Dull orange	Local dissolution and rare silicification (chalcedony)
	M1	Globose pendant cement with coalescent calcite crystals, up to 500 µm in size, with sweeping extinction in CPL (Fig. 2G). Alternation of inclusion-rich and inclusions-free zones in PPL.	Pink (Fig. 2E, G)	Non-luminescent to dull orange. Locally with bright to dull orange zones (Fig. 2H)	Minor silicification (chalcedony) (Fig. 2G)
	M2	Isopachous rims of fibrous calcite cement, 500 µm in thickness (Fig. 2E, F, G, H)	Pink (Fig. 2G)	Zoned. From bright/dull orange to non-luminescent	Dissolution at the M1 and M2 boundary (Fig. 2G, H)
	M3	Blocky calcite cement. Crystals are limpid and up to 500 µm in size (Fig. 2E, F, G, H)	Pink (Fig. 2E)	Very bright orange (Fig. 2F)	No
	SIL	Chalcedony sphaeroids, ~250 µm in size, with sweeping extinction (Fig. 2G), selectively replacing M1 cores and portions of MIC-M.	Unstained (Fig. 2E)	Non-luminescent	No

Table 2 Petrographic description of the phases identified in the three carbonate facies investigated

Reproducibility and accuracy were monitored by replicate analyses of laboratory standards calibrated by assigning δ^{13}C values of +1.95‰ to NBS19 and -47.30‰ to IAEA-CO9 and δ^{18}O values of -2.2‰ to NBS19 and -23.2‰ to NBS18. Reproducibility for δ^{13}C and δ^{18}O values measured on the studied carbonates was ±0.04 and ±0.03 ‰ (1σ), respectively.

U-Pb isotope analysis and dating. Five of the eight investigated thin sections were analysed in seven U-Pb LA-ICPMS analytical sessions at the Goethe University of Frankfurt (Germany). Prior to analysis, the sections were cleaned in an ultrasonic bath with ethanol (5% mol/L). Analyses were performed in different analytical sessions between 2016 and 2019 using a Thermo Scientific Element 2 sector field ICP-MS, coupled to a RESOlution (Resonetics) 193 nm ArF Excimer laser (CompexPro 102, Coherent) equipped with a S-155 two-volume ablation cell (Laurin Technic, Australia). During each session the ablation parameters were kept constant for all samples and reference materials. Samples were ablated in a helium atmosphere (300 ml) and mixed in the ablation funnel with argon (1 L) and nitrogen (6-8ml). Analyses were performed with a square ablation spot of 143 to 213µm in width, 8 to 12Hz frequency and fluence of around 2 J/cm2. A manual pre-screening session allowed identifying areas with variable U/Pb and ^{207}Pb/^{206}Pb ratios. Raw data were corrected off-line using an in-house Microsoft Excel spreadsheet program (Gerdes & Zeh, 2009). Fractionation of ^{206}Pb/^{238}U, ^{207}Pb/^{206}Pb ratios and the drift during the analytical session were corrected based on repeated analyses of soda-lime glass NIST-SRM 614. WC-1 calcite (Roberts et al., 2017) was used to correct for matrix offsets (5 to 9%) between NIST glass and carbonate. Reported uncertainties for each analysis are quadratic additions of the within run precision, counting statistical uncertainties and the excess of variance (2% and 0.2% for the of ^{206}Pb/^{238}U and ^{207}Pb/^{206}Pb, respectively). The excess of variance was calculated from the WC-1 reference material. Final results were plotted on U-Pb Tera-Wasserburg Concordia plots using Isoplot3 (Ludwig, 2012) where ages represent the intersection with the Concordia curve. Regression lines were constrained with 6 to 43 ablations spots (n) for each of the investigated carbonate phases. All uncertainties are reported as 2σ. The speleothem calcite ASH-15D secondary reference material (Mason et al., 2016, Nuriel et al., 2020) was analysed as an unknown during six analytical sessions between 2017 and 2019 (Table 3, Supplementary data C.1 and G.1 in section 4.1.9) to verify the reproducibility and accuracy of the applied method and to compare the datasets from different LA-sessions. The ages obtained from each session yielded a weighted average age of 2.961±0.037 Ma (MSWD = 1.4), consistent within uncertainty with the ID-TIMS age of ASH-15D (2.965 ± 0.011 Ma, 2σ; Nuriel et al., 2020).

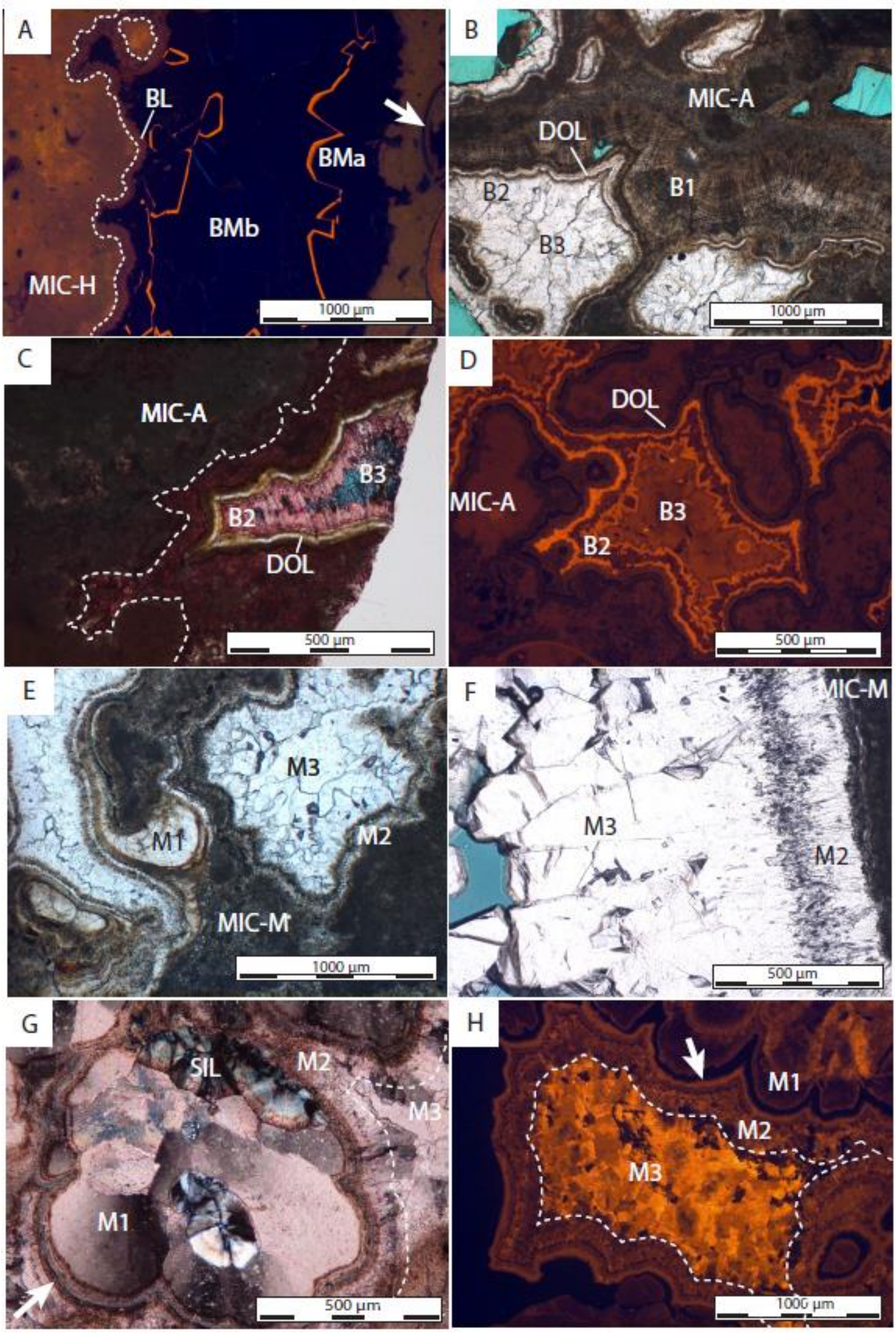
A
BL
BMa
BMb
MIC-H
1000 µm
B
MIC-A
DOL
B2
B1
B3
1000 µm
C
MIC-A
B3
B2
DOL
500 µm
D
DOL
MIC-A
B3
B2
500 µm
E
M3
M1
M2
MIC-M
1000 µm
F
MIC-M
M3
M2
500 µm
G
SIL
M2
M3
M1
500 µm
H
M1
M2
M3
1000 µm

The obtained reproducibility between the different sessions is 1.6%. The excess of variance (ε`) obtained from ASH-15D data is 1.45 % (2σ) and was added by quadratic addition to the uncertainties of each lower intercept age of the analysed carbonate phases (Table 3). A 0.34% excess of variance

Figure 20. Petrographic images of the five carbonate samples investigated. A) Microbial boundstone from Hainsfarth algal bioherm composed of clotted peloidal micrite (MIC-H). Primary framework pores are filled by isopachous fibrous calcite (BL) and blocky calcite (BM) cements. BM cement reveals two growth stages (BMa and BMb) under CL. The white arrow indicates a dissolved gastropod shell (mouldic pore). HAB2B6 sample, CL view. B) Microbial boundstone from the Adlersberg algal bioherm composed of clotted peloidal micrite (MIC-A). Pores are partially filled by four successive cement phases: pendant calcite (B1), isopachous dolomite rim (DOL), dogtooth to bladed calcite (B2) and blocky calcite (B3). ME1 sample, PPL view. C) Microbial boundstone from the Adlersberg algal bioherm composed of clotted peloidal micrite (MIC-A). Primary framework pores are filled by three successive cement generations: isopachous rims of dolomite (DOL) and dogtooth to bladed calcite (B2), followed by a blocky calcite cement (B3). Staining reveals that they consist respectively of non-ferroan dolomite (DOL), non-ferroan calcite (B2) and ferroan calcite (B3). Micrite (MIC-A) is locally replaced by micro-crystalline dolomite (see unstained area to the left of the white dashed line). ME1 sample, stained, PPL view. D) Microbial boundstone from the Adlersberg algal bioherm composed of clotted peloidal micrite (MIC-A). Primary framework pores are filled by three successive cement generations: isopachous rims of dolomite (DOL) and dogtooth to bladed calcite (B2), followed by a blocky calcite cement (B3). The micrite (MIC-A) is locally recrystallized as suggested by the mottled CL. ME1 sample, CL view. E) Leiolitic to clotted peloidal micrite (MIC-M) from the Wallerstein mound. Primary framework pores are filled by a sequence of three successive cements: globose pendant calcite (M1), isopachous fibrous calcite rim (M2) and blocky calcite (M3). M1 pendant calcite precipitated directly on the micrite laminae (MIC-M).. WA1 sample, PPL view. F) Details of fibrous calcite cement (M2) precipitated on the Wallerstein mound micrite (MIC-M) and followed by blocky calcite cement (M3). WA2 sample, PPL view. G) Details of coalescent crystals of pendant calcite cement (M1), partially affected by silicification (SIL; chalcedony sphaeroids) and followed by fibrous calcite (M2) and blocky calcite (M3) cements, grown in optical continuity. Dissolution at the boundary between M1 and M2 cements is indicated by the white arrow. WA5 sample, stained, XPL view. H) Globose pendant calcite cement (M1) filling a pore and post-dated by fibrous calcite cement (M2) and blocky calcite cement (M3) with dull red and bright orange luminescence, respectively. Dissolution at the boundary between M1 and M2 cements is pointed by the white arrow. WA5 sample, CL view.

(ε\`) for the of $^{207}Pb/^{206}Pb$ y-intercept of the regression line was obtained from the ASH-15D data (weighted mean of 0.8737±0.0014 and MSWD = 2 without ε\`, 0.8737±0.0016 and MSWD = 1 with ε\` of 0.34%) and added by quadratic addition to the y-intercept uncertainty of each analysis (i.e. on the $^{207}Pb/^{206}Pb$ initial ratio).

4.1.5 RESULTS

Petrography and C-O stable isotope geochemistry. The microbial boundstone from each of the three carbonate facies investigated (Hainsfarth bioherm, Adlersberg bioherm, Wallerstein mound; Fig. 19) display specific depositional and diagenetic features (Figure 20 and Table 2). Petrographic analysis allowed distinguishing 13 depositional and diagenetic phases (Table 1 and 2; Fig. 20). The depositional carbonate phases consist of leolitic to clotted peloidal micrites, labelled MIC-H, MIC-A and MIC-M from the Hainsfarth bioherm, Adlersberg bioherm and Wallerstein mound, respectively. The diagenetic carbonate phases consist of dolomite cement (DOL), chalcedony (SIL) and calcite cements displaying different habitus and fabric: pendant calcites (B1 and M1), isopachous rims of fibrous (BL and M2) and dogtooth to bladed (B2) calcites, as well as blocky calcites (BM, B3 and M3). The results of the C and O stable isotope analyses for the different carbonate phases sampled are summarized in Figure 21, Table 3 and Supplementary data B (section 4.1.9). All micrites (MIC-H, MIC-A, MIC-M) exhibit a covariance between $\delta^{13}C$ and $\delta^{18}O$ (R^2=0.95). $\delta^{13}C$ and $\delta^{18}O$ values for micrites (n=11) range between -5.5‰ and +2.5‰, and between -5.1‰ and +3.3‰, respectively. In particular, MIC-H and MIC-A micrites from the Hainsfarth and Adlersberg bioherm samples, respectively, display positive $\delta^{13}C$ and $\delta^{18}O$ values, whereas MIC-M micrites from the Wallerstein mound sample have negative $\delta^{13}C$ and $\delta^{18}O$ values.

$\delta^{13}C$ and $\delta^{18}O$ for B1 pendant cement (n=1) are +0.2‰ and -1.7‰, respectively, whereas B2 isopachous cement (n=1) has $\delta^{13}C$ of +1.5‰ and $\delta^{18}O$ of +0.7‰. The blocky cements from the algal bioherms (BM and B3) have a distinctive C-O isotope composition: BM (n=5) is characterized by negative and consistent $\delta^{13}C$ and $\delta^{18}O$ values with δ13C between -5.4‰ and -5‰ and $\delta^{18}O$ between -7.3‰ and -7.7‰, whereas B3 (n=3) has a uniform C-O isotope composition with $\delta^{13}C$ between +1.4‰ and +1.9‰, and $\delta^{18}O$ between -5.9‰ to -7.5‰. The $\delta^{13}C$ and $\delta^{18}O$ values of the three calcite cements from the Wallerstein mound samples (M1, M2, M3) are characterized by $\delta^{13}C$ between -1.2‰ and -3.4‰, whereas $\delta^{18}O$ values are more variable, ranging between -0.8‰ and -9.6‰. The $\delta^{18}O$ values fall in three distinct clusters: between -0.8‰ and -4.2‰ for M1 (n=4), between -1.8‰ and -5.0‰ for M2 (n=5) and between -5.7‰ and -9.6‰ for M3 (n=10).

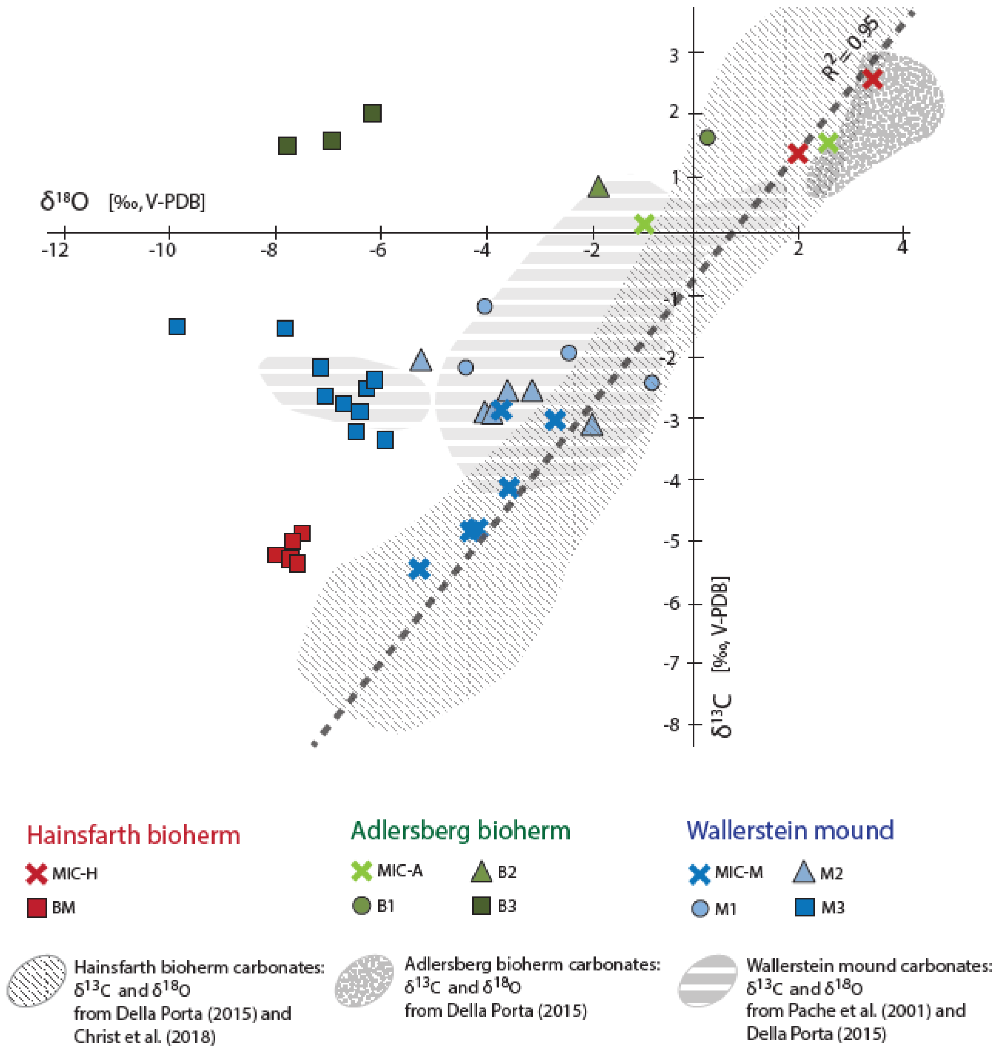

Figure 21. Cross-plot of $\delta^{13}C$ versus $\delta^{18}O$ values (in ‰, relative to V-PDB) of the carbonate phases analysed from the three facies investigated. MIC-H, MIC-A and MIC-M stand for micrite from Hainsfarth bioherm, Adlersberg bioherm and Wallerstein mound, respectively. B1 and M1 are pendant calcite cements. B2 and M2 are isopachous calcite cements. BM, B3 and M3 are blocky calcite cements. Note the covariance (R2=0.95) between $\delta^{13}C$ and $\delta^{18}O$ values that characterizes the micrites (reported as crosses). Grey areas indicate the $\delta^{13}C$ and $\delta^{18}O$ values previously published for the three carbonate facies investigated (Pache et al., 2001; Della Porta, 2015; Christ et al., 2018).

U-Pb geochronology. Concentration and isotope ratios of U and Pb of all analysed phases are summarized in Figure 22, Table 3, and Supplementary data C.1 (section 4.1.9). Due to their small volume, the BL and DOL phases were not sampled and thus not analysed. U and Pb concentrations are very variable, ranging from 10ppb to 53ppm, and 0.4ppb to 6.4ppm, respectively (Fig. 22A). The highest U concentrations can be found in micrites (MIC-H, MIC-A, MIC-M) and pendant cements (B1), mostly with values higher than 1 ppm (Fig. 22A). Figure 4B summarises the $^{238}U/^{206}Pb$ versus

^{207}Pb/^{206}Pb ratios of all analysed carbonate phases: ^{238}U/^{206}Pb varies from 0.03 to 413 and ^{207}Pb/^{206}Pb ranges from 0.87 to 0.10. All phases are characterised by a high to very high isotope ratio variability including domains with high µ-values (^{238}U/^{204}Pb) close to the Concordia. The Hainsfarth bioherm carbonates display the lowest variability, with ^{238}U/^{206}Pb ratios below 1. A clear covariance between both isotope ratios (R^2=0.99; Fig. 22B) suggests that most of the analysed carbonate phases formed at about the same time. However, MIC-A micrite and M1, M3, BM and B3 cements also include data points that define a different slope (R^2=0.79).

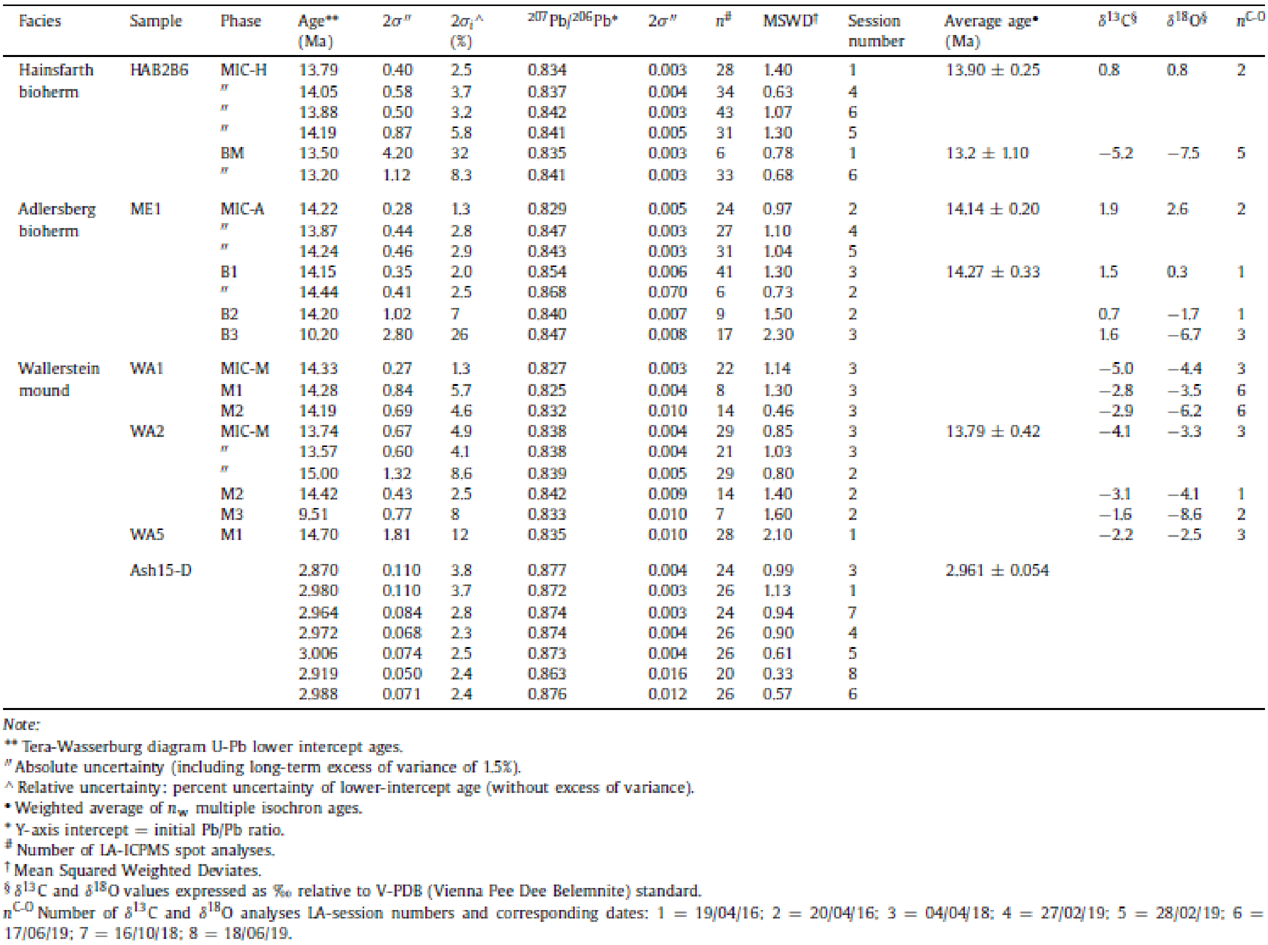

Facies	Sample	Phase	Age** (Ma)	2σ″	$2\sigma_i$^ (%)	^{207}Pb/^{206}Pb*	2σ″	n#	MSWD†	Session number	Average age• (Ma)	δ^{13}C§	δ^{18}O§	n^{C-O}
Hainsfarth bioherm	HAB2B6	MIC-H	13.79	0.40	2.5	0.834	0.003	28	1.40	1	13.90 ± 0.25	0.8	0.8	2
		″	14.05	0.58	3.7	0.837	0.004	34	0.63	4				
		″	13.88	0.50	3.2	0.842	0.003	43	1.07	6				
		″	14.19	0.87	5.8	0.841	0.005	31	1.30	5				
		BM	13.50	4.20	32	0.835	0.003	6	0.78	1	13.2 ± 1.10	−5.2	−7.5	5
		″	13.20	1.12	8.3	0.841	0.003	33	0.68	6				
Adlersberg bioherm	ME1	MIC-A	14.22	0.28	1.3	0.829	0.005	24	0.97	2	14.14 ± 0.20	1.9	2.6	2
		″	13.87	0.44	2.8	0.847	0.003	27	1.10	4				
		″	14.24	0.46	2.9	0.843	0.003	31	1.04	5				
		B1	14.15	0.35	2.0	0.854	0.006	41	1.30	3	14.27 ± 0.33	1.5	0.3	1
		″	14.44	0.41	2.5	0.868	0.070	6	0.73	2				
		B2	14.20	1.02	7	0.840	0.007	9	1.50	2		0.7	−1.7	1
		B3	10.20	2.80	26	0.847	0.008	17	2.30	3		1.6	−6.7	3
Wallerstein mound	WA1	MIC-M	14.33	0.27	1.3	0.827	0.003	22	1.14	3		−5.0	−4.4	3
		M1	14.28	0.84	5.7	0.825	0.004	8	1.30	3		−2.8	−3.5	6
		M2	14.19	0.69	4.6	0.832	0.010	14	0.46	3		−2.9	−6.2	6
	WA2	MIC-M	13.74	0.67	4.9	0.838	0.004	29	0.85	3	13.79 ± 0.42	−4.1	−3.3	3
		″	13.57	0.60	4.1	0.838	0.004	21	1.03	3				
		″	15.00	1.32	8.6	0.839	0.005	29	0.80	2				
		M2	14.42	0.43	2.5	0.842	0.009	14	1.40	2		−3.1	−4.1	1
		M3	9.51	0.77	8	0.833	0.010	7	1.60	2		−1.6	−8.6	2
	WA5	M1	14.70	1.81	12	0.835	0.010	28	2.10	1		−2.2	−2.5	3
	Ash15-D		2.870	0.110	3.8	0.877	0.004	24	0.99	3	2.961 ± 0.054			
			2.980	0.110	3.7	0.872	0.003	26	1.13	1				
			2.964	0.084	2.8	0.874	0.003	24	0.94	7				
			2.972	0.068	2.3	0.874	0.004	26	0.90	4				
			3.006	0.074	2.5	0.873	0.004	26	0.61	5				
			2.919	0.050	2.4	0.863	0.016	20	0.33	8				
			2.988	0.071	2.4	0.876	0.012	26	0.57	6				

Note:

** Tera-Wasserburg diagram U-Pb lower intercept ages.

″ Absolute uncertainty (including long-term excess of variance of 1.5%).

^ Relative uncertainty: percent uncertainty of lower-intercept age (without excess of variance).

• Weighted average of n_w multiple isochron ages.

* Y-axis intercept = initial Pb/Pb ratio.

\# Number of LA-ICPMS spot analyses.

† Mean Squared Weighted Deviates.

§ δ^{13}C and δ^{18}O values expressed as ‰ relative to V-PDB (Vienna Pee Dee Belemnite) standard.

n^{C-O} Number of δ^{13}C and δ^{18}O analyses LA-session numbers and corresponding dates: 1 = 19/04/16; 2 = 20/04/16; 3 = 04/04/18; 4 = 27/02/19; 5 = 28/02/19; 6 = 17/06/19; 7 = 16/10/18; 8 = 18/06/19.

Table 3. U-Pb geochronology and C-O stable isotope data of the carbonate phases investigated. U-Pb geochronology data for the secondary standard (speleothem calcite ASH-15d) are also reported.

Tera-Wasserburg Concordia plots with lower intercept ages are displayed in Figures 23 and 24, while the complete data set and plots can be found in Supplementary data D, E and F (Section 4.1.9). From the five analysed samples, a total of 22 lower intercept U-Pb ages were obtained from 10 depositional and diagenetic carbonate phases (Table 3). Depositional (micrite) and diagenetic (cement) carbonate phases yielded well-defined regression lines with ages between 14.44±0.41 and 9.51±0.77 Ma, and

MSWD (Mean Squared Weighted Deviation) of 0.5 to 1.6. The pendant cement (M1) from sample WA5 and the blocky calcite cement (B3) from sample ME1 display more scattered isotope ratios, and consequently higher MSWD (2.1 and 2.3, respectively). The precision obtained for the majority of the ages ranges from 1.3 to 8.6% (internal uncertainty 2σi; Table 3) and slightly decreases (1.9 to 8.7%) when the long term excess of variance is added (Table 3). After all propagated uncertainties, 60% of the ages have uncertainties below 5% and 27% (six ages) below 3.5%.

Five carbonate phases (MIC-H, MIC-A, MIC-M, BM and B1) were analysed in multiple sessions to check the reproducibility between sessions and to improve the precision of the ages (Table 3). Weighted average ages for these phases are reported with the number (nw) of analytical sessions undertaken in brackets. Micrites from samples HAB2B6, ME1, and WA2 were analysed in 3 to 4 sessions, yielding weighted average ages of 13.90±0.25Ma (n_w=4), 14.14±0.20Ma (n_w=3) and 13.79±0.42Ma (n_w=3), respectively, confirming a within-session reproducibility of 1.5-2%. The data also indicate that multiple measurements can improve the precision of the ages by a factor of about 2 to 4, since weighted average ages have uncertainties down to 1.5% (2σ).

Initial ^{207}Pb/^{206}Pb ratios (i.e. y-axis intercepts; Table 3) fall between 0.825±0.004 and 0.869±0.023 and display a slight scatter, which can be expressed in a weighted average of 0.838±0.003 with MSWD of 9.9. However, there is no discernible difference between different samples or carbonate phases (cements versus micrites).

4.1.6 Discussion

Petrography and O-C isotope geochemistry of Ries Crater carbonates. Carbonates are common minerals that precipitate in a variety of depositional and diagenetic environments. They commonly undergo diagenetic processes such as replacement or recrystallization that may induce textural and geochemical changes (e.g. Swart, 2015). If carbonates are altered by later diagenetic processes, their U-Pb isotope system may be disturbed or even fully reset. Consequently, measured carbonate U-Pb ages may represent the timing of a later diagenetic event rather than the carbonate original precipitation (Li et al., 2014; Mangenot et al., 2018). Therefore, petrography together with C-O stable isotope analyses were here used to: 1) define relative timing and precipitation environments of the carbonate phases, and 2) identify the phases that potentially preserved pristine compositions.

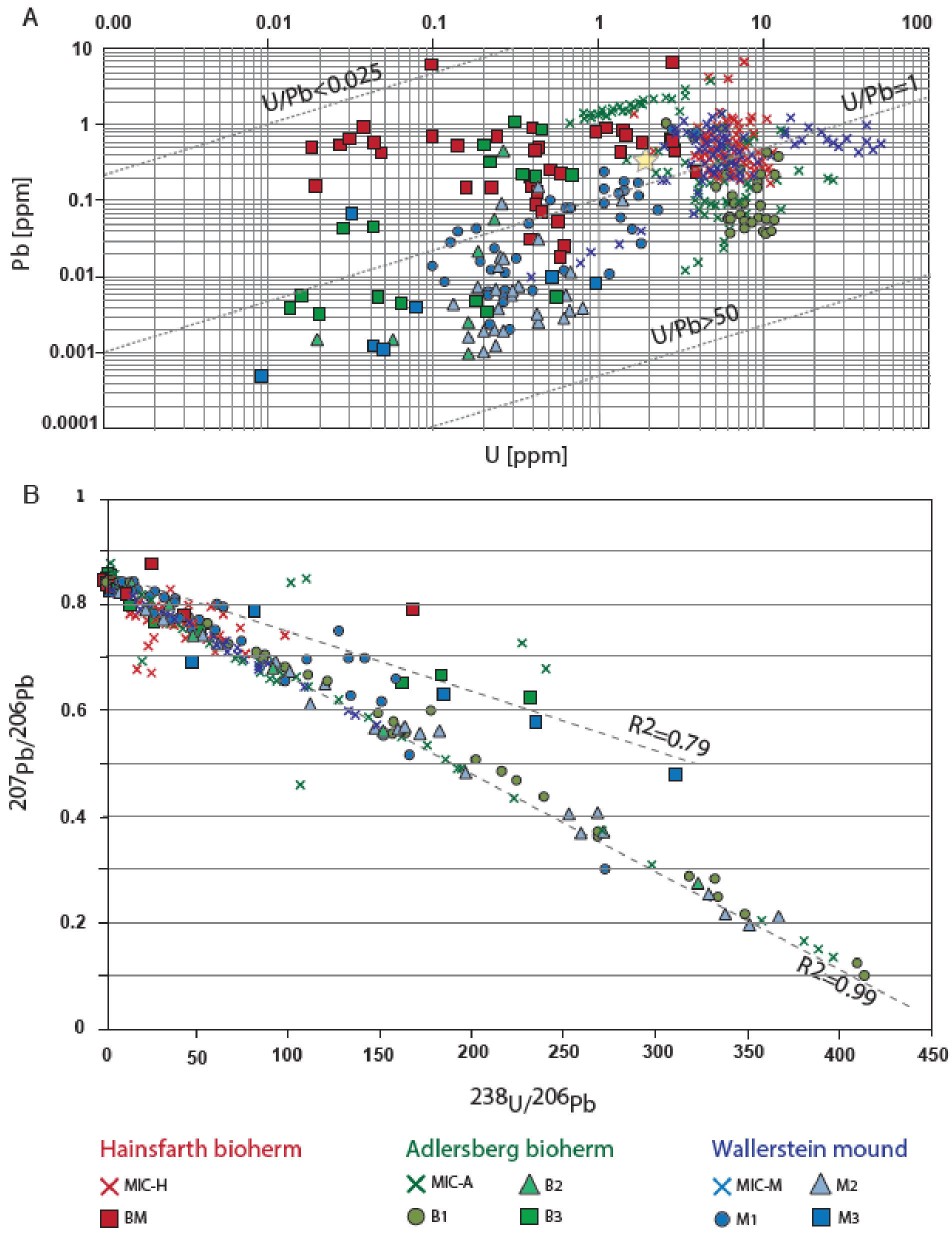

Figure 22. U and Pb geochemistry for the carbonate phases analysed from the three facies investigated. Each dot corresponds to an ablation analysis. MIC-H, MIC-A and MIC-M stand for micrite from the Hainsfarth bioherm, Adlersberg bioherm and Wallerstein mound, respectively. B1 and M1 are pendant calcite cements. B2 and M2 are isopachous calcite cements. BM, B3 and M3 are blocky calcite cements. A) Cross-plot of Uranium (U) versus Lead (Pb) concentrations expressed in parts per million (ppm). The carbonate U and Pb composition is included between the dashed lines (0.025 < U/Pb < 50). The yellow star represents the carbonate U and Pb mean composition after Roberts et al. (2020a). B) Cross-plot of $^{238}U/^{206}Pb$ versus $^{207}Pb/^{206}Pb$ ratios and corresponding main regression line (R^2=0.99). Some data points define a different slope (R^2=0.79).

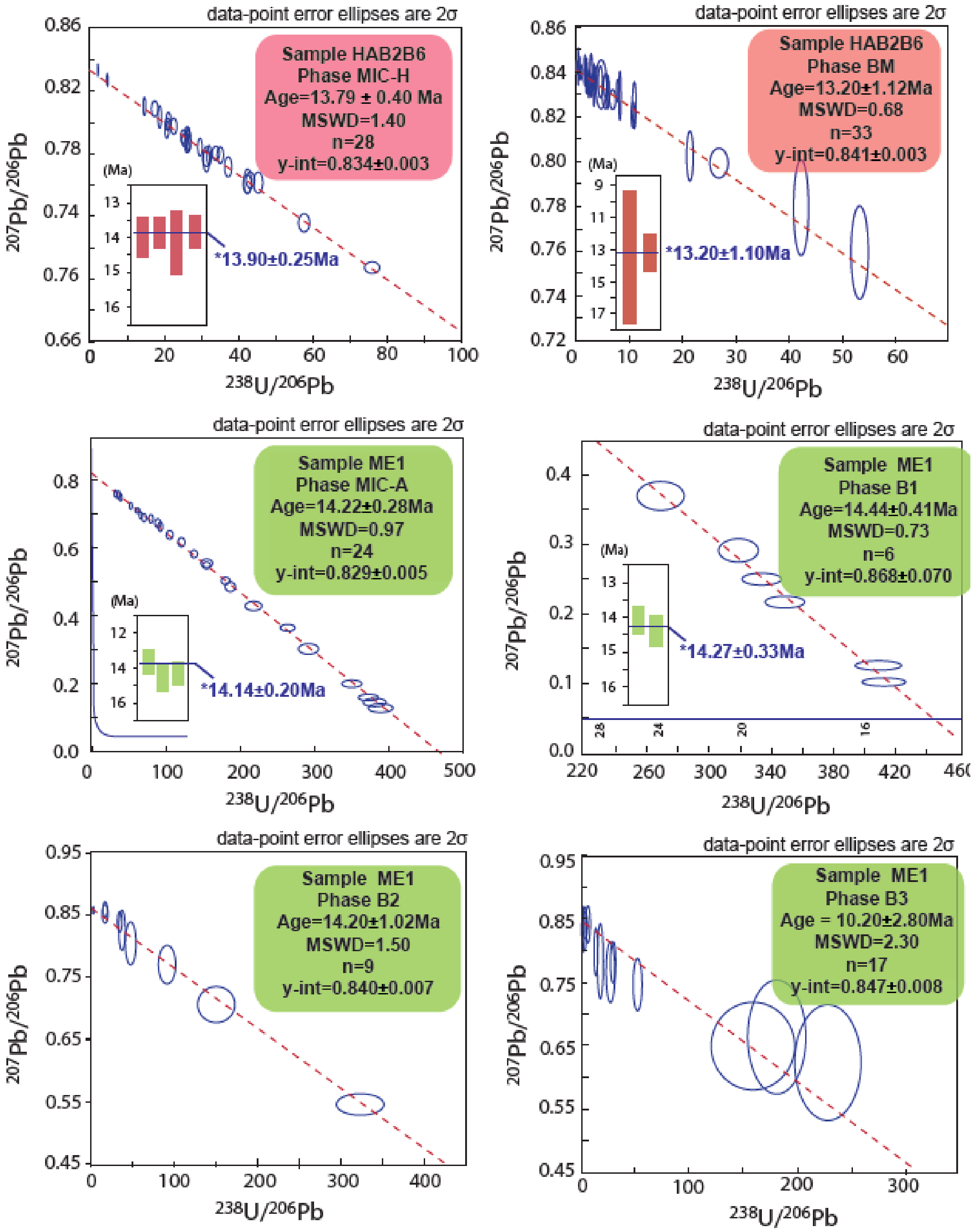

Figure 23. $^{238}U/^{206}Pb$ versus $^{207}Pb/^{206}Pb$ Tera-Wasserburg Concordia diagrams and corresponding absolute ages for MIC-H and BM carbonates from HAB2B6 sample (Hainsfarth bioherm, in red) and for MIC-A, B1, B2 and B3 carbonates from ME1 sample (Adlersberg bioherm, in green). Red dashed lines represent the isochrons. Blue ellipses represent the ‘n’ spot analyses and corresponding isotope ratios obtained. In blue are the Concordia curves. MIC-H, BM, MIC-A and B1 carbonate phases were analysed in different analytical sessions: ages obtained for each session are reported as vertical bars and the produced weighted average ages are indicated by asterisks. All ages are reported with 2σ confidence.

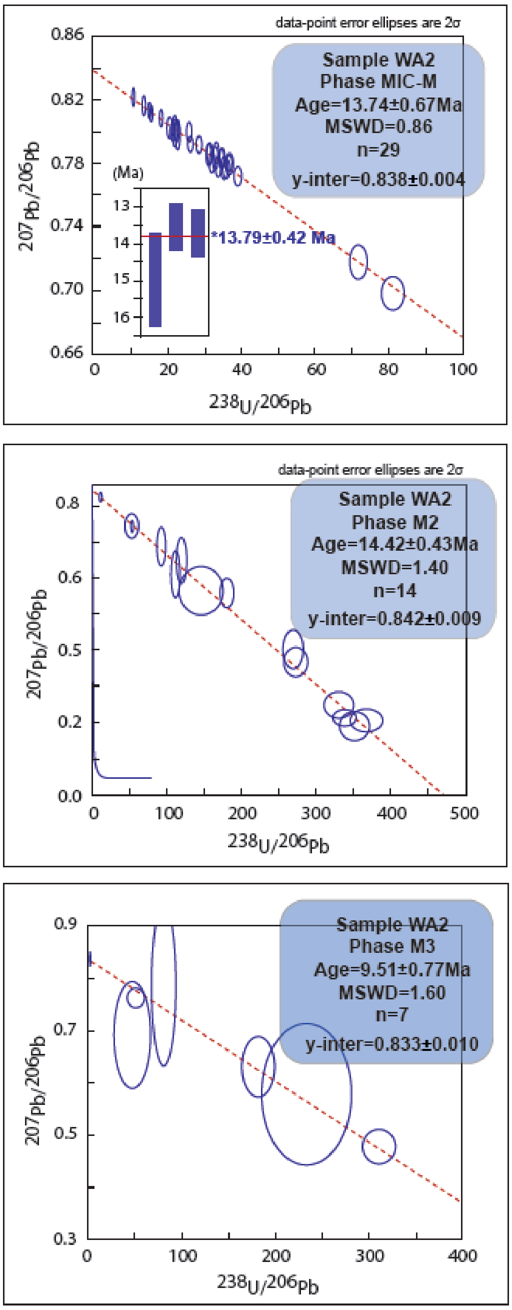

Figure 24. ^{238}U/^{206}Pb versus ^{207}Pb/^{206}Pb Tera-Wasserburg Concordia diagrams and corresponding absolute ages for MIC-M, M2 and M3 carbonates from WA2 sample (Wallerstein mound). Red dashed lines represent the isochrons. Ellipses represent the 'n' spot analyses and corresponding isotope ratios obtained. In blue are the Concordia curves. MIC-M phase was analysed in three analytical sessions: vertical blue bars represent the ages obtained, and the produced weighted average age is indicated by an asterisk. All ages are reported with 2σ confidence.

The depositional carbonate facies investigated (Hainsfarth bioherm, Adlersberg bioherm, Wallerstein mound) consist of micrites (MIC-H, MIC-A, MIC-M) which show no petrographic evidence of major diagenetic modifications, beside minor dissolution, dolomitisation and silicification (Fig. 20, Table 2). This is in line with the preservation of low-Mg calcite ostracodes reported from the Hainsfarth bioherm facies (Christ et al., 2018).

This is further supported by the covariance between micrite $\delta^{13}C$ and $\delta^{18}O$ values (R^2=0.95; Fig. 21), also reported by previous authors (e.g. Pache et al., 2001; Della Porta, 2015; Christ et al., 2018), which is typical of carbonates precipitated in closed lakes (Della Porta, 2015 and references therein).

The partial dolomitisation affecting the Adlersberg bioherm micrite (MIC-A; Fig. 20C) is considered an early diagenetic process driven by lacustrine and/or meteoric phreatic fluids (e.g. Riding, 1979; Arp et al., 2017). Hence, the ages obtained for MIC-A (Table 3) should confidently reflect the timing of deposition even if ablation spots fall within both dolomitised and undolomitised portions of the micrite.

The early cementation history of the studied samples was driven by vadose and phreatic lacustrine fluids and is recorded by the presence of pendant (B1, M1) and isopachous (B2, M2) calcite cements (Fig. 20, Table 2). These cement types are interpreted to have precipitated together or right after the bioherm and spring mound micrites (MIC-H, MIC-A, MIC-M) that host them. They are characterized by δ^{13}C and δ^{18}O covariance reasonably consistent with that defined for the depositional carbonates (micrites), though some lower δ18O values also occur (Fig. 21).

The three blocky calcite cements (BM, B3 and M3) post-date the early diagenetic phases (Fig. 20). They display distinctive CL response and negative δ^{18}O values and lack δ^{13}C and δ^{18}O covariance (Fig. 20 and 21), suggesting that they resulted from different post-depositional (i.e. precipitating during later diagenesis) cementation events (e.g. Goldstein, 1991). The CL response of BM cement (Fig. 20A), together with the negative δ^{13}C and δ^{18}O values (Fig. 21), suggest precipitation from relatively early meteoric phreatic fluids. The B3 and M3 cements occur as last pore-filling phases; their CL responses (Fig. 20D, H) and negative δ^{18}O values (Fig. 21), together with the ferroan nature of B3 (Fig. 20C), suggest precipitation from reducing fluids during burial.

The petrographic and C-O isotope analyses suggest that depositional carbonates (MIC-H, MIC-A, MIC-M micrites) and early diagenetic cements (B1, B2, M1 and M2) preserved their pristine petrographic and geochemical features. Therefore, the U-Pb ages obtained from these phases (Table 3) may be confidently used to gather insights on the original depositional timing of the three carbonate facies investigated. Diversely, the U-Pb ages produced from the BM, B3 and M3 blocky calcite cements (Table 3) should provide information on the timing of three different post-depositional cementation events.

Ries Crater carbonate U-Pb geochronology. Multiple studies aimed to resolve the general chronostratigraphy and diagenesis of the Ries Crater lacustrine deposits and focussed on: 1) the timing of sedimentation onset and the duration of the lake life-time; 2) the margin-margin and basin-margin stratigraphic correlations; and 3) the cementation history of the marginal facies. This study reports the first U-Pb ages from both depositional and diagenetic carbonates of the Ries Crater marginal deposits. The accuracy of these ages is here discussed within the Ries Crater geological framework, well-established by previous studies (see section 4.1.2 and Supplementary data A in section 4.1.9).

1) The reconstruction of the time elapsed between meteorite impact and sedimentation onset, as well as the entire lake life-time, has been attempted by several authors. The different datasets converge towards the onset of sedimentation occurring shortly after the impact (Buchner and Schmieder, 2009; Stöffler et al., 2013) and the entire succession being deposited in a time window of > 1.2 and <2 Ma (Füchtbauer et al.,1977; Pohl, 1977; Arp et al., 2017). Overall, the U-Pb ages here obtained for depositional and early diagenetic carbonate phases from marginal facies (Fig. 23 and 24, Table 3) agree with a short time gap between impact (~14.9Ma) and sedimentation onset and with the 2Ma maximum age estimate for the lake life-time previously proposed. Further constraints on lake life-time duration may be inferred by considering the oldest and youngest U-Pb ages obtained from depositional carbonate phases (Table 3). The 14.33±0.27 Ma oldest age obtained from the micrite of the Wallerstein mound (MIC-M), which is known to be coeval with basinal unit C (Arp et al., 2013a, 2017), indicates that the marginal facies analysed presumably existed already at ~14.60Ma (i.e. ~0.30Ma after the impact). This is in line with Arp et al. (2013b) that considered the older basinal unit B to be deposited around 0.25Ma after the impact (see Supplementary data A; section 4.1.9). WA2 sample micrite (MIC-M) was not taken as the youngest sample because of disturbance of the U-Pb isotope system. Indeed, multiple dating attempts provided poorly precise ages (uncertainties up to 9%; Table 3) that are appreciably younger than the fibrous calcite cement M2 (14.42±0.43Ma) held within the same sample. Therefore, the 13.9±0.25Ma (n_w=4) age of the Hainsfarth bioherm micrite (MIC-H) was taken as the youngest of the dataset. This age suggests that sedimentation has continued at least up to 13.65Ma (i.e. ~1.25Ma after the impact), in good agreement with the >1.2Ma sedimentation duration proposed for basinal units (Füchtbauer et al., 1977; Pohl, 1977; Arp et al., 2017).

2) In the last decades, several authors attempted to establish margin-margin and basin-margin stratigraphic correlations between the Ries Crater lake deposits, based on drilling campaigns and sedimentological, geochemical and magnetostratigraphic studies (Arp et al., 2017 and references therein). Correlations among marginal facies suggest that the Hainsfarth bioherm is younger than the Adlersberg bioherm and that the Wallerstein mound formed in a time window included between the growths of both bioherms (Arp et al., 2013a). The U-Pb ages of the three marginal facies overlap within uncertainties (Table 3, Fig. 25). However, the Hainsfarth and Adlersberg micrite ages (13.90±0.25Ma, n_w=4 and 14.14±0.20Ma, n_w=3, respectively, Table 3), together with the weighted

average age of the early diagenetic B1 and B2 cements (14.27±0.25Ma, n_w=3, MSWD=0.59; Table 3) are in agreement with the correlation previously proposed by Arp et al. (2013a). Diversely, the 14.33±0.27Ma age of micrite (MIC-M) from the Wallerstein mound, together with the weighted average age of the early diagenetic M1 and M2 cements (14.36±0.33Ma, n_w=4, MSWD=0.17; Table 3) suggest that the Wallerstein mound formed before and during the Adlersberg bioherm growth (Fig. 25), in contrast with what proposed by Arp et al. (2013a). Available basin-margin stratigraphic correlations based on sedimentological and geochemical investigations suggest that the basinal C and D units are coeval with the Adlersberg and Hainsfarth bioherms, respectively (Arp et al., 2017). Age estimates for the deposition of basinal units (A-B-C-D) were here constrained by coupling the meteorite impact timing with the basinal unit magnetostratigraphy data using an approach previously presented by Arp et al. (2013b) (see section 4.1.2 and Supplementary data A in section 4.1.9). By combining these age estimates for basinal units with the U-Pb ages obtained in this study from marginal carbonates, it may be concluded that the three marginal facies formed during the deposition of basinal unit C and part of unit D (Fig. 25), supporting stratigraphic correlations from previous authors.

3) Different types of post-depositional cements, precipitated from fluids of meteoric to burial origin, were recognized within the Ries Crater marginal facies (Pache et al.,2001; Christ et al. 2018). Although this study mainly focuses on the timing of the marginal facies deposition, it also provides temporal constraints on the later cementations. The BM, B3 and M3 blocky calcite cements clearly display younger ages when compared to the depositional and early diagenetic phases previously discussed (Fig. 25), in line with petrography and C-O isotope geochemistry. In particular, the age of BM cement (13.20±1.10Ma, n=2; Table 3) confirms the relatively early origin from meteoric fluids. Diversely, the B3 and M3 cements reveal younger ages respectively of 10.20±2.80Ma and 9.51±0.77Ma (Fig. 25), pointing at different burial fluid events occurring 4Ma after the deposition of the three marginal facies.

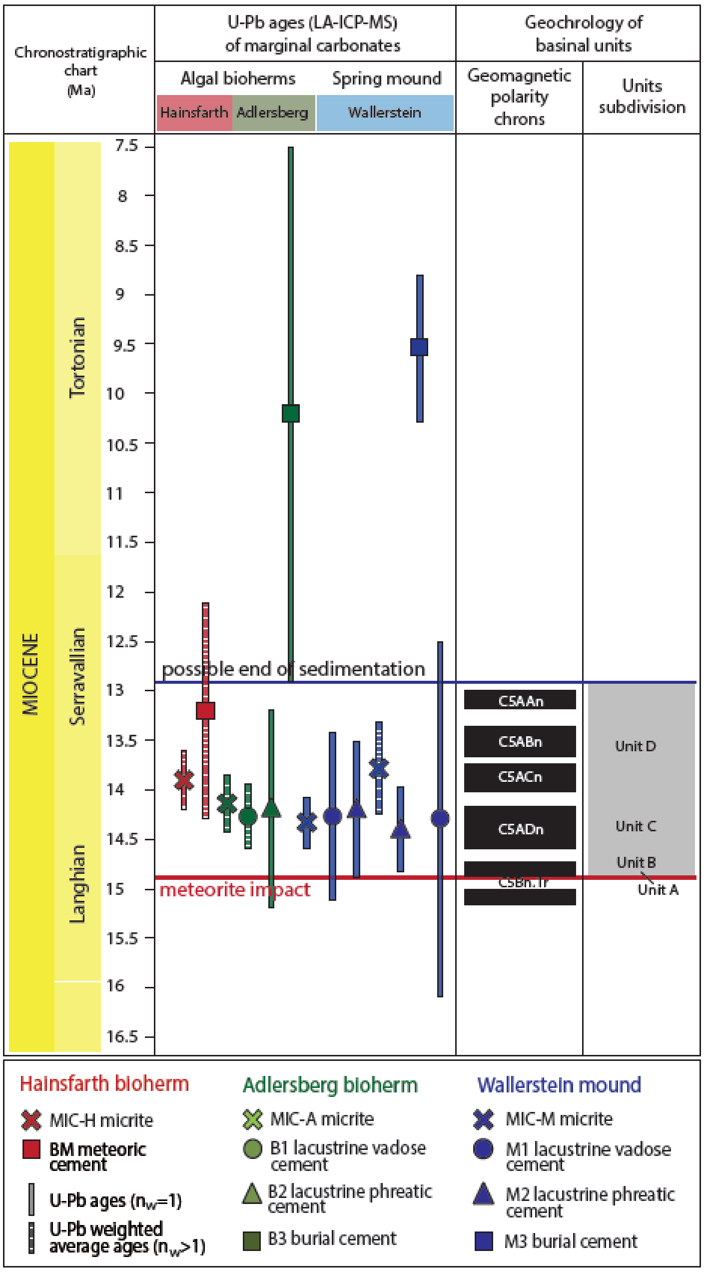

Figure 25. Chronostratigraphic chart of Miocene time (IUGS v 2020/01) with absolute ages for marginal and basinal facies of the Ries Crater lacustrine basin. Absolute ages for the depositional and diagenetic carbonate phases of the marginal facies (Hainsfarth bioherm, Adlersberg bioherm and Wallerstein mound) were obtained by U-Pb geochronology via LA-ICPMS. Dashed vertical bars represent weighted average ages produced by multiple LA-sessions on the same carbonate phases, as reported in Table 3. All age uncertainties (vertical bars) are reported as 2σ. Absolute ages of geomagnetic polarity chrons are from the Astronomical Tuned Neogene Time Scale (ATNTS2012). Normal and reverse polarity is indicated in black and white, respectively. The meteorite impact is considered as occurring at ~14.9Ma (after Schwarz et al., 2020 and references therein), whereas absolute ages of basinal units (A-B-C-D) are defined after Arp et al. 2013b and Rocholl et al. (2017, 2018).

To conclude, the carbonate U-Pb ages obtained via LA-ICPMS are consistent with the petrography and C-O isotope interpretation and with the previous literature constraints on the well-established geological evolution of the Ries Crater basin. These results allow to successfully validate the geological consistency (accuracy) of the U-Pb ages obtained and confirms the potential of this dating approach to reveal origin and precipitation timing of depositional and diagenetic carbonate phases, also in poorly time-constrained geological contexts.

U-Pb carbonate chronostratigraphy in continental. The carbonate U-Pb geochronology is considered to be poorly suitable for applications in stratigraphy, mainly due to the large age uncertainties commonly obtained (Roberts et al., 2020a). However, the results here presented indicate that in poorly time-framed geological contexts, such as most continental sedimentary systems, carbonate U-Pb dating may allow to successfully bracket the depositional time of previously undatable deposits.

Future applications of carbonate U-Pb dating for chronostratigraphic purposes in continental systems will require well-established dating protocols to overcome current limitations, such as: 1) the choice of the phases to be dated and 2) the age precision.

1) Firstly, chronostratigraphic studies require to target depositional (e.g. micrite, bioclasts) and early diagenetic (e.g. marine, lacustrine cements) carbonate phases that may inform about depositional ages of the continental deposits. Before dating, these phases need to be identified and separated from later diagenetic phases, commonly occurring in the same sample. Petrography and geochemistry studies, allowing to reconstruct cement stratigraphy and paragenesis (e.g. Goldstein, 1991), are necessary to establish relative timing and precipitation environment of the different phases. This knowledge is key to target the right phases to be dated, depending on the survey final aim. The study here presented underlines the importance to acquire U-Pb ages based on a detailed petrographic and geochemical characterization of the carbonate samples. Indeed, three diagenetic phases with post-depositional features were identified prior to date and, as expected, provided younger U-Pb ages (Fig. 25).

Once the carbonate phases to be dated for chronostratigraphic purposes are identified, the preservation of their pristine geochemical composition needs to be evaluated. Hints for diagenetic modifications may be deduced from carbonate petrography and geochemistry features. Diagenetic overprint of depositional to early diagenetic cements can be inferred, among others, from: 1) the crystal habitus and size (e.g. micrite crystals > 4µm); 2) the staining and CL response (e.g. revealing ferroan nature or mottled CL); 3) the presence of micro-fracturing, crystal reaction borders and/or bi-phase fluid inclusions; 4) the $\delta^{13}C$-$\delta^{18}O$ compositions that deviate from expected values.

2) The age precision is the key factor to understand the potentialities and limitations of the carbonate U-Pb geochronology for chronostratigraphic studies. The larger the age uncertainty, the lower the method time-resolution, resulting in a major limitation in old carbonates. Indeed, the same 1.5% age precision would result in absolute uncertainties of 0.2-0.3Ma for Miocene carbonates (this study) and of ~8Ma for Lower Cambrian carbonates. Overall, the initial U-Th-Pb isotope composition and the dating technique chosen (e.g. ID-TIMS versus LA-ICPMS), play a crucial role in determining the final age precision. Previous authors have used carbonate U-Pb dating via bulk (i.e. ID-TIMS) and in-situ (i.e. LA-ICPMS) analyses to constrain the depositional age of lacustrine deposits of known age. These studies provide useful information to understand the limitation of these dating approaches in continental carbonate settings. Isotope dilution (ID-TIMS) U-Pb geochronology was used to date the Miocene lacustrine carbonate tufa from the Barstow Fm. (California, USA), deposited within a time window of ~5 Ma (Cole et al., 2005), which is much longer than the 2 Ma depositional time interval of the Ries Crater deposits. Obtained ages are consistent with Ar/Ar geochronology absolute constraints and are precise down to 0.9%, due to their exceptionally high U contents (up to 180 ppm). Similarly, precise U-Pb (ID-TIMS) ages were reported by Hill et al. (2016) from the Upper Cretaceous-Paleocene Colorado Plateau lacustrine carbonates (U<30ppm). Geochronology by ID-TIMS is known to provide the most accurate assessment of the U-Pb age of carbonate samples. However, it is time consuming and labour intensive and it may have a lower success rate due to the limited spatial-resolution (Roberts et al., 2020a). Indeed, carbonates are characterized by low U and Pb concentrations (usually <1ppm) that are heterogeneously distributed at the sub-mm scale (Rasbury & Cole, 2009). This specific composition requires relatively large volumes of material to be analysed, increasing the risk of mixing carbonate phases with different ages.

In situ (LA-ICPMS) U-Pb geochronology was used by Frisch et al. (2019) to date the Miocene alluvial-lacustrine carbonates (U<10 ppm) from the Aktau succession (Kazakhstan). The ages reported show a very good correlation with magnetostratigraphy and cyclostratigraphy data and are precise down to 3% (2σ), in line with Roberts et al. (2020a), who stated that carbonate U-Pb (LA-ICPMS) ages are mostly associated with uncertainties of 2-3 % (2σ), or higher. New advances on 2D elemental and isotopic ratio mapping allowed Drost et al. (2018) to produce ages with uncertainties down to 1% from early diagenetic carbonate cements (U<40ppm) of the Carboniferous-Permian Rothenburg Fm. (Germany). Results are consistent with biostratigraphic constraints and zircon U-Pb geochronology from interbedded ash layers and encourage the application of this dating approach also in Paleozoic continental carbonate systems. The U-Pb (LA-ICPMS) technique was chosen in this study because it has many key benefits compared to the bulk techniques: the dating procedure is simpler, faster and analyses are preformed directly on thin sections with sampling (ablation) spot sizes of <0.2mm. This allows discarding diagenetically altered areas and enables to date volumetrically minor carbonate phases. Moreover, aiming at identifying areas with high and variable $^{238}U/^{206}Pb$ ratios, thin section isotope mapping and non-systematic (random) sample pre-screening can be performed prior to analysis (e.g. Drost et al., 2018). These technical advantages significantly enhance the success rate of carbonate U-Pb dating even if LA-ICPMS is considered to be analytically less precise than ID-TIMS (Roberts et al., 2020a).

In the present study, the Ries Crater Miocene lacustrine carbonates showed U concentration usually below 10ppm (Fig. 22) and were dated with precision mostly included between 1.5 and 3% (2σ) after propagating all necessary uncertainties. The ages produced agree with other time constraints furnished from the well-established geological framework of the Ries Crater basin validating the accuracy of the applied method. Our results show that ages from depositional and early diagenetic carbonates are consistent (Fig. 25) since the weighted average age of depositional carbonates (MIC-H, MIC-A, MIC-M) of 14.09±0.18Ma (MSWD=1.5; nw=11) is within uncertainty indistinguishable from the 14.30±0.20Ma (MSWD = 0.3; nw = 7) weighted average age of the early diagenetic carbonates (B1, M1, B2, M2). This suggests that both carbonate types may potentially be used as reliable geochronometers, as long as they retain their pristine geochemical composition. Depositional carbonates (micrites) seem to have a higher dating potential since they provided more precise ages (internal uncertainties between 1.3 to 4.7%, in 9 out of 11 samples) if compared to the early diagenetic cements. This is most likely due to the interplay of three factors characterizing the micrite samples: 1) higher U/Pb variability, 2) higher U (> 2ppm) concentrations, combined with 3) relatively low initial Pb (Fig. 22). On the contrary, the early diagenetic cements (B1, M1, B2 and M2), precipitated from lacustrine fluids, display about 30% less precise ages (internal uncertainties between 1.9 to 7%, in 6 out of 7 samples). This is not a rule of thumb and is rather due to the initial composition of the carbonates studied, as shown by previous authors providing highly precise ages from early diagenetic lacustrine cements (Drost et al., 2018).

Repeated measurements on the same carbonate phases yielded consistent ages within analytical uncertainties, allowing to assess and recheck the long-term reproducibility of the applied method (Table 3, Supplementary data G.1 in section 4.1.9). Additionally, a good strategy to improve the age precision is to determine the weighted average of the single ages produced from a specific carbonate phase, especially when the leading cause of uncertainty is the low variability of the U-Pb isotope ratios.

The age precision obtained in the present study was adequate to constrain the depositional timing of the three marginal facies investigated and to attempt stratigraphic correlations among time-equivalent (margin-margin and basin-margin) lateral facies. However, it was not sufficient to resolve their small age difference (<0.4Ma) in a depositional time window of <2Ma.

Overall, the study here presented shows that in lacustrine (and more broadly continental) deposits of Miocene age is possible to obtain geologically consistent ages with uncertainties mostly between 1.5 and 3% (2σ). This may confidently assist stratigraphic studies at the time resolution of 3rd order depositional sequences (0.5-5Ma). These results encourage the use of U-Pb (LA-ICPMS) technique as a chronostratigraphic tool for carbonates from continental settings, where other commonly applied chrono-chemo-bio-stratigraphic approaches may be insufficient and chronostratigraphic correlations are usually out of reach.

4.1.7 Conclusions

Depositional carbonates (micrites), together with early diagenetic (lacustrine) and post-depositional (meteoric and burial) calcite cements from marginal facies of the Ries Crater impact basin were investigated. Petrography and C-O stable isotope analyses indicate that depositional and early diagenetic carbonate phases preserved pristine geochemical composition and therefore are ideal targets to apply in-situ U-Pb geochronology (LA-ICPMS) in order to constrain the facies depositional timing, whereas later diagenetic phases may inform on the post-depositional cementation history.

All carbonates were successfully dated. U-Pb ages of micrites and early diagenetic cements (between 14.7±1.81 and 13.9±0.25Ma) are consistent with the geological and geochronological constraints offered by the well-framed Ries Crater basin, validating the accuracy of the dataset and of the applied method. In particular, the U-Pb dataset indicates a very short time elapsed between meteorite impact and sedimentation onset and matches the minimum and maximum duration of lake life-time. The consistency between depositional and early diagenetic carbonate ages underlines that both carbonate types may suitably be used for U-Pb geochronology, as long as they retain their pristine geochemical composition. Finally, three later calcite cements were also dated at 13.20±1.1Ma, 10.20±2.80Ma and

9.51±0.77Ma, indicating that the basin was punctuated by different post-depositional cementation events.

Overall, the time-resolution achieved by the U-Pb (LA-ICPMS) technique for Miocene carbonates (down to 1.5%, 2σ; about 0.2-0.3Ma) was adequate to bracket the depositional age of the marginal facies investigated and to correlate them with siliciclastic basinal units in a time window <2Ma. This study conclusively suggests that, with an adequate protocol of sample selection, it is possible to obtain geologically consistent and precise ages from depositional and diagenetic continental carbonates that may confidently assist chronostratigraphic studies at the resolution of the 3rd order depositional sequences (0.5-5Ma).

4.1.8 ACKNOWLEDGMENTS

We are grateful to E. Bemer (IFP Energies nouvelles) for funding the survey in the framework of D. Montano’s Master project at the University of Milan. Manuscript writing was undertaken in the framework of D. Montano’s PhD project funded by IFP Energies nouvelles. Prof. M. Joachimski (GeoZentrum Nordbayern) is thanked for O-C stable isotope analysis of carbonates. The Fürst Wallerstein Braurei is thanked for allowing publication of analytical data on three Wallerstein mound samples collected in their property. The manuscript benefitted of significant improvements from the careful revisions of Prof. David Chew and an anonymous reviewer. This is FIERCE contribution No. 68.

4.1.9 Supplementary data

Supplementary data A. In the last decade the Ries Crater meteorite impact was dated by several authors (e.g., Buchner et al., 2010; Rocholl et al., 2017, 2018; Schmieder et al., 2018a,b; Schwarz et al., 2020), with ages ranging between 15.00±0.03Ma (zircon U-Pb dating; Rocholl et al., 2018) and 14.50±0.32Ma (Ar-Ar dating of recrystallized feldspars; Buchner et al., 2010). The 0.5Ma disagreement between these ages can be related to multiple factors as discussed by Rocholl et al. (2018), Schmieder et al. (2018a, b) and Schwarz et al. (2020). In this contribution is considered to occurr at around 14.9 Ma, in line with most of the absolute ages published in the last decade (Schwarz et al., 2020 and references therein).

Absolute age estimates for the deposition of basinal units (A-B-C-D; Füchtbauer et al., 1977; Jankowski, 1977) was achieved by coupling the meteorite impact timing with the basinal unit magnetostratigraphy, as previously done by Arp et al. (2013). Accordingly, the impact related suevite (i.e. melt bearing crystalline breccia; Stöffler et al., 2013) records a distinctive reverse magnetization and at the top the transition to normal polarity (Pohl, 1977; Pohl et al., 2010; Fig. A.1). As a consequence, the impact is supposed to occur at the top of a reverse magnetization stage.

Based on the absolute ages of geomagnetic polarity chrons by Hilgen et al. (2012) the meteorite impact was possibly allocated at the top of C5Bn.1r (15.03 to 14.87 Ma) or C5ADr (14.77 to 14.61 Ma) reverse chrons (Buchner et al., 2013; Rocholl et al., 2017; Schmieder et al., 2018a,b). The ~14.9Ma impact timing would therefore correspond to the top of C5Bn.1r (14.87Ma), in agreement with the interpretation of Rocholl et al. (2017, 2018).

The Ries Crater sedimentation onset is known to have occurred shortly after the impact (Buchner and Schmieder, 2009; Stöffler et al., 2013) as demonstrated by the weathering of the impactites driven by meteoric fluids (Muttik et al., 2011) and the short-distance fluvial transport of impact related breccia (Arp et al., 2019a). However, the exact time elapsed between the impact and the onset of sedimentation is at today unconstrained (Schmieder et al., 2018b).

Pohl (1977) suggest that unit A sediments were deposited in a few thousand years at the most and Arp et al. (2013) indicated that basinal unit B was deposited around 0.25Ma after the impact, which also implies a very short time gap between meteorite impact and sedimentation onset. Indeed, in 0.25Ma both unit A and part of unit B (at least 150m of sediments) were already accumulated in the basin. Consequently, it can be deduced that the first basinal sediments (unit A) were deposited during the C5Bn.1n chron that follows C5Bn.1r (Fig. A1).

In conclusion, the absolute age estimate for the four basinal units was constrained as follows: unit A is here considered to be deposited during C5Bn.1n, the transition from unit B to unit C is inside C5Adr

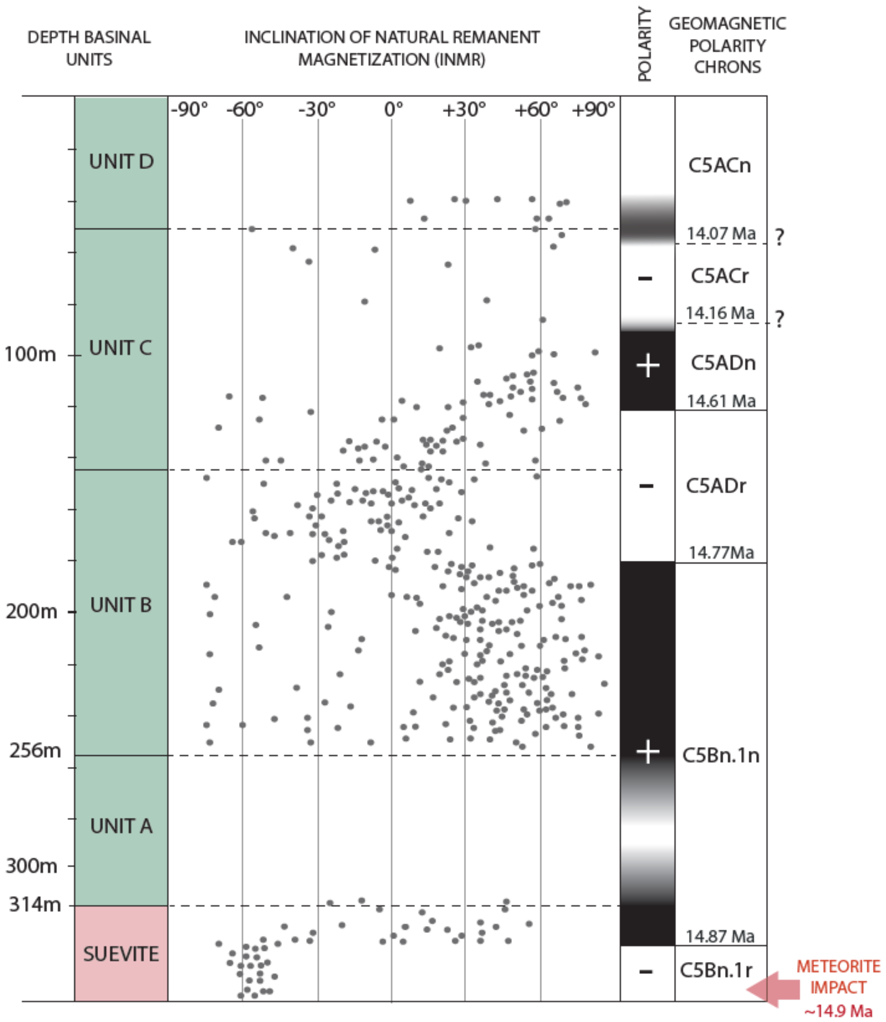

Figure A.1 Chart summarizing data from the Nördlingen 1973 borehole. Basinal lithostratigraphic units according to Füchtbauer et al. (1977) and Jankowski (1977) with corresponding Inclination of Natural Remnant Magnetization (INRM) and polarity from Pohl (1977) and Pohl et al. (2010). Normal and reverse polarity are indicated in black and white, respectively, whereas grey areas indicate insufficient INRM data and uncertain polarity. Absolute ages of geomagnetic polarity chrons are from the Astronomical Tuned Neogene Time Scale (ATNTS2012) of Hilgen et al. (2012).

chron and the onset of unit D deposition was allocated at ~14 Ma, at the limit between C5ACr and C5ACn chrons. This latter estimate is due to Pohl (1977) who highlights a transition from reverse to normal polarity at the base of unit D.

Supplementary data B

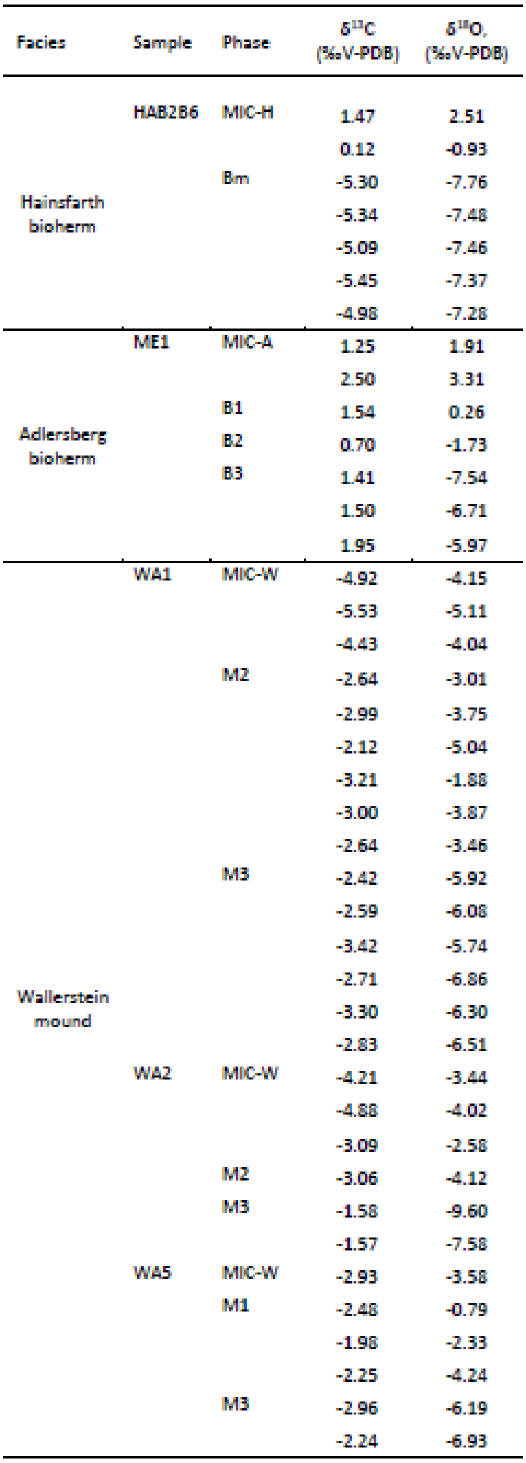

Facies	Sample	Phase	$\delta^{13}C$ (‰V-PDB)	$\delta^{18}O$, (‰V-PDB)
Hainsfarth bioherm	HAB2B6	MIC-H	1.47	2.51
			0.12	-0.93
		Bm	-5.30	-7.76
			-5.34	-7.48
			-5.09	-7.46
			-5.45	-7.37
			-4.98	-7.28
Adlersberg bioherm	ME1	MIC-A	1.25	1.91
			2.50	3.31
		B1	1.54	0.26
		B2	0.70	-1.73
		B3	1.41	-7.54
			1.50	-6.71
			1.95	-5.97
Wallerstein mound	WA1	MIC-W	-4.92	-4.15
			-5.53	-5.11
			-4.43	-4.04
		M2	-2.64	-3.01
			-2.99	-3.75
			-2.12	-5.04
			-3.21	-1.88
			-3.00	-3.87
			-2.64	-3.46
		M3	-2.42	-5.92
			-2.59	-6.08
			-3.42	-5.74
			-2.71	-6.86
			-3.30	-6.30
			-2.83	-6.51
	WA2	MIC-W	-4.21	-3.44
			-4.88	-4.02
			-3.09	-2.58
		M2	-3.06	-4.12
		M3	-1.58	-9.60
			-1.57	-7.58
	WA5	MIC-W	-2.93	-3.58
		M1	-2.48	-0.79
			-1.98	-2.33
			-2.25	-4.24
		M3	-2.96	-6.19
			-2.24	-6.93

Table B.1. $\delta^{13}C$ and $\delta^{18}O$ values for the ten carbonate phases analysed are reported in ‰ relative to the Vienna-Pee Dee Belemnite (V-PDB) standard. Most of the carbonate phases were analysed more than once in order to account for possible heterogeneities of their C-O stable isotope composition. BL isopachous fibrous cement from the Hainsfarth bioherm and DOL from the Adlersberg bioherm (described in Figure 2 and in Table 2) could not be micro-sampled and were therefore not analysed.

Supplementary data C

Table C.1

U-Pb carbonate geochronology LA-ICPMS raw data. The dataset is corrected offline using a macro-based in-house MS Excel© spreadsheet. To download go to https://doi.org/10.1016/j.epsl.2021.117011.

Supplementary data D

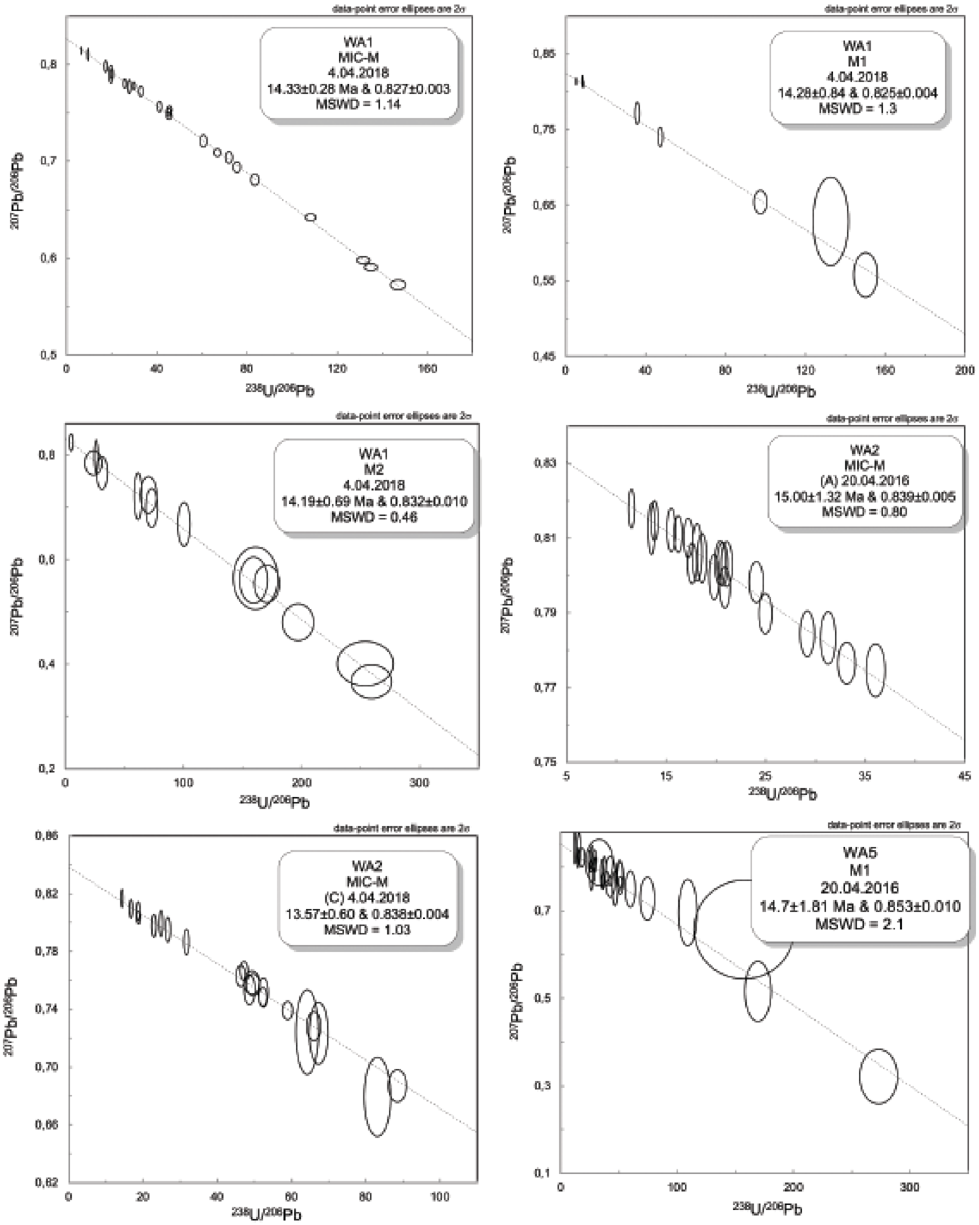

Figure D.1. $^{238}U/^{206}Pb$ *versus* $^{207}Pb/^{206}Pb$ Tera-Wasserburg Concordia diagrams and corresponding absolute ages for the Wallerstein mound samples (WA1, WA2 and WA5). Dashed lines represent the isochrons. Ellipses represent the 'n' spot analyses and corresponding isotope ratios obtained.

Supplementary data E

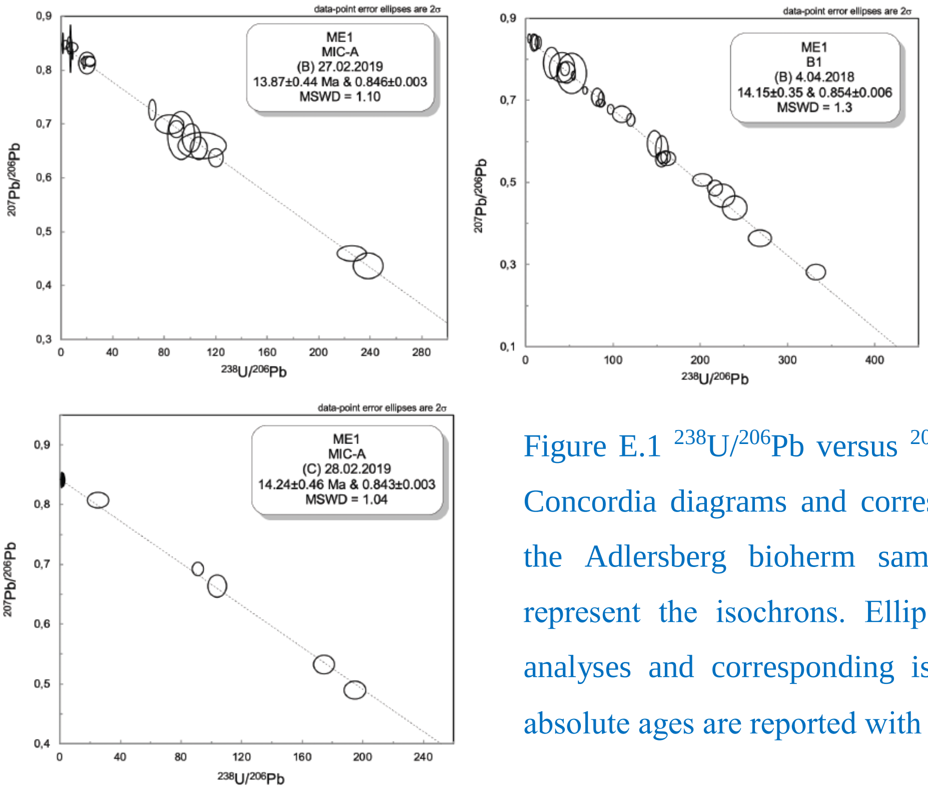

Figure E.1 ^{238}U/^{206}Pb versus ^{207}Pb/^{206}Pb Tera-Wasserburg Concordia diagrams and corresponding absolute ages for the Adlersberg bioherm sample (ME1). Dashed lines represent the isochrons. Ellipses represent the 'n' spot analyses and corresponding isotope ratios obtained. All absolute ages are reported with 2σ confidence.

Supplementary data F

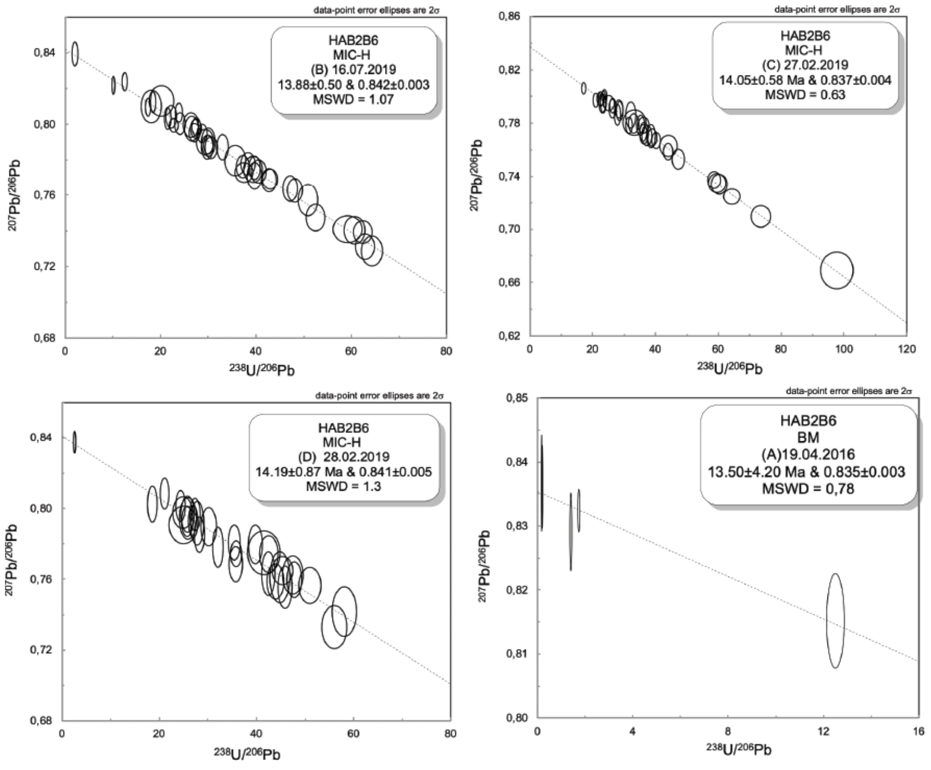

Figure F.1. ^{238}U/^{206}Pb *versus* ^{207}Pb/^{206}Pb Tera-Wasserburg Concordia diagrams and corresponding absolute ages for the Hainsfarth bioherm sample (HAB2B6). Dashed lines represent the isochrons. Ellipses represent the 'n' spot analyses and corresponding isotope ratios obtained. All absolute ages are reported with 2σ confidence.

Supplementary data G.

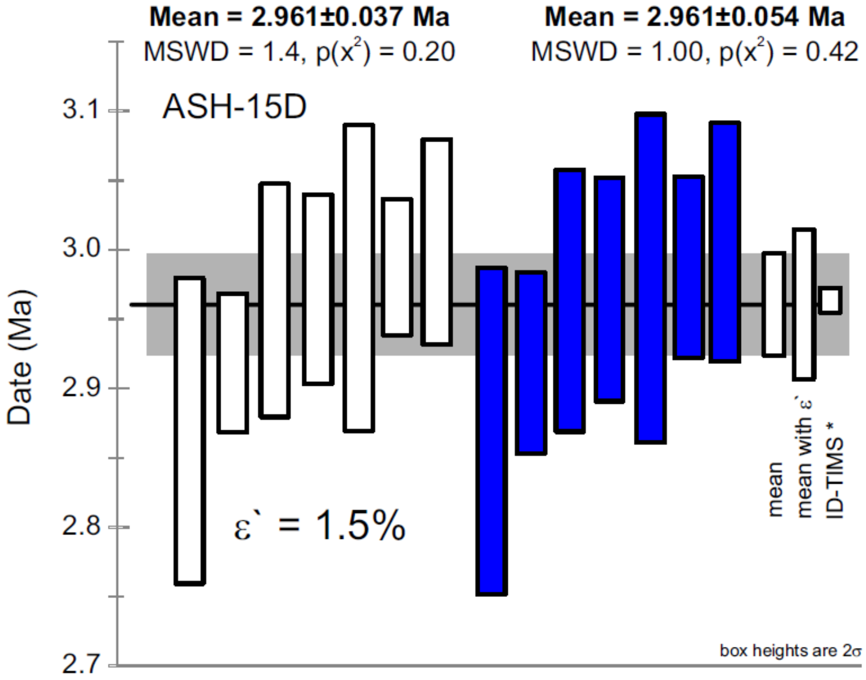

Figure G.1. Sorted intercept ages with 2σ uncertainty for ASH-15D (white; n_w = 7, MSWD = 1.4) analysed over a period of about 3 years (2016 to 2019) used to estimate the long-term excess of variance (ε`) of 1.5%. Data to the right (blue) includes the excess of variance propagated by quadratic addition. Also presented is the superpopulation mean with ε` and reference age from ID-TIMS (Nuriel et al., 2020).

5 THE CRETACEOUS-PALEOGENE YACORAITE FM.

5.1 Geological context: the Salta rift basin

The Salta rift basin, covering a surface of 150.000 km^2, is an Early Cretaceous–Middle Palaeogene basin located mostly in North-West Argentina (Fig. 26). It was initially interpreted as an aborted foreland rift basin related to the subduction of the Nazca Plate underneath the South American Plate (Galliski & Viramonte, 1988). The re-interpretation of the three magmatic and volcanic events (i.e. high alkaline composition; Viramontes et al., 1999) recognized to be coeval with the Salta rift, suggests that the rifting was probably associated to the opening of the South Atlantic Ocean that started during Early Cretaceous (Barremian). Initially the extension generated seven main isolated depocentres, bounded by structural highs. These sub-basins (i.e. Tres Cruces, Lomas de Olmedo, Métan, Alemania, El Rey, Sey and Brealito (Reyes, 1972; Salfity,1979; 1980;1982; Schwab, 1984 and Sabino, 2002) got interconnected during the Upper Cretaceous developing the Salta rift basin (Mon & Salfity, 1995) (Fig. 26).

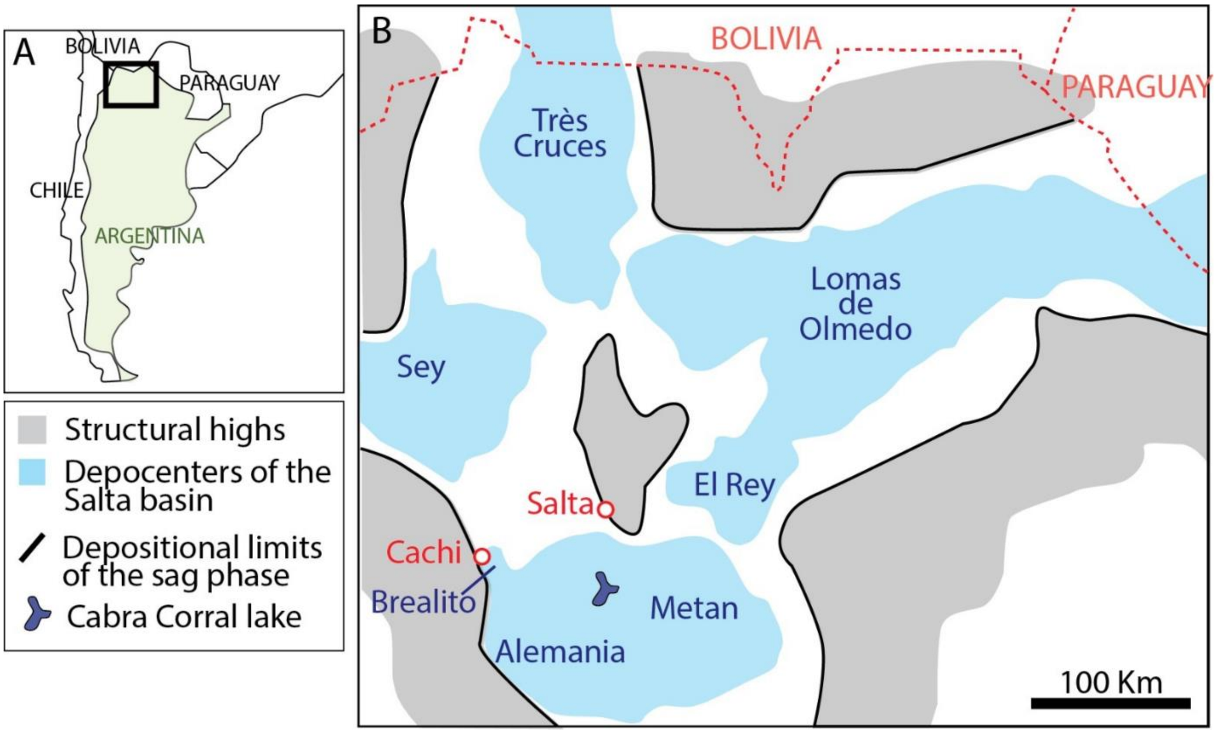

Figure 26 Location of Salta Basin and its sub-basins during the sag phase (Yacoraite Fm. deposition). Modified after Roemers et al. (2015).

The basin records 3 main tectonic stages of rifting: the syn-rift stage (Pirgua Subgroup), the transitional sag phase (Balbuena Subgroup) and the post-rift stage (Santa Barbara Subgroup). In the main depocentres, syn to post rift deposits reached a maximum thickness of around 5000m thick.

The syn-rift stage (Pirgua Subgroup; Reyes & Salfity, 1973) includes deposits of the Yasera, Las Curtiembres and Los Blanquito Fms. (Fig. 27). They mainly consist of red beds of fluvial conglomerates, sandstones, siltstones and shallow lacustrine deposits. During Las Curtiembres Fm. deposition, the rift had its climax (i.e. maximum fault growth rate controlling the tectonic subsidence).

The transitional sag phase (Balbuena Subgroup) corresponds to the onset of thermal subsidence. It includes Lecho, Yacoraite and Tunal Fms. deposits, reaching a maximum thickness of 400-500m. The Lecho Fm. is coeval with the early sag phase and mainly consists of sandstones deposited in aeolian to fluvio-lacustrine environments. The Yacoraite Fm. (up to 220 m thick) consists in lacustrine shales, mudstones, oolitic and stromatolitic limestones, interbedded with fine-grained sandstones. The Olmedo/Tunal Fm., coeval with the late sag phase, corresponds to dark shales, halite, anhydrite and gypsum deposited in lacustrine, brackish to hypersaline lake environment.

During the post-rift phase (Santa Barbara Subgroup) the basin was filled by the fluvio-lacustrine deposits of the Maella, Maiz Gordo and Lumbrera Fms. (Moreno et al., 1970).

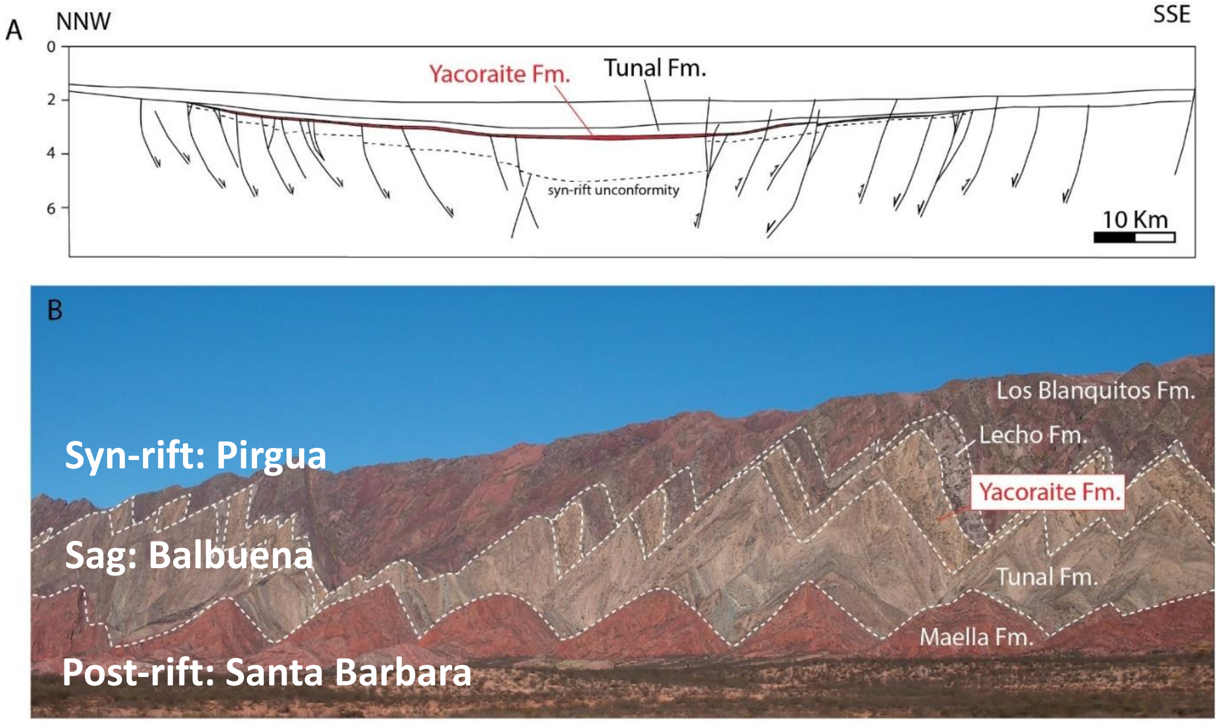

Figure 27. A) NS seismic line interpretation from the Lomas de Olmedo sub-basin. Modified from Cominguez & Ramos (1995). Panoramic view of the Salta rift deposits from the Tin Tin anticline (Amblayo locality).

After the Cretaceous rifting, the Salta deposits were involved in the Andean Orogeny (Carrera et al., 2006; Monaldi et al., 2008 and references therein). The extensional faults got inverted during Cenozoic times (Fig. 20A) and today the Salta rift deposits are folded and thrusted and exposed with masterpiece outcrops in the provinces of Jujuy, Salta and Tucumán (Fig. 27B).

5.2 Biostratigraphy and geochronology of the Salta rift deposits

The base of the Pirgua Subgroup is well time-constrained. Indeed, magmatic and volcanic deposits related to the Alto de Las Salinas Complex (Bossi, 1969) are interbedded at the base of La Yasera Fm. and provided ages of 128-112 Ma (K/Ar whole rock dating) and 126±3.5 Ma (unspecified method) (Clebsch, 1991). Further time constraints are available from basalts in La Yasera Fm. (96 ± 5, 99 ± 5 Ma; K/Ar whole rock dating; Valencio et al., 1976), in Los Curtiembres Fm. (78 ± 5 Ma, 76.4 ± 3.5 Ma; K/Ar dating; Valencio et al., 1976; Reyes et al., 1976) whereas the Los Blanquitos Fm. hosts Senonian sauropod dinosaurs (Bonaparte & Bossi, 1979). At the boundary between Los Blanquitos and Lecho Fms., volcanic deposits coeval with the Palmar Largo volcanism (Mädel, 1984) were dated at 70 ± 5 Ma (K/Ar dating, Gomez Omil et al., 1987). Data indicate that the Pirgua subgroup started to deposit during Barremian and persisted until Maastrichtian.

The depositional timing of the Balbuena subgroup has been long debated (Fig. 28). The Lecho Fm. hosts well preserved Senonian avian/non avian dinosaur bones (Bonaparte & Powell, 1980; Frankfurt & Chiappe, 1999, Weishampel et al., 2004; Cónsole-Gonella & Marquillas, 2014; Fig. 29). This, together with the 70 ± 5 Ma age obtained by Gomez Omil et al. (1987) at the top of the Los Blanquitos Fm. indicate deposition during Maastrichtian. The Yacoraite Fms. has been extensively investigated due to the occurrence of Senonian avian-non avian dinosaur tracks (Alonso, 1989; Cónsole-Gonella et & Aceñolaza, 2009; Díaz-Martinez et al., 2016; Cónsole-Gonella et al., 2017; Valais & Cónsole-Gonella; 2018) and at the top of the formation of Danian palynomorphs (Moroni, 1982). The Yacoraite Fm. is interbedded by frequent volcanic tuff ash layers known to be coeval with the Palmar Largo volcanism (Omarini et al., 1988; Fernandez, 1975). They were also attributed to the Late Cretaceous volcanic arc of northern Chile (Marquillas et al., 2011). U-Pb isotope radiometric ages from these layers were obtained by Marquillas et al. (2011), Pimentel et al. (2012) and Rohais et al. (2019) producing somewhat contradictory results (see Chapter 6).

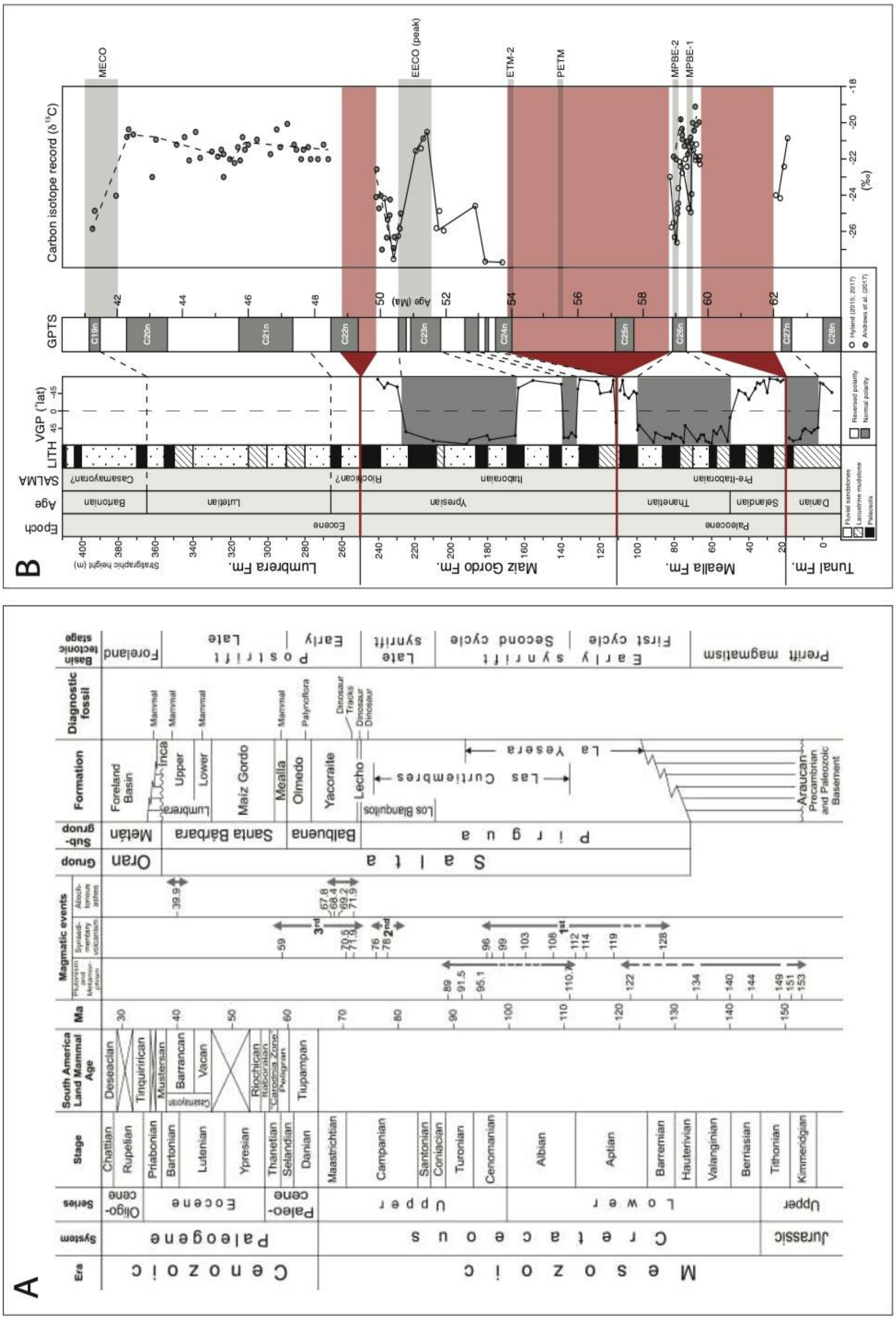

Figure 28 Examples of chronostratigraphic interpretation of the Pirgua, Balbuena and Santa Barbara groups. A) Chronostratigraphy of magmatic, sedimentary, and tectonic events of the Cretaceous Salta basin. From Marquillas et al. (2011). B) Stratigraphy and age model for the Salta Group. Age tie points shown by dashed lines, with depositional hiatuses shown by red lines/shading. Grey shaded bars indicate known climate events with recorded carbon isotope excursions during the Paleogene. From Hyland & Sheldon (2018).

In particular, Marquillas et al., (2011) ages are 3-4 Ma older than those obtained by Rohais et al. (2019) whereas Pimentel et al. (2012) provided the youngest age for the top of the Yacoraite Fm. (around 60 Ma) although with low precision and bad statistics (see Montano et al., in revision, Section 6.1). Indeed, the age of the Yacoraite Fm. remains debated, especially the base and the top. Dinosaur evidence are absent in the upper part of the Yacoraite Fm. and in the Tunal/Olmedo formation that instead presents palynological associations of Danian age (Quattrocchio & Volkheimer, 1988; 2000). Examples of dinosaur tracks in the Yacoraite Fm. are in figure 29. Conclusively the Balbuena subgroup was deposited between Maastrichtian and Danian.

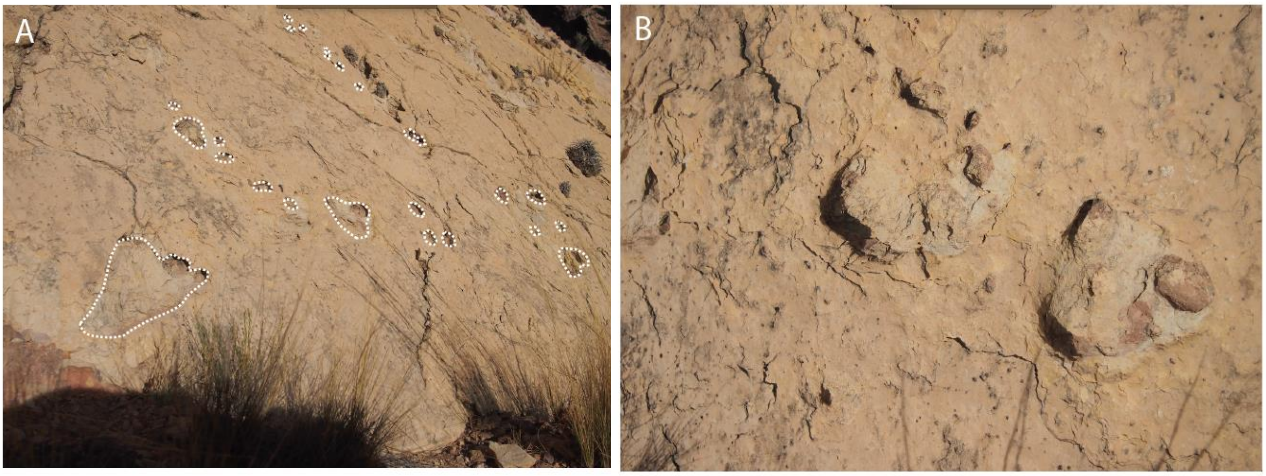

Figure 29. Yacoraite Fm. Senonian dinosaur track site from Maimarà locality in the Quebrada de Humahuaca (Jujuy, North-West Argentina). Pictures from field survey. For more details about this outcrop see Cónsole-Gonella et al. (2017).

The Santa Barbara group lacks absolute chronostratigraphic constraints as well as index taxa with short time duration. The only available constraint is an ash layer dated at 39.9 ± 0.4 Ma at the top of the Lumbrera Fm. Concerning the Maella Fm., Maiz Gordo Fm. and Lower Lumbrera Fm., chronostratigraphic interpretations were achieved by coupling available biostratigraphic, magnetostratigraphic and geochemical data. Accordingly, various scenarios have been proposed (Hyland et al., 2015; 2016; Andrews et al., 2017; White et al., 2018; Zimicz et al., 2020; Fernicola et al., 2021).

5.3 The Yacoraite Fm.

5.3.1 Geological setting and lithostratigraphy

The Yacoraite Fm. deposited in several sub-basins. The depocentre locations are shown in figure 26. This study focuses on the Métan-Alemania sub-basins. Until the end of the early sag phase, Métan and Alemania sub-basins were structured by the Guachipas palaeohigh. At the onset of the main sag phase, a wide depocentre was established in correspondence with this high. Here the Yacoraite Fm. reached its maximum thickness.

A wide body of literature deals with the depositional and palaeogeographic settings of this formation and hypotheses are still debated. According to previous authors the depositional setting could range from purely shallow marine settings (Marquillas et al., 2007) to purely lacustrine settings (Palma, 1986; Hernandez et al., 1999; Sial et al. 2001). An alternative hypothesis proposes a lacustrine system that experienced periodic marine incursions through Bolivia and possibly Peru (Marquillas et al., 2011). Rohais et al. (2012; 2014, 2019) support the scenario according to which the Yacoraite Fm. was deposited in a shallow lacustrine setting with some possible marine inlets in the northernmost sub-basins as testified by the presence of marine fish bones.

Lithostratigraphic analyses allowed to subdivide the Yacoraite Fm. in three members: Amblayo, Guemes and Alemania members (Reyes, 1972; Marquillas & Salfity, 1989). The Amblayo and Guemes members are characterized by carbonate and clastic dominated deposits, respectively. Whereas the Alemania Member, at the top, corresponds to an alternation of shallow carbonate beds and marly deposits.

5.3.2 Facies and depositional environments

Based on facies associations analysis, vertical stacking patterns, lateral facies change and overall geometry of the Yacoraite Fm. in the Mètan-Alemania basin, Deschamps et al. (2020) provides a general depositional model for this formation.

The predominance of shallow marginal facies primarily suggests that the Yacoraite Fm. deposited on a low- to medium gradient ramp margin (Deschamps et al., 2020). The depositional model is characterized by two end-members: one dominated by siliciclastic-deposition and another by carbonate deposition. The interplay of both sources results in mixed facies.

The siliciclastic-dominated facies are mainly located along previous footwall margins whereas the carbonate dominated ones preferentially occur in palaeo-highs far from the siliciclastic inputs.

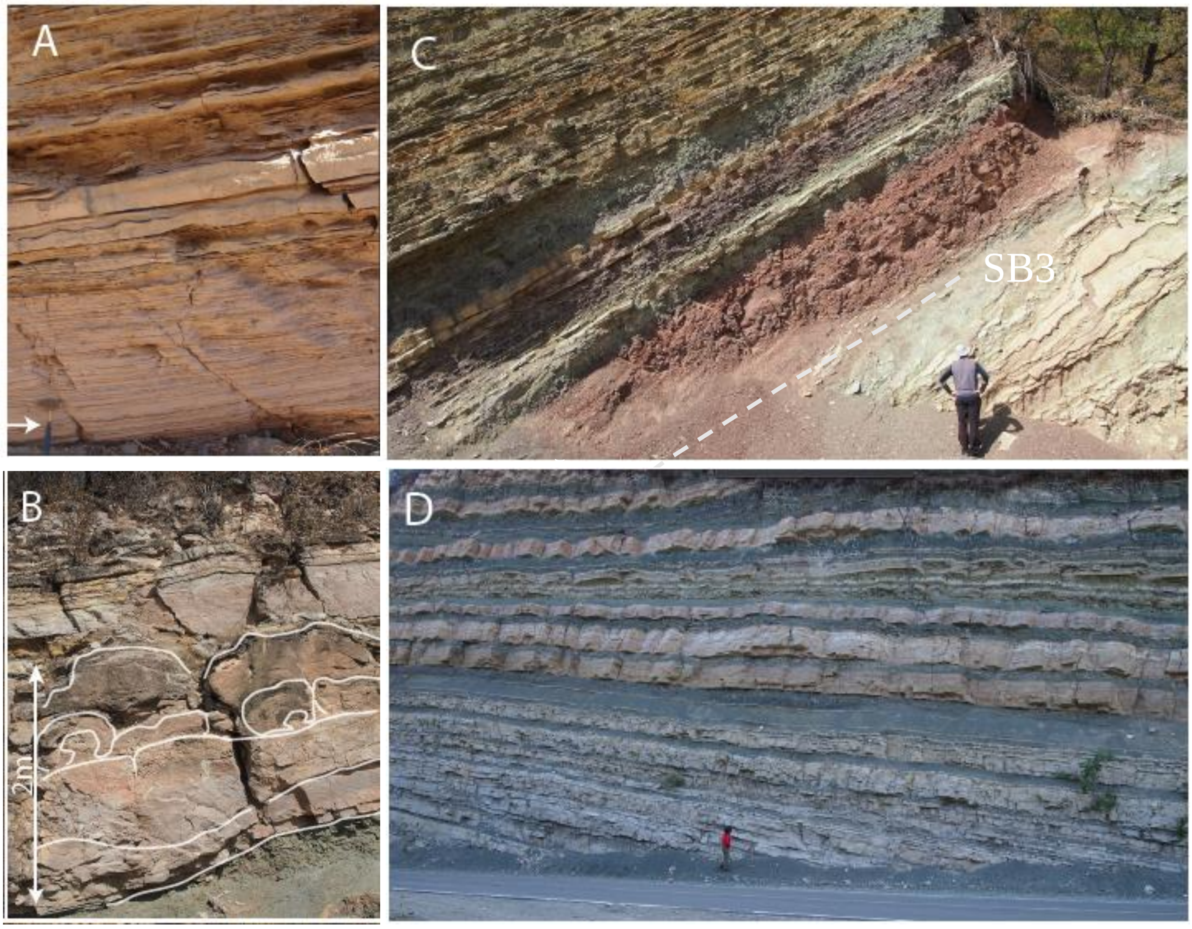

Figure 30. Field photographs from the Cabra Corral lake area. A) Fine to medium-grained sandstones with plane-parallel to wave ripples. Siliciclastic shore face deposits. Juramento section. The hammer for scale is 35cm long. B) Thick and continuous layers of large coalescent domal stromatolites with the characteristic moustache features growing on green silty dolomitic marls. Highly alternating facies of sequence 4. C) Red to grey siltstones with abundant current ripples, root traces and occasional carbonate concretions. The red body was deposited just above SB3. Clastic shore to alluvial facies. D) Masterpiece outcrop of the highly alternating facies association of the Alemania Member.

A depositional environment was attributed to each facies association (Deschamps et al., 2020).

In the western (Tintin, Los Cardones and Cachi area) and southern parts of the Mètan-Alemania basin, sedimentation is dominated respectively by high energy and low energy siliciclastic facies associations (e.g. sandstone with cross stratification or wave ripples; Fig. 30A).

Carbonate dominated facies associations are instead prevalent in the eastern and southern parts of the Métan-Alemania basin in correspondence, for example, with the old Guachipas palaeo-high where detrital input was very low (e.g. oolitic grainstone with wave ripples, stromatolite buildups; Fig.30B)

The upper part of the Yacoraite Fm. (Alemania Member) is characterized by a drastic change in the sedimentation pattern as well as the dynamic of the sedimentary system. Indeed, all over the basin it is possible to recognize some highly alternating patterns in the sediment stacking (Fig. 30D) reflecting frequent and rapid fluctuations of the lake level, favoured by the low bathymetry if compared to the basal part of the Yacoraite Fm. (i.e. the basin was almost filled by sediments). The high alternating deposits are characterized by sharp superposition of coarse grained marginal facies (usually oolitic grainstone with massive stromatolite bodies at the top and desiccation cracks) and silty deeper facies.

5.3.3 Sequence stratigraphy and palaeoenvironmental interpretation

The Yacoraite Fm. is a masterpiece example for the sequence stratigraphy of a lacustrine system since it consists of a second-order (or long-term) sequence subdivided in 4 'third-order' (or mid-term) stratigraphic sequences (Rohais et al., 2019; Deschamps et al., 2020; Fig. 31). Higher order cylicities, especially in the microbial facies, were discussed by Roemers et al. (2015), Deschamps et al. (2020) and Gomes et al. (2020) but were not considered in the present study that focuses on the third order cyclicity. In this chapter two types of key stratigraphic surfaces will be mentioned. Sequence boundaries (SB) bound the stratigraphic sequences and correspond to a basinward shift of the depositional system, with the abrupt transition from deep to very shallow environments. In proximal settings, SBs correspond to exposure events and erosion. Maximum flooding surfaces (MFS) instead, mark the climax of transgression of the depositional system. During sequence 1 deposition, the bathymetry of the basin progressively increased (transgression) passing from shallow dominated by clastic input (i.e. erosion of syn-rift shoulders) to deeper with very low clastic input an eulittoral deposits (i.e. oolitic banks and stromatolites) in correspondence with the palaeo-highs. In sequence 2 the basin become wider and there was increased accommodation space. In sequences 1 and 2 the microbial forms had their maximum development (Deschamps et al., 2020).

Just prior to SB3, sedimentary facies register a rapid flooding event with increased clastic sedimentation and shout down of carbonate production in the whole basin (Figures 30C and 31). SB3 marks then an event of complete desiccation of the lake and drastic change of the lake dynamic. After SB3 the bathymetry increased and had its climax a possible lake stratification in sequence 3. In the upper part of sequence 3 the depositional environment changed toward the highly alternating lacustrine dynamic and carbonate dominated facies reappeared. Sequence boundary 4 records another desiccation event. After SB4 the highly alternating depositional pattern persisted (Figures 30D and 31), the bathymetry progressively decreased and the basin was filled in correspondence with SB5.

Overall, the Yacoraite Fm. records a general transgressive trend up to the MFS3 surface followed by a prograding filling up trend up to SB5, corresponding to the full desiccation of the basin.

5.4 Field campaign and sample acquisition

A sampling campaign was held in June-July 2018 in the Salta province (Argentine) aiming at sampling carbonates from two stratigraphic sections of the Métan-Alemania basin, located in areas dominated by carbonate and siliciclastic sedimentation (Fig. 32). The Juramento section is located in the Cabra Corral lake area (25°18’08.01’ S, 65°17’42.91’’W) at around 1000m.s.l.m of altitude nearby the Rio Juramento dam. The outcrop is reachable with the RP47 from Coronel Moldes village (Fig. 32). It was chosen because it is located near the Guachipas palaeo-high where carbonate

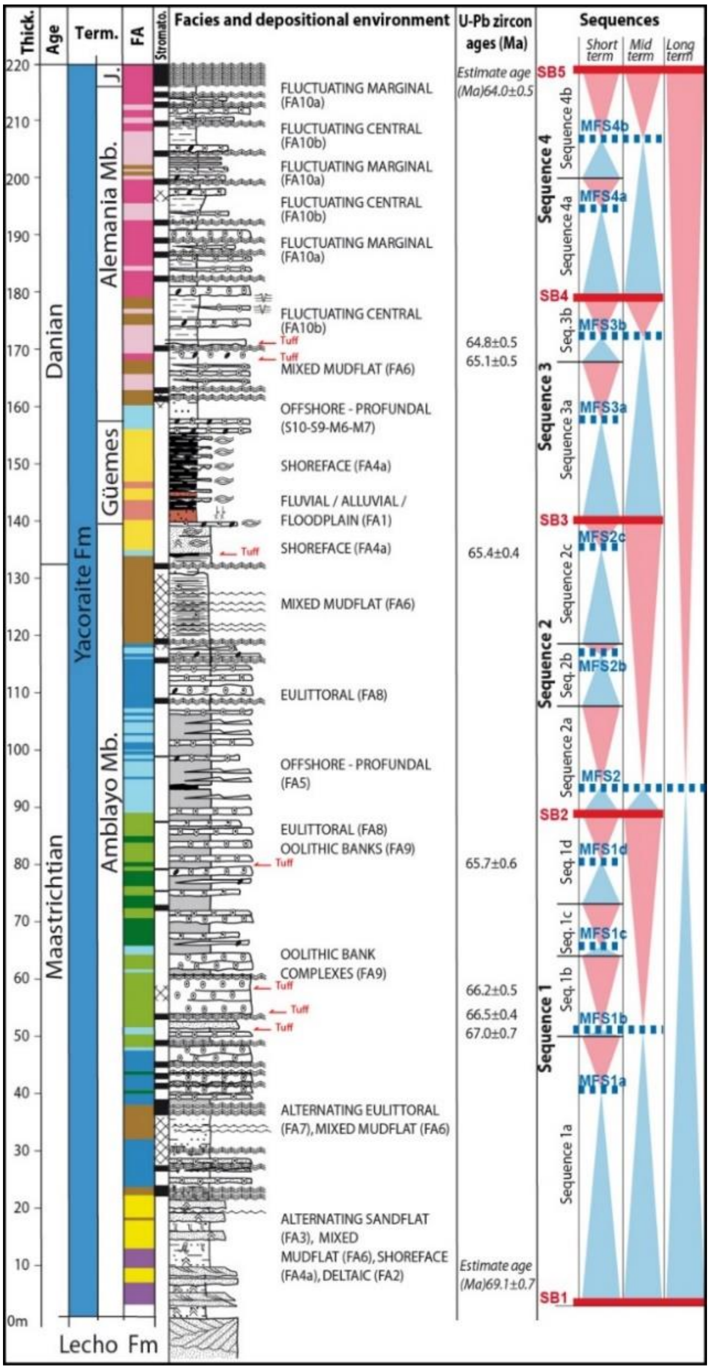

Figure 31. Reference sedimentological section of the Yacoraite Fm. (Cabra Corral lake area) and correlation between lithostratigraphic members and sequence stratigraphy. After Deschamps et al. (2020). SB=sequence boundary; MFS=maximum flooding surface. Sequences 1,2,3,4 are second order (or mid-term) stratigraphic sequences.

sedimentation was predominant. The Juramento section is one of the thickest sections of the Yacoraite Fm. (238 m), better representing the diversity of carbonates facies and the lake evolution through time. Indeed, it is a reference section for the study of the Yacoraite Fm. (e.g. Sial et al., 2001; Marquillas et al., 2005). The Cachipampa section is located in the western part of the Métan Alemania basin, in the Parque Nacional Los Cardones (25°16'03.0"S 65°55'24.2"W) at around 3200 m.s.l.m.

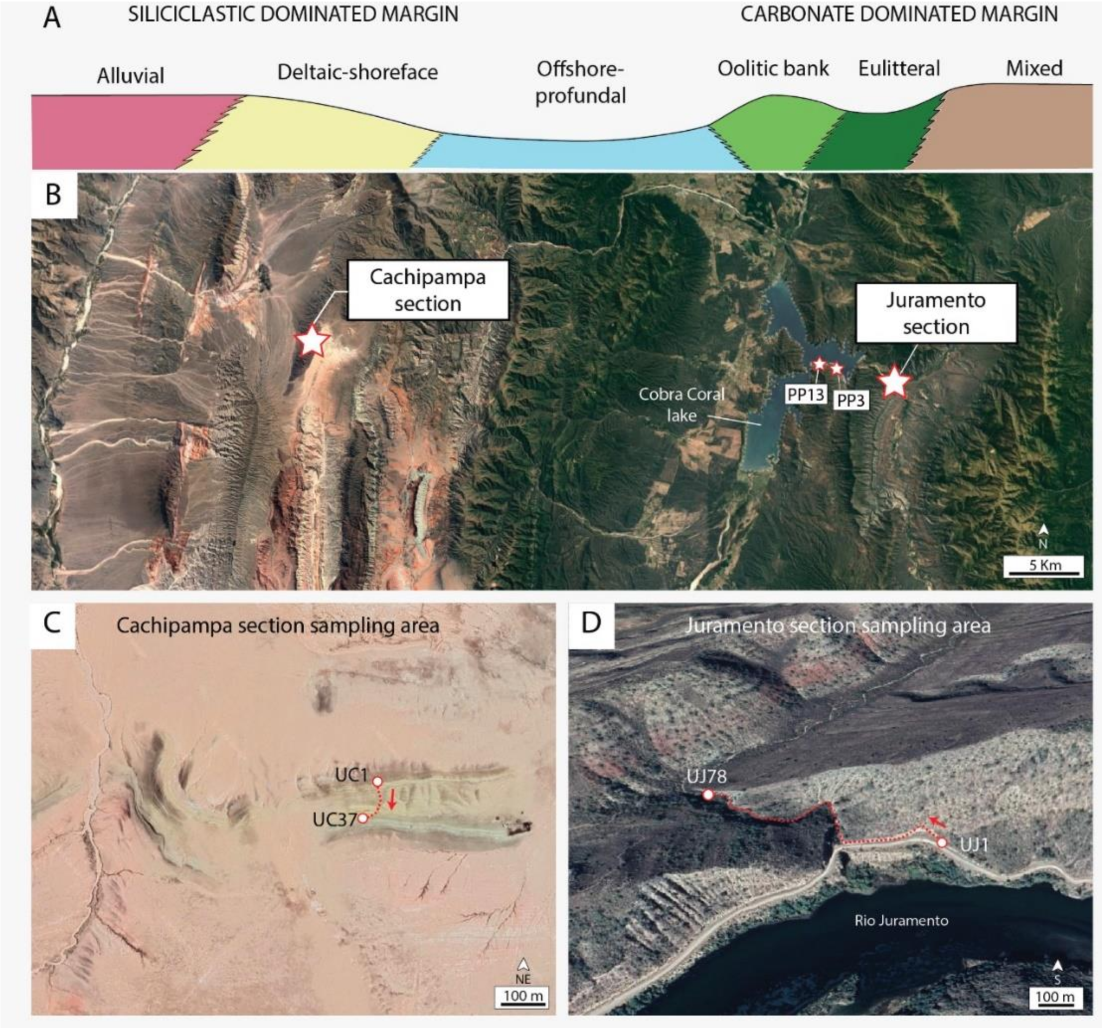

Figure 32 Sampling campaign of the Yacoraite Fm. in the Salta province (Argentina). A) Synthetic profile of the Yacoraite Fm. depositional system from the Métan –Alemania basin. Modified after Deschamps et al. (2020). B) Aerial view of the sampling area with the location of Cachipampa, Juramento, PP13 and PP3 stratigraphic sections. C) Aerial view of the Cachipampa section area nearby a breeder hut (black building to the right). UC1 and UC37 are the first and last samples acquired. D) Aerial view of the Juramento section area nearby the Juramento river dam. UJ1 and UJ78 are the first and last samples collected. The red dotted lines and arrows indicate the sampling orientations.

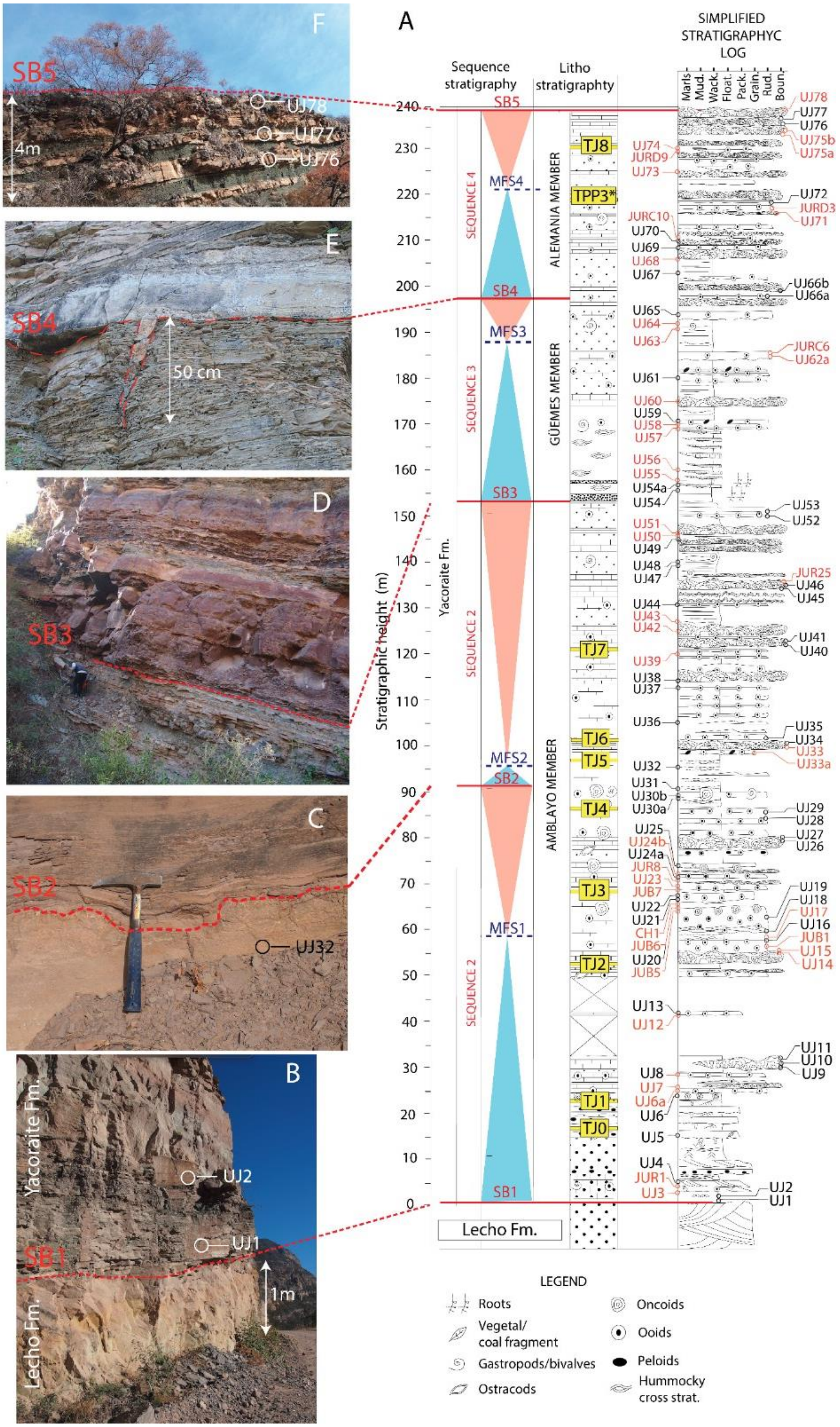
F
SB5
UJ78
UJ77
UJ76
4m
E
SB4
50 cm
D
SB3
C
SB2
UJ32
B
Yacoraite Fm.
UJ2
UJ1
SB1
1m
Lecho Fm.
A
Sequence stratigraphy
Litho stratigraphy
SIMPLIFIED STRATIGRAPHYC LOG
Marls
Mud.
Wack.
Float.
Pack.
Grain.
Rud.
Boun.
Stratigraphic height (m)
240
230
220
210
200
190
180
170
160
150
140
130
120
110
100
90
80
70
60
50
40
30
20
10
0
Yacoraite Fm.
SEQUENCE 4
SEQUENCE 3
SEQUENCE 2
SEQUENCE 2
SB5
MFS4
SB4
MFS3
SB3
MFS2
SB2
MFS1
SB1
ALEMANIA MEMBER
GÜEMES MEMBER
AMBLAYO MEMBER
TJ8
TPP3*
TJ7
TJ6
TJ5
TJ4
TJ3
TJ2
TJ1
TJ0
Lecho Fm.
UJ74
JURD9
UJ73
JURC10
UJ70
UJ69
UJ68
UJ67
UJ65
UJ64
UJ63
UJ61
UJ60
UJ59
UJ58
UJ57
UJ56
UJ55
UJ54a
UJ54
UJ51
UJ50
UJ49
UJ48
UJ47
UJ44
UJ43
UJ42
UJ39
UJ38
UJ37
UJ36
UJ32
UJ31
UJ30b
UJ30a
UJ25
UJ24b
UJ24a
JUR8
UJ23
JUB7
UJ22
UJ21
CH1
JUB6
UJ20
JUB5
UJ13
UJ12
UJ8
UJ7
UJ6a
UJ6
UJ5
UJ4
JUR1
UJ3
UJ78
UJ77
UJ76
UJ75b
UJ75a
UJ72
JURD3
UJ71
UJ66b
UJ66a
JURC6
UJ62a
UJ53
UJ52
JUR25
UJ46
UJ45
UJ41
UJ40
UJ35
UJ34
UJ33
UJ33a
UJ29
UJ28
UJ27
UJ26
UJ19
UJ18
UJ17
UJ16
JUB1
UJ15
UJ14
UJ11
UJ10
UJ9
UJ2
UJ1
LEGEND
Roots
Vegetal/ coal fragment
Gastropods/bivalves
Ostracods
Oncoids
Ooids
Peloids
Hummocky cross strat.

It is reachable by the Route 33 starting from Cachi village (Fig. 32). The Cachipampa section has been selected because it is located in a margin of the lake dominated by siliciclastic sedimentation. Being far from the main depocentre, it has a lower thickness (160m). The Cachipampa and Juramento sections are about 60 Km apart (Fig. 32) and were correlated in the framework of the JIP COMPAS project (Deschamps et al., 2020). Sedimentary logs inherited from the JIP COMPAS were updated and detailed at a higher resolution (Fig. 33).

A total number of 10 volcanic tuff deposits were sampled, 8 along the Juramento section and 2 in the proximal PP13 and PP3 sections stratigraphic sections (Fig. 32). This has been done because in sequences 3 and 4 of the Juramento section ash layers did not frequently occur and were poorly voluminous. A total number of 135 carbonate samples were collected approximately each 2-4m along Juramento (98 samples) and Cachipampa (38 samples) sections (Fig. 33). Field observations allowed to sample far from mineralized fractures and emersion surfaces to avoid carbonates potentially overprinted by later fluids. Since-the last 18 metres of the Cachipampa section (sequence 4) could not be sampled, 16 additional carbonate samples were included, belonging to the JIP COMPAS project. Results obtained from the Juramento and Cachipampa sections are in Supplementary data 1 and 2.

Figure 33 Juramento stratigraphic section with position of samples collected and field photographs of the sequence boundaries (SB). A) Lithostratigraphy is after Deschamps et al. (2020). Sequence stratigraphy is after Rohais et al. (2019) and Deschamps et al. (2020). In yellow the stratigraphic position of the volcanic ash deposits. TPP3 ash layer stratigraphic height was reported after the stratigraphic correlations provided by Rohais et al. (2019) and Deschamps et al. (2020). Simplified stratigraphic log is modified after Rohais et al. (2014). Carbonate samples are reported in both sides. Those in red were analysed via LAcarb. MFS=maximum flooding surfaces. B) Erosive and transgressive boundary between Lecho and Yacoraite Fm. (SB1). SB1 marks an abrupt change from massive aeolian (i.e. Lecho Fm.) to layered lacustrine (Yacoraite Fm.) deposits. C) SB2 is located in correspondence with the sharp change from shallow (protected eulittoral/shoal facies association) to deep (offshore facies association) lacustrine deposits. The microbial boundstone below SB2 is affected by intense recrystallization processes fairly due to exposure along the margin of the basin. The hammer for scale is 35cm long. D) SB3 marks the passage from shallow lacustrine deposits (mixed mudflat/clastic shore facies association) toward massive bodies of siliciclastic/fluvial deposits with distinctive reddish colour. E) Meter scale desiccation crack in correspondence with SB4 marking a full desiccation event of the lake. F) Top of the Yacoraite Fm. Below SB5 deposits show the high alternating depositional pattern typical of sequence 4.

6 LAcarb CHRONOSTRATIGRAPHY OF THE YACORAITE FM.

LAcarb demonstrated to be a powerful tool to constraint the sedimentation history in hardly datable continental settings, as underlined by the results achieved on the Ries Crater case study (Montano et al., 2021; Chapter 4.1) and by previous authors on other continental carbonates (e.g. Frisch et al. 2019; Parrish et al., 2019; Hoareau et al., 2021;). However, at our knowledge LAcarb has never been used to constrain a depositional age depth model of a sedimentary system along a vertical section. The Yacoraite Fm. represents an ideal case study for the purpose. The formation was deposited in a longer time (around 5 Ma; Rohais et al., 2019) if compared to the Ries Crater basin and the depositional history is well represented by masterpiece outcrops from the basin depocentres where sedimentation hiatuses are very minor and sedimentation is mostly continuous. A linear maximum depositional age depth model (MDA depth model) was obtained along the Juramento stratigraphic section by zircon geochronology to test the accuracy of the LAcarb ages.

The first LAcarb analytical session (set of 12 carbonate samples, 19 carbonate phases dated) provided accurate ages that were employed to build a minimum depositional age depth model (MIDA depth model). The results achieved (MDA and MIDA depth models) from the partial dataset of the Yacoraite Fm. already deserved valorisation and thus are included in a scientific article which is currently in revision on Sedimentology journal (Chapter 6.1).

Depositional age depth models provide essential temporal frameworks in stratigraphic and palaeoenvironmental and paleoclimate studies. In this respect, the new revised age of the Yacoraite Fm. (MDA depth model) demonstrated to have implications on the chronostratigraphy of the Balbuena and Santa Barbara subgroups that encompass the KPg extinction event and the Paleocene-Eocene hyperthermals. The location of these events were better defined based on the depositional age model obtained. Among the Paleocene-Eocene hyperthermals, the Paleocene Eocene Thermal Maximum (PETM) is considered as the closest geologic analogue for the present day anthropogenic carbon release and associated climate changes (Haynes & Honisch, 2020) since no other post-Cretaceous global warmth episodes are known to have occurred at such an accelerated rate (Zeebe et al., 2016). Discussion on these topics are in Chapter 6.3 and a scientific article is in preparation: ‘A lacustrine record for the KPg and the Paleocene-Eocene hyperthermals: the Balbuena and Santa Barbara groups, North West Argentina).

6.1 Maximum and minimum depositional age models in lacustrine systems from zircon and carbonate U-Pb geochronology

6.1.1 Abstract

The Yacoraite Fm. (Salta rift, Argentina) consists of Maastrichtian-Danian lacustrine carbonate and siliciclastic deposits interbedded with volcanic ash layers and organized in four third-order stratigraphic sequences. It offers the exceptional opportunity to jointly apply *in situ* zircon and carbonate U-Pb (LA-ICPMS) geochronology. This results in a maximum depositional age depth model (MDA, from zircon grains) together with an unprecedented minimum depositional age depth model (MIDA, from carbonates). Ages of the youngest zircon population of 10 ash layers were linearly interpolated to derive an MDA depth model. The MIDA depth model is instead based on 19 dated carbonate phases including microbialites, ooids, oncoids and early lacustrine cements of calcitic and dolomitic mineralogy. Mean ages were defined from different carbonate phases belonging to the same sample and then linearly interpolated. Sedimentation rates were calculated from both MDA and MIDA depth models between pairs of dated samples and used to estimate the age of key stratigraphic surfaces such as sequence boundaries, as well as the duration of the four stratigraphic sequences.

The MDA and MIDA depth models agree with biostratigraphic constraints and are remarkably consistent as such that the onset and end of sedimentation were estimated at 68.2 ± 0.9 Ma and 62.3 ± 0.6 Ma (duration ~5.7 Ma) via zircon geochronology and at 67.9 ± 1.7 Ma and 61.9 ± 1.3 Ma (duration ~6 Ma) via carbonate geochronology.

Results from this study demonstrate that *in situ* carbonate U-Pb dating of depositional and early diagenetic carbonate phases represents a valuable chronostratigraphic tool for estimating sedimentation rate and duration in poorly time-framed depositional systems.

Keywords: U-Pb geochronology, lacustrine deposits, depositional age model, sedimentation rate, Maastrichtian-Danian, Yacoraite Formation.

6.1.2 Introduction

Lacustrine carbonate and siliciclastic deposits represent high resolution sedimentary archives of the past that are commonly addressed to understand the response of present-day natural systems to catastrophic events (e.g. climate crisis, meteorite impacts, volcanic paroxysms; Ma et al., 2015; Tao et al., 2017; Zhang et al., 2017; Pancost, 2017; Hodgson et al., 2018). Moreover, lacustrine deposits are increasingly investigated by the oil and gas industry due to the worldwide discovery of major hydrocarbon accumulations (e.g. Bohacs et al., 2000; Katz, 2001; Thompson et al., 2015; Saller et al. 2016; Ceraldi & Green 2016). The reconstruction of the depositional history as well as the estimation of sedimentation rates in these settings is usually hampered by the scarcity of index taxa and by the problematic recovery of short duration palynomorph biozones (e.g. Wainman et al., 2018). Sedimentation rates in particular, represent key modulators of proxies used to reconstruct the depositional system paleoenvironmental conditions (Crombez et al. 2020) and are fundamental parameters for backstripping analysis and subsidence curve restoration (Berra & Carminati, 2009). Their estimation is even more challenging in lacustrine basins where they may vary by several orders of magnitude (e.g. Enos et al., 1991; Einsele, 2000).

U-Pb zircon geochronology has proven to be a useful tool to assess for the maximum depositional age (MDA) and the temporal evolution of sedimentation rates of continental sedimentary successions deposited coevally with volcanic events. Hence, the age of the youngest concordant zircon population is considered as the MDA of the host deposit (e.g., Lehrmann et al., 2006; Wotzlaw et al., 2014; Schoene et al., 2015; Rossignol et al., 2019). Biostratigraphic markers and/or absolute radiometric constraints are often absent in most continental settings. Therefore, a complex multiproxy analysis based on sedimentology, stratigraphy, magnetostratigraphy and diagenesis is usually necessary to reconstruct the depositional history and address for the sedimentation rate evolution over time (Cartier et al., 2018; Frisch et al., 2019; Schumer & Jerolmack, 2009; Crombez et al., 2020).

Radiometric age determination of carbonates was a long-standing problem in geochronology. Since the pioneering work of Smith & Farquhar (1989), it has been recognized that U-Pb carbonate geochronology has the potential to directly provide the timing of carbonate precipitation, although this was initially limited by the low success rate, moderate precision, and time-consuming dating procedures (Rabsury & Cole, 2009). The advent of the LA-ICPMS (laser ablation-inductive coupled plasma mass spectrometry) U-Pb geochronology of carbonates (LAcarb) largely increased the success rate of carbonate dating that is currently applied mainly to burial calcite cements to date fluid flow events (e.g. Mangenot et al., 2018; Walter et al. 2018; Cruset et al., 2020; Mottram et al., 2020; Roberts et al., 2020a, 2020b, 2021; Bilau et al., 2021). Recent advances on sample selection and screening techniques (e.g. Drost et al., 2018; Rasbury et al., 2021; Roberts et al., 2020a) have greatly improved the ability to target depositional and early diagenetic carbonates and to produce ages with adequate precision for chronostratigraphic and paleoenvironmental studies (e.g. Montano et al., 2021, Chapter 4.1). It is noteworthy that, in contrast to zircon geochronology, depositional and early diagenetic carbonates always provide a minimum time constraint for deposition, since they are highly susceptible to successive diagenetic reactions that may affect the U-Pb systematic and consequently degrade or reset the original ages (e.g. Jones et al., 1995, Roberts et al. 2020a). For these reasons, the wording minimum depositional age (MIDA) is here used when employing carbonate U-Pb ages for chronostratigraphic studies. In spite of this, with the correct strategy of sample selection and analytical procedure, LAcarb dating may provide MIDA consistent, within uncertainties, with biostratigraphic and radiometric constraints. This has been proven for meteoric cements in speleothems (Hopley et al., 2019; Woodhead & Petrus, 2019; Nicholson et al., 2020) and hardgrounds (Liivamägi et al., 2018; Scardia et al., 2019; Kurumada et al., 2020; Brigaud et al. 2021), lacustrine tufa, micrites and associated cements (Drost et al., 2018; Frisch et al. 2019; Hoareau et al., 2021; Parrish et al., 2019; Rasbury et al., 2021; Montano et al., 2021 in Chapter 4.1), marine cements (Meinhold et al., 2020; Hoareau et al., 2021) and bioclasts (Drost et al., 2018). Despite these remarkable results, at our knowledge no study attempted defining, solely based on LAcarb, a robust depositional age depth model along a stratigraphic section also dated by zircon geochronology. The Yacoraite Formation (Fm.) (Maastrichtian-Danian, NW Argentina) represents an ideal target for such aims. It consists of lacustrine carbonate and siliciclastic deposits interbedded with volcanic ash layers and organized in four third-order stratigraphic sequences (0.5 - 5 Ma; Van Wagoner et al., 1988; 1990). The structural asset, stratigraphic architecture and diagenetic history of this formation are well known from literature (Cesaretti et al., 2000; Sial et al., 2001; Durieux & Brown, 2007; Marquillas et al., 2007; Rohais et al., 2019; Deschamps et al., 2020; Gomes et al., 2020). In this study, volcanic ash layers were sampled together with depositional and early diagenetic carbonates along a stratigraphic section and investigated for petrography and U-Pb analysis. Ages obtained from ash layer zircon and carbonates were linearly interpolated to build a MDA and a MIDA depth models. The sedimentation rates, computed from these models, were used to constrain the ages of key stratigraphic surfaces, as well as the duration of third order stratigraphic sequences.

The present study provides a new approach to reconstruct the depositional age model and demonstrates that LAcarb based MIDA models may have the potential to assist chronostratigraphy and paleoclimate studies in poorly time-framed continental systems.

6.1.3 Geological setting and geochronological background

The Salta rift basin in NW Argentina (Fig. 34) belongs to the Andean Cretaceous-Paleogene basin system of central-western South America. Structural highs separate the southern branch of the Salta rift basin into three main sub-basins: El Rey, Alemania and Metán sub-basins (Salfity & Marquillas, 1994). The main tectonic stages of rift evolution are recorded by the Pirgua (syn-rift deposits; Reyes & Salfity, 1973), the Balbuena (transitional sag deposits) and the Santa Barbara (post-rift deposits) groups (Moreno, 1970). The Balbuena group includes, from base to top, the Lecho, the Yacoraite and the Tunal/Olmedo formations (Fms.). The Lecho formation primarily consists of eolian to fluvio-lacustrine sandstones whereas the Tunal/Olmedo Fms. is made of playa lake deposits including evaporites along with some fine-grained clastics (Salfity, 1979).

The Yacoraite Fm. was deposited in lacustrine to shallow marine environments coevally with the main stage of rift thermal subsidence and tectonic quiescence (Salfity & Marquillas, 1994; Starck, 2011). It dominantly consists of shales, mudstones, oolitic pack- to grainstones and microbial boundstones, interbedded with fine- to coarse-grained sandstones (e.g. Salfity, 1979; Marquillas, 1985; Salfity & Marquillas, 1994; Hernandez et al., 1999; Deschamps et al., 2020; Gomes et al., 2020). Volcanic ashes occur interbedded with the sedimentary succession (Marquillas et al., 2011; Rohais et al., 2019). They are known to be coeval with the Palmar Largo volcanism (70-60 Ma; Fernandez, 1975; Mädel, 1984; Gómez-Omil et al., 1987; Omarini et al., 1988; Disalvo et al., 2002), although they were also attributed to the Late Cretaceous volcanic arc of northern Chile (Marquillas et al., 2011) and have provided one of the oldest, recycled zircon grain of south America (3.7 Ga; Paquette et al., 2015).

The stratigraphic architecture of the Yacoraite Fm. was studied since the 80's (e.g. Marquillas, 1985; Salfity & Marquillas, 1994; Hernandez et al., 1999). The present contribution refers to recent studies establishing a robust basin-scale stratigraphic framework (Rohais et al., 2019; Deschamps et al., 2020). Accordingly, the Yacoraite Fm. is subdivided into four third-order sequences (mid-term sequences of ~1 Ma duration; Deschamps et al., 2020), organized in a second order sequence (long-term sequence of ~5 Ma; Deschamps et al., 2020). The four third-order sequences are bounded by five sequence boundaries (SB), corresponding to remarkable key surfaces, usually associated with a major back-stepping of the depositional system and erosion in proximal domains. According to biostratigraphic constraints, the age of the Yacoraite Fm. is Maastrichtian-Danian. Indeed, the Lecho and Yacoraite Fms. host well preserved Senonian dinosaur bones and tracks (Rascovsky, 1968; Reyes, 1972; Alonso & Marquillas, 1986; Marquillas et al. 2003, Cónsole-Gonnella et al, 2017) and palynological associations of Maastrichtian age (Moroni, 1982; Quattrocchio et al. 2005, 2006), whereas the Tunal/Olmedo Fms. is characterised by Danian palynological associations (Volkheimer et al., 2006). Hernandez et al. (1999) proposed a 12 Ma (75 to 63 Ma) depositional time duration for the Yacoraite Fm. by correlating the sediment regressive/transgressive cycles with the global sea-level curve. Such approach is hampered by the limited connection of the Salta basin with the ocean and by the fact that the lake level dynamics and the global sea-level curve were demonstrated to be out of phase by different orders of magnitude (e.g. Gebhardt et al., 2017). Zircon U-Pb geochronology of the Yacoraite Fm. ash layers provided absolute ages spanning from 71.9 ± 0.4 Ma to 60.3 ± 2.1 Ma (Marquillas et al., 2011; Pimentel et al., 2012; Rohais et al., 2019), though inconsistencies among the different datasets exist.

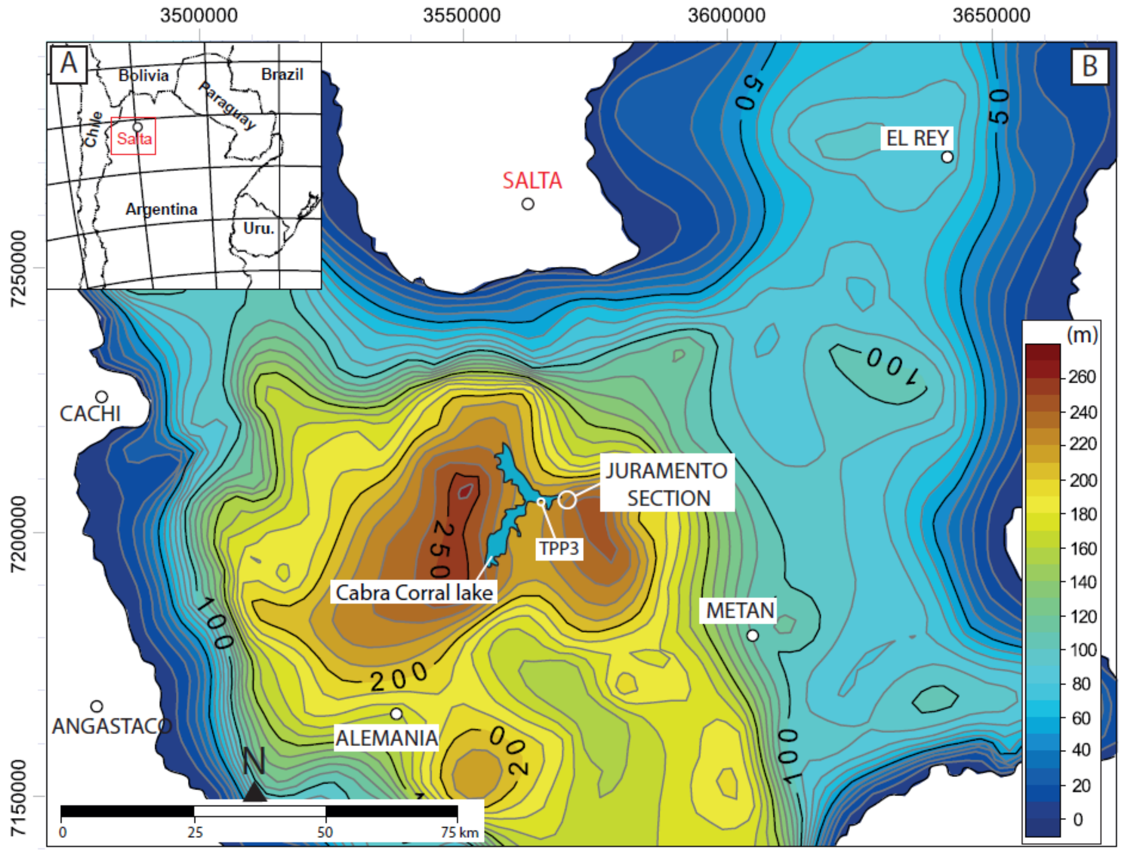

Figure 34. A) Location of the Salta rift basin in NW Argentina. B) Present day thickness map of the Yacoraite Fm. in the Metán and Alemania sub-basins with the position of Juramento stratigraphic section and TPP3 ash sample. Modified from Rohais et al. (2019).

6.1.4 MATERIALS AND METHODS

Investigated samples. Carbonates and volcanic ashes were sampled from the Yacoraite Fm. along a stratigraphic section (named Juramento; 25°18’08.01’ S, 65°17’42.91’’W) from the Cabra Corral lake area of the Metán sub-basin (Fig. 34). This section, located close to one of the main depocenters, was chosen to minimize the occurrence of major hiatuses that characterize the proximal domains (Deschamps et al., 2020). The sedimentology and stratigraphy of the Juramento section, as well as the position of all carbonate and ash layer samples are detailed in figure 35.

Twelve carbonate samples (JUR1, JUB1, JUB5, JUB6, CH1, JUB7, JUR8, JUR25, JURC6, JURC10, JURD3, JURD9) were collected, together with five volcanic ash samples (TJ0, TJ3, TJ4, TJ7, TJ8) interbedded with the sedimentary succession. One additional ash sample (TPP3) was collected from sequence 4 of a stratigraphic section located ~4 km away (25°17’27’’S, 65°21’15’’W; Fig. 34). According to the stratigraphic correlations proposed by Rohais et al. (2019) and Deschamps et al. (2020), TPP3 sample was projected at ~219 m from the base of the Juramento section, where a thin ash layer was also observed.

Macro- and microscopic analysis of ash layers and carbonates. Field observations allowed to select ash layers according to thickness, presence of eventual re-sedimentation/reworking features and naked-eye component heterogeneity. The collected material (2 to 4 kg for each ash layer) was prepared for petrographic analysis and isotope dating in the Institute of Geosciences Johann-Wolfgang-Goethe University Frankfurt (Germany). Prior to componentry study under binocular, the material was fragmented with high voltage discharge using a SelFrag Lab system and then sieved for fraction < 280 µm using disposable Nylon sieves. Heavy grains were then separated through manual panning. Up to 182 zircon grains were randomly handpicked for each ash layer sample to get a representative selection of the overall zircon populations and to minimize sampling bias. The grains were embedded in epoxy resin and ground down to about half their thickness and then polished. Zircon petrography under binocular was followed by Scanning Electron Microscope (SEM) analysis. Cathodoluminescence (CL) and back scattered electron (BSE) images were acquired using a JEOL JSM-6490 SEM.

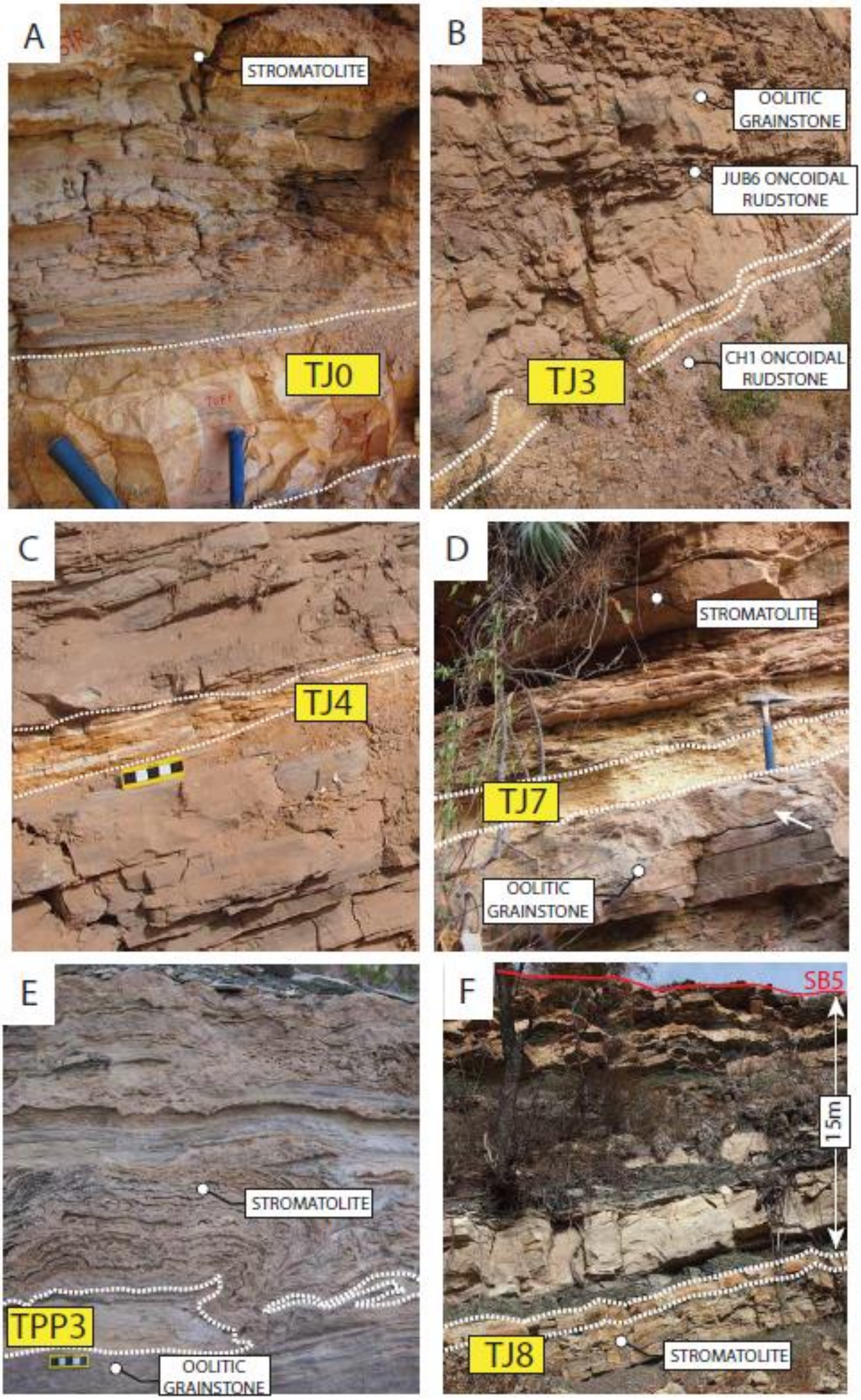
A
STROMATOLITE
TJ0
B
OOLITIC GRAINSTONE
JUB6 ONCOIDAL RUDSTONE
TJ3
CH1 ONCOIDAL RUDSTONE
C
TJ4
D
STROMATOLITE
TJ7
OOLITIC GRAINSTONE
E
STROMATOLITE
TPP3
OOLITIC GRAINSTONE
F
SB5
15m
TJ8
STROMATOLITE

Field observations allowed collecting carbonate samples far from mineralized fractures and emersion surfaces to avoid carbonates potentially overprinted by later fluids. Carbonate textures were described by using the Dunham (1962) classification, whereas facies and depositional environments were attributed following the scheme proposed by Deschamps et al. (2020). In this respect, the term stromatolite may include the microbial boundstone that will be here simply named microbialite.

Twelve polished and uncovered thin sections (50-60 µm thick), one for each carbonate sample collected, were prepared for petrography to characterize the different depositional facies and identify various depositional and diagenetic carbonate phases. Additionally, petrography aimed at selecting carbonate phases that showed no major evidence of post-depositional diagenetic modifications. Conventional optical petrography was performed using a Nikon ECLIPSE LV100 POL polarized light microscope and allowed observations under plane- and cross-polarized light (PPL and XPL). Cathodoluminescence (CL) microscopy was accomplished with a cold CL apparatus (8200 Mk5 CITL).

Figure 35. Field photographs and location of the sampled volcanic ash layers, occurring interbedded within the sedimentary deposits in the Yacoraite Fm. Ash layers are highlighted by dashed white lines. **A)** Light yellow to light pink 30 cm thick massive tabular volcanic ash layer overlaid by laminated siltstone to sandstone with current ripples. The dm-size rounded domes at the top represents the first stromatolite occurring along the Juramento section. TJ0 ash layer, Sequence 1, clastic shoreface facies association, 15 m from the base. Photo width corresponds to approximately 1.5 m. GPS coordinates: 25°18'06.12''S – 65°18'52.7''W. **B)** Light yellow, ~ 30 cm thick lenticular ash layer in a carbonate dominated outcrop. TJ3 ash layer, Sequence 1, ooid banks facies association, 68 m from the base. Photo width corresponds to approximately 3m. GPS coordinates: 25°18'05.7''S – 65°17'49.1''W. **C)** White to light yellow lenticular ash layer, 5 to 10 cm thick, showing internal lamination. TJ4 ash layer, sequence 1, eulittoral facies association, 87 m from the base. Photo width corresponds to approximately 70 cm. GPS coordinates: 25°18'05.7''S – 65°17'47.8''W. **D)** Tabular 20 cm thick ash layer overlying oolitic grainstone with fluid expulsion features (see white arrow). TJ7 ash layer, Sequence 2, high-energy eulittoral facies association, 121 m from the base. The hammer for scale is 35 cm long. GPS coordinates: 25°18'08''S – 65°17'47.8''W. **E)** Moustache-like thinly laminated stromatolite growing into a lenticular yellowish ash layer. TPP3 ash layer, Sequence 4, alternating marginal lacustrine facies association, 219 m from the base. The yellow scale is 5 cm. GPS coordinates: 25°17'01.5''S – 65°21'34.6''W. **F)** Tabular, dm-thick ash layer interbedded within greenish marl and massive carbonate deposits. TJ8 ash layer, Sequence 4, alternating marginal lacustrine facies association, 232 m from the base. GPS coordinates: 25°18'13.8''S – 65°17'36.3''W.

The electron beam worked under vacuum (< 0.1 mbar) with acceleration voltage of 10 kV, and current of 250 µA. All thin sections were partially stained with a solution of 10 % diluted HCl, Alizarin red-S and potassium ferricyanide (Dickson, 1966). Calcite cement habitus were described based on Flügel (2004) classification.

Zircon U-Pb geochronology. Zircon grains from the six ash layers sampled were analysed for U, Th and Pb isotope by LA-ICPSMS at FIERCE (Frankfurt Element and Isotope Research Center), Goethe University Frankfurt following the methods described by Gerdes and Zeh (2006, 2009). A Thermo Scientific Element XR sector field ICP-MS was coupled to a RESOlution 193 nm ArF Excimer laser (Compex Pro 102, Coherent) equipped with an S-155 two-volume ablation cell (Laurin Technic, Australia). The data were acquired in four analytical sessions in 2018-2019. The settings of the laser and the ICP-MS instrument are given in supplementary data S1. The GJ-1 zircon (Jackson et al., 2004) was used as primary zircon reference material (RM) and BB-16 (Santos et al., 2017), 91500 (Wiedenbeck et al. 1995), Plešovice (Slama et al., 2008) and Monastery (Kamenetsky et al., 2014) zircon RMs for validation of the analytical results. The results obtained on these RMs were within 0.8 % or better of the reported ages. Data processing (including common Pb correction) was performed using an Isoplot (Ludwig, 2012) supported Microsoft Excel-based spreadsheet (Gerdes and Zeh, 2006, 2009). Uncertainties are reported at the 2σ level (i.e. 95 % confidence) and are calculated by quadratic addition of: the internal uncertainties (SE), the counting statistics, the gas-background uncertainties, the common Pb corrections, the excess of scatter derived from the primary RM and the excess of variance calculated from the offset (or calibrator) RM. A second uncertainty is reported and expands the previous one with systematic uncertainties. These are the long-term variance (0.8 %, 2σ) and the decay constant uncertainties (see Horstwood et al., 2016). Concordia diagrams (2σ precision ellipses) and Concordia ages were calculated using Isoplot 4.15 (Ludwig, 2012) and associated $\mathrm{MSWD}_{\mathrm{C+E}}$ (i.e. mean squared weighted deviation of concordance and equivalence).

Carbonate U-Pb geochronology. Twelve thin sections were analysed in one U-Pb LA-ICPMS analytical session at FIERCE, Goethe University Frankfurt (Germany), using the same instrumentation as for zircon grains. Prior to analysis, thin sections were cleaned in an ultrasonic bath with ethanol. During the LA-session the ablation parameters were kept constants for all samples and reference materials. Samples were ablated in a helium atmosphere (300 ml/min) and mixed in the ablation funnel with argon (1 L/min) and nitrogen (6-8 ml/min). Analyses were performed with squared ablation spots with side of 213 µm, 8 Hz frequency and fluence of about 2 J/cm^2. A manual pre-screening session allowed identifying areas with high and variable U/Pb and $^{206}Pb/^{207}Pb$ ratios. The settings of the Laser and the ICP-MS instrument are given in supplementary data S1.

Raw data were corrected off-line using the same Isoplot (Ludwig, 2012) supported Microsoft Excel-based spreadsheet (Gerdes and Zeh, 2006; 2009) as for zircon analyses. Fractionation of $^{206}Pb/^{238}U$, $^{207}Pb/^{206}Pb$ ratios and their drift were corrected based on repeated analyses of soda-lime glass NIST-SRM 614. WC-1 calcite RM (Roberts et al., 2017) was used to correct for matrix offset (5 %) between NIST glass and carbonate. Results were plotted in U-Pb Tera-Wasserburg Concordia plots using Isoplot 4.15 (Ludwig, 2012) and ages were calculated as the intersection of the regression lines with the Concordia curve. Regression lines were constrained over 13 to 40 ablation spots (N) for each of the investigated carbonate phases. All uncertainties are reported with 95 % confidence and were calculated as described in the zircon dating methodology. Speleothem calcite ASH-15D (Nuriel et al. 2021) was measured as the validation RM. No common Pb corrections were applied and the long-term variance used is 1.5 % (2σ; Montano et al., 2021, Chapter 4.1).

6.1.5 RESULTS

Ash layer and zircon description. The sampled volcanic ash deposits (TJ0, TJ3, TJ4, TJ7, TJ8, TPP3) consist of consolidated cm- to dm- thick tabular to lenticular layers characterised by a white to yellowish colour easily recognizable in fresh outcrops (Fig. 36). Grain mineralogy is heterogeneous, so that ash layers consist of variable amounts of quartz, feldspar, plagioclase, biotite, hornblende, monazite, muscovite, garnet, apatite, zircon and other unidentified opaque minerals. Zircon grains are 50-150 µm long and mostly clear and colourless, only rarely yellowish or pinkish. They commonly exhibit euhedral long-prismatic to needle-like habitus. Some grains show signs of resorption and rounded edges. SEM images show the presence of well-preserved oscillatory zoning in most of the grains. Many of them display a central gas tube or a channel filled with glassy material, which together with the CL zonation indicates a volcanic origin (Pupin, 1976).

Carbonate facies and petrography. The analysed carbonate samples include five different sedimentary facies: fine-grained stromatolite (JUR25, JURC10 and JURD3 samples; Fig. 37A, B), sandy oolitic grainstone (JUR1 sample), grapestone-ooid grainstone to packstone (JURD9 sample; Fig. 37C), oolitic grainstone (JUB1, JUB7, JUR8 and JURC6 samples; Fig. 4D, E, F) and oncoidal rudstone (JUB5, JUB6 and CH1 samples; Fig. 37G, H and Supplementary data S2). Petrographic analysis allowed identifying different depositional carbonate phases characterized by calcitic, dolomitic or mixed (i.e. calcite + dolomite) mineralogy. The phases analysed are: calcitic ooids (OC), mixed ooids (OM), calcitic microbialites (MIC-C), dolomitic microbialites (MIC-D) and dolomitic oncoids (OND).

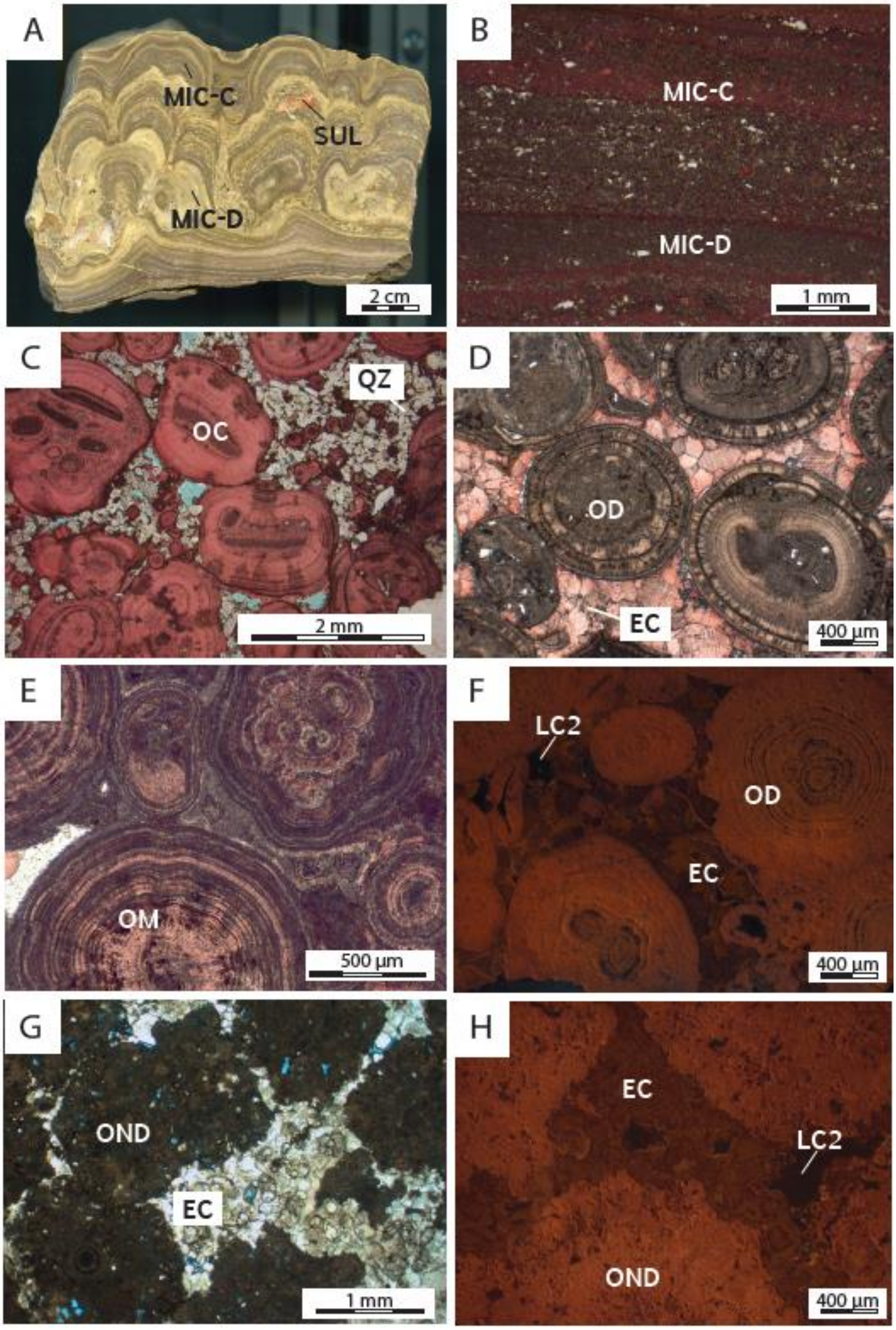

The fine-grained stromatolite samples are always characterized by the alternation of calcitic (MIC-C) and dolomitic (MIC-D) planar to convoluted microbial laminae that reach a few millimeters in thickness (Fig. 36A, B) and may build up cm- to dm-sized domal structures (Fig. 36A). The laminae have heterogeneous mineralogy, in particular the dolomitic ones, and may host calcite and dolomite microcrystals together with authigenic pyrite, and quartz grains (Fig. 36B). The sandy oolitic grainstone sample is poorly sorted and made of > 50 % rounded to subangular, mostly monocrystalline, quartz grains, 100 to 500 µm in size as well as dispersed ooids. The grapestone-ooid grainstone to packstone sample includes flat calcitic stromatolite clasts (MIC-C), calcitic ooids (OC) locally organized in lumps, and angular to subangular quartz grains, 100-200 µm in size (Fig. 36C). The oolitic grainstone samples (Fig. 36D, E, F) include calcitic ooids (OC), dolomitic ooids (OD) and mixed ooids (OM), the latter displaying an alternation of calcitic and dolomitic cortex laminae (Fig. 36E). The oncoidal rudstone samples are made of dolomitic spongiostromate oncoids (OND) with size up to 2 mm and a microporous center (Fig. 36G, H).

Most samples are cemented by an early diagenetic calcite, named EC (Fig. 36D) and made by blocky crystals, ~ 150 µm in size, with zoned dull orange luminescence. The EC precipitated in the interparticle pores between the loose grains before sediments underwent mechanical compaction. This is suggested by the limited grain-to-grain contacts observed in samples where this cement occurs

Figure 36. Mesoscopic and petrographic images of the carbonate samples investigated. **A)** Laminated to columnar fine-grained stromatolite displaying an alternation of calcitic (grey) and dolomitic (beige) sub-millimetric laminae. Authigenic minerals such as sulphates (SUL) also occur. JUR25, rock-slab scan. **B)** Fine-grained laminated stromatolite characterised by the alternation of pink stained (non-ferroan) calcitic laminae (MIC-C) and unstained (non-ferroan) dolomitic laminae (MIC-D). JURD3 sample, stained, PPL view. **C)** Grapestone-ooid grainstone to packstone composed by non-ferroan calcitic ooids (OC) and quartz grains (QZ). JURD9 sample, stained, PPL view. **D)** Oolitic grainstone made of non-ferroan dolomitic ooids (OD), cemented by a non-ferroan blocky calcite (EC). JUR8 sample, stained, PPL view. **E)** Oolitic grainstone given by mixed ooids (OM) displaying an alternation of calcitic and dolomitic cortex laminae (OM). JUB1 sample, stained, PPL view. **F)** Oolitic grainstone made of dolomitic ooids (OD) cemented by early blocky calcite (EC) with a zoned dull orange luminescence, followed by non-luminescent calcite (LC2). JUB7 sample, stained, CL view. **G)** Oncoidal rudstone composed by porous dolomitic spongiostromate oncoids (OND) cemented by early blocky calcite (EC). JUB5 sample, PPL view. **H)** Oncoidal rudstone with dolomitic spongiostromate oncoids (OND) cemented by early blocky calcite (EC) with dull orange zoned luminescence, followed by non-luminescent calcite (LC2). JUB5 sample, CL view.

(Fig. 36D, F). EC is post-dated by other blocky calcite cements, named LC1 and LC2, which also fill interparticle pores and are respectively bright orange and non-luminescent (Fig. 36F, H and Supplementary data 1).

Zircon U-Pb geochronology. Zircon grains of magmatic origin were selected for analysis based on grain shape and internal oscillatory zoning. The aim of this selection was to determine the youngest zircon crystallization event in order to date the deposition of the ash layer. It must be taken into account that the selected grains may also include zircon antecrysts crystallizing during an earlier pulse in the magma chamber, as well as xenocrysts that the magma assimilated from the wall rocks or during transport.

The 294 zircon grains analysed yielded $^{206}Pb/^{238}U$ dates ranging between 3.5 Ma to 1.1 Ga, with dominant density distribution peaks around 60-70 Ma and around 500 Ma (S1). About half of the zircon grains (141) produced $^{206}Pb/^{238}U$ dates < 100 Ma. Among them, 119 fall in a tight cluster at 63-68 Ma on the Concordia curve (i.e. concordant zircon dates) and 14 do not overlap with their error ellipses on the Concordia curve (i.e. discordant zircon dates). The remaining 8 analyses have apparently concordant $^{206}Pb/^{238}U$ dates and form together with 5 of the discordant analyses, a cluster between 60 to 35 Ma. These grains were found only in samples TJ4 and TPP3 (S1). It is worth noting that no grains yielded concordant ages between 71 and 90 Ma. The Th/U ratios of the 63-68 Ma cluster range from 0.36 to 2.5, being consistent with a magmatic origin (Williams and Claesson, 1987).

Zircon grains from the 63-68 Ma cluster were detected in all samples except for TJ8. They form statistically meaningful and equivalent populations of concordant ages associated with $MSWD_{C+E} \leq 2$ (Table 4 and Fig. 37). In TJ0 ash layer the young population is poorly represented, with 9 over 71 zircon grains yielding a Concordia age of 67.55 ± 0.60/0.89 Ma ($MSWD_{C+E}$ of 1.3). The remaining 62 analysed grains were all xenocrysts clustering on Concordia around 430-570 Ma and 1.0-1.1 Ga. In TJ3 ash layer, 29 out of 55 analysed grains form an equivalent age group, with a Concordia age of 67.87 ± 0.33/0.64 Ma ($MSWD_{C+E}$ of 1.5). In addition, four grains with Concordia age of 70.69 ± 0.72/0.91 Ma ($MSWD_{C+E}$ of 0.88) constitute another independent population, probably associated to an earlier magma pulse. In TJ4 ash layer, 27 zircon grains were analysed and among them, 20 grains define a homogeneous group with a Concordia age of 66.27 ± 0.27/0.59 Ma ($MSWD_{C+E} = 1.4$). The remaining discordant to apparently concordant analyses produced $^{206}Pb/^{238}U$ dates ranging from 63 to 45 Ma. In TJ7 sample, 11 equivalent dates were detected over 55 zircon grains analysed. They yielded a Concordia age of 65.35 ± 0.56/0.77 Ma ($MSWD_{C+E}=2.0$). The remaining 55 grains are xenocrysts, as demonstrated by their ^{206}Pb/^{238}U dates ranging from 150 Ma to 1.1 Ga. All zircon grains selected in TPP3 ash layer sample yielded ^{206}Pb/^{238}U of < 65 Ma. Forty-five grains defined an equivalent group, with a Concordia age of 63.33 ± 0.26/0.56 Ma (MSWD$_{C+E}$ =1.3). The remaining 9 grains gave apparently concordant ages that range from 55 to 43 Ma. Sample TJ8 was characterized

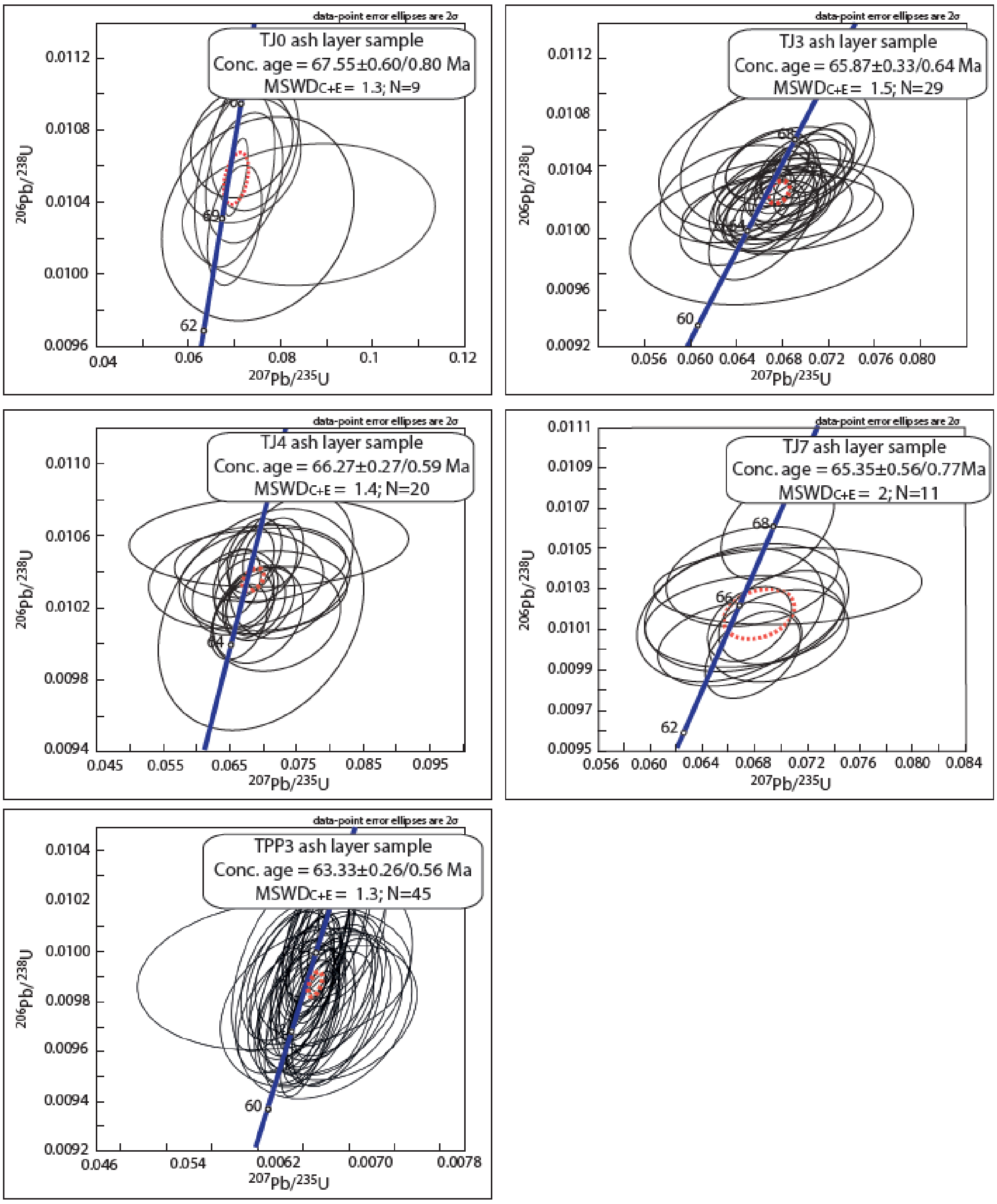

Figure 37. ^{206}Pb/^{238}U *versus* ^{207}Pb/^{235}U Wetherill Concordia diagrams showing U-Pb analytical data of the zircon grains analysed from five ash layer samples. Data point error ellipses indicate 2σ uncertainty (95% confidence). Blue line is the Concordia curve. Red dashed ellipses indicate the derived Concordia age and relative 2σ uncertainty. Concordia age results are reported with internal uncertainty (first number) and with long term excess of variance (second number). Rejected analyses are not shown (see Supplementary data 13).

by poor zircon content and by the occurrence of xenocrysts only. Eight out of 21 grains provided ^{206}Pb/^{238}U values plotting on the Concordia between 420 and 720 Ma. Raw data is in Supplementary data 13.

Carbonate U-Pb geochronology. From the 12 samples studied, a total of 22 carbonate phases were analysed: calcitic, dolomitic and mixed ooids (N=6), calcitic and dolomitic microbialites (N=7), dolomitic oncoids (N=3) and EC cement (N=6). U and Pb concentrations resulted to be very variable,

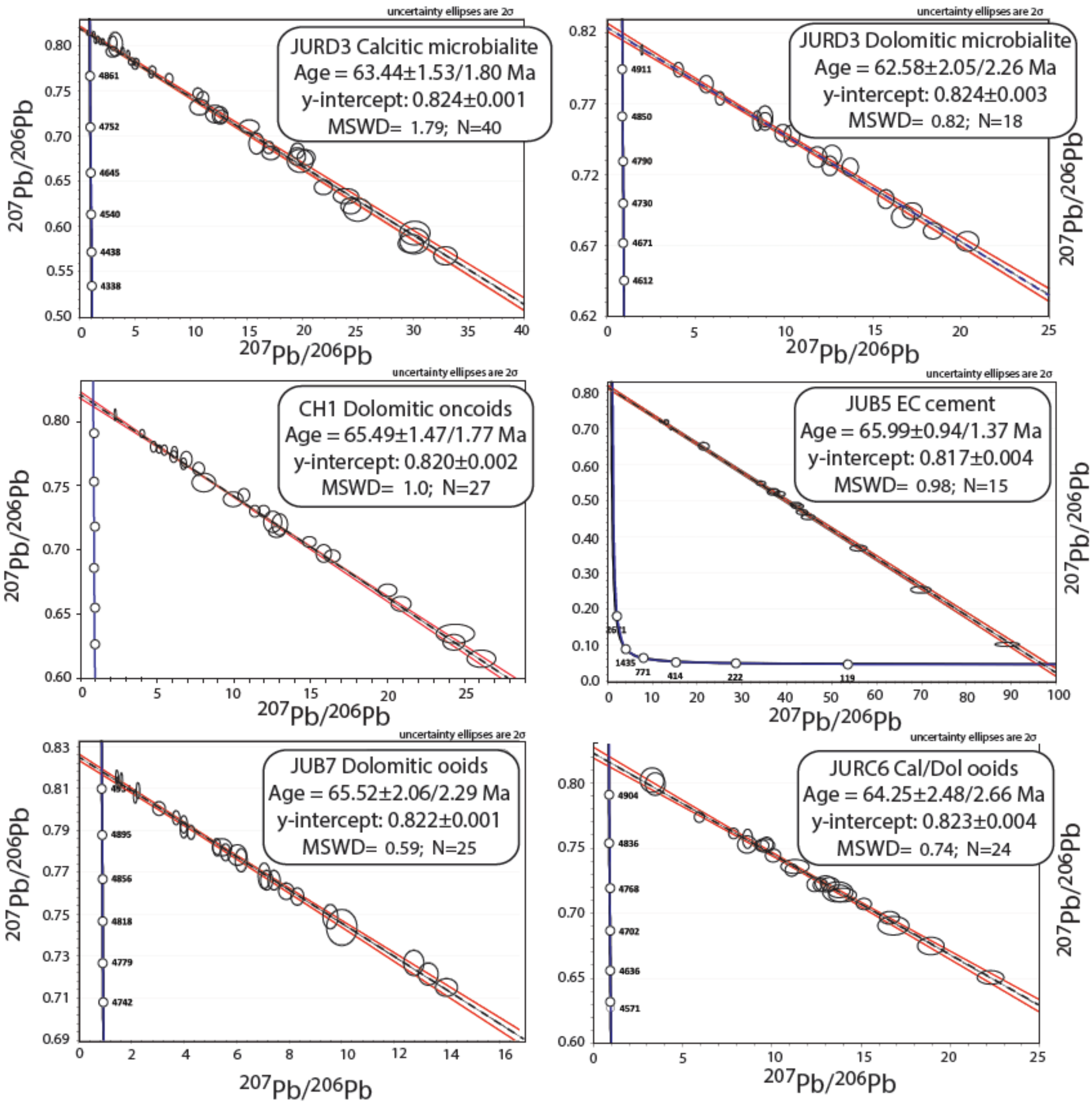

Figure 38. ^{238}U/^{206}Pb versus ^{207}Pb/^{206}Pb Tera-Wasserburg Concordia diagrams and corresponding absolute ages for the carbonate samples investigated. Data point error ellipses indicate 2σ internal uncertainty (95% confidence) of the isotope ratios on 'N' analyses. Red dashed lines represent the envelopes of the regression lines (isochrons). In blue are the Concordia curves.

ranging from 0.23 to 7.30 µg/g and from 0.02 to 12.55 µg/g, respectively. The $^{238}U/^{206}Pb$ and $^{207}Pb/^{206}Pb$ isotope ratios of all analysed carbonate phases vary from 0.25 to 89.06 and from 0.09 and 0.84, respectively. The highest $^{238}U/^{206}Pb$ and $^{207}Pb/^{206}Pb$ isotope ratio variability characterizes the EC cement, whereas all the other phases display $^{238}U/^{206}Pb$ isotope ratios mostly below 20. Only a calcitic microbialite phase (from JURC10 sample) has $^{238}U/^{206}Pb$ up to 69.

Tera-Wasserburg Concordia diagrams with lower intercept ages are displayed in figure 6, while the complete dataset is reported in Supplementary data S1, S2, S3, S4. Three carbonate phases (calcitic

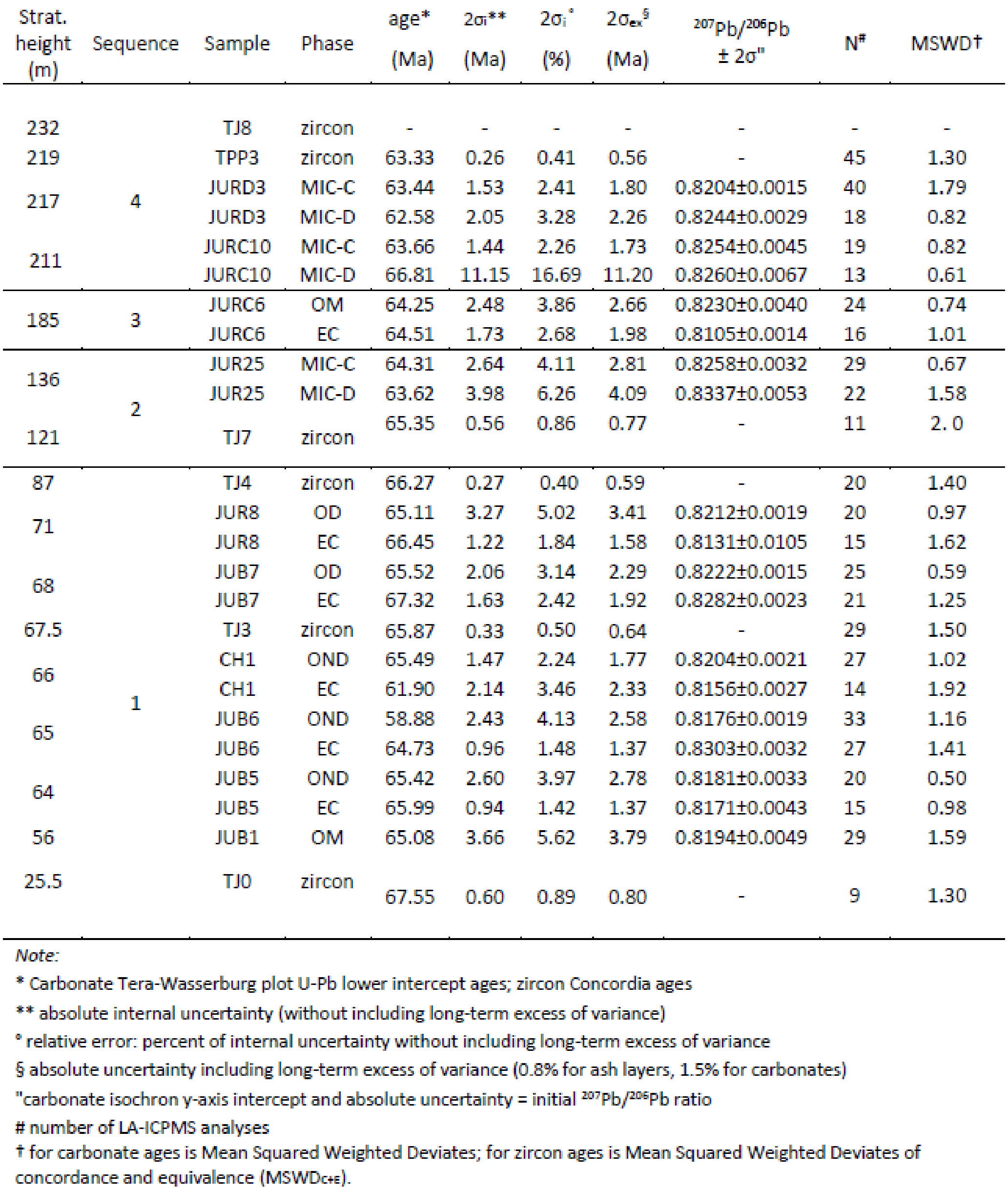

Strat. height (m)	Sequence	Sample	Phase	age* (Ma)	$2\sigma_i$** (Ma)	$2\sigma_i$° (%)	$2\sigma_{ex}$§ (Ma)	$^{207}Pb/^{206}Pb$ ± 2σ"	N#	MSWD†
232		TJ8	zircon	-	-	-	-	-	-	-
219		TPP3	zircon	63.33	0.26	0.41	0.56	-	45	1.30
217	4	JURD3	MIC-C	63.44	1.53	2.41	1.80	0.8204±0.0015	40	1.79
		JURD3	MIC-D	62.58	2.05	3.28	2.26	0.8244±0.0029	18	0.82
211		JURC10	MIC-C	63.66	1.44	2.26	1.73	0.8254±0.0045	19	0.82
		JURC10	MIC-D	66.81	11.15	16.69	11.20	0.8260±0.0067	13	0.61
185	3	JURC6	OM	64.25	2.48	3.86	2.66	0.8230±0.0040	24	0.74
		JURC6	EC	64.51	1.73	2.68	1.98	0.8105±0.0014	16	1.01
136	2	JUR25	MIC-C	64.31	2.64	4.11	2.81	0.8258±0.0032	29	0.67
		JUR25	MIC-D	63.62	3.98	6.26	4.09	0.8337±0.0053	22	1.58
121		TJ7	zircon	65.35	0.56	0.86	0.77	-	11	2. 0
87	1	TJ4	zircon	66.27	0.27	0.40	0.59	-	20	1.40
71		JUR8	OD	65.11	3.27	5.02	3.41	0.8212±0.0019	20	0.97
		JUR8	EC	66.45	1.22	1.84	1.58	0.8131±0.0105	15	1.62
68		JUB7	OD	65.52	2.06	3.14	2.29	0.8222±0.0015	25	0.59
		JUB7	EC	67.32	1.63	2.42	1.92	0.8282±0.0023	21	1.25
67.5		TJ3	zircon	65.87	0.33	0.50	0.64	-	29	1.50
66		CH1	OND	65.49	1.47	2.24	1.77	0.8204±0.0021	27	1.02
		CH1	EC	61.90	2.14	3.46	2.33	0.8156±0.0027	14	1.92
65		JUB6	OND	58.88	2.43	4.13	2.58	0.8176±0.0019	33	1.16
		JUB6	EC	64.73	0.96	1.48	1.37	0.8303±0.0032	27	1.41
64		JUB5	OND	65.42	2.60	3.97	2.78	0.8181±0.0033	20	0.50
		JUB5	EC	65.99	0.94	1.42	1.37	0.8171±0.0043	15	0.98
56		JUB1	OM	65.08	3.66	5.62	3.79	0.8194±0.0049	29	1.59
25.5		TJ0	zircon	67.55	0.60	0.89	0.80	-	9	1.30

Note:

* Carbonate Tera-Wasserburg plot U-Pb lower intercept ages; zircon Concordia ages

** absolute internal uncertainty (without including long-term excess of variance)

° relative error: percent of internal uncertainty without including long-term excess of variance

§ absolute uncertainty including long-term excess of variance (0.8% for ash layers, 1.5% for carbonates)

"carbonate isochron y-axis intercept and absolute uncertainty = initial $^{207}Pb/^{206}Pb$ ratio

number of LA-ICPMS analyses

† for carbonate ages is Mean Squared Weighted Deviates; for zircon ages is Mean Squared Weighted Deviates of concordance and equivalence ($MSWD_{c+E}$).

Table 4. U-Pb geochronology data obtained for the zircon and carbonate samples investigated. Carbonate phases are: calcitic microbialite (MIC-C), dolomitic microbialite (MIC-D), dolomitic ooids (OD), mixed ooids (OM), dolomitic oncoids (OND), early blocky calcite cement (EC

ooids from samples JURD9 and JURC10 and calcitic microbialite from sample JURD9) could not be dated since characterized by too homogeneous or scattered U-Pb isotope ratios. Nineteen carbonate phases (86% of the total) yielded well-defined regression lines with lower intercept ages between 67.32 ± 1.92 Ma and 58.88 ± 2.58 Ma and MSWD from 0.5 to 1.8. The precision obtained (expressed as 2σ) ranges from 1.4 to 6.3 % (Table 4), with just one age (dolomitic microbialite from JURC10 sample) displaying internal uncertainty of 16.7 %. Raw data of LAcarb ages is in supplementary data 13.

6.1.6 DISCUSSION

MDA depth model via zircon geochronology

Aiming at defining a robust maximum depositional age (MDA) depth model for the Yacoraite Fm., six volcanic ash layers (TJ0, TJ3, TJ4, TJ7, TPP3 and TJ8) cropping out in the Metán sub-basin (Fig. 1 and 2) were examined and mostly showed no reworking features (Fig. 35). Except for TJ8 ash layer, all the samples included a group of equivalent and concordant zircon ages between 63 and 68 Ma (Fig. 38). Unlike the high precision methods available (e.g. Wotzlaw et al., 2014), the LA-ICPMS technique employed resolved relative differences in zircon age population down to ± 0.6% (2σ; around ± 0.4 Ma for 66 Ma deposits). The precision achieved resulted suitable for the present study. The obtained ash layer MDA agree with the Maastrichtian-Danian biostratigraphic constraints (e.g. Moroni, 1982, 1984; Volkheimer et al., 2006; Valais & Cónsole-Gonella, 2019) and get clearly younger upsection, with the exception of TJ4 (66.3 ± 0.3/0.6 Ma), which appears to be slightly older than TJ3 (65.9 ± 0.3/0.6 Ma), although within uncertainties (Figures 38 and 39).

In order to build a most robust depositional age depth model of the Yacoraite Fm., MDA obtained in this study and by previous authors (Marquillas et al., 2011; Pimentel et al., 2012; Rohais et al., 2019) were taken into account (Table 5; Fig. 39). To do so, dated ash layers that do not crop out along the Juramento section were projected onto it according to Rohais et al. (2019) and Deschamps et al. (2020) stratigraphic correlations. It is worth mentioning that Marquillas et al. (2011), Pimentel et al. (2012) and Rohais et al. (2019) produced somewhat contradictory results (Fig. 39). Additionally, in contrast with the results of previous authors, the MDA here obtained take account of the expanded uncertainties which include the long-term external reproducibility of the method and only Rohais et al. (2019) followed the uncertainty propagation recommended by Horstwood et al. (2016).

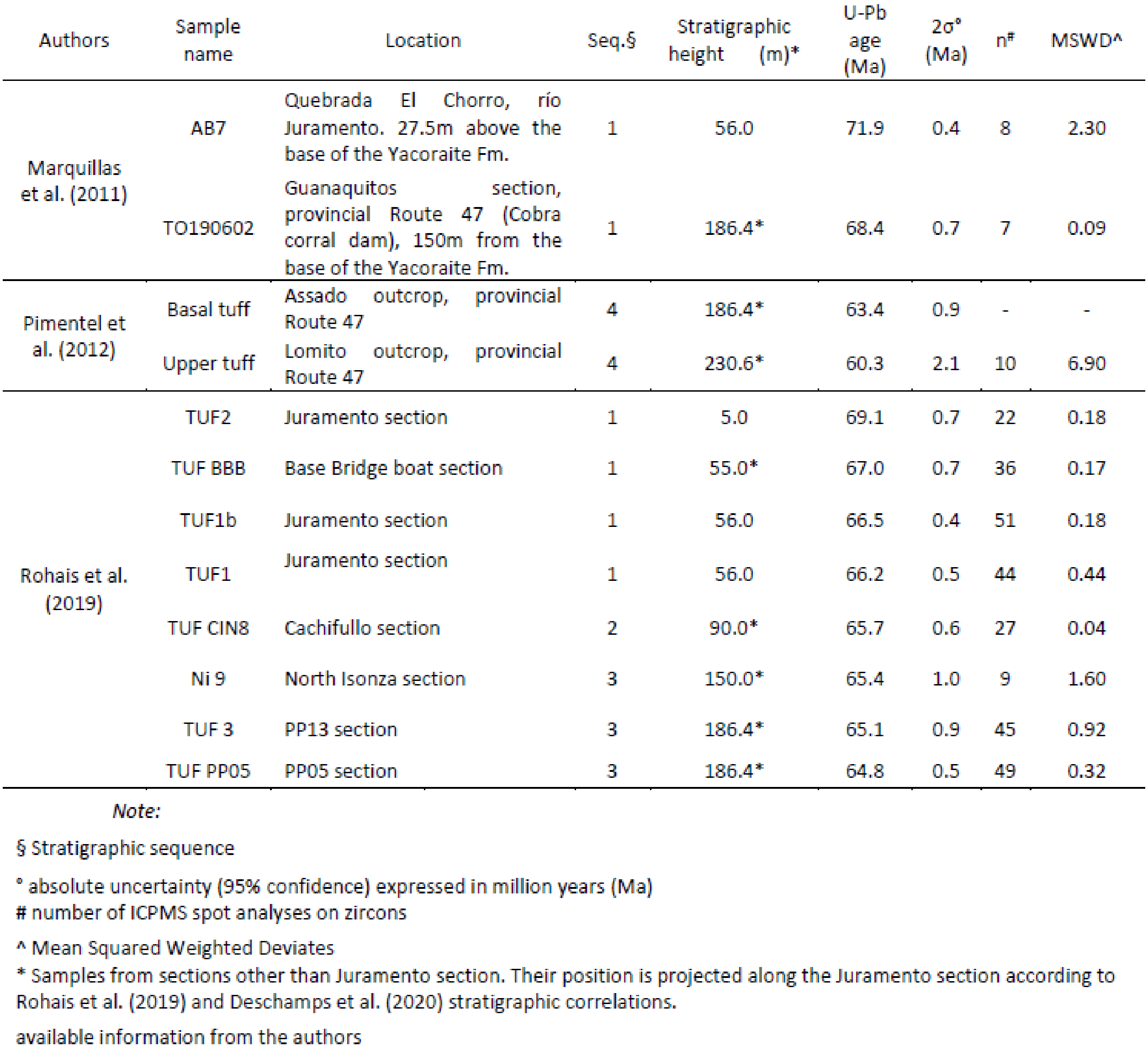

Authors	Sample name	Location	Seq.§	Stratigraphic height (m)*	U-Pb age (Ma)	2σ° (Ma)	n#	MSWD^
Marquillas et al. (2011)	AB7	Quebrada El Chorro, río Juramento. 27.5m above the base of the Yacoraite Fm.	1	56.0	71.9	0.4	8	2.30
	TO190602	Guanaquitos section, provincial Route 47 (Cobra corral dam), 150m from the base of the Yacoraite Fm.	1	186.4*	68.4	0.7	7	0.09
Pimentel et al. (2012)	Basal tuff	Assado outcrop, provincial Route 47	4	186.4*	63.4	0.9	-	-
	Upper tuff	Lomito outcrop, provincial Route 47	4	230.6*	60.3	2.1	10	6.90
Rohais et al. (2019)	TUF2	Juramento section	1	5.0	69.1	0.7	22	0.18
	TUF BBB	Base Bridge boat section	1	55.0*	67.0	0.7	36	0.17
	TUF1b	Juramento section	1	56.0	66.5	0.4	51	0.18
	TUF1	Juramento section	1	56.0	66.2	0.5	44	0.44
	TUF CIN8	Cachifullo section	2	90.0*	65.7	0.6	27	0.04
	Ni 9	North Isonza section	3	150.0*	65.4	1.0	9	1.60
	TUF 3	PP13 section	3	186.4*	65.1	0.9	45	0.92
	TUF PP05	PP05 section	3	186.4*	64.8	0.5	49	0.32

Note:

§ Stratigraphic sequence

° absolute uncertainty (95% confidence) expressed in million years (Ma)
number of ICPMS spot analyses on zircons

^ Mean Squared Weighted Deviates
* Samples from sections other than Juramento section. Their position is projected along the Juramento section according to Rohais et al. (2019) and Deschamps et al. (2020) stratigraphic correlations.

available information from the authors

Table 5. U-Pb geochronology data from zircon (ash layers) of the Yacoraite Fm. published by previous authors.

MDA obtained in the present study agree within uncertainties with the MDA reported by Rohais et al. (2019) but not with those from Marquillas et al. (2011) and Pimentel et al. (2012) (Fig. 39). Marquillas et al. (2011) dated zircon grains from two volcanic ash layers, one located at 56 m and the other projected at 186.4 m from the base of the section, obtaining ages of 71.9 ± 0.4 and 68.4 ± 0.7 Ma, respectively (Table 5; Fig. 39). These ages are about 3-4 Ma older than those obtained by Rohais et al. (2019) via replicate analyses on the same ash layers. Thus, Marquillas et al. (2011) ages possibly represent older volcanic pulses. Pimentel et al. (2012) dated two layers, Basal tuff (63.4 ± 0.9 Ma) and Top tuff (60.3 ± 2.1Ma), which are projected on the Juramento section at 185 and 230m, respectively (Fig. 39). Basal tuff has been dated in multiple analytical sessions by Rohais et al. (2019)

producing younger and consistent MDA of 65.1 ± 0.5 Ma (see TUF3 in Table 2) and 64.8 ± 0.5 (see TUFF PP05 in Table 5). Top tuff age (Pimentel et al., 2012), the youngest ever proposed for the top of the Yacoraite Fm., led authors believe that sedimentation ended at around 60 Ma (Bento-Freire, 2012; Sial et al., 2013; Gomes et al., 2020). However, the low accuracy (3.5%, 2σ; Table 2) and the high MSWD (6.9; Table 5), together with the unconsistency with biostratigraphic constraints (e.g. Moroni, 1982, 1984; Volkheimer et al., 2006; Valais & Cónsole-Gonella, 2019) may indicate poor reliablility. Rohais et al. (2019) provided the most comprehensive dataset, with robust MDA from eight ash layers cropping out in different sub-basins of the Salta rift (TUF1/1bis, TUFBBB, TUF3, PP05, CIN 8 and Ni 9; Table 5). Evidence for possible re-sedimentation (i.e. currents and reworking features) were reported only for TUF2 ash layer whose U-Pb age (61.9 ± 0.7 Ma) is possibly much older than deposition. In addition, Rohais et al. (2019) ages show good agreement with biostratigraphy (e.g. Moroni, 1982, 1984; Volkheimer et al., 2006; Valais & Cónsole-Gonella, 2019).

In light of what discussed above, ages from Marquillas et al. (2011), Pimentel et al. (2012) and TUF2 sample of Rohais et al. (2019) were not considered for the computation of the MDA depth model. Moreover, to limit the possible bias due to long distance stratigraphic correlations, only robust MDA from the ash layers cropping out in the Cabra Corral lake area were used (Table 5). These are TJ0, TJ4, TJ4, TJ7 and TPP3 from this study and TUF1/1bis, TUFBBB, TUF3 and PP05 from Rohais et al. (2019).

Various approaches may be employed to interpolate linear and non-linear age datasets along a stratigraphic section in order to build a depositional age depth model (e.g. Blaauw 2010; Blaauw et al., 2012; 2018; Lougheed & Obrochta, 2019). The choice relies on the presence and duration of hiatuses and on the ages distribution along the section. The Juramento stratigraphic section here investigated is located close to a basin depocenter (Fig. 34) where hiatuses > 0.1-0.4 Ma are not expected to occur (Deschamps et al., 2020) and hiatuses < 0.1-0.4 Ma are within the age resolution achieved (~ 0.6 Ma; 2σ). Moreover, the MDA considered to build the model show linear distribution and get younger going from the bottom to the top of the section (Fig. 39). For these reasons, the MDA depth model was inferred via MDA linear interpolation. The approach used does not only provide point age depth estimates as the classic linear interpolation (e.g. Watson et al., 2017), but also takes into account the MDA uncertainties.

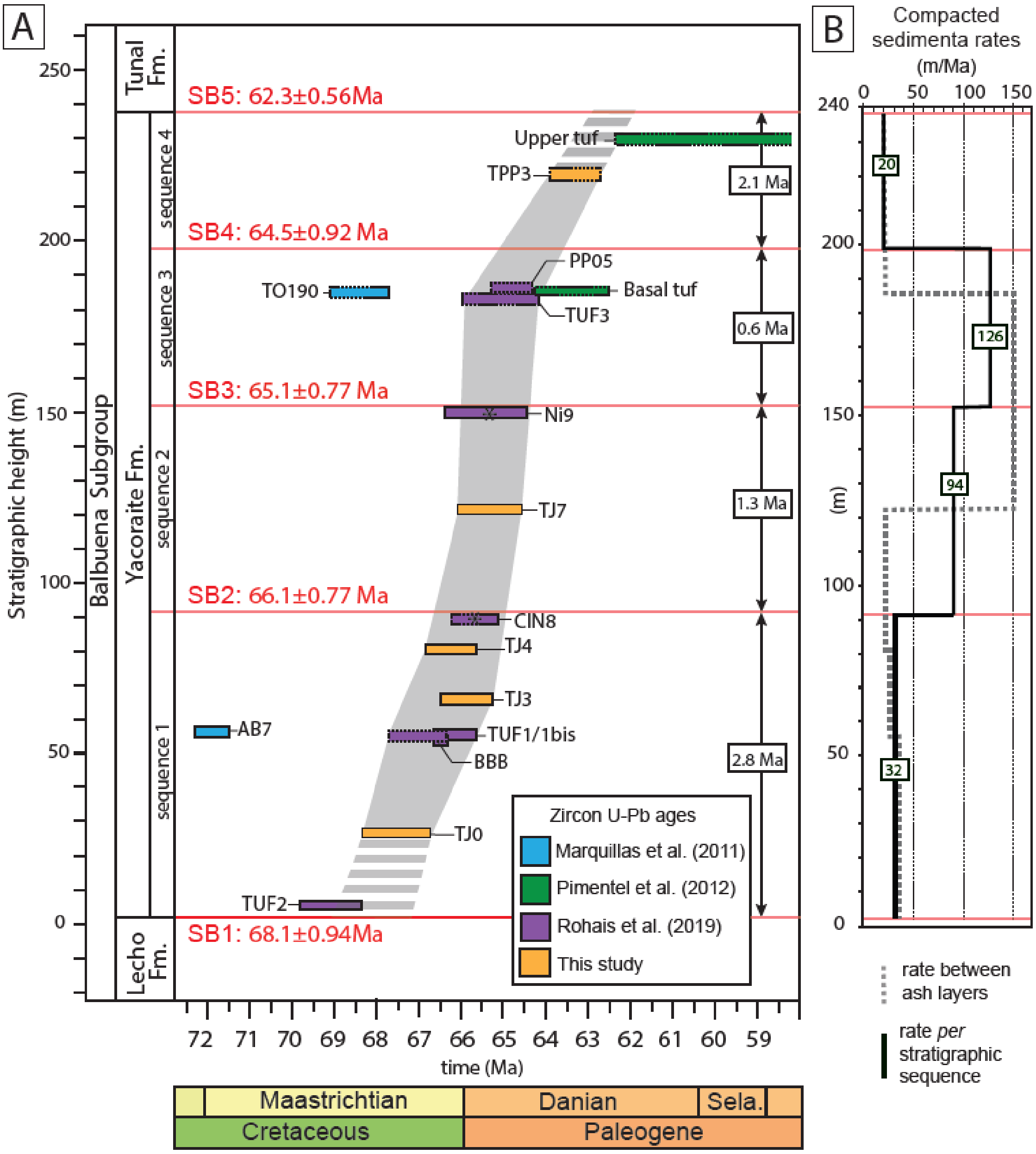

Figure 39. Maximum depositional age (MDA) depth model of the Yacoraite Fm. via zircon (ash layer) U-Pb geochronology. Red lines are the sequence boundaries (SB). **A)** Ages, uncertainties and stratigraphic positions are reported as coloured bars for all the available ash layers dated (Marquillas et al., 2011; Pimentel et al., 2012; Rohais et al., 2019; this study). All reported uncertainties are 2σ (95% confidence). Dashed bars refer to of ash layers from the Metán and Alemania sub-basins though not along the Juramento section. Asterisks indicate ash layers from other sub-basins. The dark grey area represents the MDA depth model obtained by linear interpolation of the zircon MDA. The duration of each stratigraphic sequence is given in the black frames. **B)** Evolution of the compacted sedimentation rates. The grey dashed line refers to rates calculated between dated surfaces, whereas the black line refers to weighted mean rates of each stratigraphic sequence.

In this respect, confidence intervals for the discrete undated parts of the stratigraphic section are assigned by considering the age uncertainties of the ash layers located in proximity (i.e. the uncertainties do not increase with distance from the dated layers).

The main limitation of the model produced is the absence of MDA in proximity with the bottom and top sequence boundaries of the Yacoraite Fm. (i.e. SB1 and SB5, respectively). The same issue was afforded by Rohais et al. (2019) that estimated the age of these surfaces by calculating the sedimentation rates from compacted sediments occurring between adjacent pairs of dated layers. With this approach, sedimentation rates are assumed to remain constant during the deposition of sequences 1 and 4. The same strategy was here employed and considered TJ0 (67.5 ± 0.6/0.8 Ma) and TPP3 (63.3 ± 0.3/0.6 Ma) samples as the lowermost and uppermost ash layers dated (Fig. 7). Based on a calculated sedimentation rate of 32 m/Ma for sequence 1, the sedimentation onset (SB1) was estimated at 68.2 ± 0.9 Ma (Fig. 39). Similarly, by considering a constant sedimentation rate of 20 m/Ma for sequence 4, the sedimentation end (SB5) was constrained at 62.3 ± 0.6 Ma.

MIDA depth model via carbonate geochronology

In the framework of chronostratigraphic and paleoenvironmental studies the limitations of LAcarb may be twofold. The first issue is the achievable age precision (e.g. Rasbury & Cole, 2009). Roberts et al. (2020a) argued that after propagating all necessary uncertainties most studies so far only reached a precision of 2.5-3% (2σ) or worse. For Upper Cretaceous carbonates this would correspond to an uncertainty of ≥ 2 Ma. However, Guillong et al. (2020) and Montano et al. (2021, Chapter 4.1) reported for a Pliocene speleothem RM (Ash-15) a long-term excess uncertainty of 2% and 1.45 % (2σ), respectively. In additionally, accurate depositional ages were provided from marine and lacustrine carbonates by Brigaud et al. (2021) and Montano et al. (2021, Chapter 4.1) yielding the resolution of the third order stratigraphic sequences. This suggests that Upper Cretaceous carbonates with sufficient U/Pb isotope ratio variations can be dated with precision better than 2% (2σ). The second issue is related to the age accuracy and to the intrinsic nature of carbonates that are sensitive to geochemical changes, potentially causing post-depositional age reset or degradation (e.g. Jones et al., 1995; Roberts et al., 2020a). Consequently, depositional and early diagenetic carbonates may provide younger ages, recording the timing of later diagenetic modifications (e.g. Li et al., 2014; Mangenot et al., 2018; Brigaud et al., 2021). For this reason and in accordance with the definition of MDA from zircon geochronology, carbonate U-Pb ages should be always considered as minimum depositional ages (MIDA). In order to maximize the chances to produce precise and accurate ages for chronostratigraphic purposes, it is essential to apply a suitable protocol to select depositional and early diagenetic phases. This requires carbonate petrographic and geochemical characterization (Rasbury et al., 2021; Montano et al., 2021, Chapter 4.1).

Previous studies suggest that depositional and early diagenetic carbonates of the Yacoraite Fm. from the Métan and Alemania sub-basins were only locally overprinted by burial diagenesis and mostly preserved pristine petrographic and geochemical features (Marquillas et al, 2007; Sial et al., 2001; Durieux & Brown, 2007; Rohais et al., 2019; Gomes et al., 2020). As such, their C and O isotope signatures have been used to reconstruct the evolution of lacustrine water composition (Sial et al., 2001; Marquillas et al., 2007; Rohais et al., 2019). The depositional and early diagenetic carbonates here investigated may therefore be considered as good candidates to supply reliable MIDA. This also applies to the dolomitic phases that have been interpreted as syn-depositional and driven by microbial activity (Gomes et al., 2020). To further minimize the risk of analysing carbonates disturbed by later diagenetic modifications, petrographic analyses were carried out to select favourable domains from depositional carbonates (i.e. microbialites, ooids, oncoids) with calcitic, dolomitic and mixed mineralogies and from the early blocky EC calcite cement (Fig. 37).

The nineteen carbonate phases successfully dated yielded ages from 67.30 ± 1.92 Ma to 58.88 ± 2.58 Ma (Table 4, Figure 38, Supplementary data S2, S3, S4) associated with representative number of measurements and good statistics ($13 < N < 40$; $2\sigma_i$ down to 1.4 %; MSWD < 2; Table 1). Different carbonate phases coexisting in the same sample provided consistent results (Fig. 40A), although most dolomitic phases turned out to be associated to higher uncertainties (usually > 3 %, 2σ) if compared to calcitic phases (Table 4).

Two carbonate phases provided younger ages and thus were not used to build the MIDA depth model. These are the dolomitic oncoids from JUB6 sample and the early blocky EC calcite cement from CH1 sample (Table 1, Fig. 40A). The age of the dolomitic oncoids may be due to a local recrystallization process that is known to commonly affect early dolomites (Kupecz & Land, 1994; Machel, 1997; Kaczmarek & Sibley, 2014). This has been extensively discussed by Elisha et al., (2020). Whereas, the age of the EC calcite cement may be due to the additional ablation of some late blocky calcite cements (see Supplementary data S2 for further details).

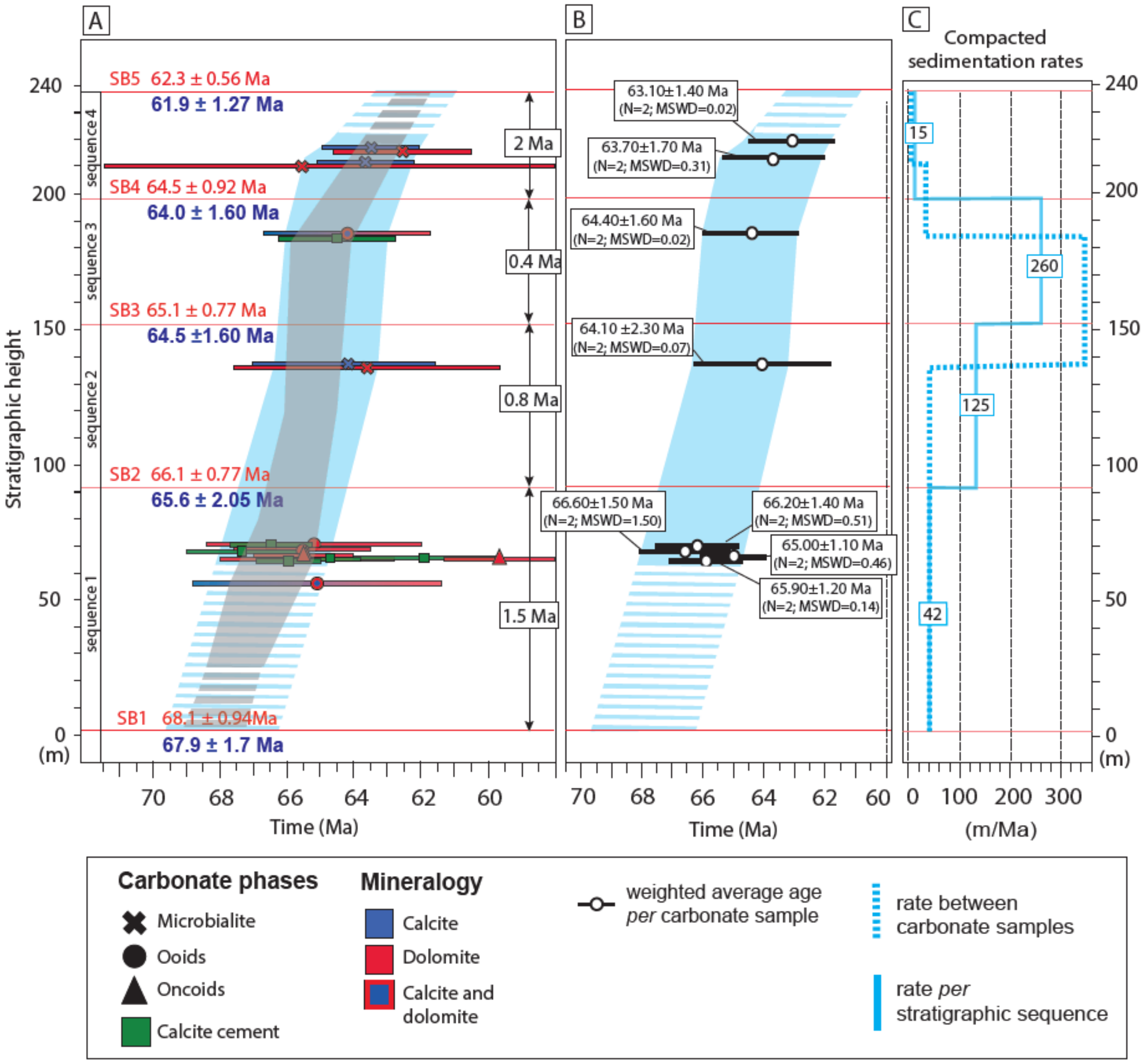

Figure 40. Minimum depositional age (MIDA) depth model of the Yacoraite Fm. via carbonate U-Pb geochronology (LAcarb). Red lines are the sequence boundaries (SB). **A)** Ages, uncertainties and stratigraphic positions are reported for all carbonate phases dated in this study. The blue area represents the MIDA depth model. For comparison, the MDA depth model (light grey area) is also reported. SB ages were inferred from the MDA (in red) and MIDA (in blue) depth models. All reported uncertainties are 2σ (95% confidence). The duration of each stratigraphic sequence is given in the black frames. **B)** Weighted average ages (MIDAw) of carbonate phases from the same sample are reported in the black frames together with the number of single MIDA considered (N) and the Mean Squared Weighted Deviates (MSWD) of the weighted average ages. The blue area represents the depth model obtained by MIDAw linear interpolation. **C)** Evolution of the compacted sedimentation rates along the stratigraphic section. The blue dashed line refers to rates calculated between dated carbonate samples (MIDAw), whereas the blue continuous line refers to weighted mean rates for each stratigraphic sequence.

The MIDA depth model was therefore derived from seventeen carbonates with statistically robust U-Pb ages recording an overall youngening upward trend. The construction of the MIDA depth model was afforded by computing weighted average ages ($MIDA_w$) from carbonate phases occurring in the same sample (Fig. 40B). Prerequisite to adopt this approach is that each $MIDA_w$ derives from a statistically concordant MIDA population (i.e. U/Pb lower intercept ages overlapping within their uncertainties; MSWD < 1.5). The $MIDA_w$ used (Fig. 40B) are between 66.6 ± 1.5 (sample JUB7; N = 2; MSWD = 1.4) and 63.1 ± 1.4 Ma (sample JURD3; N = 2; MSWD = 0.02).

The lack of hiatuses > 0.1-0.4 Ma along the stratigraphic section investigated (Deschamps et al., 2020) and the overall linear distribution of the MIDAw, allow to perform a linearly interpolation to derive a MIDA depth model. By applying the same procedure as for the zircon MDA, the strati graphically lowest and highest carbonate samples dated (i.e. JUB5, 65m above SB1 and JURD 3, 20m below SB5; Table 4) were used to estimate the onset and end of sedimentation. Sedimentation rates of 42 m/Ma and 15 m/Ma were calculated for sequences 1 and 4 via the MIDA depth model (Fig. 40C). Accordingly, the onset and end of sedimentation were respectively estimated at 67. 9 ± 1.74 Ma and 61.9 ± 1.27 Ma.

The novel approach presented allowed to define a depositional age depth model (i.e. the MIDA depth model) for the Yacoraite Fm. solely based on LAcarb ages that revealed to be consistent with biostratigraphic constraints (e.g. Moroni, 1982, 1984; Volkheimer et al., 2006; Valais and Cónsole-Gonella, 2019). The temporal resolution achieved is between 2 and 2.6 % (2σ) and agrees with the known precision of LAcarb dating technique.

MDA versus MIDA depth models

The Yacoraite Fm. gave the opportunity to build two depositional age depth models., one derived from zircon geochronology (MDA depth model; Fig. 39) and the other from LAcarb (MIDA depth model; Fig. 40). The two models were used to calculate the compacted sedimentation rates between adjacent pairs of dated layers, as well as the ages of the five sequence boundaries (SB1 to SB5) and the duration of the four third order stratigraphic sequences that compose the Yacoraite Fm. (Fig. 39B and 40C).

Zircon geochronology, a well-established chronostratigraphic tool for continental depositional systems, served the prime scope to evaluate the reliability of the newly proposed LAcarb based age depth model. The two models remarkably overlap and describe the same sedimentation rate dynamics (Fig. 39B, 40B). Between SB1 and SB2, they provided sedimentation rates respectively of 32 and 42 m/Ma, which agree with the long transgressive trend established for sequence 1 (Deschamps et al., 2020). In sequences 2 and 3, the sedimentation rates progressively increased, with mean values of 94 and 125 m/Ma in sequence 2 and 126-260 m/Ma in sequence 3. In correspondence with SB3 sedimentation rates reach their maximum peak, with values up to 150 and 330 m/Ma, respectively (Fig. 39B, 40B). This peak in line with a pulse of carbonate production and sediment supply known for this stratigraphic interval (Rohais et al., 2019). The higher sedimentation rates recorded in sequence 3 by the LAcarb model (Fig. 8C) may be due to a Sadler effect (Sadler, 1981) induced by the presence of only one sample analysed in between 70 and 180 m (i.e. JUR25 = 64.1 ± 2.3 Ma, N = 2; MSWD = 0.2). Starting from SB4 the sedimentation rates decreased respectively down to 20 and 15 m/Ma. This agrees with the depositional system of sequence 4 being characterized by multiple emersion events that culminated in a major exposure in correspondence with SB5 (Deschamps et al., 2020).

Sequence boundary ages estimated from the two models are consistent within uncertainties, although the ones inferred via LAcarb are in average 0.4 Ma younger (Fig. 8A). This reflects the notions of maximum and minimum age estimates provided by the two chronostratigraphic tools. LAcarb ages are also less precise than zircon ages so that zircon and LAcarb based age depth models provided precisions of ~ 0.9 to 1.4 % and ~ 2.0 to 2.6 %, respectively (Fig. 39 and 40).

Ages of SB1 and SB5 were inferred from both models (Fig. 39 and 40). Accordingly, the Yacoraite Fm. was deposited between 68.1 ± 0.9 Ma and 62.3 ± 0.6 Ma and between 67.9 ± 1.7 Ma to 61.9 ± 1.3 Ma. Thus, the total sedimentation duration inferred is of ~5.7 Ma and ~6.0 Ma, respectively. It is therefore possible to assess that sedimentation started at ~68 Ma and ended at ~62 Ma, respectively during the Maastrichtian and the Danian times. These results agree with the presence of Maastrichtian dinosaur footprints in sequence 2 of the Yacoraite Fm. (Cónsole-Gonella et al., 2017) and of Danian palynomorphs in the overlying Tunal Fm. (Volkheimer et al., 2006).

The duration of the four third order stratigraphic sequences which compose the Yacoraite Fm. was then calculated (Fig. 39 and 40). It spans from 0.7 Ma (sequence 3) to 2.8 Ma (sequence 1) based on zircon geochronology and from 0.4 Ma (sequence 3) to 2 Ma (sequence 4) based on LAcarb data. This supports the third order cyclicity (i.e. cycle duration of 0.5 to 5 Ma; Van Wagoner et al., 1988; 1990) recorded in the Yacoraite Fm. by previous authors (Marquillas, 1985; Salfity & Marquillas, 1994; Hernandez et al., 1999; Rohais, et al., 2019; Deschamps et al. 2020).

The remarkable match between the zircon and LAcarb based age depth models, together with their consistency with biostratigraphic constraints, suggest that LAcarb may be used as a reliable chronostratigraphic tool to compute depositional age depth models in sedimentary systems. The workflow followed, that included an accurate sample selection prior to LAcarb analyses, the use of expanded uncertainties which additionally include the long-term external reproducibility of the method and the implementation of an unprecedented carbonate age data averaging approach (Fig. 9B), is therefore highly encouraged.

In respect to the LAcarb age data interpolation, the absence of major depositional hiatuses and the availability of carbonate ages linearly distributed along the section (Fig. 40B) allowed to apply a classical linear interpolation approach (e.g. Blaauw, 2010; Blaaw et al., 2018). This is known to produce plausible age depth models which comparable to those obtained by more advanced interpolation methods (e.g. Bayesian statistic). However, future applications to more complex carbonate age datasets may require advanced interpolation approaches to produce robust depositional age depth models (e.g. Blaauw, 2010; Blaauw et al., 2018; Lougheed & Obrochta, 2019).

It is worth mentioning that the accuracy of the results achieved in the context of the Yacoraite Fm. may have been promoted by the minor diagenetic overprint of the carbonates analysed (Marquillas et al, 2007; Sial et al., 2001; Durieux & Brown, 2007; Rohais et al., 2019; Gomes et al., 2020) and/or by the specific geochemical composition of the Salta rift waters.

Carbonates precipitated from lacustrine and especially groundwaters are notably more prone to be dated with U-Pb geochronology (Rasbury & Cole, 2009) and often provide accurate and precise ages (Drost et al., 2018; Liivamägi et al., 2018; Frisch et al. 2019; Hopley et al., 2019; Parrish et al., 2019; Scardia et al., 2019; Kurumada et al., 2019; Brigaud et al. 2020; 2021; Nicholson et al., 2020; Nuriel et al., 2021; Rasbury et al., 2021; Hoareau et al., 2021; Montano et al., 2021, Chapter 4.1). This suggests that the lacustrine origin of the Yacoraite Fm. carbonates and the influence of groundwaters discharging into the lake could be major reasons for the remarkable match between the zircon and the LAcarb based age depth models compiled (Fig. 39 and 40). Other factors could have promoted the incorporation of favourable U-Pb contents in the Yacoraite Fm. carbonates: (1) the widespread microbial activity (Gomes et al., 2020; Deschamps et al., 2020); (2) the fluid reducing conditions recorded in correspondence with anoxia periods (Rohais et al. 2019); and (3) the high fluid alkalinity witnessed by, among others, the precipitation of syn-depositional smectite authigenic mineral (Gomes et al., 2020).

Due to the common lack of chronostratigraphic constraints, lacustrine and more broadly continental are among the most challenging materials to be dated. In these settings, the reconstruction of the sedimentation rate dynamics commonly requires a complex multiproxy analysis (Schumer & Jerolmack, 2009; Cartier et al., 2018; Frisch et al., 2019). Noteworthy, the high dating potential of lacustrine carbonates demonstrated by recent LAcarb application (Montano et al., 2021, Chapter 4.1

and this study), leads to a new scenario in which they are possibly among the best candidates for successful LAcarb based chronostratigraphy.

6.1.7 CONCLUSIONS

The Yacoraite Fm. (Maastrichtian-Danian, Salta rift basin), composed by volcanic ashes and lacustrine deposits organized in four third order stratigraphic sequences, represents the ideal target to validate the reliability of carbonate U-Pb geochronology for chronostratigraphic studies. Maximum and minimum depositional age depth models (respectively, MDA and MIDA) were constrained via zircon and carbonate U-Pb geochronology along the same stratigraphic section.

Zircon geochronology produced youngening upsection ages (between 68.2 ± 0.9 and 62.3 ± 0.6 Ma) that were linearly interpolated. The derived MDA depth model provided a precision of 0.9-1.4 %.

Lacustrine carbonates, including microbialites, ooids, oncoids and early cements, were dated. A novel approach to develop the MIDA depth model was implemented: weighted average ages (between 66.6 ± 1.5 and 63.1 ± 1.4 Ma) were derived from dated carbonate phases coexisting in each sample and were then linearly interpolated along the section. The model provided a precision of 2 to 2.6%.

The MDA and MIDA depth models remarkably overlap and suggest that sedimentation started at ~68 Ma and ended at ~62 Ma, in agreement with biostratigraphic constraints. The sedimentation rates calculated from the two models agree with sedimentological and stratigraphic evidence. In addition, the duration inferred for the stratigraphic sequences (0.4 – 2.1 Ma) is consistent with the known third order cyclicity of the Yacoraite Fm.

Results from this study demonstrate that carbonate U-Pb geochronology can be reliably used to provide depositional ages at the resolution of the third order stratigraphic sequence. This is particularly relevant to reconstruct chronostratigraphy, sedimentation rate dynamics and paleoenvironmental evolution of hardly datable sedimentary rocks from continental settings.

6.1.8 Acknowledgments

This research was undertaken during D. Montano PhD project, funded by IFP Energies nouvelles. This is FIERCE contribution No. XX. FIERCE is financially supported by the Wilhelm and Else Heraeus Foundation and by the Deutsche Forschungsgemeinschaft (DFG, INST 161/921-1 FUGG and INST 161/923-1 FUGG), which is gratefully acknowledged. We are grateful for the scientific exchange with Prof. J.L. Paquette.

6.1.9 Supplementary data

Supplementary data 1.

Excel file S1. Settings of the Laser and of the ICP-MS instrument and raw data for zircon and carbonate dating sessions. The raw data of this article is included in Supplementary data 13.

Supplementary data 2.

Two of the 22 carbonate phases analysed yield U-Pb ages younger than the rest of the dataset. They do not agree with the zircon U-Pb ages of volcanic ashes from stratigraphically close layers (compare figures 7 and 8). These phases consist of the dolomitic oncoids from JUB6 sample (58.88 ± 2.43 Ma) and the blocky calcite cement (EC) from the CH1 sample (61.9 ± 2.14 Ma).

The most likely explanation for the younger age of the oncoids from JUB6 sample resides in their dolomitic mineralogy (see also Elisha et al., 2020). Dolomites are known to be very susceptible to recrystallization process, especially when formed during early stages of diagenesis (Kupecz and Land, 1994; Machel, 1997). Despite the existence of empiric petrographic hints (e.g. crystal coarsening, increase in non-planar crystal boundaries, irregular contacts between crystal cores and rims revealed by UV-light or CL petrography; Montañez and Read, 1992; Kaczmarek and Sibley, 2014), early dolomite recrystallization was reliably disclosed only by isotope and elemental analyses and more recently by Δ_{47} thermometry (Al-Aasm, 2000; Winkelstern and Lohmann, 2016; Lukoczki et al, 2019; Veillard et al., 2019). In this study, there is a lack clear petrographic hints and geochemical/thermometric data to prove recrystallization. AS such, the choice of the dolomite samples to be analysed for U-Pb geochronology relied on the good preservation of the sample syn-depositional features. The spongiostromate oncoids from JUB6 sample, beside local dolomite crystal coarsening, display good preservation of the internal structure (Fig. S2.a). It is thus suspected that they only underwent local recrystallization during the early stages of burial, possibly promoted by the microporous cores (Fig. S2.a) favouring fluid-rock interaction. The most likely explanation for the younger age of the early blocky cement (EC) from CH1 sample resides in the occurrence of also two later blocky calcite cements (LC1 and LC2), as revealed by CL petrography (Fig. S2.b). The three cements occur spatially close to each other and were hardly distinguishable during ablation.

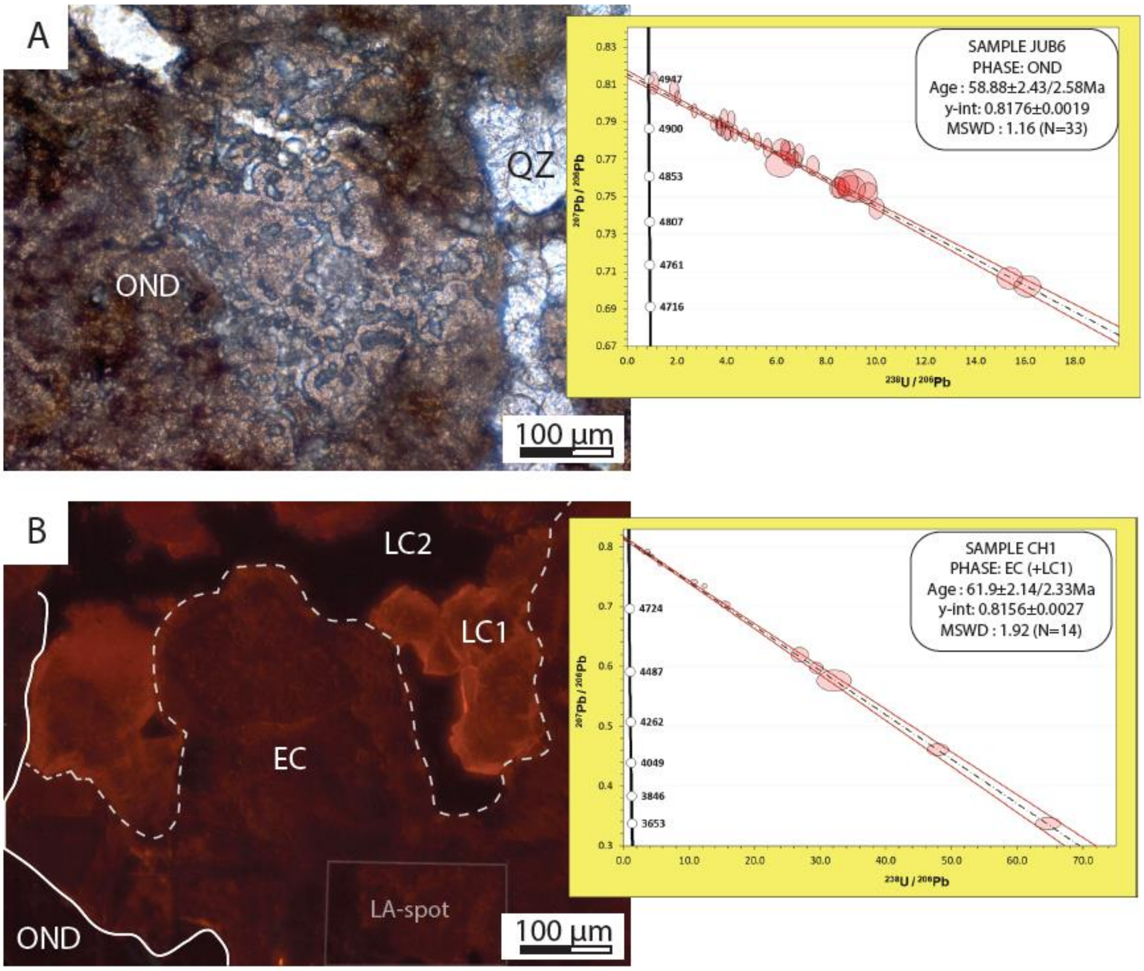

Figure Supplementary data 2. **A)** Petrographic details of the carbonate phases with younger ages and corresponding $^{238}U/^{206}Pb$ versus $^{207}Pb/^{206}Pb$ Tera-Wasserburg Concordia diagrams. Internal structure of dolomitic oncoids (OND) with microporous cores that could have promoted fluid-rock interaction and dolomite recrystallization. JUB6 sample, oncoid rudstone, PPL view. To the right: $^{238}U/^{206}Pb$ versus $^{207}Pb/^{206}Pb$ Tera-Wasserburg Concordia diagram and corresponding absolute ages for JUB6 dolomitic oncoids. Data point error ellipses indicate 2σ internal uncertainty (95% confidence) of the isotope ratios on 'N' analyses. Red dashed lines represent the envelopes of the regression lines (isochrons). In blue are the Concordia curves. B) Dolomitic oncoids (OND) cemented by three spatially close calcite generations. The blocky calcite with dull orange zoned luminescence (EC) is post-dated by two blocky calcites (LC1 and LC2) which are bright orange and non-luminescent, respectively. The trace of a LA-spot is also illustrated. CH1, oncoidal rudstone, CL view. To the right: $^{238}U/^{206}Pb$ versus $^{207}Pb/^{206}Pb$ Tera-Wasserburg Concordia diagram and corresponding absolute age of EC calcite from sample CH1. Data point error ellipses indicate 2σ internal uncertainty (95% confidence) of the isotope ratios on 'N' analyses. Red dashed lines represent the envelopes of the regression lines (isochrons). In blue are the Concordia curves.

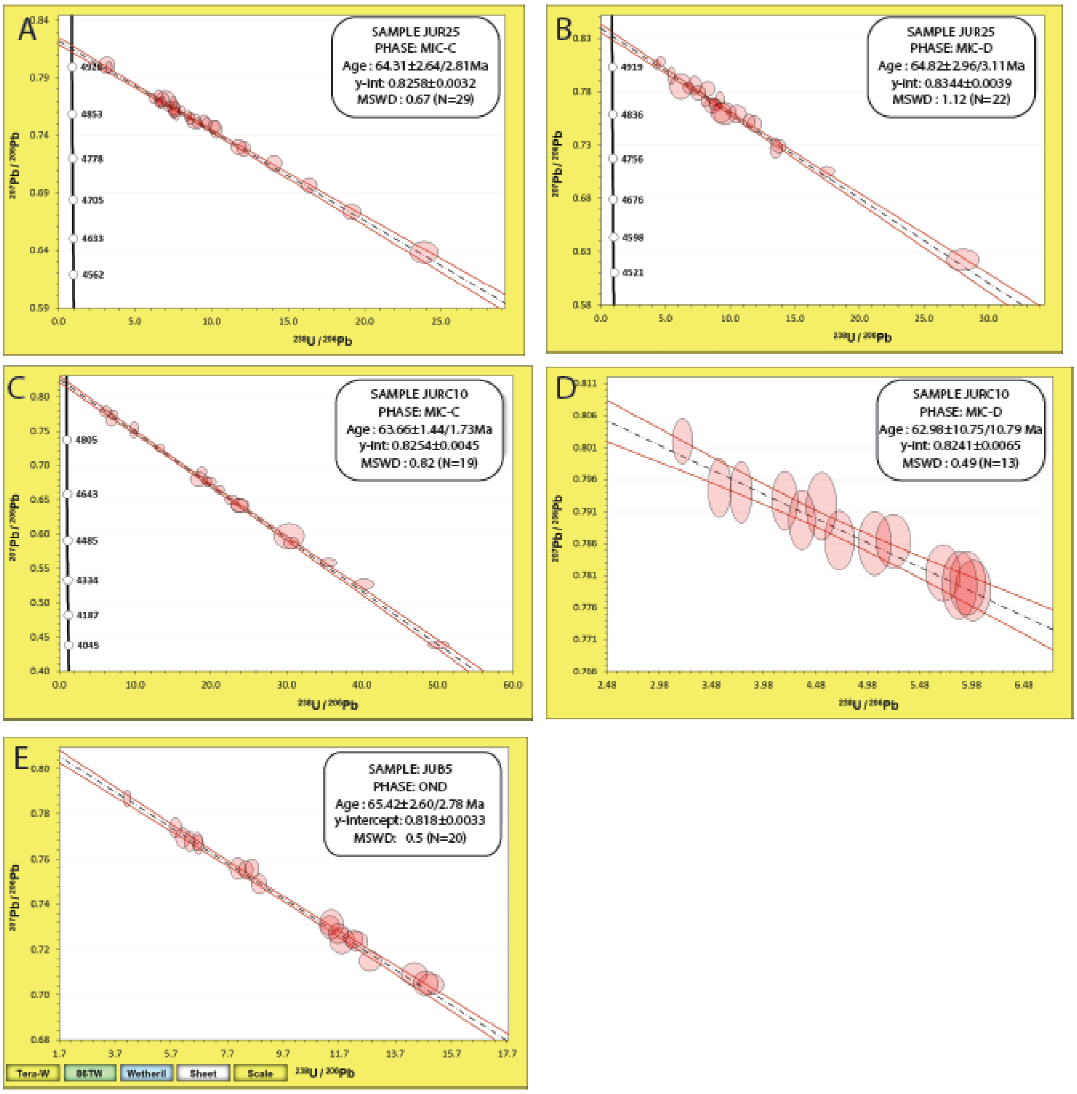

Supplementary data S3. ^{238}U/^{206}Pb *versus* ^{207}Pb/^{206}Pb Tera-Wasserburg Concordia diagrams and corresponding absolute ages for the carbonate samples investigated. Data point error ellipses indicate 2σ internal uncertainty (95% confidence) of the isotope ratios on ‘N’ analyses. Red dashed lines represent the envelopes of the regression lines (isochrons). In blue are the Concordia curves.

The age of EC cement in this sample was therefore possibly due to some LA-analyses erroneously performed on these coexisting calcites. The later LC1 calcite was tested multiple times from different samples. This calcite always characterised by low radiogenic Pb content and low spread of the $^{238}U/^{206}Pb$ ratio. Its U-Pb composition possibly falls close to the upper intercept to the Concordia, causing an 'artificial' anchoring of EC cement regression and thus a younger age.

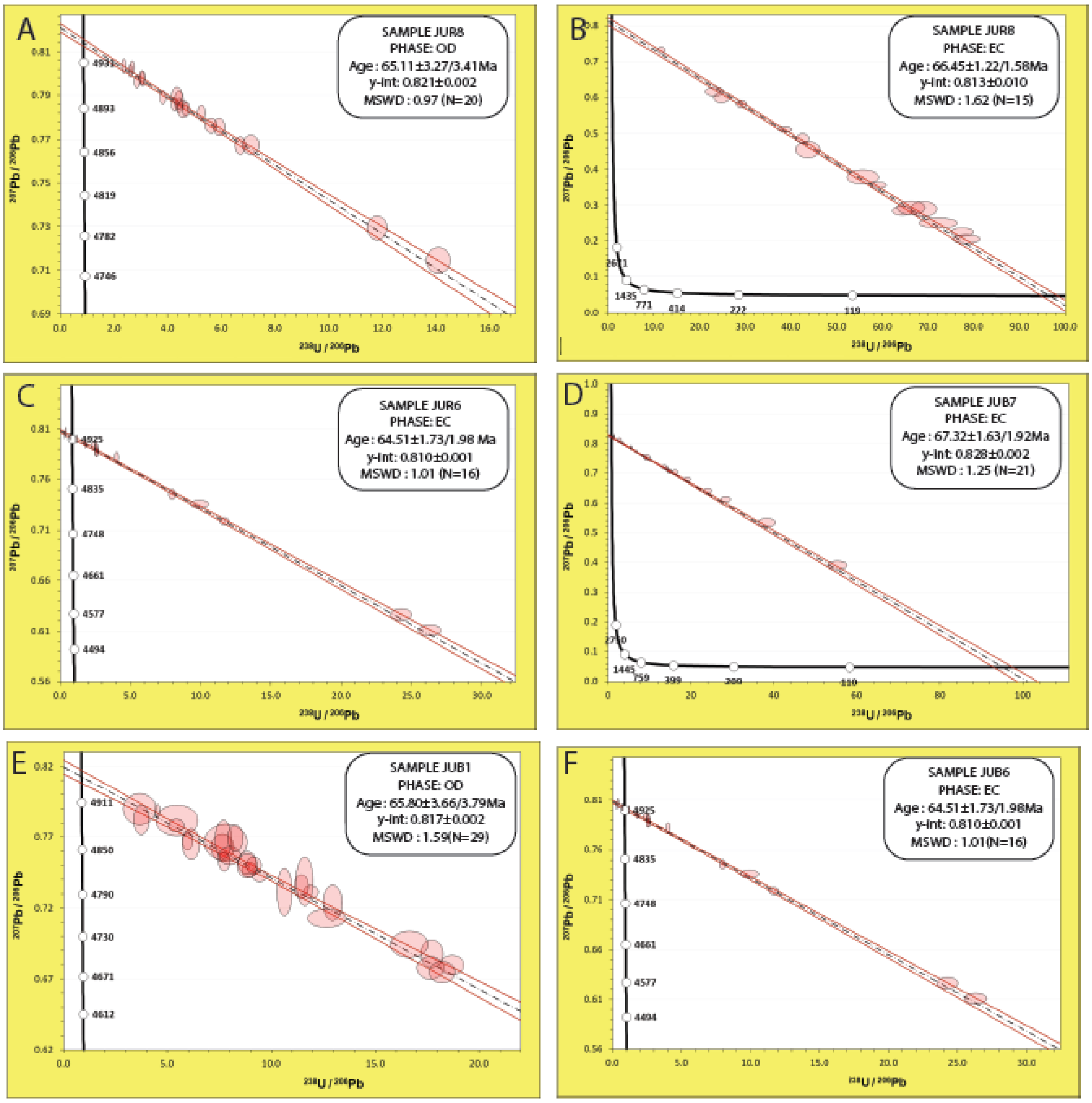

Supplementary data S3. $^{238}U/^{206}Pb$ *versus* $^{207}Pb/^{206}Pb$ Tera-Wasserburg Concordia diagrams and corresponding absolute ages for the carbonate samples investigated. Data point error ellipses indicate 2σ internal uncertainty (95% confidence) of the isotope ratios on 'N' analyses. Red dashed lines represent the envelopes of the regression lines (isochrons). In blue are the Concordia curves.

6.2 Chronostratigraphic implications for KPg, PETM and EECO events

The Balbuena and Santa Barbara groups consist of the sag to post-rift deposits of the Salta rift basin (Fig. 27). They are some of the best candidates to show the importance of lacustrine carbonates as environmental recorders. Indeed, biostratigraphic evidence (Rascovsky, 1968; Reyes, 1972; Moroni, 1982; Alonso & Marquillas, 1986; Marquillas et al. 2003, Quattrocchio et al. 2005, 2006; Volkheimer et al., 2006; Cónsole-Gonnella et al, 2017) indicate that they accumulated coevally with pivot events of the Earth history. These are the KPg extinction event (precisely dated at 66 Ma; Sprain et al., 2018) and the Paleogene-Eocene hypertermals such as the Paleocene-Eocene Thermal Maximum (i.e. PETM; dated at 55.9-56 Ma, e.g. Zeebe & Lourens, 2019) and the Early Eocene Climate Optimum (i.e. EECO, dated at 51-53 Ma, Raine et al., 2013).

Consequently, formations included in the Balbuena and Santa Barbara groups (Lecho, Yacoraite, Tunal, Maella, Maiz Gordo and Lumbrera Fms.) have been extensively investigated for the purpose to locate these events (e.g. Hyland et al., 2015, 2016; White et al., 2018; Rohais et al., 2019; Zimicz et al., 2020; Fernicola et al., 2021; Fig. 28).

Geochemical (i.e. C-O stable isotopes) and magnetostratigraphic data are provided by previous authors for some of these formations (e.g. Sial et al., 2001; Marquillas et al., 2007; Del Papa et al., 2010; Sial et al., 2013; Hyland et al., 2015; 2016; Andrews et al., 2017; White et al., 2018; Rohais et al., 2019; Zimicz et al., 2020) along three main stratigraphic sections: Juramento section, Tin-Tin section and Cerro Bayo section (Fig. 41). However, the lack of robust absolute time constraints (i.e. available only for the Lumbrera Fm.; Del Papa et al., 2010; Fernicola et al., 2021) limited to tie the local geomagnetic polarity patterns to the polarity timescale (GTPS; Gradstein et al., 2012). Consequently, it was challenging to associate specific geochemical signals recorded by the sediments with those events of known timing.

In this chapter available magnetostratigraphic and biostratigraphic data will be coupled with the zircon absolute ages obtained in Montano et al. (in revision; Chapter 6.1) to attempt defining the depositional age of Tunal, Maella, Gordo and Lumbrera Fms. Since geochemical data from previous authors were mainly obtained by bulk analysis (carbonates) or from organic matter, in this study new C-O stable isotope analyses were carried out along the Juramento stratigraphic section from depositional and early diagenetic carbonate phases (i.e. microbialites, ooids, oncoids and lacustrine cements) that were selected after an accurate petrographic analysis. Geochemical data (from this study and previous authors) will be discussed to best locate the KPg boundary and the Paleogene hypertermals in these formations.

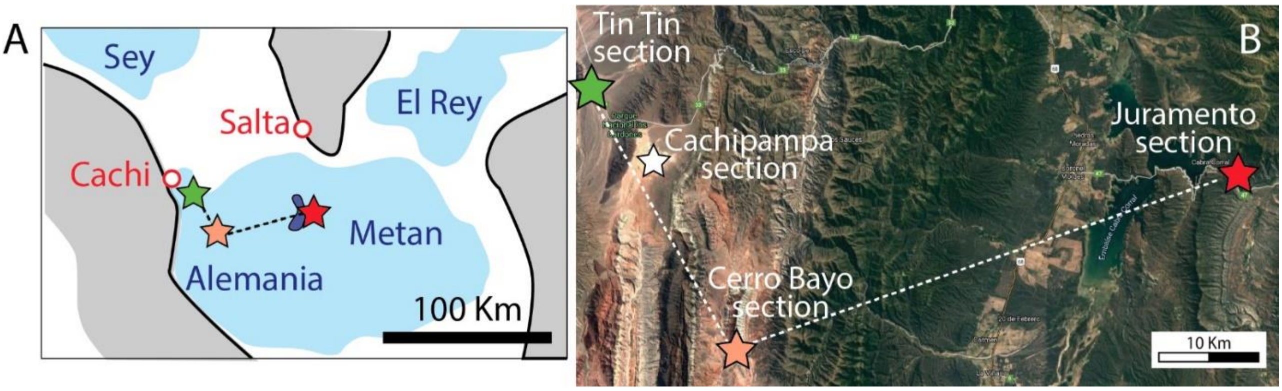

Figure 41. Location of the stratigraphic sections considered for the chronostratigraphic analysis of the Balbuena and Santa Barbara groups. A) Map of the Salta rift sub-basins (Alemania, Metan, Sey and El Rey) during the sag phase (Yacoraite Fm. deposition). Modified after Roemers et al. (2015). The dark blue area nearby the red-star is the Cabra Corral lake. B) Aerial view with the location of the Juramento (red star), Cerro Bayo (orange star), Cachipampa (white star) and Tin Tin (green star) stratigraphic sections.

6.2.1 Chronostratigraphy of the Balbuena Santa Barbara group

A multiproxies chronostratigraphic model of part of the Balbuena and Santa Barbara groups is shown in Figure 42 that resumes all the biostratigraphic (Rascovsky, 1968; Reyes, 1972; Moroni, 1982; Alonso & Marquillas, 1986; Quattrocchio & Volkheimer, 2000; Marquillas et al. 2003, Quattrocchio et al. 2005; Volkheimer et al., 2006; Cónsole-Gonnella et al, 2017; Fernicola et al., 2021), chemostratigraphic (i.e. C-O stable isotopes obtained from carbonates in this study and from organic matter by Hyland, 2015, 2017 and Andrews et al., 2017), chronostratigraphic (i.e. U-Pb ash layer ages; Del Papa et al., 2010; Rohais et al., 2019; Fernicola et al., 2021; Montano et al., in revision, Section 6.1) and magnetostratigraphic (Del Papa et al., 2010; Sial et al., 2013; Hyland et al., 2015; 2016; Andrews et al., 2017; White et al., 2018; Zimicz et al., 2020) data available for the formations investigated. The data listed are from three stratigraphic sections of the Salta rift basin: Juramento section (i.e. Montano et al., in revision, Chapter 6.1), Cerro Bayo section (i.e. Hyland et al., 2015) and Tin Tin section (i.e. Fernicola et al., 2021). In order to properly interpret all data, it is worth underlining that previous authors (e.g. Marquillas et al., 2005) mentioned the occurrence of unquantified sedimentary hiatuses at the boundaries between Yacoraite, Tunal, Maella, Maiz Gordo and Lumbrera Fms where erosive surfaces were detected in the proximal domains.

Key points to decipher the chronostratigraphic history of the Balbuena-Santa Barbara continental series is to attribute an identity to the normal polarized intervals recorded by the sediments in the Tunal and Maella formations, which are currently highly debated (e.g. Hyland et al., 2015; 2016; Andrews et al., 2017; White et al., 2018; Zimicz et al., 2020; Fernicola et al., 2021). Hyland et al. (2015; 2016) and Hyland & Sheldon (2018) presented a chronostratigraphic interpretation that identifies in C27n (~63 - 62.11 ± 0.3 Ma; Gradstain et al., 2012) the normal polarized chron of the Tunal Fm. (Cerro Bayo section). The same polarity chron is interpreted to be C28n (~ 64.6 - 63.4 ± 0.3 Ma; Gradstein et al., 2012) by White et al. (2018) and C29n (65.72 ± 0.01 - 64.86 ± 0.3 Ma, Gradstein et al., 2012; Sprain et al. 2018) by Zimicz et al. (2020). This clearly affects the interpretation of the ages of the overlying formations.

The depositional age depth model obtained from zircon geochronology (MDA depth model in Montano et al. in revision; Chapter 6.1) suggest that the top of the Yacoraite Fm. is at 62.3 ± 0.56 Ma, thus between 62.86 (i.e. older age limit) and 61.74 (i.e. younger age limit) Ma.

By taking into account: 1) this age interval; 2) the occurrence of Danian palynomorphs at the bottom of the Tunal Fm. (Quattrocchio et al., 1997; Volkheimer et al., 2000); and 3) the reverse magnetization recorded at the top of the Yacoraite Fm. and at the base of the Tunal Fm. (Hyland et al., 2015), the only possible time scenario identifies the limit between Yacoraite and Tunal Fms. in chron C27r (Figure 42A). Accordingly, the previously unquantified sedimentation hiatus between Yacoraite and Tunal Fms. results to have a minor duration, possibly < 0.5 Ma.

Following this interpretation, the Maella Fm. was deposited during the polarity chrons C26r, C26n and C25r, in agreement with: 1) the occurrence of Selandian Palynomorphs (Quattrocchio & Wolkheimer, 2000); and 2) the reverse magnetization at the base of the Maiz Gordo Fm. (corresponding to the top of C25n). Thus, the sedimentary hiatus at the top of the Tunal Fm. is < 2.5 Ma (Figures 42A and 42B).

The Maiz Gordo Fm. hosts Late Paleocene-Eocene palynomorphs and mammals (Quattrocchio & Volkheimer, 2000, Marquillas et al., 2005). This, together with the chronostratigraphic interpretation previously discussed, suggests that the Maiz Gordo Fm. was deposited during chrons C25n, C24r and possibly C24n (?) (Figures 42B and 42C). The low sampling resolution of magnetostratigraphic data in this formation possibly does not capture the short duration subchrons of C24n (i.e. C24n.3n, C24n.2n and C24n.3n) and thus the upper limit of the Maiz Gordo Fm. remains unclear (Figures 42B and 42C).

The Lumbrera Fm. is subdivided in two units separated by an erosive surface (Del Papa et al., 2010). This formation lacks magnetostratigraphic data but includes in the lower unit Lutetian mammal fossils (Quattrocchio & Volkheimer, 2000; Quattrocchio et al., 2005; Del Papa et al., 2010; Quattrocchio et al., 2015) and at the top of the lower unit an ash layer of 46.2 Ma (Fernicola et al., 2021) supporting the Lutetian age of the lower Lumbrera (Fig. 42C). The absence of further age constraints or information about sedimentation rates hinders to know if the onset is in the upper Ypresian or in lower Lutetian. The top of the Lumbrera Fm. instead, is marked by an ash layer dated at 39.9±0.4 Ma (Bartonian; Del Papa et al., 2010; Fig. 42C).

To conclude, according to the chronostratigraphic scenario proposed in Figure 42, in the Metan Alemania basins the Yacoraite Fm. is Maastrichtian-Danian (~ 68-62 Ma), the Tunal Fm. is late Danian (~ 62.7-62.2 Ma), the Maella Fm. is deposited during the late Selandian and early Thanetian (~ 59.5-58.5 Ma), the Maiz Gordo Fm. during late Thanetian and Ypresian (~ 57 – 53? Ma) whereas the Lumbrera Fm. during late Ypresian or Lutetian and Bartonian. Durations inferred are calculated from the preserved deposits and do not consider possibly eroded stratigraphic intervals.

Figure 42. Integrated chronostratigraphic model of part of the Balbuena and Santa Barbara groups. Juramento section (this study), Cerro Bayo section (Hyland et al., 2015) and Tin Tin section (Fernicola et al., 2021). Biostratigraphic data (Bio.) from Rascovsky (1968), Reyes (1972), Moroni (1982), Alonso & Marquillas (1986), Marquillas et al. (2003), Quattrocchio et al. (2005), Volkheimer et al. (2006), Cónsole-Gonnella et al. (2017). Biostratigraphic marker positions along the Juramento section are after Rohais et al. (2019) and Deschamps et al. (2020) stratigraphic correlations. $\delta^{13}C$ and $\delta^{18}O$ are the Carbon (C) and Oxygen (O) stable isotope values calculated from carbonates (this study, expressed as relative to Vee Pedebee Belemnite standard) and from organic matter (δ^{13}Corg., Hyland et al., 2015). Blue arrows point to negative shifts of $\delta^{13}C$ associated to events of temperature raise. The Geomagnetic polarity scale (GTS 2012) is from Gradstein et al. (2012) whereas ICS 2021/05 stands for International chronostratigraphic chart (Cohen et al., 2013). Barred areas of magnetostratigraphic correlations represent sedimentation hiatuses. KPg = Cretaceous Paleogene extinction event (age from Sprain et al., 2018); PETM= Paleocene Eocene Thermal Maximum (age from Zeebe & Lourens, 2019). EECO = Early Eocene Climate Optimum (age from Raine et al., 2013).

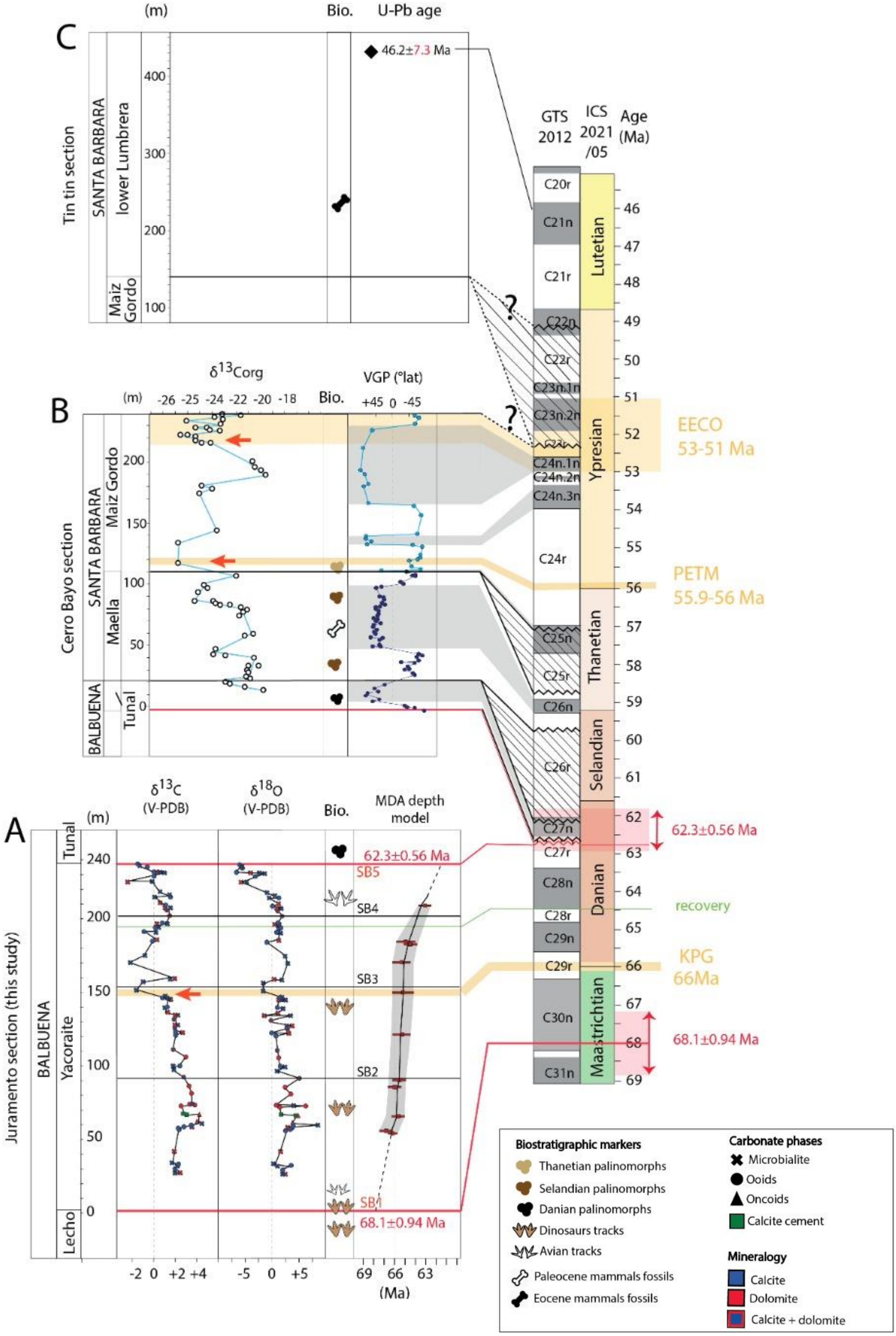
C
(m)
Bio.
U-Pb age
46.2±7.3 Ma
Tin tin section
SANTA BARBARA
lower Lumbrera
Maiz Gordo
400
300
200
100
B
δ13Corg
(m)
-26 -25 -24 -22 -20 -18
Bio.
VGP (°lat)
+45 0 -45
Cerro Bayo section
SANTA BARBARA
Maiz Gordo
Maella
BALBUENA
Tunal
200
150
100
50
0
A
δ13C (V-PDB)
δ18O (V-PDB)
Bio.
MDA depth model
Juramento section (this study)
BALBUENA
Yacoraite
Tunal
Lecho
240
200
150
100
50
0
62.3±0.56 Ma
SB5
SB4
SB3
SB2
SB1
68.1±0.94 Ma
-2 0 +2 +4
-5 0 +5
69 66 63
(Ma)
GTS 2012
ICS 2021 /05
Age (Ma)
C20r
C21n
C21r
C22n
C22r
C23n.1n
C23n.2n
C24n.1n
C24n.2n
C24n.3n
C24r
C25n
C25r
C26n
C26r
C27n
C27r
C28n
C28r
C29n
C29r
C30n
C31n
Lutetian
Ypresian
Thanetian
Selandian
Danian
Maastrichtian
46
47
48
49
50
51
52
53
54
55
56
57
58
59
60
61
62
63
64
65
66
67
68
69
?
?
EECO 53-51 Ma
PETM 55.9-56 Ma
62.3±0.56 Ma
recovery
KPG 66Ma
68.1±0.94 Ma
Biostratigraphic markers
Thanetian palinomorphs
Selandian palinomorphs
Danian palinomorphs
Dinosaurs tracks
Avian tracks
Paleocene mammals fossils
Eocene mammals fossils
Carbonate phases
✖ Microbialite
● Ooids
▲ Oncoids
🟩 Calcite cement
Mineralogy
🟦 Calcite
🟥 Dolomite
Calcite + dolomite

6.2.2 The KPg boundary in the Yacoraite Fm.

The KPg boundary marks one of the ‘big five’ biologic turnovers, the most important extinction events of the Earth history (e.g. Song et al., 2021). They concerned the extinction of the non-avian dinosaurs and about 50–75% of all terrestrial and marine taxa. In the oceans, this crisis has influenced the food chain and caused almost a complete extinction (99%) of planktonic foraminifera (e.g. Molina et al., 1988).

The extinction event is known to be coeval with the Chicxulub meteorite impact (Yucatan peninsula, Mexico) and the Deccan trap volcanism (India). The meteorite impact is considered as the primary driving force for the mass extinction (Hull et al., 2020 and references therein). However, recent literature (e.g. Hull et al., 2020) suggest that the Deccan volcanism (active before and after the meteorite impact) could have promoted the climatic changes by releasing Giga tons of CO_2 and SO_2 in the atmosphere, predisposing faunas to the extinction.

The sedimentary layers deposited coevally with the meteorite impact are enriched in extra-terrestrial siderophilic elements such as iridium, defining the so called ‘iridium anomaly’(Smith et al., 1980). Tephra layers located a few centimetres from the Iridium anomaly allowed to produce precise time constraints for the impact. Accordingly, the KPg has been precisely dated at 66 Ma (66.021 ± 0.081 from Clyde et al., 2016, 66.038 ± 0.098 Ma from Renne et al. 2013, 66.05 ±0.008/0.043Ma from Sprain et al. 2018). Thus, it is coeval with the geomagnetic polarity chron C29r (65.688- 66.398 Ma; Gradstein et al., 2012).

In sedimentary series the occurrence of the KPg horizon is usually associated with different geochemical anomalies, witnesses of the environmental crisis (e.g. Hull et al., 2020). The $\delta^{13}C$ negative excursion is the most commonly known geochemical anomaly existing in correspondence with the biotic extinction. It is recorded in calcite and organic matter that formed in ocean and continental waters (2-3‰ in marine settings, 1.5-2% in continental settings). During late Maastrichtian, around 0.3-0.2 Ma before the meteorite impact, a +2°C warming event, probably associated with the onset of the Deccan volcanism is recorded by an increase in $\delta^{18}O$ signal (Schoene et al. 2019). In correspondence with the impact, temperature strongly decreased in the so called ‘impact winter’. This brief period of global cooling was possibly caused by the thick cloud of materials ejected in the atmosphere by the meteorite impact (e.g. Vellekoop et al., 2016). The impact winter was followed by a period of greenhouse warming caused by CO_2 released into the atmosphere (Vellekoop et al., 2016). Other geochemical anomalies are known, such as the sulphur anomaly (Witts et al., 2018) and Osmium anomaly (Schoene et al., 2019).

According to the MDA depth model here presented for the Yacoraite Fm. (Montano et al., in revision, Chapter 6.1) the KPg boundary event could have occurred between 50 and 180m along the Juramento section. There are several reasons to believe that the event was recorded just below SB3 at around 150m from the base of the Juramento section (Fig. 42A).

1) **Biostratigraphic evidence.** Dinosaur tracks were recognized at the base of the Yacoraite Fm. (Díaz-Martinez et al., 2016; Cónsole-Gonella et al., 2017) and few metres below SB3 in the Maimarà section (Cónsole-Gonella et al., 2017; stratigraphic interpretation from Rohais et al., 2019). No evidence of dinosaur life is found in sequences 3 and 4.
2) **Sedimentologic/lithostratigraphic evidence:** the SB3 marks a sharp transition from carbonate dominated deposits to clastic deposits, with a complete shout down of carbonate production. Sedimentological evidence indicate that this change is sedimentation dynamic started few metres below SB3 (Deschamps et al., 2020). The shutdown of carbonate production may have been promoted by dust clouds related to the meteorite impact and volcanic events, blocking sunlight for enough time to hinder photosynthesis. The reappearance of clastic deposits should instead correspond to an increase of sediment supply due to erosion, possibly favoured by the disappearance of soils and vegetation in association with the KPg event (Deschamps et al., 2020).
3) **Geochemical evidence.** Few metres below SB3 there is a negative pulse of $\delta^{13}C$ values (down to -5‰) that was recognized in the present study (Fig. 41A), and by Marquillas et al. (2007), Sial et al. (2001, 2013) and Rohais et al. (2019). Such negative values are considered not compatible with processes such as an increase in water supply from the catchment area and consequent increase in isotopically light carbon flowing into the basin. Thus, it thus should be triggered by an external force (Rohais et al., 2019). It is worth mentioning that no Iridium anomaly has been recognized around SB3 (Rohais et al., 2019).
4) **Sedimentation rates and palaeoenvironmental evidence**. The MDA model (Montano et al., in revision, Chapter 6.1) indicates that sedimentation rates had a major peak (up to 150m/Ma) around SB3, with the highest values recorded in the formation. After this event, sedimentation rates tend to initial values (around 10m/Ma). Similar results were obtained by MIDA depth model (Chapter 6.1). Sedimentation rates in lacustrine settings are influenced by tectonic and climate changes. Backstripping analysis (Stark, 2011) did not highlight any major peak in the subsidence. Thus, such sedimentation rate dynamic has to be attributed to a major environmental change. The possible involvement of the KPg event into the changes in catchment dynamic, erosion processes, carbonate production and environmental conditions in correspondence with SB3 are extensively discussed by Rohais et al. (2019) and Deschamps et al. (2020).

After catastrophic events, ecosystems and biodiversity require time to recover. It is not clear if the recovery is coeval (e.g. Coxal et al., 2006) or not (e.g. Brich et al., 2021) with the re-establishment of pre-KPg C-O stable isotope values (i.e. carbon pump recovery). However, by assuming that the negative δ^{13}C peak at 150m along the Juramento section corresponds to the KPg event, the δ^{13}C and δ^{18}O recovered to pre-KPg values (values measured before 150m) at around 195m from the base of the section (45m after the supposed KPg event). According to the MDA depth model (Montano et al., in revision, Chapter 6.1) this stratigraphic height corresponds to approximately 64.5 Ma. This evidence indicates that in the Yacoraite Fm. area the carbon cycle possibly recovered around 1.5 Ma after the KPg event (Fig. 42A) in agreement with Birch et al. (2021) that reported a period of 1.8 Ma.

6.2.3 Paleocene Eocene hyperthermals

The early Cenozoic (Paleocene and Eocene, 56-48 Ma) was a period characterized by long-term warming punctuated by periods of rapid global hyperthermal events named Paleocene-Eocene hyperthermals (e.g. PETM and EECO; Zachos et al., 2008; Cramwinckel et al., 2018; Inglis et al., 2020). They have been recognized in different localities in the world and a masterpiece outcrop belongs to the Zumaia Fm. in Spain (e.g. Bernaola et al., 2009). The most common evidence in the sedimentological record are the carbon isotope excursions with negative shifts of δ^{13}C values in both carbonates and organic matter due to temperature driven carbon-cycle instabilities (e.g. McInerney & Wing, 2011).

Paleocene Eocene Thermal Maximum. In correspondence with the Paleocene Eocene Thermal Maximum (PETM; ~ 56-55.9 Ma; e.g. Zeebe & Lourens, 2019) global surface temperatures rose rapidly by +4 to +8 ° (e.g. Westerhold et al., 2018; Inglis et al., 2021). For reasons which are currently highly debated (e.g. Stokke et al., 2020), a large input of ^{12}C rich carbon was released into the biosphere leading to rapid oceans acidification and extinction of deep-sea organisms (McInherney & Wing, 2011). In the marine and terrestrial sedimentologic records this corresponds to a 2.5-8 ‰ negative carbon isotope excursion (e.g. McInerney & Wing, 2011).

In the Salta rift basin the PETM has been located by Andrews et al. (2017) at the top of the Maiz Gordo Fm., whereas according to Hyland & Sheldon (2018) it is hidden inside the sedimentation hiatus between Maella and Maiz Gordo Fms.

Based to the time scenario discussed in Chapter 6.2 (Fig. 42), the 55.9-56 Ma PETM interval correlates at the base of the Maiz Gordo Fm., in contrast with what previously proposed. This interpretation is further supported by geochemical data. Indeed, $\delta^{13}C$ shows the lowest values (down to -26‰) with a drop of - 5‰ (Fig. 42B) right in correspondence with the base of the Maiz Gordo Fm. Moreover, in this stratigraphic interval it is possible to recognize the typical PETM variations of $\delta^{13}C$, usually characterized by a rapid onset followed by a stable phase and a gradual recovery to initial conditions (McInerney and Wing, 2011).

Early Eocene climatic optimum. The early Eocene climatic optimum (EECO; 53-49 Ma; Crouch et al., 2020) was a period of major climate and environmental change caused by a peak of greenhouse gas concentrations, especially CO_2, and general perturbation of the global carbon cycle (e.g. Zachos et al., 2008).

In the Salta rift basin, the EECO was located by Hyland & Sheldon (2018) at the base of the Maiz Gordo Fm. (in correspondence with the $\delta^{13}C$ drop that in this study have been attributed to the PETM).

According to the time scenario proposed in Chapter 6.2, part of the EECO should be recorded in the upper Maiz Gordo Fm. and part hidden in the hiatus between Maiz Gordo and Lumbrera Fms. (Fig. 42B and 42C). This interpretation is further supported by the occurrence of high frequency variations of organic $\delta^{13}C$ reported by Andrews et al. (2017) in the upper Maiz Gordo Fm. (Fig. 24C).

The Balbuena and Santa Barba groups deserve further investigation due to their pivot importance as recorders of the PETM and EECO thermal events. Isotope radiometric constraint and more detailed sedimentological, geochemical and magnetostratigraphic data of the Maiz Gordo and Lumbrera Fms, would allow to better constrain the boundary between the formations, evaluate the extent of the corresponding sedimentary hiatuses and more accurately constrain the position of the Paleocene Eocene hyperthermals for future paleoclimate studies.

7 LACUSTRINE CARBONATES DATING POTENTIAL

In the framework of the chronostratigraphic application of U-Pb carbonate dating, the term ‘dating potential’ refers to the probability to produce precise carbonate U-Pb ages that most possibly approximate the true depositional age (TDA) of the system (i.e. accurate depositional age). Thus, evaluating the dating potential requires to establish the dating success rate (i.e. percentage of carbonates that provide a depositional age) and the age precision (i.e. time resolution of the method).

At today there is a lack of predicting criteria for the dating potential of various carbonates, mineralogies, and environmental conditions. A better comprehension of the driving forces for the dating potential would allow to organize the field work and the analytical strategy potentially reducing the number of needed LAcarb analytical sessions, limiting costs and the overall time required to produce a robust a depositional age depth model of a sedimentary system.

The possibility to obtain accurate and precise depositional ages is directly linked to the pristine U-Pb isotope composition and preservation during diagenesis (e.g. Rasbury & Cole, 2009). In ideal conditions for dating, statistically robust (i.e. well regressed) lower intercept U-Pb ages are produced from carbonates that initially incorporated high and variable amounts of U and low and homogeneous amounts of Pb (i.e. common Pb) (Rasbury & Cole, 2009) and did not suffered post depositional diagenetic modifications (Chapter 2.4).

These specific initial conditions lead to an isotope configuration that is deterministic at any given time and characterized by high and variable μ ($^{238}U/^{204}Pb$) ratio. In a Tera-Wasserburg Concordia diagram this is expressed by high, variable and well aligned $^{238}U/^{206}Pb$ isotope ratios, with data-points most possibly close to the Concordia curve. Ages derived from carbonates characterized by a well-behaved U-Pb systematics are associated with MSWD ~1 and low relative uncertainties (i.e. age uncertainty in %). Unfortunately, these ideal conditions are not always met in natural carbonates because: (1) they are heterogeneous in texture and in elemental/isotope composition; (2) coeval carbonates from the same paleoenvironment may display large variations in U and Pb isotope contents as well as various ranges of the $^{238}U/^{206}Pb$ and $^{207}Pb/^{206}Pb$ ratios, (3) natural carbonates usually incorporate huge amounts of common Pb and low amount of U which are the major limiting factor for dating (i.e. in particular when U has low concentration and variability) and (4) common diagenetic processes affecting carbonates may induce age reset and/or degradation.

For this reason, since the advent of U-Pb carbonate geochronology, the comprehension of the mechanisms for U-Pb sequestration, as well as modification of U-Pb composition during diagenesis, became relevant for the comprehension of the dating potential. Specific carbonate types such as speleothems are known to produce more accurate and precise ages due to the initial incorporation of favourable U-Pb isotope concentrations (e.g. Woodhead & Petrus, 2019) Noteworthy, according to the present knowledge of the mechanism for U and Pb incorporation in carbonates, also different mineralogies could be potentially associated to different dating potentials.

In order to investigate the factors possibly affecting the carbonate dating potential, a statistical analysis was achieved in the framework of the Yacoraite Fm. Petrography and geochemistry analyses were used for sample characterization as discussed in Montano et al. (in revision, Chapter 6.1) and allowed to select 80 carbonate phases showing no major evidence of post-depositional (burial) diagenetic modifications and were further dated via LAcarb (Chapter 7.1). The impact of early and late diagenesis on the dating potential was discussed based on petrography, geochemistry (C-O and U-Pb) and LAcarb data (Chapter 7.2). The dating success was estimated by calculating the % of depositional ages (i.e. consistent with the MDA depth model) obtained for each carbonate type and mineralogy among the 80 carbonate phases selected. Similarly, the precision of the technique was evaluated by analysing the distribution of the uncertainties into the dataset (chapter 7.3). Results from this study are included in a scientific article in preparation: ‘U-Pb LA-ICPMS dating potential of Cretaceous-Paleogene lacustrine carbonates’.

7.1 Petrography, geochemistry and LAcarb

A pre-analytical sample characterization was achieved via petrographic (optical and CL-petrography) and geochemical (staining and C-O stable isotope) analysis along the Juramento stratigraphic section following the approach already presented in Montano et al. (2021; Chapter 4.1) and Montano et al. (in revision; Chapter 6.1). This study aimed at delineating a paragenesis for the Metan-Alemania basin and was achieved with the purpose to understand which process is actually being dated via LAcarb (e.g. carbonate deposition or later diagenetic process) and discard, for further LAcarb analysis, carbonates pervasively affected by later diagenesis.

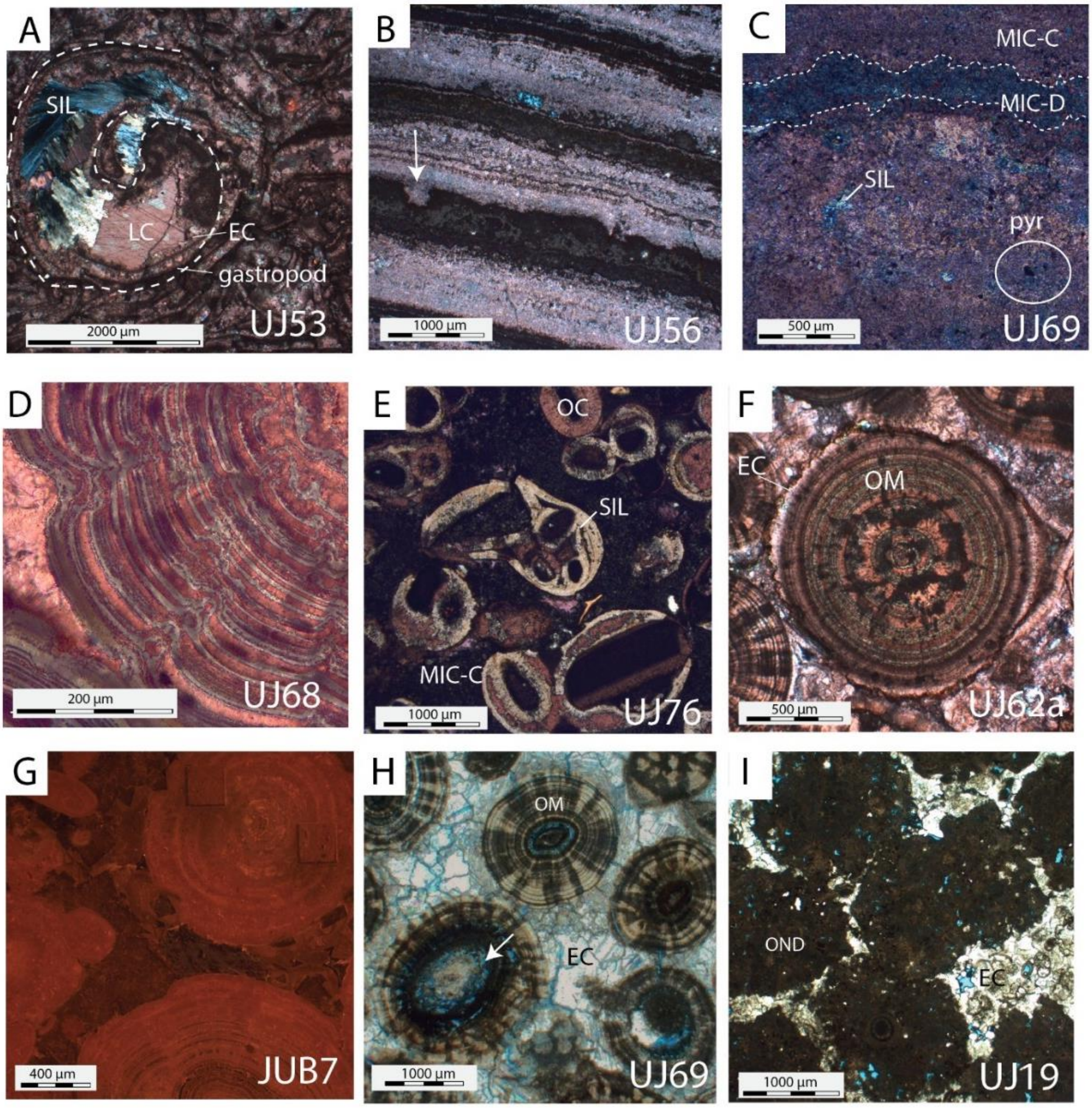

The Juramento section from Métan Alemania sub basin was selected because in this area the burial overprint on pristine carbonate composition was interpreted to be minor (Marquillas et al, 2007; Sial et al., 2001; Durieux & Brown, 2007; Rohais et al., 2012; 2014, 2019; Gomes et al., 2020; Montano et al., in revision, Chapter 6.1) and thus carbonates should mostly preserve their initial geochemical composition and depositional age.

Field survey along the Juramento section provided a total number of 97 carbonate samples consisting mainly of gastropod rudstone (Fig. 43A), microbial boundstone (Fig. 43B,C), oolitic grainstone (Fig. 43 D,E,F,G,H,I) and oncoid rudstone. A description of sedimentary facies is in Montano et al. (in revision; Chapter 6.1). The diagenetic study here presented strongly benefited from the prexisting literature about the diagenesis of the Yacoraite Fm. (Marquillas et al, 2007; Cesaretti et la., 2000; Sial et al., 2001; Durieux & Brown, 2007; Rohais et al., 2012; 2014, 2019; Gomes et al., 2020), in particular for the recognition of burial diagenetic phases.

Figure 43. Petrographic images of the samples investigated. The sample name is to the right corner of each image. A) Gastropod rudstone. The gastropod shell has micritised borders and was subsequently leached and filled by later blocky calcite cement (LC) and chalcedony (SIL). Stained, XPL view. B) Microbial boundstone characterized by the typical alternation between calcitic (MIC-C) and dolomitic (MIC-D) mineralogy. Bioturbation features can be recognized between laminae. Stained, PPL view. C) Calcitic microbial boundstone characterized by dolomitized and un-dolomitized areas hosting framboidal pyrite crystals. Microbialite is affected by partial silica replacement and presence of areas with coarser crystals (possible evidence of recrystallization). Stained, XPL view. D) Detail of an ooid characterized by the mimic dolomitization. At the top of each lamina it is possible to recognize borrowing features. Stained, PPL view. E) Oolitic grainstone with evidence of selective replacive silicification (SIL) of calcitic ooids (OC). Stained, PPL view. F) Oolitic grainstone made by ooids characterized by typical alternation between stained calcitic and unstained dolomitic laminae. Compaction features (e.g. indented borders and few stylolites) occur. Relicts of an isopachous rim (around 30µm thick) of a very early fibrous calcite (EEC) are preserved around the ooids. Stained, PPL view. Oolitic grainstone with ooids cemented by a blocky calcite cement (EC) characterized by a concentring zoning under CL with the alternation between dull and slightly luminescent orange zones. CL view. H) Oolitic grainstone affected by pervasive microfracturation and dissolution (white arrow). PPL view. I) Oncoid boundstone made by dolomitic oncoids (OND) cemented by a blocky calcite cement (EC). PPL view.

Depositional carbonate phases identified are calcitic, dolomitic and mixed (calcitic and dolomitic) microbialites (MIC-C, MIC-D and MIC-M, respectively), calcitic dolomitic and mixed ooids (OC, OD and OM, respectively) and dolomitic oncoids (OND). Diagenetic carbonate phases instead are the isopachous fibrous cement EEC (Fig. 43A and 43F), the blocky calcites EC and LC1 and the drusy mosaic calcite LC2 (Fig. 43 A,G,H,I). Two types of chalcedony (SIL 1 and SIL2; Fig. 43A, E, C,E) were also identified.

Carbon and Oxygen stable isotopes are well known proxies for hydrologic and climate conditions in terrestrial settings (e.g. Talbot, 1999, Leng & Marshall, 2004; Bernasconi & Mckenzie, 2013; Boever et al., 2017) and provide precious insights about the diagenetic history of the samples analysed.

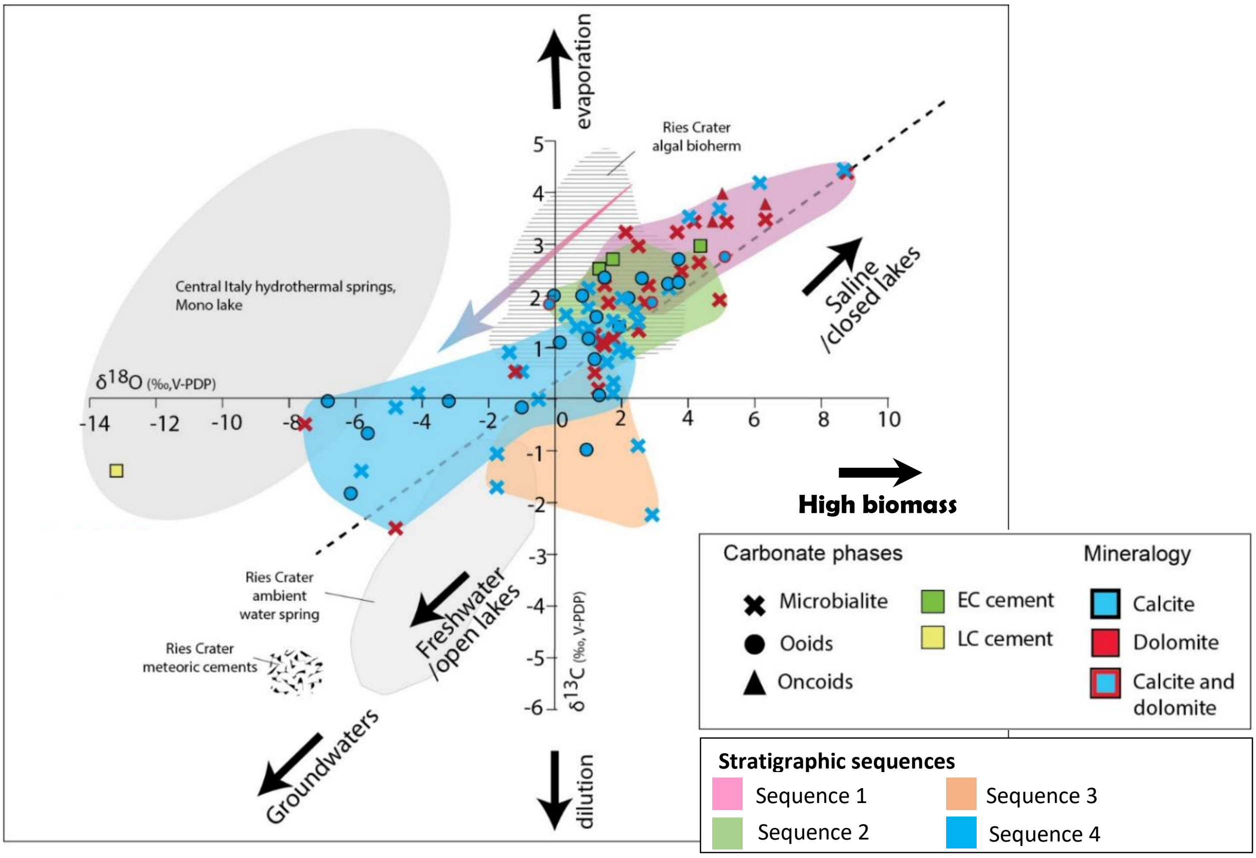

Figure 44 Cross plot of δ18O vs δ13C values of the carbonates investigated from the Yacoraite Fm. at the Juramento section. The black dashed line indicates the covariance between δ18O and δ13C values. The coloured arrow shows the evolution of the lacustrine water from the bottom (sequence 1) to the top (sequence 4) of the formation. Information about the meaning of carbon and oxygen stable isotope signatures (black arrows) and the signature of other lacustrine carbonates (grey areas) are from Talbot (1990), Leng & Marshall, (2004), Della Porta (2015) and De Boever et al. (2017). The composition of Ries Crater carbonates was implemented with the results obtained in Montano et al. (2021, Chapter 4.1).

The C-O stable isotope data was acquired for microbialites, ooids, oncoids and for EC and LC1 cements. Depositional carbonates and the blocky calcite cement EC from the 4 stratigraphic sequences record the isotope composition covariance typical of carbonate formed in closed basins (Fig. 44). This was also discussed in the framework of the Ries Crater case study (Montano et al., 2021, Chapter 4.1). Carbonate from the Juramento section have mostly positive values of δ^{13}C and δ^{18}O ratios (up to +4 and +10, respectively; Figures 42A and 44).

This usually suggest precipitation in relative evaporative conditions along the lake margin. Only few carbonates provided δ^{18}O values < -1 (and down to -8). They occur in correspondence with SB3 and 10 metres below SB5 (Fig. 42A). This is consistent with infiltration of light meteoric waters during emersion events along the lake margin. Few data points from sequence 3 have instead positive δ^{18}O and negative δ^{13}C (Fig. 42A) which agrees with the high amounts of organic material accumulated at the base of sequence 3 (High TOC; Rohais et al., 2019).

Here follows the discussion about the diagenesis in the Juramento stratigraphic section. Paragenesis is in figure 45.

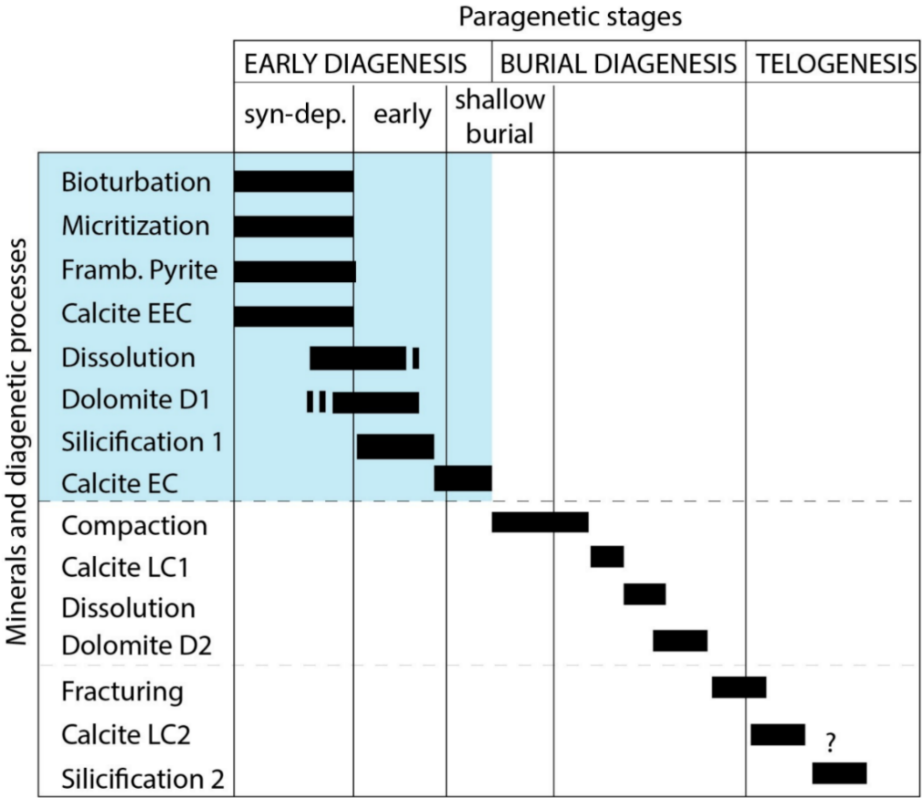

Figure 45. Paragenesis of the Yacoraite Fm. based on petrographic and carbon oxygen stable isotope data from the Yacoraite Fm. In blue the minerals and diagenetic processes occurring during early diagenesis.

Micritization. During deposition, bioclasts (e.g. gastropods and ostracods) and ooids were affected by syn-depositional micritization (Fig. 43A). Bioturbation and borrowing instead involves most depositional facies (Fig. 43B).

Framboidal pyrite. Microbial carbonates include framboidal pyrite (Fig. 43C) which is usually associated to syn-depositional microbial activity and reducing conditions (e.g. Tucker & Wright, 1990).

Early calcite 1 (EEC). In the grain-supported facies (rudstone and grainstone) a very thin isopachous rim of fibrous non-ferroan calcite (EEC) occurs around the grains, hindering their contact (Fig. 43F). Due to the habitus, fabric and occurrence before mechanical compaction, EEC was interpreted as a very early phreatic lacustrine cement with an aragonite or HMC precursor. Cross-cut relationship indicate that EEC is followed by the blocky calcite cement EC (Fig. 43G).

Dissolution 1. Early dissolution involves all carbonate phases (microbialite, ooids, oncoids) but especially EEC cement and the gastropod shells (Fig. 43A) possibly due to their less stable mineralogy.

Dolomitization 1. Microbial carbonates (i.e. initially calcitic/aragonitic microbialites, ooids and oncoids) underwent an early diagenetic fabric preserving dolomitization (Dolomitization 1) as demonstrated by the typical alternation between calcitic and dolomitic laminae in both microbialites (Fig. 43B and 43C) and ooids (Fig. 43C) and by the pervasive dolomitization in oncoids. This process is considered a mimic dolomitization (Dolomite 1) driven by the presence of microbial activity, high evaporation and high Mg/Ca ratio in the waters (e.g. Corsetti et al., 2006; Boever et al., 2017) and was discussed in the framework of the Yacoraite Fm. by Gomes et al. (2020). Dolomitic and calcitic phases show similar C-O stable isotope values (Fig. 44), assessing for a very early/syn-depositional diagenetic process.

Silicification 1. Calcitic and dolomitic microbialites and ooids are affected by replacive pseudomorphic silicification by microcrystalline chalcedony aggregates (Figures 43A, 43C and 43E) (especially at the top of sequence 4 and locally at the base of the section in sequence 1). Silicification is common in high alkaline and evaporative lacustrine environments with the presence of microbial activity and is considered an early diagenetic process (e.g. Boever et al. 2017).

Early calcite 2 (EC). EC is a non-ferroan blocky calcite that exhibits a concentring zoning under CL with the alternation between dull and slightly luminescent orange zones. It lines grains/pores hindering the contacts in grainstone and rudstones textures, dedolomitizes dolomitic microbialite and ooids and fills moldic pores (dissolved gastropod shells). Thus it formed after/together with early dissolution, after dolomitization 1 and before chemical compaction. EC shows positive $\delta^{13}C$ and $\delta^{18}O$ values consistent with those of depositional carbonates (Fig. 44). This, together with petrographic features and cross-cutting relationships, supports precipitation during early shallow burial in the interparticle and moldic pores.

Burial diagenesis. Later diagenesis is marked by the occurrence of chemical compaction and fracturing. Late diagenetic phases are mainly: a bright orange luminescence blocky calcite cement (LC1), a ferroan dolomite cement (DOL2) and a non-luminescent drusy mosaic calcite cement (LC2) occurring mainly in fractures and veins (i.e. it postdates or is coeval with a second fracturation event). After LC2, late gypsum occludes the remaining interparticle pores (SIL 2). The blocky calcite LC1, the only one analysed for C-O stable isotopes shows a distinctive negative isotope signature with $\delta^{18}O$ down to -13‰ (V-PDB) that could be explained with precipitation at high temperatures during burial (Fig. 44). A more exhaustive discussion about burial diagenesis in the Mètan-Alemania basin is in Sial et al. (2001) and in Durieux & Brown (2007).

After the diagenetic study, depositional carbonates with evidence of the burial diagenetic modifications previously listed were not analysed for LAcarb because they may easily provide younger or errorochron ages. It derives that 43 samples have been judged suitable for chronostratigraphic studies. From them, 80 carbonate phases (microbialites, oncoids, ooids and early lacustrine cements) were randomly screened via LAcarb in seven analytical sessions and provided 50 U-Pb ages (i.e. 62% of carbonate analysed provided an age) (Fig. 46 and supplementary data 4 to 13). Only 6 ages resulted appreciably younger (CH1-EC, JUB6-OND, UJ24b-OM, UJ43 MIC-C, UJ62a-OM and UJ7-EC carbonate phases) than the depositional age of the system as constrained by zircon geochronology (MDA depth model, Montano et al., in revision, Chapter 6.1) whereas, only sample UJ73 produced an older age. This latter was dated in multiple dating sessions obtaining consistent results. The reason for the older age may reside in a wrong sampling or in the possible re-sedimentation of an older grain. In total, only the 8% of carbonates analysed provided ages unconsistent with the MDA depth model and 33% were undatable due to very homogeneous isotope ratios and very high Pb composition ($^{207}Pb/^{206}Pb > 0.75$ which means high common Pb composition).

It is worth mentioning that 3 carbonate phases providing younger ages showed very mild evidence of diagenetic modifications. The issue of undetected neomorphism involves only the 7% of analysed phases and it is not a limiting factor when chronostratigraphic investigations are based on multiple samples and younger phases can be easily discarded.

In this respect, literature provides various microanalytical tools, destructive or not, for LAcarb sample selection (e.g. Petrus et al., 2017; Drost et al., 2018; Roberts et al., 2020a; Rasbury et al., 2021; Roberts et al., 2021). Among them, elemental/isotope mapping techniques demonstrated to be precious tool to avoid altered areas based on their chemical compositions and target areas that ensure high and heterogeneous μ ratio (i.e. high dating potential). These techniques may be important allies when dealing with samples that underwent a complex diagenetic history.

Noteworthy, the results achieved in this study on a wider dataset if compared to Montano et al., 2021, Chapter 4.1) and Montano et al. (in revision, Chapter 6.1) still demonstrates that petrography, geochemistry and U-Pb screening via random spot selection are sufficient to evaluate the origin of the carbonate to be dated, detent the isotope ratios variability and obtain robust depositional ages. If no ‘hot spots’ are found with the random spot selection, the sample has to be considered generally undatable or hardly datable (33% of samples analysed) and thus clearly associated with a low dating potential.

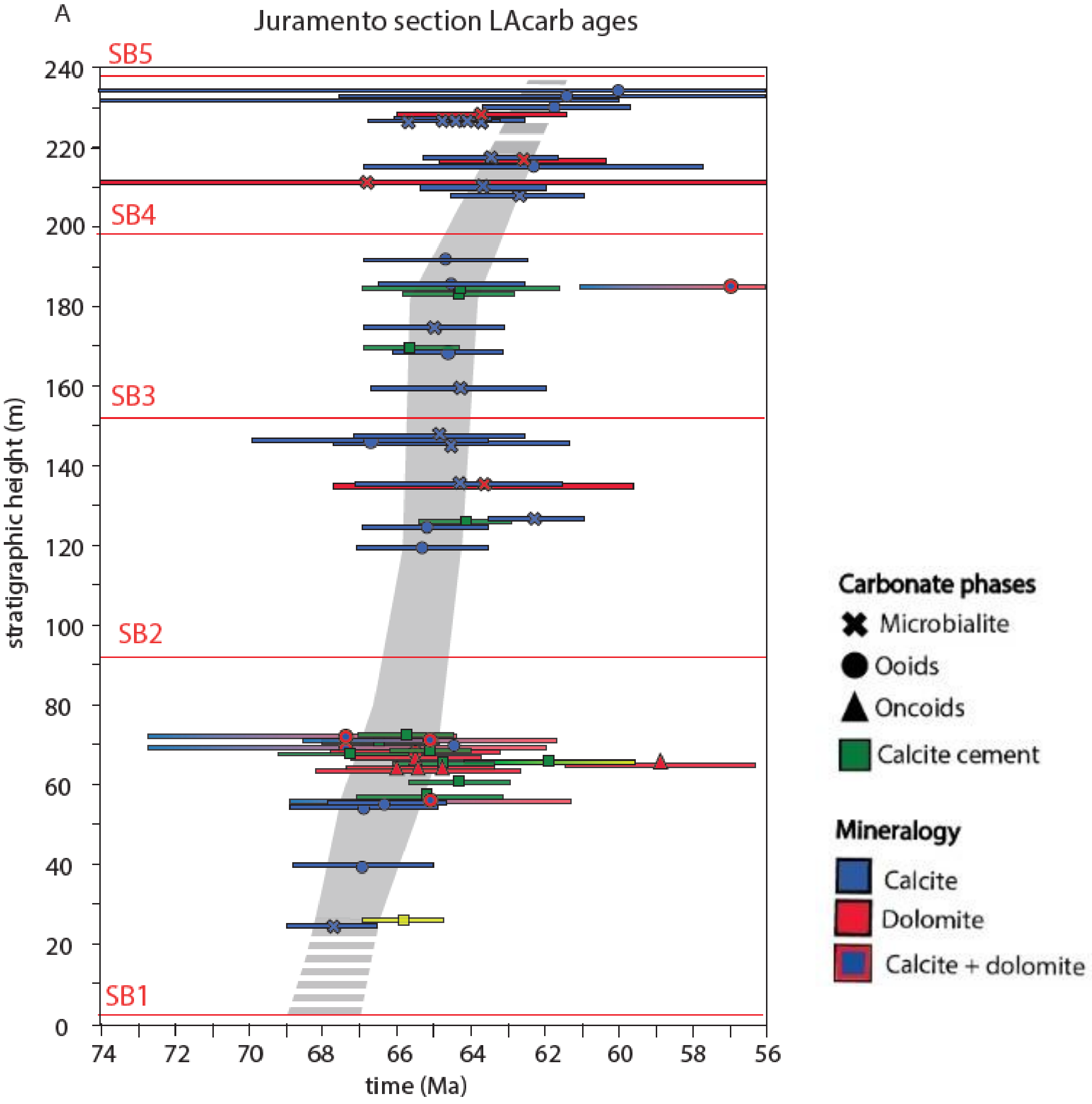

Figure 46 LAcarb geochronology of the Juramento section. U-Pb Ages (symbols), uncertainties (2σ, 95% confidence, horizontal bar) and stratigraphic positions are reported for all carbonate dated. For comparison, the grey area is the MDA depth model (Montano et al., 2021b). All reported uncertainties are 2σ.

7.2 Diagenetic overprint on the pristine U-Pb isotope composition

At today the impact of early and late diagenesis on the pristine isotope composition and dating potential (i.e. possibility to obtain precise ages that inform on the depositional age of the system) is not well understood and few questions still require comprehensive answers. Do different diagenetic processes cause specific U-Pb disturbances? Are U and Pb inherited in the newly recrystallized phases? Is diagenesis a blocking factor to obtain accurate ages? This Chapter aims at better understanding the role of diagenesis by focusing on the dataset obtained from the Juramento stratigraphic section. Results from field survey (Chapter 5.4), petrography, C-O stable isotope and LAcarb analyses (Chapter 7.1) were discussed in light of pre-existing literature about the mechanism for U-Pb sequestration in carbonates (Chapter 2.4).

Carbonates are highly susceptible to diagenesis from initial deposition to deep burial and exhumation, particularly when fluid chemistry and temperature change bringing them out of their stability field. Carbonate geochronologists usually refer to processes of ‘opening system behaviour” when they discuss the isotope system disturbance due to diagenesis (e.g. Roberts et al., 2020a). However, this is erroneously employed because ‘opening system behaviour’ refers to processes of solid state diffusion or generally elemental mobility in conditions of high temperature and/or pressure. In this manuscript, the term ‘disturbance’ and ‘diagenetic overprint’ are also used at the place of ‘opening system behaviour’. It is well accepted that the disturbance on the U-Pb isotope system due to diagenesis is far from systematic and it results in a complete reset of the isotope ratio configuration or in a data scatter which is greater than the one attributed to analytical uncertainty or initial Pb isotope heterogeneity (Rasbury & Cole, 2009). Accordingly, samples in which the geochemical composition have been completely reset are assumed to inform on the timing of the diagenetic reset (i.e. new crystallization, younger age). Conversely, carbonates partially ‘overprinted’ by diagenesis should produce less precise ages which are either consistent with deposition, younger or are dates without any geologic meaning (i.e. ‘errorochron’ (e.g. Jones et al., 1995; Roberts et al., 2020a). Indeed, as discussed in Montano et al. (in revision, Chapter 6.1) the impact of diagenesis is one of the main reasons for the necessity to consider carbonate U-Pb ages as minimum depositional ages (MIDA), in agreement with the definition of maximum depositional ages (MDA) used in zircon geochronology.

The Tera-Wasserburg Concordia diagram, representing the most common way to show the U-Pb isotope composition of carbonates, provides precious insights regarding the eventual diagenetic overprint. Proxies to be considered are mainly the distribution (i.e. alignment and μ ratio heterogeneity) and uncertainty (i.e. ellipses data points) of the U-Pb analyses. On these diagrams, U mobility will appear as a subhorizontal shift of the data-points to the right reflecting U gain (apparently younger age) and to the left reflecting loss of U (apparently older age).

Here follow the discussion regarding the most common processes affecting carbonates after deposition. Specific focus is given to neomorphism by stabilization and replacement, and cementation.

Stabilization is a form of neomorphism associated with the metastability of mineral polymorphs (e.g. aragonite, high magnesium calcite) that are 'stabilized' into more stable phases (low magnesium calcite, LMC) preserving most textural features. It is considered a combination of slow and coeval dissolution-precipitation processes that usually occur at any times after deposition (e.g. Frisia et al., 2002, De Boever et al., 2017). The behaviour of U-Pb elements as well as the impact on the U-Pb age during stabilization is still a matter of debate (Morrison & Brand, 1988; Chung & Swart, 1990; Smith et al., 1994; Jones et al., 1995; Kelly et al., 2003; Li et al., 2014; Hansman et al., 2018). It is well accepted that age obtained from an inverted LMC represents the timing of stabilization (e.g. Li et al., 2014) because stabilization causes precipitation of a 'new' more stable carbonate phase (i.e. isotope system reset). Results from Jones et al. (1995) and Kelly et al. (2003) that suggest during stabilization an important U-loss occurrs due to the higher solubility of U, in particular in oxidizing environments (Chung & Swart, 1990; Smith et al., 1994; Lachniet et al., 2012 Li et al., 2014). Regarding the behaviour of Pb, it can be inherited (Morrison & Brand, 1988) or lost (Smith et al., 1994) during stabilization.

Based on these findings, it is expected that: 1) if stabilization occurred during or shortly after deposition the age of the inverted carbonate should faithfully represent the timing of deposition (within uncertainties); 2) stabilized carbonates lose part of their U with consequent reduction of the initial dating potential (i.e. dating potential is higher when U is high and heterogeneously distributed into the sample); and 3) the presence of carbonates with slightly different ages (due to the slow process of stabilization) may induce a scatter of the U-Pb data points in the TW Concordia diagram with consequent lower age precision.

In the framework of the Yacoraite Fm., a possible example is given by the ooids from sample UJ62a (located at 135m from the base of the Juramento stratigraphic section; Fig. 26). These ooids preserve their pristine petrographic features (Fig. 47), show slightly lower $\delta^{18}O$ values (0.9‰ against 2‰ of the adjacent samples; Fig. 42A) and produced an appreciably younger age (Fig. 47). These features agree with a stabilization process that involved this sample around 3-4 Ma after deposition. In the TW Concordia diagram of sample UJ62a, the isotope ratio data points have higher uncertainty (i.e. bigger ellipses) and are slightly scattered and shifted toward lower values (possible U-loss) if compared to those of preserved ooids (Fig. 47A). The U/Pb ratio values are more homogeneous (U/Pb < 18 vs < 35 in preserved ooids) and common Pb fraction is higher (Pb/Pb > 0.68 vs > 54 in preserved ooids). This specific U-Pb isotope composition may possibly describe the impact of a process of stabilization.

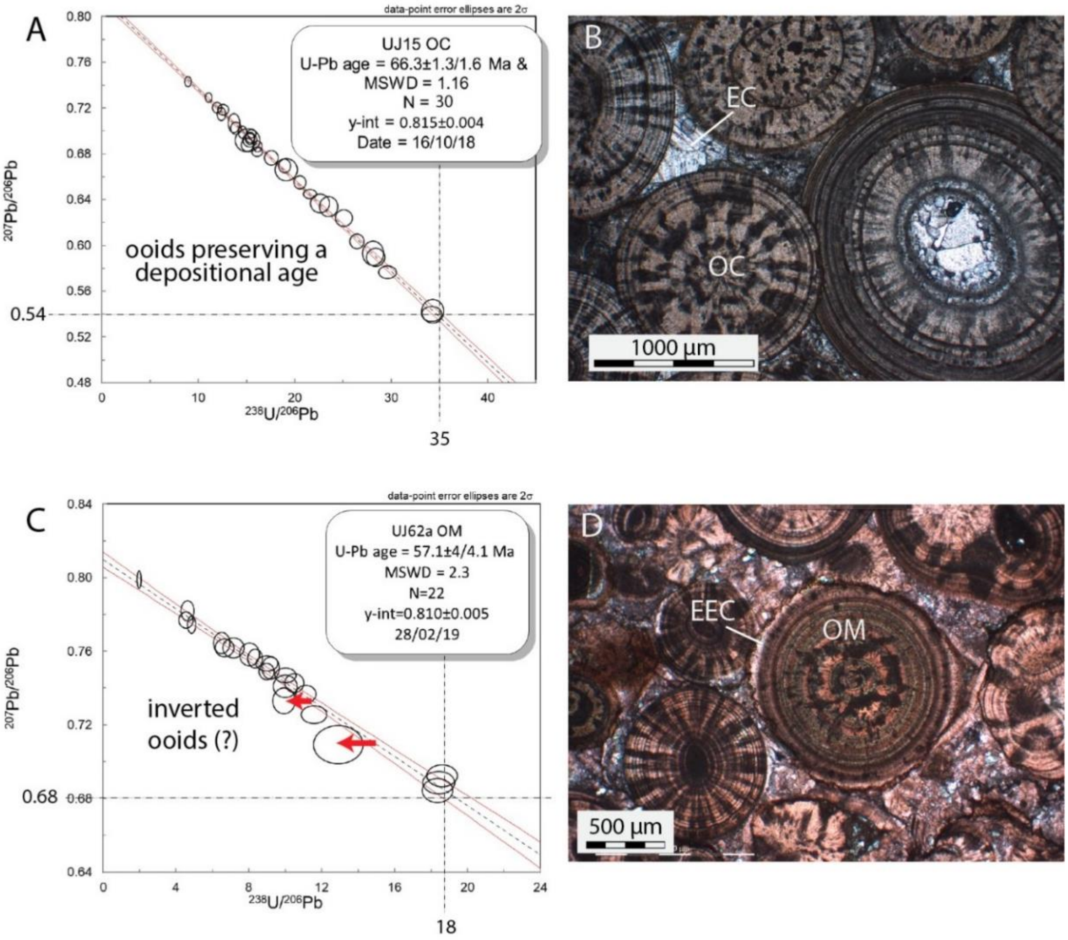

Figure 47 Tera-Wasserburg Concordia diagrams and petrographic images of preserved ooids and in ooids affected by fabric preserving diagenesis (stabilization?). The red arrows indicate possible U-loss. OM= mixed ooids, OC= calcitic ooids, EEC= early lacustrine fibrous aragonite/HMC cement, EC=early lacustrine blocky calcite cement.

Replacement. Neomorphic replacement refers to a complete dissolution and very fast crystallization which cause a reset of the chemical composition and usually a textural change (i.e. increased crystals size with mosaic fabric, sweeping extinction). The fast geochemical reset suggests that replaced carbonates reliably inform on the timing of the replacement. Results from Kelly et al. (2003) demonstrate that replacement may also allow partial retention of U in the newly formed carbonate with a possible U-loss, similar to what described for the stabilization process. In lacustrine settings common replacement processes during early diagenesis are dolomitization and silicification which are both associated to microbial activity and OM degradation by sulphate reduction (De Boever et al., 2017).

The impact of early diagenetic mimic dolomitization on the pristine U-Pb composition was observed in the framework of the Yacoraite Fm.

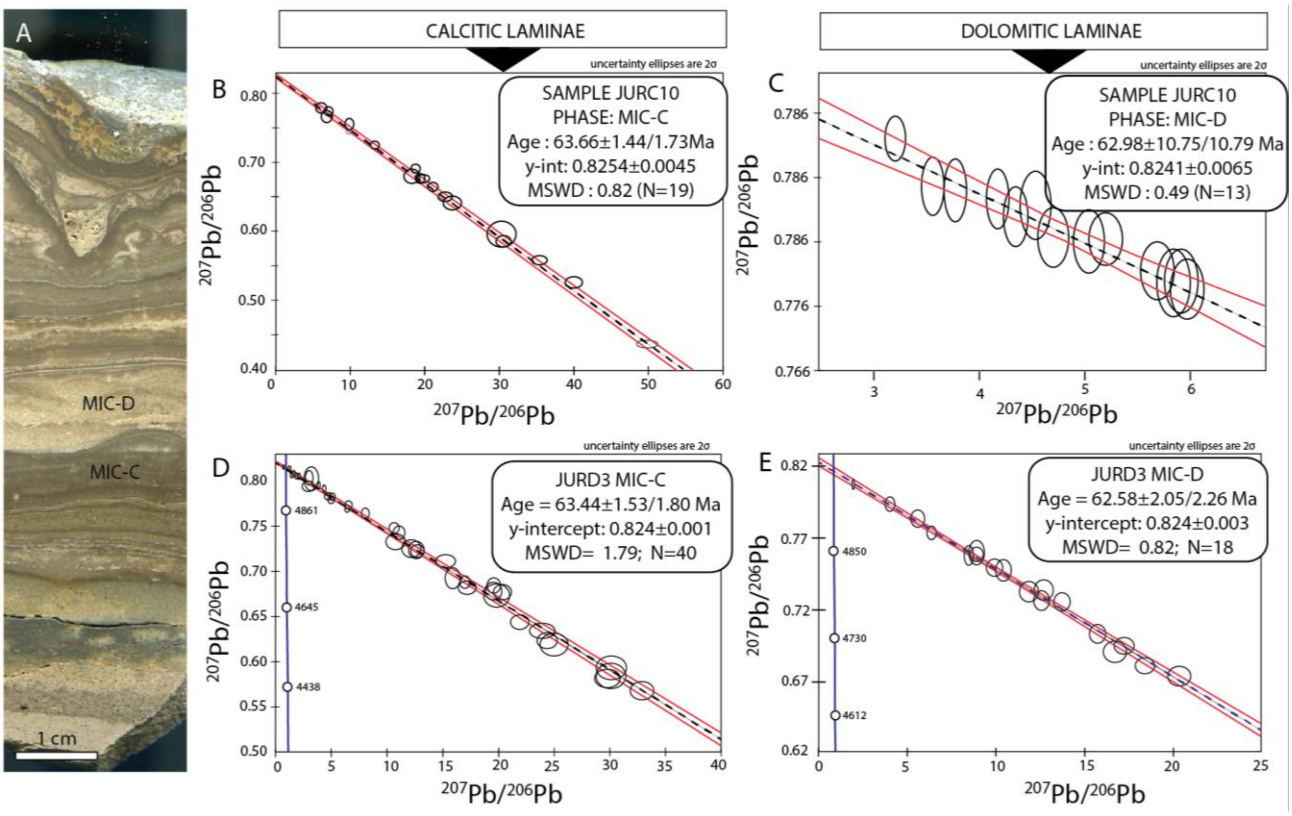

Figure 48. Mesoscopic image and Tera-Wasserburg Concordia diagrams of JURC10 and JURD3 microbial boundstone samples from the Juramento stratigraphic section. A) Laminated fine-grained stromatolite displaying an alternation of calcitic (dark areas, MIC-C) and dolomitic (beige areas, MIC-D) laminae. JURC10, rock-slab scan. B,C,D,E) Calcitic and dolomitic laminae show consistent depositional U-Pb ages that agree with the MDA depth model from Montano et al. (in revision, Chapter 6.1). Dolomite is characterized by lower spread of U-Pb isotope ratio and lower U concentration.

Figure 48 shows the TW Concordia diagrams of two microbial samples providing depositional ages. Dolomitic laminae are usually characterized by lower spread of the U-Pb isotope ratios if compared to calcitic phases as well as lower U concentration (Chapter 7.3). In many samples this hindered to produce an age. The lower spread of U-Pb isotope ratios may be due to U-loss during dolomitization. Another possible explanation is that dolomite is also less prone to incorporate U if compared to calcite. Further discussion about the topic is in Chapter 7.4.

Cementation (i.e. precipitation and growth of crystals in pores of an existing fabric decreasing porosity; Flügel, 2004) is not believe to cause any geochemical reset, although small cements in the interparticle pores (e.g. in microbial carbonates) may alter the bulk composition of the carbonate that would appear as partially overprinted. In a TW Concordia diagram this would results in a scatter of

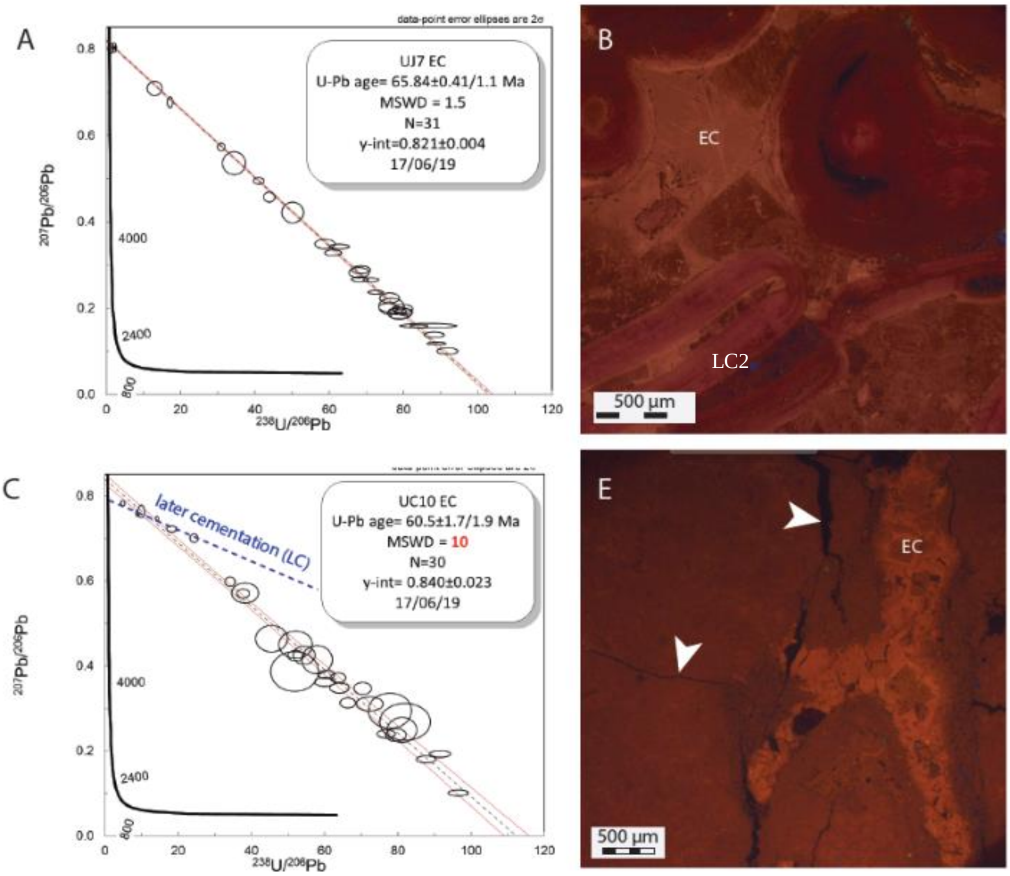

Figure 49. Tera Wasserburg Concordia diagrams and cathodoluminescence petrographic images of the early calcite cement EC. In sample UJ7 EC is characterized by precise data points (small ellipses) well aligned along the regression line. The age obtained is precise ($2\sigma_i = 0.6\%$) and MSWD is < 2.5. All these factors suggest that this age could reliably inform on the depositional age of the system. C) The cement EC in sample UC10 shows scattered U-Pb isotope composition. Ellipses data points are big indicating heterogeneity in the ablation spot. It is also possible to recognize a secondary alignment fairly associated to a younger event (blue dotted line).

data point and consequent lower age precision (Fig. 49). Cements are also important witnesses of high temperatures and chemical changes during burial. The occurrence of burial cements has to be a wakeup call. Indeed, lab experiments already demonstrate that high temperatures during burial diagenesis promote U and Pb mobility (Roberts et al., 2021) and deep buried carbonates more favourable lose their pristine isotope composition. This is the reason why it is highly encouraged to select for chronostratigraphic studies based on LAcarb, only geologic areas which are not affected by high T deep burial diagenesis. (ndf. This do not imply that deep buried carbonates can never be used as proxies for the pristine composition, as demonstrated by depositional ages obtained by Meinhold et al. (2020) from preserved Ediacaran spherulites.)

Other factors affecting the pristine isotope composition during diagenesis. A specific focus has to be given to the changes in redox conditions occurring during diagenesis. Oxidizing conditions promote the mobilisation of U as U^{+6} because it is very soluble. This leads to higher U loss during fluid-mineral interaction in oxidized systems. Conversely, in reducing conditions the reduced U^{+4} has lower solubility if compared to U^{+6}. Thus it can be hypothesized that diagenetic modifications in reducing environments may be favourable for the retention of U and limit U-loss. Diagenesis affects carbonates according to various factors: mineralogy (i.e. stability of pristine mineralogy), grain size (i.e. small particles such as micrite particle dissolve more rapidly than large grains) and porosity (i.e. higher permeability for later fluids). For this reason, some carbonates are more prone to be recrystallized and lose their pristine composition. Another factor to consider is the occurrence of meteoric diagenesis. Indeed, meteoric waters are known to preferentially leach U during their infiltration thus causing preferential disturbance of the U-Pb isotope ratio and dating potential (Rasbury & Cole, 2009). Samples from the last metres of the Juramento stratigraphic section provided mostly errorochron dates or very imprecise ages (Fig. 46). This may be caused by the infiltration of meteoric waters in correspondence with a major emersion event at the top of the Yacoraite Fm. (Chapter 6.2).

Focus on high common Pb composition. According to Roberts et al. (2021) this type of configuration could have evolved from a pristine geochemical composition characterized by high Pb (i.e. natural low dating potential) or it could be due to common Pb addition during diagenesis. As a general principle diagenesis is known to affect more U composition rather than Pb composition (Roberts et al., 2021) because at environmental temperatures U is highly soluble and tends to be mobilized inducing a U loss (or more rarely an addition). Pb is usually insoluble and tends to remain in the solid system and diagenetic fluids can be highly enriched in Pb resulting in possibly high common Pb composition in diagenetically disturbed samples.

In the framework of the Yacoraite Fm. around 33% of the carbonates analysed exhibits a lack of spread in U/Pb ratios and the composition is dominated by common Pb ($^{238}U/^{206}Pb < 2$; $^{207}Pb/^{206}Pb > 0.75$; Fig. 34) hindering to establish a robust regression line (Fig. 36A) (Fig. 36). Samples characterized by this isotope composition were carefully re-analysed for petrography and geochemistry that did not highlight differences with preserved carbonates. This suggest that the high common Pb composition may be pristine or further Pb was possibly added during syn-depositional/ early diagenetic stabilization as demonstrated for sample UJ78 which is affected by silicification (Fig. 50).

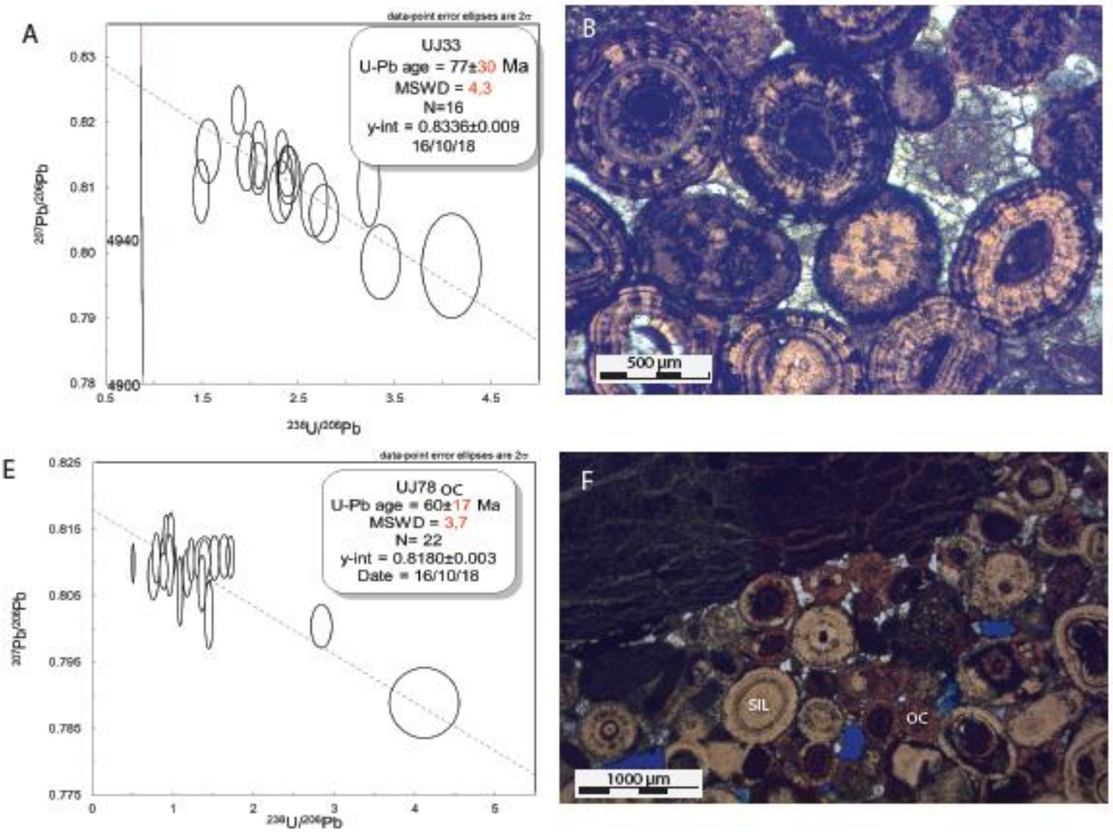

Figure 50 Tera Wasserburg Concordia diagrams and petrographic images of calcitic ooids (OC) and microbialites (MIC-C) presenting very high common Pb (Pb/Pb>0.7,0.8) and low spread of U/Pb isotope ratio (<4.5). Data points are scattered and/or have big uncertainty. Resulting ages are imprecise and unreliable (MSWD >3). In sample UJ33 petrographic analysis do not show evidence of diagenetic overprint whereas sample UJ78 is strongly affected by silicification (SIL). Black arrow indicates the subhorizontal trend-line of data points due to a possible U gain.

This study highlights that LAcarb, together with a careful petrographic and geochemical analyses, may be considered as an additional tool to detect diagenetic modifications in carbonates. Carbonates with very precise ages, well spread U-Pb isotope ratio and low common Pb should most possibly preserve their pristine composition. This implication of LAcarb may be relevant for paleoclimate studies requiring to target samples preserving the pristine geochemical composition. According to the results of this study, LAcarb may not be an ideal ‘diagenesis detector’ only when carbonates are characterized by very homogeneous/high common Pb composition. The perspective about the use of LAcarb as a ‘diagenesis detector’ is introduced in Chapter 9.2.

7.3 Success rate and time resolution of LAcarb

In this Chapter, a statistical analysis has been done along the Juramento stratigraphic section. The Yacoraite Fm. is here considered a 'lacustrine test case' to understand the general success rate and time resolution of LAcarb technique in lacustrine settings. Success rate of LAcarb and the uncertainty distribution were observed for the total dataset (i.e. general dating potential) and according to the mineralogy (i.e. calcite and dolomite) and carbonate types (i.e. microbialite, ooids and lacustrine cement). Phases considered are calcitic and dolomitic ooid (OC and OD), calcitic and dolomitic microbialite (MIC-C and MIC-D), dolomitic oncoids (OND) and lacustrine calcitic cement (EC). This study is based on 80 carbonate phases selected because they do not show major evidence of burial diagenetic modifications (samples discussed Chapters 7.1 and 7.2). In this respect, it is worth mentioning that this statistical analysis is influenced by the diagenetic overprint (early and late) on the carbonate analysed. Depositional systems which are strongly affected by later fluid migrations may provide lower success rate and time resolution. As a consequence, specific attention is given to the diagenetic processes that may have affected each carbonate type or mineralogy analysed.

General dating potential. Data indicate that 62% of the carbonates analysed (50 over 80 phases) were characterized by isotope composition suitable for dating (Fig. 51A). Indeed, the ages obtained were well regressed and associated with MSWD < 2.5 (except 4 samples; Fig. 51B). The 54% of them (43 over 80 phases) produced ages consistent with the depositional age of the system as known from zircon geochronology and 8% (7 over 80 phases) resulted younger or older (Fig. 51A). The remaining samples (30 phases, 38%) are either undatable (high common Pb composition Pb/Pb > 0.75-0.8, U/Pb < 2-4, high data scatter; Fig. 37 and 38) or errorochron dates (MSWD > 11, uncertainty >20%; Fig. 51A).

This indicates that the general dating success for chronostratigraphic studies is of about 54%. The uncertainty distribution ($2\sigma_{exp}$) analysis (Fig. 51C) indicate that 38% of carbonate phases analysed (30 phases) are associated with uncertainty between 1.7 and 4%, thus perfectly suitable for chronostratigraphic studies. In the need of a higher precision (e.g. paleoclimate studies), it is worth mentioning that only 13 among the 80 carbonate phases analysed (16%), showed a robust depositional age with uncertainty below 2% (Fig. 51C). This is in agreement with the known time resolution of the method (e.g. Montano et al., 2021 in Chapter 4.1; Montano et al. in revision in Chapter 6.1 and Roberts et al., 2021).

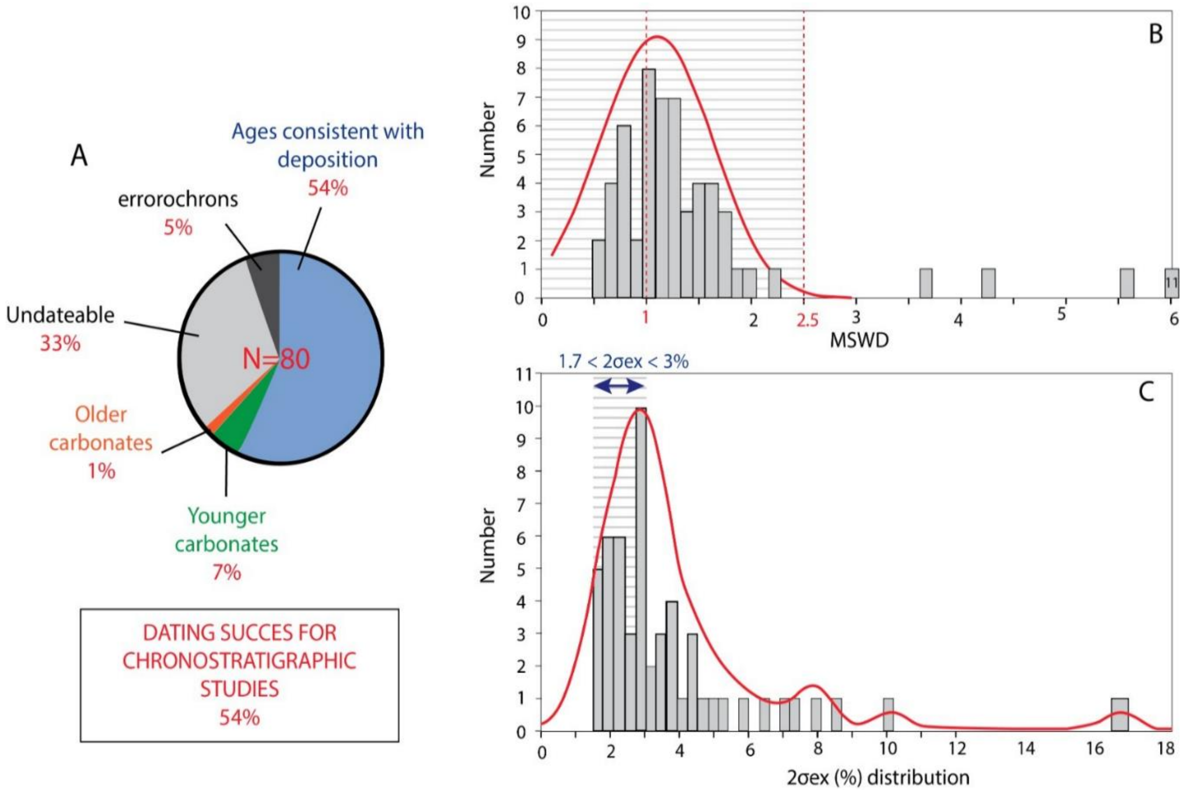

Figure 51 Statistical analysis for the general dating potential of LAcarb for chronostratigraphic studies. The study was achieved along the Juramento stratigraphic section based on 80 carbonate phases analysed. A) Pie chart showing the percentage of carbonates providing ages consistent, younger and older than the MDA depth model (Montano et al., in revision, Chapter 6.1). Undatable carbonates are characterized by homogeneous and high common Pb composition (Pb/Pb>0.7-0.8) and low spread of U/Pb isotope ratios that hindered to obtained a U-Pb age. This composition is considered pristine in most samples (see section 7.2), Errorochrons are dates associated with uncertainty > 15% and MSWD>>2.5 suggesting diagenetic overprint. B) Density distribution plot (50bins) of the MSWDs from the ages obtained. C) Density distribution plot (50 bins) of the associated expanded uncertainties. Most carbonates have uncertainty between 1.7 and 3% thus suitable for chronostratigraphic studies. Density distribution plots were obtained via Isoplot 4 software.

Mineralogy. Calcitic phases (calcitic microbialite, ooids, and early cements; N=52) and dolomitic phases (dolomitic microbialite, ooids and oncoids; N=12) provided the same dating success, 57% and 58%, respectively, although ages obtained from dolomitic phases were less precise (Fig. 53) since the samples are usually characterized by a lower spread of their U/Pb isotope ratios (Fig. 52B). In contrast, mixed dolomite/calcite phases are associated with the lowest success rate (33%) and highest average uncertainty, between 5 and 9% (Fig. 53). The reason for the lower dating potential of dolomitic and mixed phases was discussed by Elisha et al. (2020) that dated various types of dolomites highlighting a strong sub-millimetre scale heterogeneity of calcite and dolomitic microcrystals. This lower dating potential may be due to: (1) the instability of dolomite that is prone to be subjected to multistep neomorphic processes after its first nucleation (Elisha et al., 2020); (2) the effects of mimic dolomitization discussed in Chapter 7.2; and (3) sequestration of lower amounts of U due to a mineralogical control on the incorporation of U (e.g. Rasbury et al., 2021). Thus, in the need of accurate and precise ages, calcitic phases should be preferentially targeted for LAcarb studies.

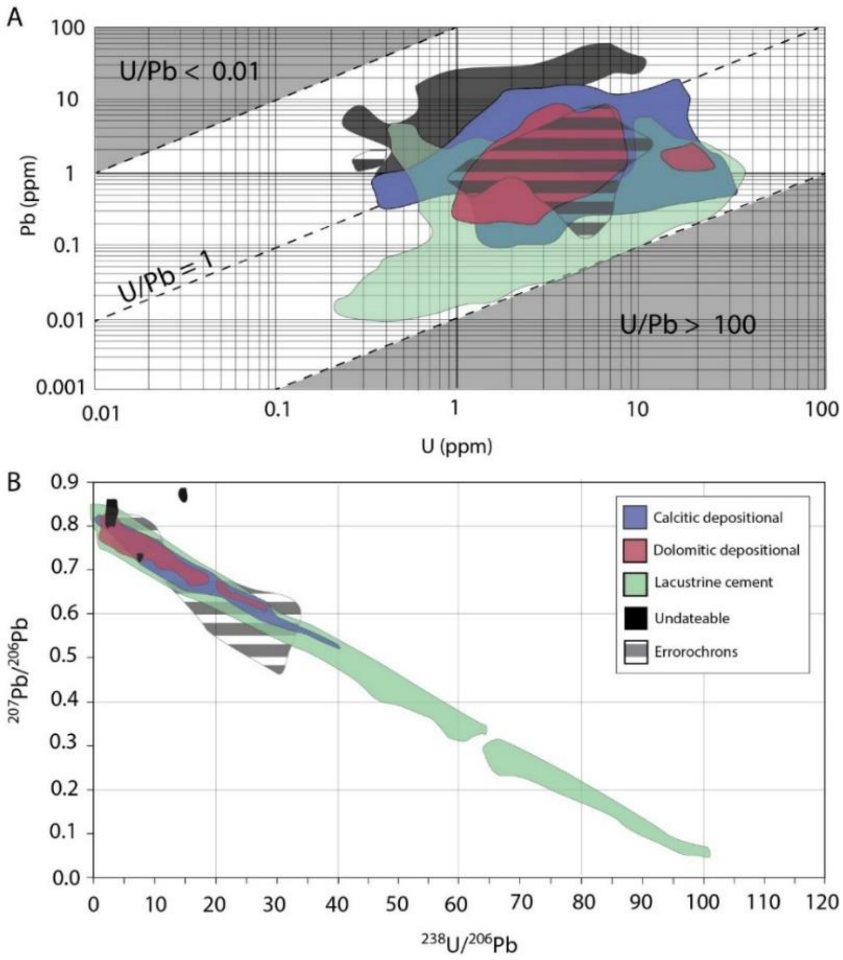

Figure 52 U and Pb geochemistry for the carbonate phases analysed A) Cross-plot of Uranium (U) versus Lead (Pb) concentrations expressed in parts per million (ppm). The carbonate U and Pb composition is included between the dashed lines (0.01 <U/Pb <100). B) Cross-plot of ^{238}U/^{206}Pb versus ^{207}Pb/^{206}Pb ratios. Calcitic depositional carbonates (blue area) include calcitic microbialite (MIC-C) and calcitic ooids (OC). Dolomitic depositional carbonates (red area) include dolomitic and mixed microbialite (MID-D and MIC-M), dolomitic and mixed ooids (OD and OM) and dolomitic oncoids (OND). Undatable phases (black area) are carbonate phases where a robust regression line could not be established due to very low U/Pb isotope ratio variability. Errorochrons (barred area) are dates with poor statistics (MSWD > 11, uncertainty >20%).

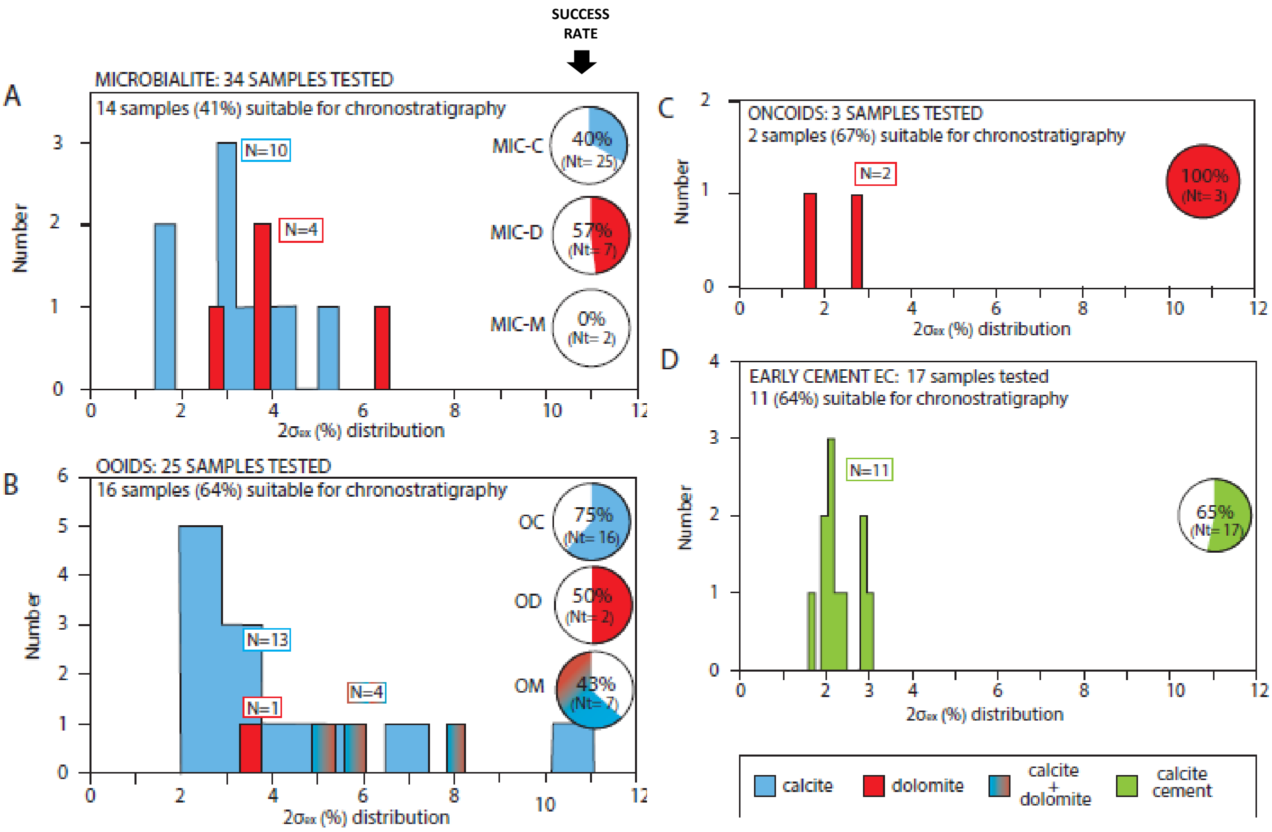

Figure 53 Success rate for chronostratigraphic studies and uncertainty distribution of the different carbonate phases and relative mineralogies from the Juramento section. Pie charts represent the dating success of for each mineralogy if compared to the total number of carbonate samples analysed (Nt). N is the number of carbonate phases with age consistent with the MDA depth model (Montano et al., in revision, Chapter 6.1).

Carbonate type. Microbialites (N=34), ooids (N=25), oncoids (N=3) and lacustrine cements (N=16) provided a dating success rate for chronostratigraphic studies of 41, 64, 67 and 64% (Fig. 53). These percentages are biased by the fact that the different carbonate phases are not represented by the same numerical population, especially the oncoids whose dating potential will not be discussed (only 3 oncoid rudstone samples dated). Microbialites provided the lowest success rate (41%). Concerning the age precision, all carbonate types provided some accurate ages with precision below 3-4%, although microbialite and ooids statistically produced less precise ages with uncertainties up to 6-8% (Fig. 53). By considering the mutual importance of dating success and age precision in the dating potential, microbialite is the carbonate type that provided in average less precise and accurate ages. In contrast, 60% of calcite cement EC analysed provided depositional ages with precision always below 3%. Indeed, EC cements results to be the carbonate phase with the highest dating potential for chronostratigraphic studies. The dating potential of the different carbonate phases analysed is here discussed in light of their U-Pb composition and diagenetic features.

Microbialite. Microbialites showed U concentrations of 0.4-40 ppm consistent with those from the early lacustrine calcite EC (0.2-40 ppm) that provided the highest dating potential. However, Pb concentration is higher (up to 20 ppm against 5 ppm of EC cement). Concerning the U-Pb isotope ratios, microbialites provided $^{207}Pb/^{206}Pb$ ratio > 0.5 (high common Pb composition; Fig. 54) and U/Pb isotope ratio up to 40-50, which is 50% lower than the maximum U/Pb isotope ratio values of EC cement (Fig. 54). This specific U-Pb composition suggests that the lower dating potential of microbialites may be due to the high Pb concentration. What may have caused the incorporation of high amounts of Pb in microbialites? Microbialites are organo-mineralized carbonate rocks whose precipitation is induced and/or influenced by microbial communities (mainly filamentous cyanobacteria) enveloped by an organic extracellular polymeric substance (EPS, Decho, 1990) and organized in microbial mats (e.g. Suarez-Gonzales et al., 2019). Cyanobacteria EPS traps detrital material (e.g. quartz grains, clay minerals) possibly causing an enrichment in detrital Pb (or common Pb). This is evident in the microbialites from the Yacoraite Fm. that are characterized by the occurrence of frequent interlayered clays and quartz grains (Gomes et al., 2020).

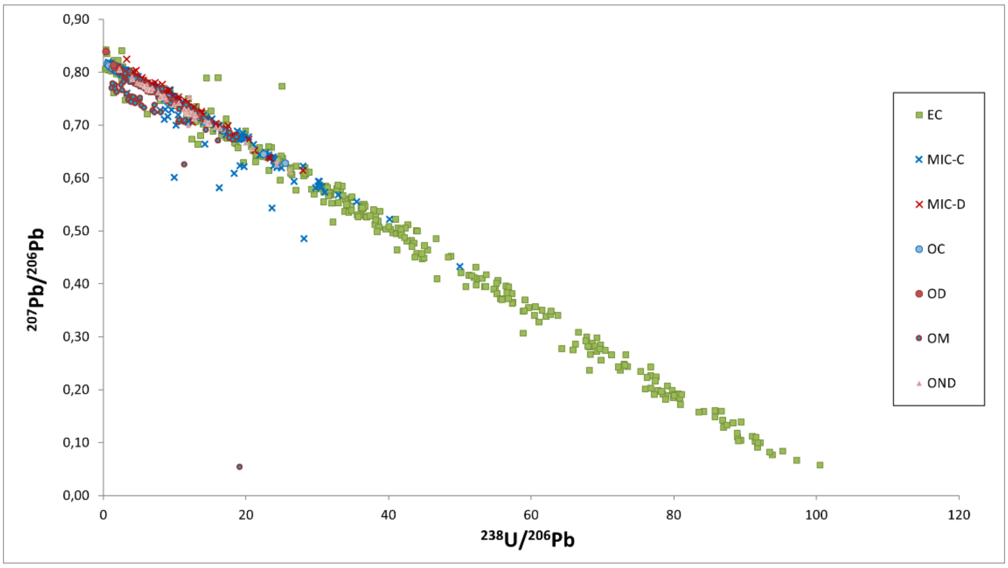

Figure 54. Cross-plot of $^{238}U/^{206}Pb$ versus $^{207}Pb/^{206}Pb$ ratios of the carbonate analysed according to carbonate type (symbol) and mineralogy (colour).

Roberts et al. (2020a) suggests that the low dating potential of microbialites is mainly promoted by neomorphic processes. Indeed, microbialites are highly porous (e.g. 20% porosity, Hargrave et al., 2014) and are formed from low-density carbonate, more susceptible to chemical leaching and U-Pb mobilization during neomorphism. In the framework of the Yacoraite Fm. it is not possible to exclude the impact of neomorphic processes in the low dating success (around 60% of microbialites are undatable) because petrographic analysis detected neomorphic features such as syn-depositional mimic dolomitization and early diagenetic dissolution (dissolution 1) (Chapter 7.1 and 7.2).

Microbial carbonates were also analysed in the framework of the Ries Crater basin (Montano et al., 2021, Chapter 4.1) were they showed a very high dating success rate and provided the most accurate assessment of the depositional age of the system, with precision down to 1.3% (2σ). The U and Pb concentrations in the Ries Crater microbial carbonates are similar with those from the Yacoraite Fm. but the Ries Crater microbialites showed a higher radiogenic proportion of Pb (^{207}Pb/^{206}Pb down to 0.1 against 0.5 of the Yacoraite Fm.) suggesting that initial U was higher and common Pb was lower. This specific isotope composition could have been boosted by the high alkalinity of the Ries Crater lacustrine waters (Arp et al., 2013). Indeed, alkalinity is known to promote the incorporation of actinides in carbonates (e.g. Simpson et al., 1982). This was discussed by Cole et al. (2004, 2005) and Rasbury & Cole (2009) for the microbial/tufa mounds of the lacustrine Barstow Fm. (Miocene).

Ooids. Ooids form via organomineralization through biologically induced and influenced mechanisms (e.g. Harris et al., 2019). This suggests that the low dating potential of ooids may be due to the same processes previously described for microbialites. In the framework of the Yacoraite Fm. the U/Pb isotope ratio values of ooids (<15-20, Fig. 54) are less heterogeneous if compared with those from microbialites (<40-50; Fig. 54) and EC blocky calcite cement (<100; Fig. 54). Petrographic analysis also highlighted the presence of quartz grains and clay layers within their cortex (Fig. 43). These features suggest that the low dating potential of microbialites may be possibly due to high initial Pb, as discussed for microbialites (Fig. 55).

However, the low precision of some ages obtained, in particular from ooids with mixed calcitic/dolomitic mineralogy or with dissolution evidence, may be also related to processes of dissolution and neomorphism. The fibrous radial structure of ooids, still visible in most samples (Fig. 29) suggest an aragonite (or HMC) precursor. Aragonite/HMC dissolution and stabilization (Chung & Swart, 1990; Reeder et al., 2001; Kelly et al., 2003) together with the mimic dolomitization (Elisha et al., 2020 and Chapter 7.2) could have possibly induce a disturbance of the pristine U-Pb isotope composition of ooids (Fig. 55).

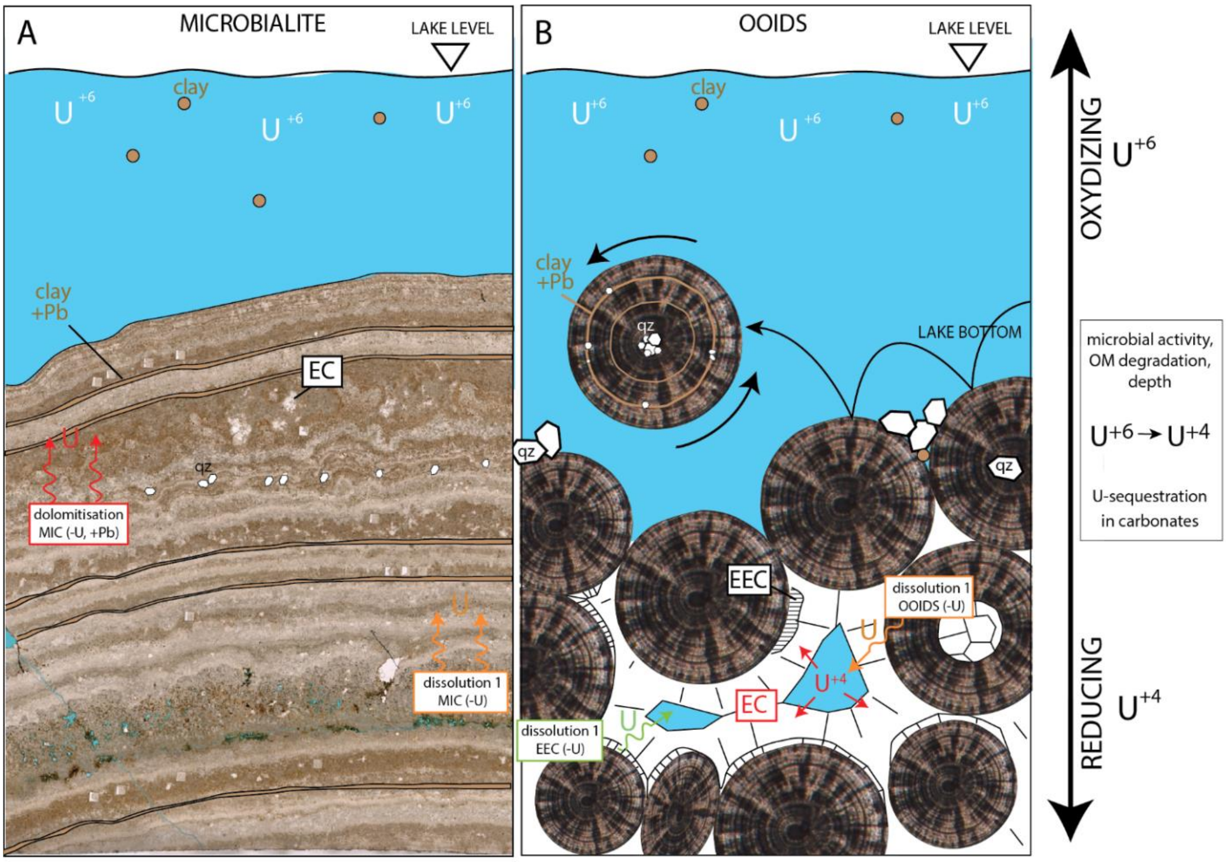

Figure 55. Simplified schematic depositional and diagenetic processes for the incorporation of U and Pb in microbialite (A), ooids (B) and early lacustrine cement (B) in the Yacoraite Fm. Microbialite and ooids incorporate clay particles and quartz crystals during their formation. Reducing conditions increase according to depth, microbial activity and organic matter (OM) degradation. In addition, microbialite and ooids were affected by syn-depositional (e.g. mimic dolomitisation) to early diagenetic (e.g. dissolution) processes. The low dating potential of these carbonate types is thus an interplay of both depositional mechanisms and syn-depositional to early diagenetic processes.

Lacustrine cement. The blocky calcite cement EC provided the highest dating potential in terms of success rate and precision. EC is characterized by a very favourable U-Pb elemental and isotope composition which is the reason for the high dating potential: U is heterogeneously distributed with concentrations between 0.01 and 34 ppm whereas Pb concentration is low, between 0.001 and 10ppm (Fig. 52). Pb composition has a high radiogenic proportion (Pb/Pb < 0.5) with values included between 0.06 and 0.84 and U/Pb ratio well spread between 0 and 100 (Fig. 52). Indeed, in contrast with all depositional phases, EC preferentially rejected Pb and incorporated huge amounts of U.

There are several factors that could have promoted such specific U-Pb composition (Fig. 55).

EC blocky calcite was interpreted as an early shallow burial cements precipitated in the interparticle pores within the sediment (Chapter 7.1). Here the reducing conditions are higher due to lower connection with the oxidized lacustrine waters from the surface. Moreover, degradation of organic matter and microbial activity usually cause increased reducing conditions. As previously explained (see Chapter 7.2) reducing conditions promote the incorporation of U in carbonates because the reduced specie of Uranium (U^{4+}) has a size more suitable to enter the carbonate crystal lattice (Shannon, 1976; McManus et al. 2006; Weyer et al., 2008, Cumberland et al., 2016).

A second reason for the high U concentration may reside in the timing of this cementation event. Paragenetic analysis suggest that EC precipitated coevally or right after an early dissolution event (Dissolution 1, Fig. 45). Dissolution involved some gastropods, ooids (especially the cores) and the isopachous fibrous cement EEC that was interpreted as an early lacustrine aragonitic/HMC cement (EEC). Since U is soluble, it tends to be lost during dissolution/stabilization. Thus, it is fairly possible that EC precipitated from a fluid enriched in U derived from the dissolution of other carbonate phases. A third consideration is the petrographic and geochemical preservation of EC cement. This is due to its stable mineralogy and low reactive surface area (if compared with microbialite).

All these factors (reducing conditions, precipitation coeval/right after a dissolution event and petrographic/geochemical preservation) potentially promoted the high dating potential of the lacustrine blocky calcite EC.

In the framework of the Ries Crater basin, two early cements were also analysed, one vadose/pendant calcite and one lacustrine/fibrous isopachous calcite (Chapter 4.1). The vadose cement provided dating success and precision similar with those obtained from the EC blocky cement of the Yacoraite Fm., in agreement with the high dating potential previously demonstrated for cements formed from mixed meteoric/lacustrine waters (e.g. Rasbury & Cole, 2009, Woodhead & Petrus, 2019). The lacustrine fibrous cements, due to its pristine aragonitic/HMC mineralogy was extensively affected by dissolution and usually provided very imprecise ages and general low dating potential.

In conclusion, results from this study highlight that the estimation of the dating potential for the different carbonate types to be dated via LAcarb has to be considered in light of the mechanisms for the carbonate formation (i.e. organomineralization or chemical precipitation), petrographic features (i.e. habitus, texture, reactive surface area) and mineralogy (i.e. stable vs unstable pristine mineralogy).

8 STRATEGIES TO BUILT A DEPOSITIONAL AGE MODEL

8.1 MIDA depth model: full dataset (Juramento section)

The consistency between MDA and MIDA depth models (Montano et al., in revision, Chapter 6.1) showed that it is possible to use LAcarb to build accurate depositional age depth model for chronostratigraphic and palaeoenvironmental studies.

In this chapter, a second minimum depositional age depth model (MIDAfull; Fig. 56) was built based on the full dataset of the Juramento stratigraphic section (Chapter 7.1). A total number of 43 ages were linearly interpolated following the approach proposed in Montano et al. (in revision, Chapter 6.1). Noteworthy, in this case weighted average ages were produced from carbonate phases belonging to the same sample or from samples located at a stratigraphic distance of maximum ±2 m, this adding an uncertainty expressed in metres in the vertical axis (i.e. stratigraphic height; Fig. 56). This approach implies the assumption that no major sedimentary hiatuses occurred in the ±2 m intervals considered. Thus, a sedimentological analysis was achieved to limit the bias due to this assumption.

The sedimentation rates and sequence boundaries age constraints obtained by zircon geochronology (MDA depth model, Montano et al., in revision Chapter 6.1) have been compared with those obtained by LAcarb in Montano et al. (in revision, Chapter 6.1) (MIDApart, 19 ages) and by considering the full dataset of the Yacoraite Fm. (this chapter, 43 ages, MIDAfull) (Fig. 43). The sedimentation rate dynamics described by the three datasets are consistent and underline a similar peak of sedimentation rates around SB3 (Figures 56B and 57). Sequence boundary ages derived by the 3 models also agree within uncertainties (Fig. 57). MIDA models provided ages which are in average 0.5 Ma younger compared with those from zircon geochronology. This is in agreement with the principle of ‘minimum depositional age’ explained in Montano et al. (in revision, Chapter 6.1). Concerning the method time resolution, the precision reached by the 3 models (calculated over the uncertainties of the SB ages) is ~ 2.0 to 2.6 % (MIDApart), 1.5 to 2% (MIDAfull) and 0.9-1.4% (MDA).

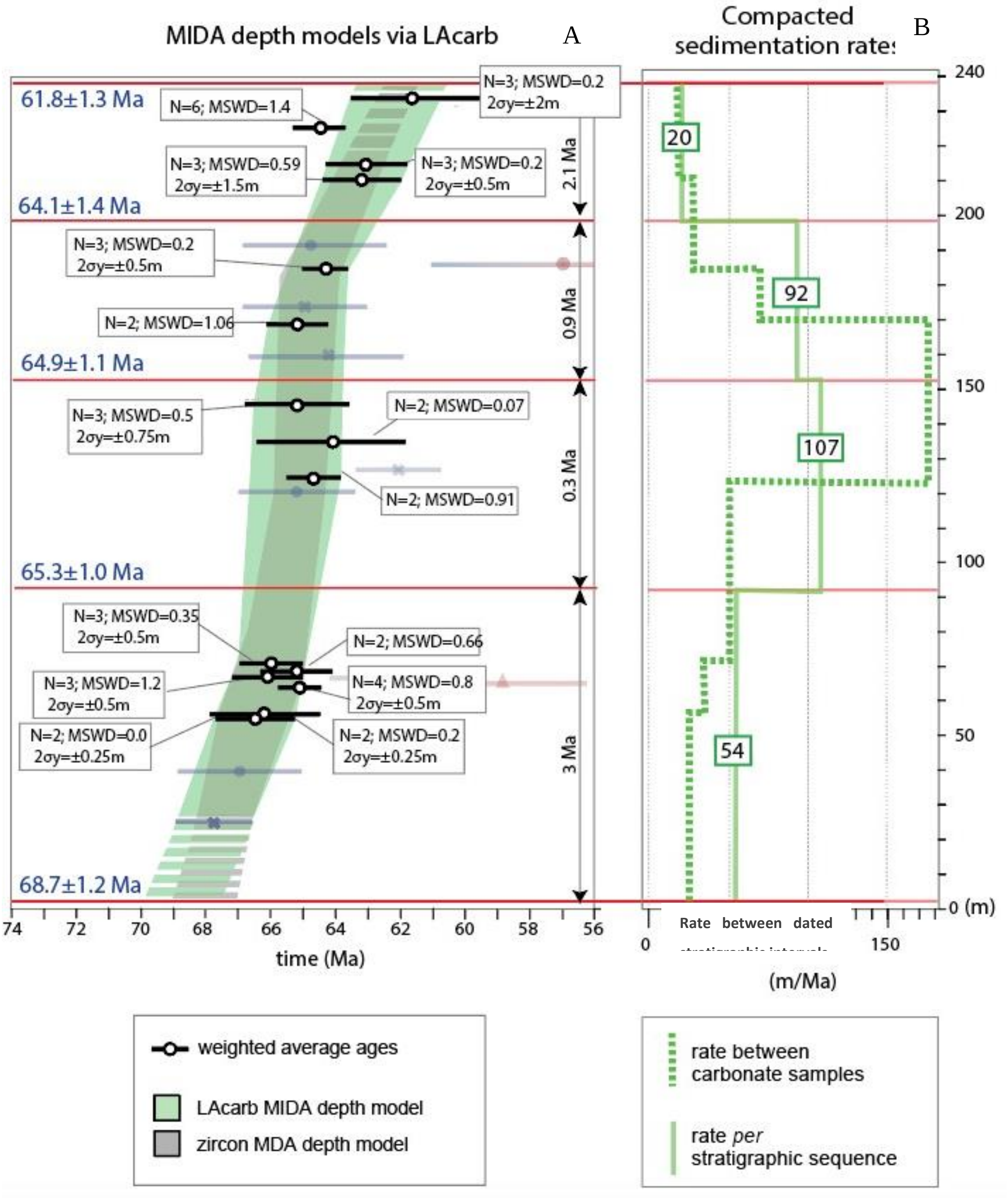

Figure 56 Minimum depositional age (MIDA) depth model of the Yacoraite Fm. via LAcarb based on the full dataset. A) Weighted average ages of carbonate phases located at a stratigraphic distance < ±2 m are reported in black. Frames include the number of single MIDA considered (N) and the Mean Squared Weighted Deviates (MSWD) of the weighted average ages. Shaded ages are younger or could not be averaged due to the distance from other dated samples. The green and grey areas represent the MIDA (full dataset model) and MDA depth models (Montano et al., in revision, Chapter 6.1). Red lines are the sequence boundaries (SB) and their ages (in blue) were estimated via MIDA model. All uncertainties are 2σ (95% confidence). B) Evolution of the compacted sedimentation rates along the stratigraphic section.

Values obtained by MDA and MIDAfull are mostly consistent (Fig. 57) and suggest that LAcarb based chronostratigraphic studies should be achieved on a large set of samples (i.e. high-n sampling) to reach an accuracy and time resolution comparable with those from zircon geochronology. This is specifically important when high age precision is required, from example in paleoenvironmental and paleoclimate studies.

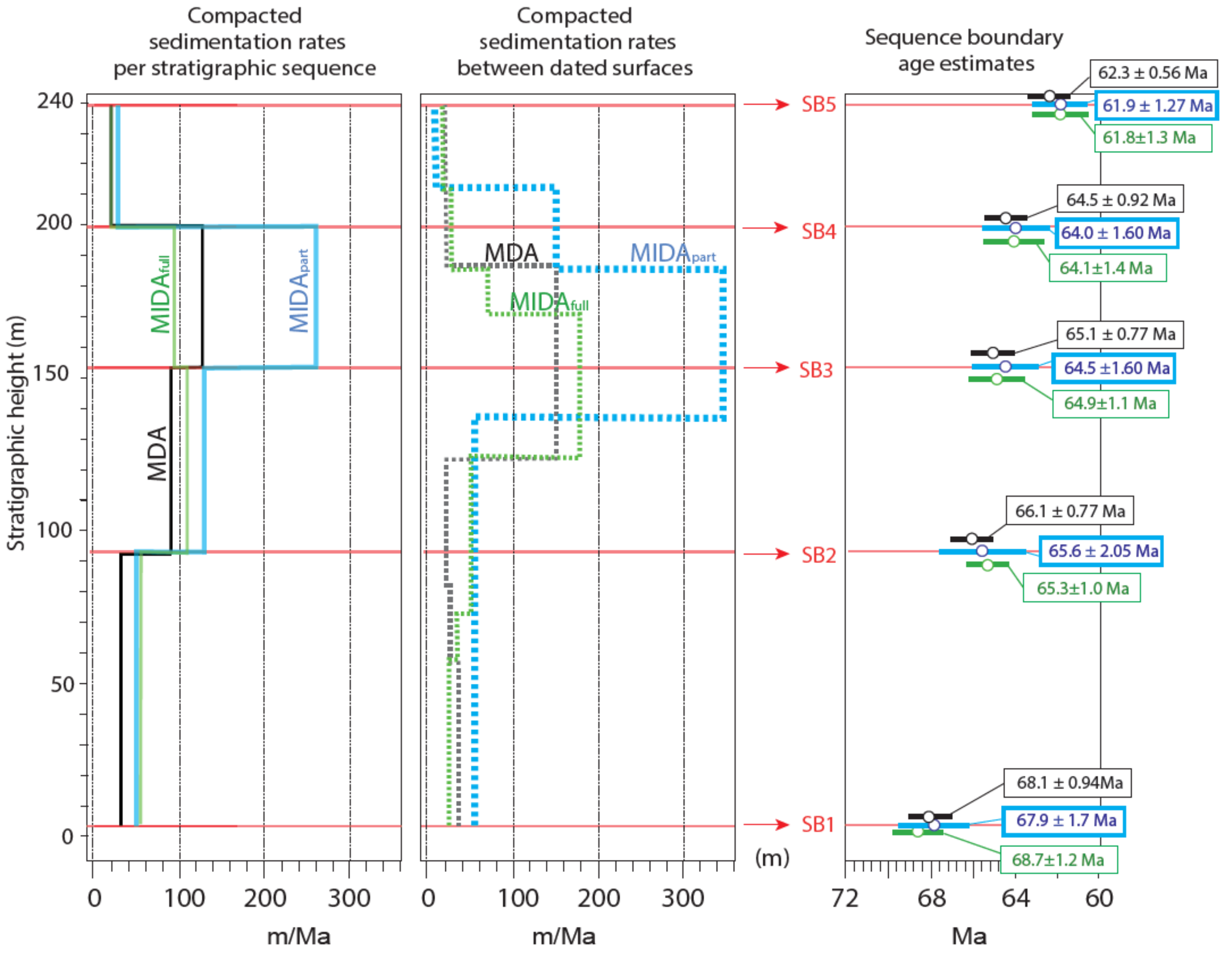

Figure 57 Comparison between depositional age depth models obtained by zircon geochronology (MDA depth model, black line) and by LAcarb considering the partial dataset (MIDApart, 19 ages, 1 LA session from Montano et al., in revision, chapter 6.1, blue line) and the full dataset (MIDAfull, 43 ages, 7 LA sessions, green line). Note that the SB age estimates do not overlap in the diagram to better show the age difference.

8.2 WORKFLOW FOR FUTURE STUDIES

Based on the results achieved in this PhD project, a workflow to build robust depositional age depth models is proposed (Fig. 58).

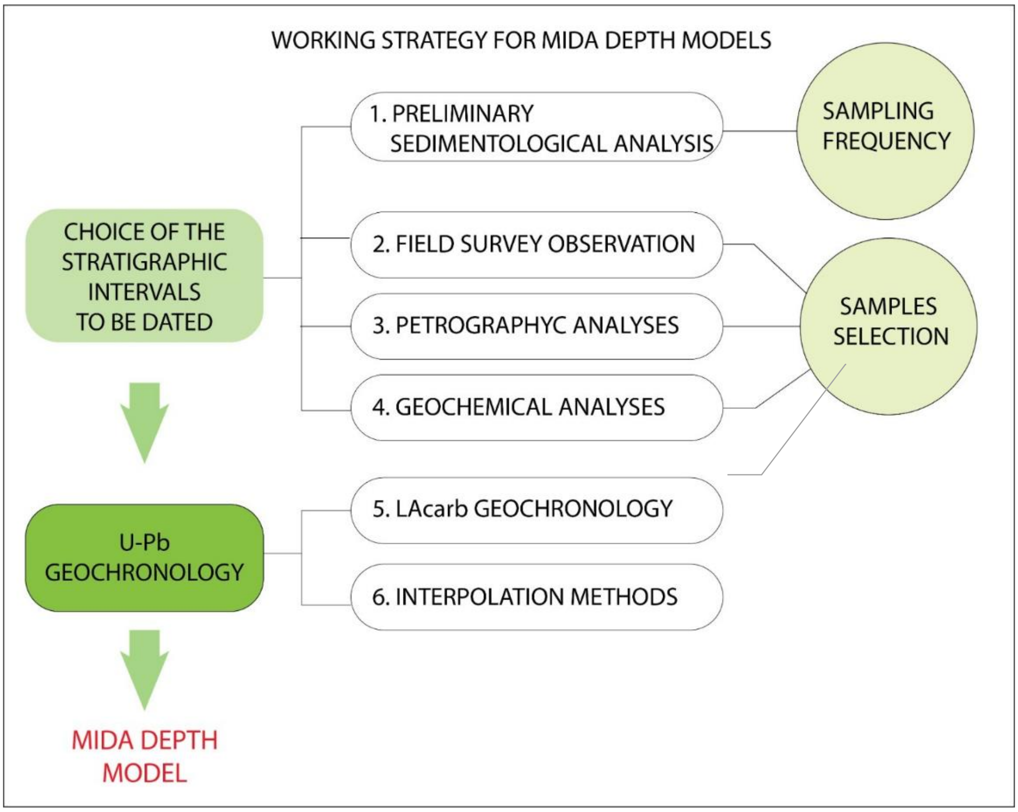

Figure 58. Working strategy to build a depositional age model along a vertical stratigraphic section via LAcarb.

Frequency along the stratigraphic section. The frequency of the stratigraphic layers or intervals be dated has to be carefully evaluated after a preliminary sedimentological analysis. Indeed, it depends on the distribution and availability of carbonate facies along the section, the presence of eventual sedimentary hiatuses and the sedimentation rates dynamic. High sedimentation rates do not require high frequency sampling in contrast with condensed and low sedimentation rates intervals (Chapter 8.1)

Samples selection. The selection of promising samples to be dated starts from the field survey observations. Carbonate samples need to be selected far from mineralized surfaces and faults. This is required to limit the disturbance of the U-Pb isotope composition and age caused by the migration of later fluids (Chapter 5.4). Carbonates along emersion surfaces (e.g. sequence boundaries) should be sampled with the aim to target meteoric cements related to the emersion event. Indeed, carbonates precipitated from meteoric waters or under the influence of meteoric waters (e.g. vadose cements, speleothems) are usually associated with a high dating potential (e.g. Woodhead & Petrus, 2019; Gomes et al., 2020; Montano et al., 2021 and Montano et al. in revision in Chapters 4.1 and 6.1). Instead, it was demonstrated (Chapter 7.2) that meteoric diagenesis on depositional phases may cause a reduction of the age precision due to U leaching (e.g. carbonates in the last 2-3 m of the Yacoraite Fm. below SB5). The analysis done in the framework of the Yacoraite Fm. showed that early lacustrine cements statistically provide the most accurate assessment of the depositional age of the system (if compared to microbialite and ooids from the same palaeoenvironment), with a dating success rate for chronostratigraphic studies of about 65% and uncertainties mostly below 2-3% (2σ). It derives that lacustrine cements should also be preferentially targeted for chronostratigraphic studies. In contrast, phases characterized by mixed calcitic/dolomitic mineralogy provided the lowest dating success (33%) and age precision, thus less suitable for chronostratigraphic studies (Chapter 7.3).

Pre-analytical sample characterization is required to reduce the time wasted on unsuitable samples, improving the quality of collected data, enhancing the overall efficacy of U-Pb dating for chronostratigraphic studies. Petrographic and geochemical analyses were adequate to select most preserved carbonate phases (Chapter 7.1) although samples with a complex diagenetic history may require to be mapped for various geochemical proxies as demonstrated by Drost et al. (2018). A second approach that can be consider to detect post-depositional diagenetic modification is the analysis of the U-Pb isotope composition of carbonates in the Tera-Wasserburg Concordia diagram (Chapter 7.2).

LAcarb dating and spot selection. Spot selection via random screening is highly encouraged and demonstrated to be adequate to detect hot spots providing a general idea on the dating potential of specific phases. Samples with very homogeneous U-Pb isotope ratios or very high common Pb can be easily discarded prior to be analysed (Chapter 7.1).

Age data points interpolation Literature provides various approaches to interpolate the age data point along a vertical section in order to build MDA depth models via zircon geochronology (e.g. Blaauw 2010; Blaauw et al. 2012; 2018; Lougheed & Obrochta, 2019). Similar approaches can be applied with LAcarb ages. Advanced methods of interpolation such as the Bayesian statistics rely on numerical methods to run iterations and select the best depositional scenario. These approaches are required when dealing with un-linear datasets associated with depth and age uncertainties and in particular when age-reversals (i.e. ash layers becoming older upsection) occur within the dataset (e.g. Blaauw & Christen, 2005; Baresel et al., 2017). Classical approaches, such as the commonly used linear interpolation are ideal in simple geologic contexts with no major sedimentation hiatuses and with age data points regularly distributed along the stratigraphic section (e.g. Watson et al., 2017). The linear interpolation approach generally provides a point age depth estimate without considering MDA uncertainties and assumes that abrupt changes in sedimentation rate took place exactly at the dated depths with no smoothening of the depositional curve. Although this latter assumption is often likely to be wrong, linear interpolation is known to produces plausible age depth models (e.g. Blaauw, 2010 and Blaauw et al., 2012) which are not far from those obtained by more advanced interpolation method and resulted successful in the framework of the Yacoraite Fm. (Chapters 6.1 and 8.1).

9 CONCLUSIONS AND PERSPECTIVES

9.1 Conclusions

The present PhD project focused on carbonate U-Pb dating via LA-ICPMS (LAcarb) as additional chronostratigraphic tool for lacustrine deposits. The Ries Crater basin (Chapter 4) and the Yacoraite Fm. (Chapters 5,6,7 and 8) demonstrated to be the ideal case studies to test the accuracy, precision, potentialities, and limitations of LAcarb in the framework of chronostratigraphic investigations.

In the Ries Crater basin (Chapter 4) LAcarb ages obtained from preserved depositional (calcitic and dolomitic microbial carbonate) and early diagenetic (lacustrine and meteoric cements) carbonates were precise down to 1.5% and allowed chronostratigraphic correlations between discontinuous marginal facies and between marginal facies and basinal siliciclastic units. The depositional ages and chronostratigraphic correlations achieved were consistent with the known depositional age of the system based on U-Pb and Sr/Sr dating applied on non-carbonate material. Results from this study suggested that LAcarb may allow chronostratigraphic investigations at the resolution of the third order stratigraphic sequence (0.5-5Ma).

In the framework of Yacoraite Fm. (Chapters 6 and 8), the depositional age was calculated via zircon geochronology (MDA depth model, Chapter 6.1) from volcanic ash layers interbedded within the stratigraphic section. LAcarb ages obtained from depositional carbonates (calcitic and dolomitic microbialite, dolomitic oncoids and calcitic/dolomitic ooids) and lacustrine calcite cements were interpolated to build two linear depositional age depth models for the same stratigraphic section dated by zircon geochronology. One model was based on the results obtained from a single LAcarb analytical session (MIDApart, 19 ages; Montano et al., in revision, Chapter 6.1) and the other on the full dataset consisting of 7 analytical sessions (MIDAfull, 43 ages, Chapter 8.1). The LAcarb models obtained are consistent with the depositional age reconstructed from zircon geochronology and yielded a time resolution down to 1.5-2% (Chapter 8.1).

The new revised age of the Yacoraite Fm. showed implication for the general chronostratigraphy of the Salta rift basin deposits (Chapter 6.2). Based on multiple sedimentologic, chronostratigraphic, geochemical and palaeontological evidence the most possible position of the KPg extinction event and of the Paleocene Eocene hyperthermals (PETM and EECO) events have been defined.

Results from this study also provided precious insights regarding the dating potential of various lacustrine carbonates (Chapter 7). This is specifically important to better understand the mechanisms of U sequestration in carbonates from lacustrine settings and boost the dating success of LAcarb technique. The dating potential is given by an interplay of various factors: the mechanism of carbonate formation (i.e. organomineralization or chemical precipitation) and how the carbonate is prone to maintain the pristine composition. This in turns depends on petrographic features (i.e. habitus, texture, reactive surface area) and mineralogy (i.e. stable vs unstable original mineralogy) (Chapter 7.2). Although all carbonate types (microbialite, oncoids, ooids and lacustrine cements) provided some depositional ages, the early lacustrine cements yielded the highest dating success and higher age precision (i.e. 65% depositional ages, precision below 3%). Conversely, microbialite provided the lowest dating success (i.e. 41 % of depositional ages) and low age precision (i.e. uncertainties up to 6-8%), similar to those of ooids. Dolomitic carbonates and those with mixed dolomitic/calcitic mineralogies yielded statistically less precise ages and thus demonstrated to be less suitable for chronostratigraphic studies. The high dating potential of the lacustrine calcite cement was interpreted to be due to precipitation in more reducing conditions from a fluid enriched in U. In contrast, microbialites and ooids lower dating potential is interpreted to be mainly due to incorporation of high amounts of Pb during their formation.

Considering the better comprehension of potentialities and limitations of LAcarb acquired in this PhD project, a protocol to build a robust depositional age depth model solely via LAcarb is proposed (Chapter 8.2) and consists of four steps: 1) the choice of the number of samples to be dated along the chosen stratigraphic section; 2) the most promising sample selection; 3) the LAcarb dating and spot selection approach and 4) the strategy of data point interpolation.

Some future perspectives of the project are discussed in Chapter 9.2.

9.2 Perspectives

The success of LAcarb in the Ries Crater basin a Yacoraite Fm. lacustrine successions opened a wide array of possible applications. Here three perspectives are discussed: 1) the study of the Ries Crater basin as analogue of paleolakes on Mars, 2) the use of LAcarb to select pristine carbonates for chronostratigraphic studies and 3) further LAcarb analyses to achieve chronostratigraphic correlations of the Yacoraite Fm. at basin scale. Preliminary analyses were conducted during this PhD project regarding the third prospective mentioned.

9.2.1 Chronostratigraphic model of the Ries Crater basin: an analogue for paleolakes on Mars

In the last years The Ries Crater impact basin has attracted great attention since it is considered as a valuable analogue of impact-related paleolakes on Mars, such as the Jazero and Gale craters (e.g. Arp et al., 2019b; Svensson et al., 2021; Arp et al., 2021). These craters are currently explored by NASA Curiosity and Perseverance Rover (Carr, 2021) because life possibly existed on their margins before Mars lost its own atmosphere and water could be still present beneath their surfaces (e.g. Horgan et al., 2020; Bosac et al., 2021; Scheller et al., 2021; Svensson et al., 2021). Appraising the temporal relationship of carbonate facies in these settings is thus of prime importance in the framework of astrobiology (Osinski et al., 2020) because it would allow to understand when and where environmental conditions could have been suitable for life after the meteorite impact occurred.

In the framework of this PhD project, LAcarb technique provided time constraints for the Ries Crater deposits (Chapter 4), particularly the time elapsed between meteorite impact and bioherm growth. Future studies may concern high resolution chronostratigraphic analyses, involving older bioherm and hydrothermal spring mound, with the aim to produce a temporal/spatial depositional model for the Ries Crater facies. It is worth mentioning that meteorite impacts often induce hydrothermal fluid migrations and consequent development of hydrothermal spring mounds. Due to favourable chemical and temperature conditions, hydrothermal vents are known to play an important role in the origin of life (e.g. Osinski et al., 2020). Thus, hydrothermal spring mounds from the Ries Crater (e.g. Arp et al., 2013b) should be preferentially target for future LAcarb based investigations.

9.2.2 Implications of LAcarb for paleoenvironmental and paleoclimate studies

Due to the alerting impact of present-day anthropogenic CO_2 release to the ecosystems and general global warming, there is an increasing interest to examine intervals in the geological past tha record major environmental changes and biologic turnovers occurred (e.g. Keltz & Talbot, 1990; Leng & Marshall, 2004; Elias, 2021; Shuman, 2021). Mandatory prerequisite for these investigations is the assumption that the carbonate samples selected preserve their pristine geochemical composition. Although various tools are commonly employed to detect possible diagenetic modifications, (e.g. Drost et al., 2018; Li et al., 2021; Rasbury et al., 2021), the evaluation of carbonate geochemical preservation remains a matter of debate and is one of the most discussed topics in palaeoenvironmental/paleoclimate research (e.g. McCormack & Kwiecien, 2021). In such scenario LAcarb may be considered as an additional tool to discriminate geochemically pristine and disturbed carbonate samples. As extensively discussed in this text, since U is very soluble, it tends to be easily leached during neomorphic processes, also during early diagenesis, resulting in an age reset or degradation (Chapter 7.2).

In the context of paleoclimate studies, the lacustrine Yacoraite Fm. can be considered as an ideal object to test the use of LAcarb as both dating tool and diagenesis detector. The formation has been already dated via zircon and carbonate geochronology (Montano et al., in revision; Chapter 6.1), allowing to work in a well time-framed geologic context to test the accuracy of LAcarb ages. Previous authors demonstrate that the lacustrine deposits record important changes in environmental conditions (e.g. alkalinity, salinity, lake dynamic, KPg extinction; Rohais et al., 2019; Deschamps et al., 2020). Moreover, carbonates from the sub-basin investigated (Chapter 5.4) showed a minor burial diagenetic overprint on the pristine isotope composition (Chapters 7.1 and 7.2), good dating success (54% of ages consistend with zircon geochronology; Montano et al. submitted; Chapter 6.1) and good age precision (uncertainties down to 1.8%, 2σ).

A possible workflow for a future project may involve the following steps:

1) Petrography and elemental geochemistry are used to discard carbonates with clear evidence of diagenetic modifications, as usually done in any paleoclimate study (Chapter 6 and 7).
2) Carbonates selected are dated via LAcarb (Chapter 7). Only carbonates with U-Pb ages that become younger going from the base to the top of the stratigraphic section and with uncertainty < 3%, well alignment of isotope ratio datapoints and high radiogenic proportion of Pb has to be targeted fort paleoclimate analyses (Chapter 7.2).

3) The palaeoenvironmental/paleoclimate evolution of the lake is investigated through elemental/isotope analyses via LA-ICPMS on the carbonates selected. Some proxies to be considered are Cu/Al Ni/Al for OM flux and palaeoproductivity, U/Th, V/Cr and V/V+Ni for the redox conditions, B for the evaporative conditions, Ph and salinity (e.g. Rohais et al., 2019). In the framework of this PhD project, elemental analytical sessions were attempted but resulted mostly unsuccessful due to quartz contamination and issues with the spectrometer. Moreover, the Covid-19 health emergency hindered to repeat the measurements in further sessions.

9.2.3 Basin scale chronostratigraphic correlations of the Yacoraite Fm.

The possibility to use LAcarb for inner basin-margin and margin-margin chronostratigraphic correlations in a lacustrine basin has been investigated in the framework of the Ries Crater meteorite impact basin (Miocene, SW Germany, Chapter 4). The study demonstrated that LAcarb allows chronostratigraphic correlations in small lacustrine basins (< 30 Km in diameter) of Miocene age that persisted for around 1.2-2 Ma (Montano et al., 2021, Chapter 4.1). The time resolution achieved was down to 1.5% (2σ) and suggest that LAcarb may be even more useful in larger basins that evolved in a longer time.

A good case study to investigate this application is surely the Yacoraite Fm. (Cretaceous-Paleogene, NW Argentina) that covers a massive surface of 150 000 Km^2 (diameter > 200 Km) and was deposited in around 6Ma (Chapters 6 and 8). In the framework of this PhD project, field survey allowed collecting samples from two stratigraphic sections of the basin located at the margins of the lake, one dominated by carbonates (Juramento section) and the other by siliciclastics (Cachipampa section) (Chapter 5.4).

The first aim of a potential future project could be to attemp correlating via LAcarb these two stratigraphic sections that are characterized by different thicknesses, sedimentation rates, depositional profiles and influxes of continental waters. The possibility to work on coeval samples from two different areas of the basin would also allow to better understand the role of specific environmental conditions (e.g. different detrital imput and continental water influx) on the dating potential.

Preliminary results and future research

The Juramento stratigraphic section has been dated via zircon geochronology and LAcarb. Results are in Chapters 6, 7 and 8. Concerning the Cachipampa section, field survey allowed collecting 38 carbonate samples a no ash layers because poorly voluminous. Preliminary analyses were achieved on these carbonate samples.

Petrographic analysis underlined diagenetic features consistent with those observed in the Juramento section. Similarly, C-O stable isotope analysis indicates the same covariance typical of closed lakes (Fig. 60). This suggests that also carbonates from the Cachipampa section did not suffer a strong diagenetic overprint.

The absence of ash layer samples does not allow to produce a MDA model as previously done for the Juramento section. To overcome this issue, the sequence boundary ages estimated from Juramento section (Chapter 8) were reported along the Cachipampa section according to the chronostratigraphic correlations provided by Rohais et al., (2012; 2014, 2019) and Deschamps et al., (2020) (Fig.61).

LAcarb analyses revealed that depositional and early diagenetic carbonates from the Cachipampa section are characterized by lower U concentration and similar Pb concentration if compared with those from the Juramento section. Moreover, the same carbonate types from the two sections provided similar U-Pb

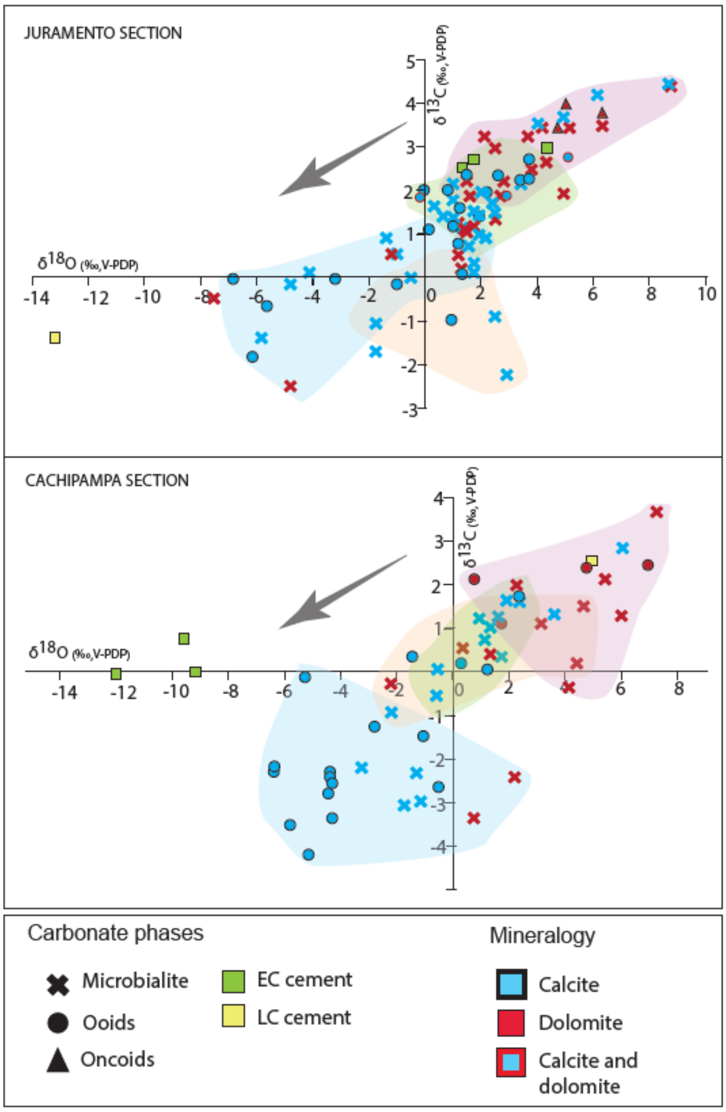

Figure 59. Comparison of C-O stable isotope data from the two stratigraphic sections investigated. Pink, green, orange and blue areas represent the isotope signal of carbonates from sequence 1, 2, 3 and 4, respectively.

elemental and isotope composition suggesting the carbonate type has an important influence on the U-Pb incorporation and dating potential. LAcarb provided some depositional ages (Fig. 61) with an apparently lower average age precision. However, the present dataset requires further refinement and new analytical sessions have to be achieved. Indeed, due to the lower sedimentation rates of the Cachipampa section and the lower age precision observed, a robust depositional age depth model may possibly be obtained only via a higher sampling frequency (Chapter 8.2).

Figure 60 A) Juramento stratigraphic section. Carbon ($\delta^{13}C$) and oxygen ($\delta^{18}O$) stable isotope data (to the left), and minimum depositional age (MIDA) depth model (to the right) from figure 56 (Chapter 8.1). B) Cachipampa stratigraphic section. To the left Carbon ($\delta^{13}C$) and oxygen ($\delta^{18}O$) stable isotope data. To the right, the depositional model (in green) is built considering the position of the sequence boundaries (Rohais et al., 2019; Deschamps et al., 2020) and their age estimated along the Juramento section. A cluster of younger ages (dashed area) obtained in Sequence 1 from both Juramento and Cachipampa sections indicates a possible event of fluid migration and neomorphism at around 61.5 Ma. C, D, E) Petrographic image and TW Concordia diagram of calcitic ooids (OC) calcitic microbialite (MIC-D) and burial cement (LC1). Carbon and Oxygen stable isotope values are expressed as relative to the Vienna Pee Dee Be Standard (V-PDB).

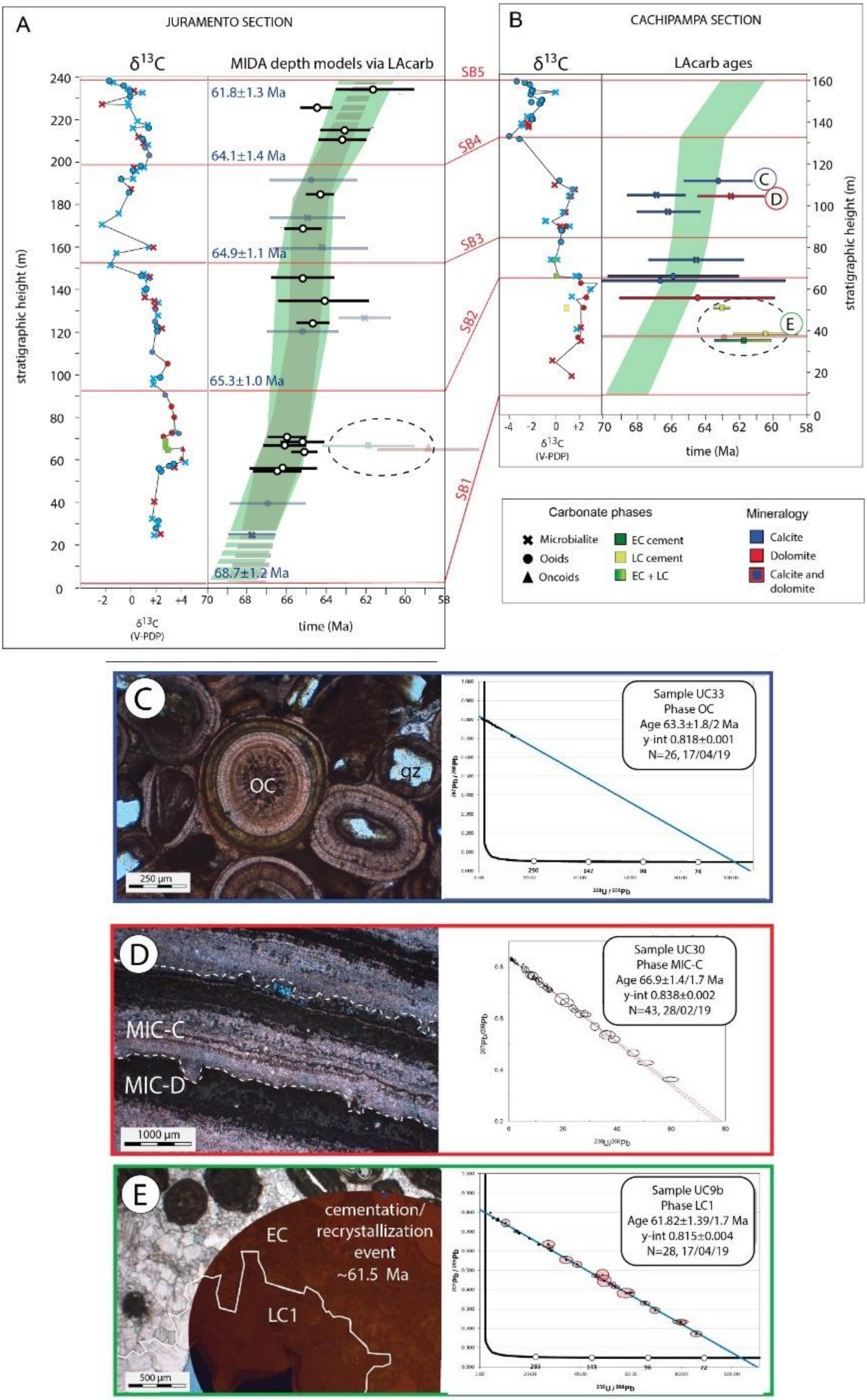
A
JURAMENTO SECTION
δ13C
MIDA depth models via LAcarb
61.8±1.3 Ma
64.1±1.4 Ma
64.9±1.1 Ma
65.3±1.0 Ma
68.7±1.2 Ma
stratigraphic height (m)
240
220
200
180
160
140
120
100
80
60
40
20
0
-2
0
+2
+4
70
68
66
64
62
60
58
δ13C (V-PDP)
time (Ma)
SB5
SB4
SB3
SB2
SB1
B
CACHIPAMPA SECTION
δ13C
LAcarb ages
160
140
120
100
80
60
40
20
0
-4
-2
0
+2
stratigraphic height (m)
C
D
E
time (Ma)
Carbonate phases
✖ Microbialite
● Ooids
▲ Oncoids
EC cement
LC cement
EC + LC
Mineralogy
Calcite
Dolomite
Calcite and dolomite
C
OC
qz
250 µm
Sample UC33
Phase OC
Age 63.3±1.8/2 Ma
y-int 0.818±0.001
N=26, 17/04/19
207Pb/206Pb
238U/206Pb
D
MIC-C
MIC-D
1000 µm
Sample UC30
Phase MIC-C
Age 66.9±1.4/1.7 Ma
y-int 0.838±0.002
N=43, 28/02/19
207Pb/206Pb
238U/206Pb
E
EC
LC1
cementation/ recrystallization event ~61.5 Ma
500 µm
Sample UC9b
Phase LC1
Age 61.82±1.39/1.7 Ma
y-int 0.815±0.004
N=28, 17/04/19
207Pb/206Pb
238U/206Pb

10 References

Al-Aasm, I.S (2000). Chemical and Isotopic Constraints for Recrystallization of Sedimentary Dolomites from the Western Canada Sedimentary Basin. Aquatic Geochemistry 6, 227–248 (2000). DOI:10.1023/A:1009611224589.

Alloway, B.V., Larsen, G. Lowe, D.J. Shane, P.A.R., Westgate, J.A. (2007). Tephrochronology. S.A. Elias (Ed.), Encyclopaedia of Quaternary Science, Elsevier, London (2007), pp. 2869-2898.

Alonso, R.N., Marquillas, R.A. (1986). Nueva localidad con huellas de dinosaurios y primer hallazgo de huellas de aves en la Formacion Yacoraite (Maastrichtiano) del Norte Argentino. 2. Actas 4th Congr Arg Paleont Bioestrat, pp. 33–41.

Alonso, R. N., (1980). Icnitas de dinosaurios (Ornithopoda, Hadrosauridae) en el Cretácico superior del Norte de Argentina. Acta Geológica Lilloana, 15: 55-63.

Andrews, E., White T., Del Papa, C. (2017). Paleosol-based paleoclimate reconstruction of the Paleocene-Eocene Thermal Maximum, northern Argentina Palaeogeography, Palaeoclimatology, Palaeoecology 471. Pages 181-195.

Arp, G., (1995). Lacustrine bioherms, spring mounds, and marginal carbonates of the Ries-impact-crater (Miocene, Southern Germany). Facies. 33 (1), 35-89. https://doi.org/10.1007/bf02537444.

Arp, G., Blumenberg, M., Hansen, B.T., Jung, D., Kolepka, C., Lenz, O., Nolte, N., Poschlod, K., Reimer, A., Thiel, V., (2013a). Chemical and ecological evolution of the Miocene Ries impact crater lake, Germany: a re-interpretation based on the Enkingen (SUBO 18) drill core. Geol Soc Am Bull. 125 (7-8), 1125-1145. https://doi.org/10.1130/B30731.1.

Arp G., Hansen B. T., Pack A., Reimer A., Schmidt B. C., Simon K., and Jung D. (2017). The soda lake—mesosaline halite lake transition in the Ries impact crater basin (drilling Löpsingen 2012, Miocene, southern Germany). Facies. 63 (1). https://doi.org/10.1007/s10347-016-0483-7.

Arp, G., Kolepka, C., Simon, K., Karius, V., Nolte, N., Hansen, B. T., 2013b. New evidence for persistent impact-generated hydrothermal activity in the Miocene Ries impact structure, Germany. Meteorit. Planet Sci. 45 (12), 2491–2516 https://doi.org/10.1111/maps.12235.

Arp, G., Reimer, A., Simon, K., Sturm, S., Wilk, J., Kruppa, C., Hecht, L., Hansen, B.T., Pohl, J., Reimold, W.U., Kenkmann, T., Jung, D. 2019a. The Erbisberg drilling 2011: Implications for the structure and postimpact evolution of the inner ring of the Ries impact crater. Meteorit. Planet. Sci. 1-35. https://doi.org/10.1111/maps.13293.

Arp, G. Schultz, S., Karius, V., Head, J.W. (2019b). Ries impact crater sedimentary conglomerates: Sedimentary particle 'impact pre-processing', transport distances and provenance, and implications for Gale crater conglomerates, Mars. Icarus, Volume 321, Pages 531-549, DOI: 1016/j.icarus.2018.12.003.

Arp, G., Dunkl, I., Jung, D., Karius, V., Lukács, R., Zeng, L., Reimer, A., Head. J.M. (2021). A volcanic ash layer in the Nördlinger Ries impact structure (Miocene, Germany): Indication of crater fill geometry and origins of long-term crater floor sagging. Journal of Geophysical Research: Planets, 2021; DOI: 10.1029/2020JE006764.

Bateman, H. (1910). Solution of a system of differential equations occuring in the theory of radioactive transformations. Proceedings of the Cambridge Philosophical Society, 15:423–427.

Beaudoin, N., Lacombe, O., Roberts, N.M.W., Koehn. D. (2018). U-Pb dating of calcite veins reveals complex stress evolution and thrust sequence in the Bighorn Basin, Wyoming, USA. Geology, Geological Society of America, 2018, 46 (11), pp.1015-1018. DOI. 0.1130/G45379.1.

Bento-Freire, E. (2012). High Resolution Sequence Stratigraphic characterization of microbial carbonate from Palaeocene interval of

Yacoraite Formation – Argentine. Master Thesis, Federal Univ. Rio de Janeiro, Rio de Janeiro (in Portuguese with English abstract).

Baresel, B., Bucher, H., Brosse, M., Cordey, F., Guodun, K., and Schaltegger, U. (2017). Precise age for the Permian–Triassic boundary in South China from high-precision U-Pb geochronology and Bayesian age–depth modeling, Solid Earth, 8, 361–378, DOI: 10.5194/se-8-361-2017

Bernaola, G., Martín-Rubio, M., Baceta, J.I. (2009). New high resolution calcareous nannofossil analysis across the Danian/Selandian transition at the Zumaia section: comparison with South Tethys and Danish sections. Geologica Acta, Vol.7, Nos 1-2, March-June 2009, 79-92. DOI: 10.1344/105.000000272.

Berra, F., Carminati, E. (2010). Subsidence history froma backstripping analysis of the Permo-Mesozoic succession of the Central Southern Alps (Northern Italy). Basin research, 22, 952–975, DOI: 10.1111/j.1365-2117.2009.00453.x.

Bilau, A., Rolland, Y., Schwartz, S., Godeau, N., Guihou, A., Deschamps, P., Brigaud, B., Noret, A., Dumont, T., Gautheron, C. (2021). Extensional reactivation of the Penninic Frontal Thrust 3 Ma ago as evidenced by U-Pb dating on calcite in fault zone cataclasite, Solid Earth, 12, 237–251. DOI: 10.5194/se-12-237-2021.

Birch H., Schmidt D. N., Coxall H. K., Kroon D. and Ridgwell A. (2021). Ecosystem function after the K/Pg extinction: decoupling of marine carbon pump and diversity. Proc. R. Soc. B.288. DOI: 10.1098/rspb.2021.0863

Blaauw, M. (2010): R-Code for 'classical' age-modelling (CLAM V1.0) of radiocarbon sequences. PANGAEA. DOI: 10.1594/PANGAEA.873023.

Blaauw, M., Holliday, V.T., Gill, J. L., Nicoll, K. (2012). Age models and the Younger Dryas Impact Hypothesis. 109 (34). DOI; 10.1073/pnas.1206143109

Blaauw, M., Christen, J. (2005). Radiocarbon peat chronologies and environmental change. Applied Statistics. Vol 54. Issue 4. Pages 805-816.DOI: 10.1111/j.1467-9876.2005.00516.x.

Blaauw, M., Christen, J., Bennett, K., Reimer, P. (2018). Double the dates and go for Bayes — Impacts of model choice, dating density and quality on chronologies. Quaternary Science Reviews. 188. 58-66. DOI: 10.1016/j.quascirev.2018.03.032.

Bohacs, K. M., Carroll, A. R., Neal, J. E., Mankiewicz P. J., 2000. Lake-basin type, source potential, and hydrocarbon character: an integrated-sequence-stratigraphic–geochemical framework, in: E. H. Gierlowski-Kordesch & K. R. Kelts, eds., Lake basins through space and time: AAPG Studies in Geology. 46, 3–34. https://doi.org/10.1306/St46706C1.

Bolten R., and Müller D., 1969. Das Tertiär im Nördlinger Ries und in seiner Umgebung. Geol. Bavarica. 61, 87-130.

Bossi G.E. (1969). Geologıa y estratigrafıa del sector sur del Valle de Choromoro. Acta Geol Lilloana 10:17–64

Brigaud, B., Andrieu, S., Blaise, T., Haurine, F. and Barbarand, J. (2021). Calcite uranium–lead geochronology applied to hardground lithification and sequence boundary dating. Sedimentology, 68: 168-195. DOI:10.1111/sed.12795

Brooks, C., Hart, S. R., and Wendt, I. (1972). Realistic use of two-error regression treatments as applied to Rubidium-Strontium data, Rev. Geophys. Space Phys., 10, 551–577.

Bonaparte, J.F., Bossi, G.E. (1967). Sobre la presencia de dinosaurios en la Formacion Pirgua del Grupo Salta y su significado cronologico. Acta Geol Lilloana 9:25–44.

Bonaparte, J. F., Powell, J. E. (1980). A continental assemblage of tetrapods from the Upper Cretaceous beds of El Brete, northwestern Argentina (Sauropoda-Coelurosauria-Carnosauria-Aves). Société Géologique de France, Mémoir, N. S., 139, 19-28

Bosak, T., Moore, K.R., Gong, J. et al. (2021). Searching for biosignatures in sedimentary rocks from early Earth and Mars. Nat Rev Earth Environ 2, 490–506. https://doi.org/10.1038/s43017-021-00169-5

Buchner, E., Schwarz, W. H., Schmieder, M., Trieloff, M., (2010). Establishing a 14.6 ± 0.2 Ma age for the Nördlinger Ries impact (Germany)—A prime example for concordant isotopic ages from various dating materials. Meteorit. Planet. Sci. 45 (4). DOI: 10.1111/j.1945-5100.2010.01046.x.

Buchner, E., Schmieder, M. (2009). Multiple fluvial reworking of impact ejecta-A case from the Ries crater, southern Germany. Meteoritics & Planetary Science 44, Nr 7, 1051-1060. DOI; 10.1111/j.19455100.2009.tb00787.x.

Buchner, E. & Schmieder, M. 2013. Das Ries–Steinheim-Ereignis – Impakt in eine miozäne Seen- und Sumpflandschaft—the Ries–Steinheim event – impact into a Miocene swampy lakescape. Z. Deutsch. Geol. Ges. 164, 459–470 (2013).

Burke, W. M., Denison, R. E., Hetherington, E. A., Koepnik, R. B., Nelson, M., and Omo, J., (1982). Variation of seawater 87Sr/86Sr throughout Phanerozoic time. Geology, 10, 516–519.

Burisch, M., Gerdes, A., Walter, B. F., Neumann, U., Fettel, M., & Markl, G. (2017). Methane and the origin of five-element veins: Mineralogy, age, fluid inclusion chemistry and ore forming processes in the Odenwald, SW Germany. *Ore GeologyReviews*, **81**, 42– 61. https://doi.org/10.1016/j.oregeorev.2016.10.033.

Burisch M, Walter BF, Gerdes A, Lanz M, Markl G (2018). Late-stage anhydrite-gypsum-siderite-dolomite-calcite assemblages record the transition from a deep to a shallow hydrothermal system in the Schwarzwald mining district, SW Germany. Geochim Cosmochim Acta 223:259–278.

Carr, C. (2021). Resolving the History of Life on Earth by Seeking Life As We Know It on Mars. 2102.02362v1 [astro-ph.EP].

Carrera, N., Munoz, J.A., Sabat, F., Roca, E., Mon, R., (2006). The role of inversion tectonics in the structure of the Cordillera Oriental (Argentinean Andes). Journal of Structural Geology 28, 1921– 1932.

Carroll, S.A., Bruno, J., Petit, J. C, Dran J.C. (1992). Interaction of U(VI), Nd, and Th(IV) at the calcite-solution interface. Radiochim. Acta, 58/59 (1992), pp. 245-252.

Cartier, R. Brisset, E., Guiter, F., Sylvestre, F., Kazuyo, T., Anthony, E.J., Paillès, C., Bruneton, H., Bard, E., Miramont C. (2018). Multiproxy analyses of Lake Allos reveal synchronicity and divergence in geosystem dynamics during the Lateglacial/Holocene in the Alps. Quaternary Science Reviews, Elsevier. 186, 60-77. DOI: 10.1016/j.quascirev.2018.02.016

Ceraldi, S., T., Green, D. (2016). Evolution of the South Atlantic lacustrine deposits in response to Early Cretaceous rifting, subsidence and lake hydrology. Geological Society, London, Special Publications. 438. DOI: 10.1144/SP438.10.

Cesaretti, N.N., Parnell, J. and Dominguez, E.A. (2000). Pore fluid evolution within a hydrocarbon reservoir: Yacoraite formation (Upper Cretaceous), Northwest Basin, Argentina. J. Petrol. Geol., 23, 375–398. DOI: 10.1111/j.1747-5457.2000.tb00493.x.

Cassata, W.S. Singer, B.S., Liddicoat, J.C., Coe, R.S. (2010). Reconciling discrepant chronologies for the geomagnetic excursion in the Mono Basin, California: insights from new 40Ar/39Ar dating experiments and a revised relative paleointensity correlation Quaternary Geochronology, 5 (2010), pp. 533-543.

Catuneanu, O., Abreu, V., Bhattacharya, J.P., Blum, M.D., Dalrymple, R.W., Eriksson, P.G., Fielding, C.R.,. Fisher, W.L., Galloway, W.E., Gibling, M.R., Giles, K.A., Holbrook, J.M., Jordan, R. Kendall, C.G.St.C., Macurda, B., Martinsen, O.J.,

Miall, A.D., Neal, J.E., Nummedal, D., Pomar, L., Posamentier, Pratt, B.R. Sarg, J.F., Shanley K.W., Steel, R.J., Strasser, A., Tucker, M.E. Winker, C. (2009). Towards the standardization of sequence stratigraphy, Earth-Science Reviews, Volume 92, Issues 1–2, Pages 1-33, DOI: 10.1016/j.earscirev.2008.10.003.

Chatterjee, S. (2021). From Stardust to First Cells—The Origin of Life, Editor(s): David Alderton, Scott A. Elias, Encyclopedia of Geology (Second Edition), Academic Press, Pages 555-560, DOI: 10.1016/B978-0-12-409548-9.12029-9.

Cheng, T., Zhao, J., Feng, Y., Pan, W., and Liu, D. (2020). In-situ LA-MC-ICPMS U-Pb dating method for low-uranium carbonate minerals. Chinese Science Bulletin. VOL 65. Issue 2-3pages 150-154. DOI: 10.1360/TB-2019-0355

Chew, D. M., Petrus, J. A., & Kamber, B. S. (2014). U–Pb LA–ICPMS dating using accessory mineral standards with variable common Pb. Chemical Geology, 363(Supplement C), 185– 199. DOI: 10.1016/j.chemgeo.2013.11.006.

Christ, N., Maerz, S., Kutschera, E., Kwiecien, O., Mutti, M., 2018. Palaeoenvironmental and diagenetic reconstruction of a closed-lacustrine carbonate system – the challenging marginal setting of the Miocene Ries Crater Lake (Germany). Sedimentology. 65 (1). https://doi.org/ 10.1111/sed.12401

Chung, G. S., & Swart, P. K. (1990). The concentration of uranium in freshwater vadose and phreatic cements in a Holocene ooid cay: a method of identifying ancient water tables. Journal of Sedimentary Research, 60(5).

Claire M.A. Veillard, Cédric M. John, Samuel Krevor, Jens Najorka (2019), Rock-buffered recrystallization of Marion Plateau dolomites at low temperature evidence by clumped isotope thermometry and X-ray diffraction analysis, Geochimica et Cosmochimica Acta, 252, 190-212. DOI: 10.1016/j.gca.2019.02.012.

Clebsch C.A. (1991). The geological evolution of the Paraguayan Chaco. PhD Thesis, Texas Tech University.

Clyde, W.C., Ramezani, J. Johnson, K.R., Bowring, S.A., Jones, M.M. (2016). Direct high-precision U–Pb geochronology of the end-Cretaceous extinction and calibration of Paleocene astronomical timescales. Earth andPlanetaryScienceLetters. 452. Pages 272–280

Cohen, K. M., Harper, D. A. T., and Gibbard, P. L. (2018). International Chronostratigraphic Chart 2018/08. International Commission on Stratigraphy. Paris: IUGS.

Cole, J. M., Rasbury, E. T., Montañez, I. P., Pedone, V. A., Lanzirotti, A., and Hanson, G. N. (2004). Petrographic and trace element analysis of uranium-rich tufa calcite, middle Miocene Barstow Formation, California, USA: Uranium-rich tufa deposits, California, Sedimentology, 51, 433–453, DOI: 10.1111/j.1365-3091.2004.00631.x.

Cole, J. M., Rasbury, E. T., Hanson, G. N., Montañez, I. P., Pedone, V. A. (2005). Using U-Pb ages of Miocene tufa for correlation in a terrestrial succession, Barstow Formation, California. Geol. Soc. Am. Bull. 223 (3), 127-146. DOI:10.1130/B25553.1.

Cominguez, A.H., Ramos, V.A. (1995). Geometry and seismic expression of the Cretaceous Salta Rift System, Northwestern Argentina. In: Tankard AJ, Suarez R, Welsink HJ (eds) Petroleum basins of South America. Am Assoc Petrol Geol Mem 62:325–340.

Connelly, J.N., Bizzarro, J. B. (2017), Vol 201, page 345-363. DOI: 10.1016/j.gca.2016.10.044.

Cóonsole-Gonella, C.A. & Aceñolaza, F.G. (2009). Icnologıa de laFormacion Yacoraite (Maastrichtiano- Daniano) al sur de lalocalidad de Maimara, Cordillera Oriental de Jujuy, Argentina.Acta Geologica Lilloana 21, 100–110.

Cónsole-Gonella, C., Marquillas, R.A., (2014). Bioclaustration trace fossils in epeiric shallow marine stromatolites: The Cretaceous-Palaeogene Yacoraite Formation, Northwestern Argentina. Lethaia. 47 (1). DOI: 10.1111/let.12043.

Cónsole-Gonella, C., de Valais, S., Marquillas, R. A., & Sánchez, M. C. (2017). The Maastrichtian–Danian Maimará tracksite (Yacoraite Formation, Salta Group), Quebrada de Humahuaca, Argentina: Environments and ichnofacies implications. Palaeogeography, Palaeoclimatology, Palaeoecology, 468, 327–350. DOI: 10.1016/j.palaeo.2016.11.008**.**

Cónsole-Gonella, C., et al 2018

Coogan, L.A., Parrish, R.R. and Roberts, N.M. (2016). Early hydrothermal carbon uptake by the upper oceanic crust: Insight from in situ U-Pb dating. Geology, 44, 147-150.

Coxal, H.K., D'Hondt, S., Zachos, J.C. (2006). Pelagic evolution and environmental recovery after the Cretaceous-Paleogene mass extinction. Geology. v. 34; no. 4; p. 297–300; doi: 10.1130/G21702.1

Craig, G., Horstwood, M. S. A., Reid, H. J., Sharp, B. L. (2020). 'Blind time' – current limitations on laser ablation multi-collector inductively coupled plasma mass spectrometry (LA-MC-ICP-MS) for ultra-transient signal isotope ratio analysis and application to individual sub-micron sized uranium particles. Journal of Analytical Atomic Spectrometry. **35**, 1011-1021. DOI: **10.1039/D0JA00066C.**

Cramwinckel, M. J., Huber, M., Kocken, I. J., Agnini, C., Bijl, P. K., Bohaty, S. M., ... & Peterse, F. (2018). Synchronous tropical and polar temperature evolution in the Eocene. Nature, 559(7714), 382-386. DOI: 10.1038/s41586-018-0272-2

Crombez, V., Rohais, S., Euzen, T., Riquier, L., Baudin, F., Hernandez-Bilbao, E., (2020). Trace metal elements as paleoenvironmental proxies: Why should we account for sedimentation rate variations? Geology. 48 (8): 839–843. DOI: 10.1130/G47150.1

Crouch, E.M., Shepherd C.L., Morgans, H.E.G., Naafs, B.D.A., Dallanave, E., Phillips, A. Hollis, C.J. Pancost, R.D. (2020). Climatic and environmental changes across the early Eocene climatic optimum at mid-Waipara River, Canterbury Basin, New Zealand. Earth-Science Reviews. Vol 200, 102961.

Cruset, D., Vergés, J., Albert, R., Gerdes, A., Benedicto, A., Cantarero, I., Travé, A. (2020). Quantifying deformation processes in the SE Pyrenees using U-Pb dating of fracture-filling calcites. Journal of the Geological Society. DOI: 10.1144/jgs2020-014.

Cumberland, S.A., Douglas, G., Grice, K., Moreau, J.W. (2016). Uranium mobility in organic matter-rich sediments: A review of geological and geochemical processes. Earth-Science Reviews. VOL 159. Pages 160-185. DOI: 10.1016/j.earscirev.2016.05.010.

De Boever, E., Brasier, A., Foubert, A., Kele, A. (2017). What do we really know about early diagenesis of non-marine carbonates? Sedimentary Geology 36. DOI: 10.1016/j.sedgeo.2017.09.011

Della Porta, G. (2015). Carbonate build-ups in lacustrine, hydrothermal and fluvial settings: comparing depositional geometry, fabric types and geochemical signature. In: Bosence, D. W. J., Gibbons, K. A., Le Heron, D. P., Morgan, W. A., Pritchard, T. & Vining, B. A. (eds), Microbial Carbonates in Space and Time: Implications for Global Exploration and Production. Geological Society, London, Special Publications, 418, 17-68. DOI:10.1144/SP418.4

Del Papa, C.E., Kirschbaum, A., Powell, J., Brod, A., Hongn, F., and Pimentel, M., (2010). Sedimentological, geochemical and paleontological insights applied to continental omission surfaces: a new approach for reconstructing Eocene foreland basin in NW Argentina: Journal of South American.Earth Sciences, v. 29, p. 327-345.

Deino, A.L., Scott, G.R., Saylor, B., Alene, M., Angelini, J.D., Haile-Selassie, Y. (2010). 40Ar/39Ar dating, paleomagnetism, and tephrochemistry of Pliocene strata of the hominid-bearing Woranso-Mille area, west-central Afar Rift, Ethiopia Journal of Human Evolution, 58. pp. 111-126

Deocampo, D.M. (2010). The Geochemistry of Continental Carbonates. In Developments in Sedimentology, Volume 62, Chapter 1. DOI: 0.1016/S0070-4571(09)06201-3

Deschamps, R., Rohais, S., Hamon, Y., Gasparrini, M. 2020. Dynamic of a lacustrine sedimentary system during late rifting at the Cretaceous–Palaeocene transition: Example of the Yacoraite Formation, Salta Basin, Argentina. Depositional Rec. 00:1-34. DOI : 10.1002/dep2.116.

Díaz-Martínez, I., De Valais, S., & Cónsole-Gonella, C. (2016). First evidence of Hadrosauropodus in Gondwana (Yacoraite Formation, Maastrichtian–Danian), northewestern Argentina. Journal of African Earth Sciences, 122, 79–87.

Dickson, J. A. D., 1966. Carbonate identification and genesis as revealed by staining. J. Sediment. Res. 36 (2), 491–505. DOI :10.1306/74D714F6-2B21-11D7-8648000102C1865D.

Dickinson, W. R., Gehrels, G. E. (2009). Use of U-Pb ages of detrital zircons to infer maximum depositional ages of strata: A test against a Colorado Plateau Mesozoic database. Earth and Planetary Science Letters, 288(1-2), 115-125. DOI :10.1016/j.epsl.2009.09.013.

Disalvo, A., Hoffman, C., Luquez, J., Rodriguez Schelotto, M. (2002). Los reservorios de la Formaciónes Palmar Largo y La Tigra. Rocas Reservorio de la Cuencas Productivas de la Argentina. 739-752.

Doe, B. R. (1983). The past is the key to the future. Geochimica et Cosmochimica Acta. Vol 47. Issue 8. Pages 1341-1354. DOI : 10.1016/0016-7037(83)90293-4

Drake, H., Heim, C., Roberts, N. M. W., Zack, T., Tillberg, M., Broman, C., Ivarsson, M., Whitehouse, M. J., and Astrom, M. E. (2017). Isotopic evidence for microbial production and consumption of methane in the upper continental crust throughout the Phanerozoic eon, Earth Planet. Sc. Lett., 470, 108–118, https://doi.org/10.1016/j.epsl.2017.04.034, 2017.

Drake, H., Mathurin, F.A., Zack, T., Schäfer, T., Roberts, N.M.W., Whitehouse, M., Karlsson, A., Broman, C. and Åström, M.E. (2018). Incorporation of metals into calcite in a deep anoxic granite aquifer. Environmental science & technology, 52, 493-502.

Drake, H., Roberts, N.M.W., Heim, C., Whitehouse, M.J., Siljeström, S., Kooijman, E., Broman, C., Ivarsson, M. and Åström, M.E., 2019. Timing and origin of natural gas accumulation in the Siljan impact structure, Sweden. Nature communications, 10, 1-14.

Drake, N., Roberts., M W., Whitehouse, M.J. (2020). Geochronology and Stable Isotope Analysis of Fracture-fill and Karst Mineralization Reveal Sub- Surface Paleo-Fluid Flow and Microbial Activity of the COSC-1 Borehole, Scandinavian Caledonides. Geosciences 2020, 10, 56; doi:10.3390/geosciences10020056.

Drost, K., Chew, D., Petrus, J. A., Scholze, F., Woodhead, J. D., Schneider, J. W., & Harper, D. A. T. (2018). An image mapping approach to U-Pb LA-ICP-MS carbonate dating and applications to direct dating of carbonate sedimentation. Geochemistry, Geophysics, Geosystems, 19, 4631–4648. DOI. 10.1029/2018GC007850.

Ducassou, C. Mercuzot, M. Bourquin, S. Rossignol, C. Pellenard, P. Beccaletto, L. Poujol, M Hallot, E. Pierson-Wickmann, A.C. Hue, C. Ravier E. (2019). Sedimentology and U-Pb dating of Carboniferous to Permian continental series of the northern Massif Central (France): Local palaeogeographic evolution and larger scale correlations, Palaeogeography, Palaeoclimatology, Palaeoecology, Volume 533, DOI: 10.1016/j.palaeo.2019.06.001.

Dunham R.J. (1962). Classification of Carbonate Rocks according to depositional texture. In: Ham, W.E. (Ed.), Classification of Carbonate Rocks. AAPG Memoir, 1, p.108-121.

Durieux, C.G., Brown, A.C. (2007). Geological context, mineralization, and timing of the Juramento sediment-hosted stratiform copper-silver deposit, Salta district, Northwestern Argentina. Miner. Deposita, 42, 879–899. DOI: 10.1007/s00126-007-0138-2

Eggins, S.M., Kinsley, L.P.J., Shelley, J.M.M., (1998). Deposition and element fractionation processes during atmospheric pressure laser sampling for analysis by ICPMS. Appl. Surf. Sci. 127–129, 278–286.

Einsele, G. (2001). Sedimentary Basins: Evolution, Facies, and Sediment Budget. SERBIULA (sistema Librum 2.0). 143. DOI: 10.1016/S0037-0738(01)00061-6.

Einsele, G., W. Ricken (1991): Limestone-marl alternation – an overview. In: Einsele, G.W. Ricken & A. Seilacher (eds.): Cycles and events in stratigraphy. – Springer-Verlag: 23 – 47.

Elias, S.A. (2021). Terrestrial Biological Proxies of Climate Change. Encyclopedia of Geology (Second Edition). Elsevier 2021. Pages 328-347. DOI: 10.1016/B978-0-12-409548-9.12521-7.

Elisha, B., Nuriel, P., Kylander-Clark, A., Weinberger, R. (2020) Towards in-situ U–Pb dating of dolomites. Geochronology Discuss., DOI: 10.5194/gchron-2020-19, 2020.

Elzinga, E.J., Tait, C.D., Reeder, R.J Rector, R.J. Donohoe, K.D. Morris, D.E. (2004). Spectroscopic investigation of U(VI) sorption at the calcite-water interface. Geochim. Cosmochim. Acta, 68. pp. 2437-2448

Enos, P. (1991). Sedimentary parameters for computer modeling. In: Franseen, E.K., Watney, W.L., Kendall, C.G.ST.C. & Ross, W. (eds): Sedimentary modeling, computer simulations and methods for improved parameter definition. Kansas Geol. Survey Bull., 233, 63-101.

Fawzy, S., Osman, A.I., Doran, J. et al. (2021). Strategies for mitigation of climate change: a review. Environ Chem Lett 18, 2069–2094 (2020). DOI: 0.1007/s10311-020-01059-w

Fernandez, J., (1975). Hallazgo de peces pulmonados fosiles en la Puna Jujena. Anales de la Sociedad Cientifica Argentina 2 (41), 13-18.

Fernandes, F., De Oliveira, A.S., Sampaio, L.M., Rezende, F.H., Dos Santos, E.R., & Siqueira, C.Y. (2020). Drilling developments in Pre-Salt of Brazil: background and new horizons. DOI:10.48072/2525-7579.ROG.2020.151.

Fernicola, J. C., Zimicz, A.N., Chornogubsky, L., Ducea, M., Cruz, L.E., Bond, M., Arnal, M., Cárdenas, M., Fernández, M. (2021). The Early Eocene Climatic Optimum at the Lower Section of the Lumbrera Formation (Ypresian, Salta Province, Northwestern Argentina): Origin and Early Diversification of the Cingulata. Journal of Mammalian Evolution DOI: 10.1007/s10914-021-09545-w

Finzel, E. S., Rosenblume, J. A. (2021). Dating lacustrine carbonate strata with detrital zircon U-Pb geochronology. Geology (2021) 49 (3): 294–298. DOI: 10.1130/G48070.1

Flügel E. (2004). Microfacies of carbonate rocks. Analysis, interpretation and application. Springer, Berlin, 976 p.

Font, E., Bond, D. P. G. (2021). Volcanism and Mass Extinction, Editor(s): David Alderton, Scott A. Elias, Encyclopedia of Geology (Second Edition), Academic Press, Pages 596-606, DOI: 10.1016/B978-0-12-409548-9.12108-6.

Frankfurt, N.G., Chiappe, L.M., (1999). A possible oviraptorosaur from the Cretaceous of Northwestern Argentina. Jounral of Vertebrate Paleontology. Vol. 19 (1). Pages 101-105. DOI: 10.1080/02724634.1999.10011126.

Frisch, K., Voigt, S., Verestek, V., Appel, E., Albert, R., Gerdes, A., Arndt, I., Raddatz, J., Voigt, T., Weber, Y., Batenburg, S.J. (2019). Laser ablation Uranium-Lead dating of the Miocene alluvial-lacustrine Aktau succession in south-east Kazakhstan. PANGAEA. DOI: 10.1594/PANGAEA.906093.

Frisia, S. Borsato, A. Fairchild, I.J., McDermott, F., Selmo, E.M. (2002). Aragonite-calcite relationships in speleothems (Grotte de Clamouse, France): environment, fabrics, and carbonate geochemistry. Journal of Sedimentary Research, 72, pp. 687-699.

Füchtbauer, H., von der Brelie, G., Dehm, R., Förstner, U., Gall, H., Höfling, R., Hoefs, J., Hollerbach, A., Hufnagel, H., Jankowski, B., Jung, W., Malz, H., Mertes, H., Rothe, P., Salger, M., Wehner, H., Wolf, M., (1977). Tertiary lake sediments of the Ries, research borehole Nördlingen 1973—A summary. 75, 13-19. Geol. bavarica.

Galliski M..A, Viramonte J.G. (1988). The Cretaceous paleorift in northwestern Argentina: a petrologic approach. J S Am Earth Sci 1:329–342

Gebhardt, C., Naudts, L., De Mol, L. et al., (2017). “High-amplitude lake-level changes in tectonically active Lake Issyk-Kul (Kyrgyzstan) revealed by high-resolution seismic reflection data,” Clim. Past. 13 (1), 73–92. DOI: 10.5194/cp-13-73-2017

Geipel, G., Reich, T., Brandler, V., Bernhard, G. Nitsche, H. (1997). Laser and X-ray spectroscopic studies of uranium-calcite interface phenomena. J. Nucl. Mater., 248 pp. 408-411.

Gerdes, A. and Zeh, A., (2006). Combined U–Pb and Hf isotope LA-(MC-) ICP-MS analyses of detrital zircons: comparison with SHRIMP and new constraints for the provenance and age of an Armorican metasediment in Central Germany. Earth and Planetary Science Letters. 249 (1-2) 47-61. DOI: 10.1016/j.epsl.2006.06.039

Gerdes, A., Zeh, A., (2009). Zircon formation versus zircon alteration-new insights from combined V-Ph and Lu-Hf in situ LA-ICP-MS analyses, and consequences for the interpretation of Archean zircon from the Central Zone of the Limpopo Belt. Chem. Geol. 261 (3-4), 230-243. https://doi.org/ 10.1016/j.chemgeo.2008.03.005.

Gilbert, G. K. (1895): Sedimentary measurement of Cretaceous time. – J. Geol. 3:121 – 127.

Godeau, N., Deschamps, P., Guihou, A., Leonide, P., Tendil, A., Gerdes, A., Hamelin, J.G., 2018. U-Pb dating of calcite cement and diagenetic history in microporous carbonate reservoirs: case of the Urgonian Limestone, France. Geology. 46 (3), 247-250. DOI: 10.1130/G39905.1.

Goodfellow B.W., Viola G, Bingen B, Nuriel P and Kylander-Clark ARC (2017). Palaeocene faulting in SE Sweden from U–Pb dating of slickenfibre calcite. Terra Nova 29, 321–28

Gomes, J. P. B., Bunevich, R.B., Tonietto, S.N., Alves, D.B., Santos, J.F., Whitaker, F.F. (2020). Climatic signals in lacustrine deposits of the Upper Yacoraite Formation, Western Argentina: Evidence from clay minerals, analcime, dolomite and fibrous calcite. Sedimentology. Doi: 10.1111/sed.12700

Gómez-Omil, R.J., Boll, A., Hernández, R.M., (1987). Cuenca cretácico-terciaria del Noroeste argentino (Grupo Salta). In: X Congr. Geol. Argent., 5, Tucumán, p. 9 (inédit). Gomez Omil RJ, Boll A, Hernandez RM (1989) Cuenca cretacicoterciaria del Noroeste argentino (Grupo Salta). In: Chebli GA, Spalletti LA (eds) Cuencas Sedimentarias Argentinas. Universidad Nacional de Tucuman, Serie de Correlacion Geologica 6:43–64.

Gradstein, F.M., Ogg, J.G., (2012). The ChronostratigraphicScale. In: Gradstein et al., The Geologic Time Scale 2012.Elsevier Publ. Co.

Guillong, M., Wotzlaw, J. F., Looser, N., and Laurent, O. 2020. Evaluating the reliability of U–Pb laser ablation inductively coupled plasma mass spectrometry (LA-ICP-MS) carbonate geochronology: matrix issues and a potential calcite validation reference material. Geochronology. 2, 155–167, DOI:10.5194/gchron-2-155-2020.

Haynes, L.L., Bärbel Hönisch. (2020). The seawater carbon inventory at the Paleocene–Eocene Thermal Maximum. Proceedings of the

National Academy of Sciences. 117 (39) 24088-24095. DOI: 10.1073/pnas.2003197117.

Hansman, R. J., Albert, R., Gerdes, A., Ring, U., (2018). Absolute ages of multiple generations of brittle structures by U-Pb dating of calcite. Geology. 46 (3), 207-210. DOI:0.1130/G39822.1.

Hargrave, J.E., Hicks, M.K., Scholz, C.A. (2014). LACUSTRINE CARBONATES FROM LAKE TURKANA, KENYA: A DEPOSITIONAL MODEL OF CARBONATES IN AN EXTENSIONAL BASIN. Journal of Sedimentary Research. Vol 84. Pages 224-237. DOI: 10.2110/jsr.2014.22.

Harris, p.m., Diaz, M.R., Eberli, G.P. (2019). The formation and distribution of Modern Ooids on Great Bahama Bank. Annual review of Marine Science. Vol 11. 491-516. DOI: 10.1146/annurev-marine-010318-095251

Hernandez, R., Disalvo, A., Boll, A. and Gomez Omil, R. (1999). Sequence Stratigraphy of Salta Group, focusing at sub-basins Metan-Alemania, Northwest Argentine. In Congreso geologico argentino. Nacional Univ. Salta, Salta, 264–284.

Hilgen, F. J., Lourens, L. J., van Dam, J. A., (2012). The Neogene Period, in: Gradstein, F., Ogg, J., Schmitz, M. & Ogg, G. (Eds). The Geological Time Scale 2012. Elsevier, Amsterdam. https://doi.org/ 10.1016/B978-0-444-59425-9.00029-9.

Hilgen, F. J., W. Schwarzacher& A. Strasser (2004): Concepts and definitions in cyclostratigraphy (second report of the cyclostratigraphy working group). – SEPM. Spec. Publ. 81:303 – 305.

Hill, C. A., Polyak, V. J., Asmerom, Y., Provencio, P. P. 2016. Constraints on a Late Cretaceous uplift, denudation, and incision of the Grand Canyon region, southwestern Colorado Plateau, USA, from U-Pb dating of lacustrine limestone. 35 (4), 896-906. DOI:10.1002/2016TC004166.

Hiess, J., Condon, D. J., McLean, N., Noble, S.R. (2012). ^{238}U/^{235}U Systematics in Terrestrial Uranium-Bearing Minerals. Science 335, 1610. DOI: 10.1126/science.1215507.

Hyland, E.G., Sheldon, N.D. (2018). Comment on “Paleosol-based paleoclimate reconstruction of the Paleocene-Eocene ThermalMaximum, northern Argentina” by Andrews, E., White, T., and del Papa, C. [Palaeogeography, Palaeoclimatology, Palaeoecology, v. 471, p. 181–195]. Palaeogeography, Palaeoclimatology, Palaeoecology 511 (2018) 639–642.

Hyland, E.G., Sheldon, N.D., Cotton, J.M., (2015). Terrestrial evidence for a two-stage mid-Paleocene biotic event. Palaeogeogr. Palaeoclimatol. Palaeoecol. 417, 371–378.

Hyland, E.G., Sheldon, N.D., Cotton, J.M., (2017). Constraining the early Eocene climatic optimum: a terrestrial interhemispheric comparison. Geol. Soc. Am. Bull. 129, 244–252.

Hoareau, G., Claverie, F., Pecheyran, C., Paroissin, C., Grignard, P., Motte, G., Chailan,O., Girard, J. (2021). Direct U–Pb dating of carbonates from micron-scale femtosecond laser ablation inductively coupled plasma mass spectrometry images using robust regression. Geochronology, 3, 67–87, 2021. DOI: 10.5194/gchron-3-67-2021

Hodgson, D.M., Bernhardt, A., Michael C.A., Da Silva A., Fosdick J.C., Mauz B., Midtkandal, I., Owen, A., Romans, B. W. (2018) Grand Challenges (and Great Opportunities) in Sedimentology, Stratigraphy, and Diagenesis Research. Frontiers in Earth Science. 6. DOI: 10.3389/feart.2018.00173.

Holdsworth, R. E., McCaffrey, K. J. W., Dempsey, E., Roberts, N.M. W., Hardman, K., Morton, A., Feely, M., Hunt, J., Conway, A., and Robertson, A. (2019). Natural fracture propping and earthquakeinduced oil migration in fractured basement reservoirs, Geology, 47, 700–704.

Holdsworth, R. E., Trice, R., Hardman, K., McCaffrey, K. J. W., Morton, A., Frei, D., Dempsey, E., Bird, A., Rogers, S. (2020). The natureand age of basement host rocks and fissure fills in the Lancasterfield fractured reservoir, West of Shetland, J. Geol. Soc.,177, 1057–1073.

Holmes, A. 1911. The association of lead with uranium in rock-minerals, and its application to the measurement of geological time. Proceedings of the Royal Society (A), 85, 248-256.

Hopley, P.J., Reade, H., Parrish, R., De Kock, M. and Adams, J.W (2019).: Speleothem evidence for C3 dominated vegetation during the Late Miocene (Messinian) of South Africa. Review of Palaeobotany and Palynology, 264, 75-89. DOI: 10.1016/j.revpalbo.2019.02.006

Horgan, B.H.N., B. R. Anderson, Dromart, D., Amador, E.S., Rice, M.S. (2020). The mineral diversity of Jezero crater: Evidence for possible lacustrine carbonates on Mars. Icarus, Volume 339, https://doi.org/10.1016/j.icarus.2019.113526.

Horstwood, M.S.A., Košler, J., Gehrels, G., Jackson, S.E., McLean, N.M., Paton, C., Pearson, N.J., Sircombe, K., Sylvester, P., Vermeesch, P., Bowring, J.F., Condon, D.J. and Schoene, B. (2016), Community-Derived Standards for LA-ICP-MS U-(Th-)Pb Geochronology – Uncertainty Propagation, Age Interpretation and Data Reporting. Geostand Geoanal Res, 40: 311-332. DOI: 10.1111/j.1751-908X.2016.00379.x

Herrero, M.J., Escavy, J.I. (2010). Chapter 6 Economic Aspects ofContinental Carbonates and Carbonates Transformed under Continental Conditions, Editor(s): A.M. Alonso-Zarza, L.H. Tanner, Developments in Sedimentology, Elsevier. Volume 62, 2010, Pages 275-296, DOI:10.1016/S0070-4571(09)06206-2

Hull P.M., Bornemann A., Penman D.E., Henehan M.J., Norris R.D., Wilson P.A., Blum P., Alegret L., Batenburg S.J., Bown P.R., Bralower T.J., Cournede C., Deutsch A., Donner B., Friedrich O., Jehle S., Kim H., Kroon D., Lippert P.C., Loroch D., Moebius I., Moriya K., Peppe D.J., Ravizza G.E., Röhl U., Schueth J.D., Sepúlveda J., Sexton P.F., Sibert E.C., Śliwińska K.K., Summons R.E., Thomas E., Westerhold T., Whiteside J.H., Yamaguchi T., Zachos J.C. (2020). On impact and volcanism across the Cretaceous-Paleogene boundary. Science. 17; 367(6475): 266-272. Doi: 10.1126/science.aay5055.

Hutton, James (1788). "Theory of the Earth; or an Investigation of the Laws observable in the Composition, Dissolution, and Restoration of Land upon the Globe". Transactions of the Royal Society of Edinburgh. Royal Society of Edinburgh. **1** (Part 2): 209–304.

Incerpi, N., Martire, L., Manatschal, G., Bernasconi, S.M., Gerdes, A., Czuppon, G., Palcsu, L., Karner, G.D., Johnson, C.A. and Figueredo, P.H. (2019). Hydrothermal fluid flow associated to the extensional evolution of the Adriatic rifted margin: Insights from the pre-to post-rift sedimentary sequence (SE Switzerland, N ITALY). Basin Research, in press, DOI:10.1111/bre.12370.

Inglis, G. N., Bragg, F., Burls, N. J., Cramwinckel, M. J., Evans, D., Foster, G. L., Huber, M., Lunt, D. J., Siler, N., Steinig, S., Tierney, J. E., Wilkinson, R., Anagnostou, E., de Boer, A. M., Dunkley Jones, T., Edgar, K. M., Hollis, C. J., Hutchinson, D. K., and Pancost, R. D. (2020). Global mean surface temperature and climate sensitivity of the early Eocene Climatic Optimum (EECO), Paleocene–Eocene Thermal Maximum (PETM), and latest Paleocene, Clim. Past, 16, 1953–1968, DOI:10.5194/cp-16-1953-2020.

Yokoyama, T., Kimura, J. I., Mitsuguchi, T., Danhara, T., Hirata, T., Sakata, S., Iwano, H., Maruyama, S., Chang, Q., Miyazaki, T., Murakami, H., and Saito-Kokubu, Y. (2018). U-Pb dating of calcite using LA-ICP-MS: Instrumental setup for non-matrix-matched age dating and determination of analytical areas using elemental imaging, Geochemical Journal, 52, 531-540, DOI: 10.2343/geochemj.2.0541, 2018

Jackson, S.E., Pearson, N.J., Griffin, W.L., ì Belousova, E.A. (2004). The application of laser ablation-inductively coupled plasma-mass spectrometry to in situ U–Pb zircon geochronology, Chemical Geology, 211 (1–2), 47-69. DOI: 10.1016/j.chemgeo.2004.06.017.ì

Jankowski B., (1977). Die Postimpakt-Sedimente in der Forschungsbohrung Nördlingen 1973. *Geol. Bavarica.* 75, 21– 36.

Jankowski, B. 1981. Die Geschichte der Sedimentation im Nördlinger Ries und Randecker Maar. Bochumer geologische und geotechnische Arbeiten 6: 1– 315.

Jarvis, J. E., Williams J.G. (1993). Laser ablation inductively coupled plasma mass spectrometry (LA-ICP-MS): a rapid technique for the direct, quantitative determination of major, trace and rare-earth elements in geological samples. Chemical Geology. Vol 105, Issue 3-4. Pages 251-262.

Jones, C.E., Halliday, A.N., Lohmann, K.C. (1995). The impact of diagenesis on high-precision UPb dating of ancient carbonates: An example from the Late Permian of New Mexico, Earth and Planetary Science Letters. 134 (3–4), 409-423. DOI: 10.1016/0012-821X(95)00128-Y.

Kaczmarek, S.E., Sibley, D.F. (2014). Direct physical evidence of dolomite recrystallization. Sedimentology, 61: 1862-1882. DOI: 10.1111/sed.12119

Kamenetsky, V., Belousova, E., Giuliani, A., Kamenetsky, M., Goemann, K., Griffin, W. (2014). Chemical abrasion of zircon and ilmenite megacrysts in the Monastery kimberlite: Implications for the composition of kimberlite melts. Chemical Geology. 383. 76–85. DOI: 10.1016/j.chemgeo.2014.06.008.

Katz, Barry. (2001). Lacustrine basin hydrocarbon exploration - Current thoughts. Journal of Paleolimnology. 26, 161-179. DOI: 10.1023/A:1011173805661.

Kelly, S.D. Newville, M., Cheng L.R., Kemner, K. M., Sutton, S.R., Fenter, P., Sturchio, N.C., Spötl, C. (2003). Uranyl Incorporation in Natural Calcite. Environmental Science and Technology. 37. DOI: 10.1021/es025962f.

Kelts K., Talbot M. (1990) Lacustrine Carbonates as Geochemical Archives of Environmental Change and Biotic/Abiotic Interactions. In: Tilzer M.M., Serruya C. (eds) Large Lakes. Brock/Springer Series in Contemporary Bioscience. Springer, Berlin, Heidelberg. DOI:10.1007/978-3-642-84077-7_15.

Kirkland, C.L., Yakymchuk, C., Szilas, K., Evans, N., Hollis, J., McDonald, B., Gardiner, N.J. (2018). Apatite: a U-Pb thermochronometer or geochronometer? Lithos, Volumes 318–319, Pages 143-157, DOI: 10.1016/j.lithos.2018.08.007.

Klinkhammer, G. P. and Palmer, M. R (1991). Uranium in the Oceans: Where it goes and why. Geochim. Cosmochim. Acta 55, 1799-1806.

Kupecz, J.A., Land, L.S. (1994). Progressive Recrystallization and Stabilization of Early-Stage Dolomite: Lower Ordovician Ellenburger Group, West Texas. In Dolomites (eds B. Purser, M. Tucker and D. Zenger). DOI: 10.1002/9781444304077.ch15

Kurumada, Y., Aoki, S., Aoki, K., Kato, D., Saneyoshi, M., Tsogtbaatar, K., Windley, B. F., Ishigaki, S. (2020). Calcite U–Pb age of the Cretaceous vertebrate-bearing Bayn Shire Formation in the Eastern Gobi Desert of Mongolia: Usefulness of caliche for age determination. Terra Nova, 00:1-7. DOI: 10.1111/ter.12456.

Kreissl, S., Gerdes, A., Walter, B.F., Neumann, U., Wenzel, T., Markl, G. (2018). Reconstruction of a >200 Ma multi-stage “five element” Bi-Co-Ni-Fe-As-S system in the Penninic Alps, Switzerland, Ore Geology Reviews, Volume 95, Pages 746-788. DOI: 10.1016/j.oregeorev.2018.02.008.

Lachniet, M.S., Bernal, J.P., Asmerom, Y., Poylak, V. (2012). Uranium loss and aragonite and calcite

age discordance in a calcitized aragonite stalagmite. Quaternary Geochronology. Vol. 14, pp. 26-37.

Langereis, C.G., Krijgsman, W., Muttoni, G., and Menning, M. (2010). Magnetostratigraphy – concepts, definitions, and applications. Newsletter on Stratigraphy. Vol 43/3. Page 207-233.

Langmuir, D. (1978), Uranium solution-mineral equilibria at low temperatures with applications to sedimentary ore deposits, Geochim. Cosmochim.

Acta, 42, 547– 569, doi:10.1016/0016-7037(78)90001-7.

Lawson, M., Shenton, B.J., Stolper, D.A., Eiler, J.M., Rasbury, E.T., Becker, T.P., Phillips-Lander, C.M., Buono, A.S., Becker, S.P., Pottorf, R. and Gray, G.G. (2018). Deciphering the diagenetic history of the El Abra Formation of eastern Mexico using reordered clumped isotope temperatures and U-Pb dating. GSA Bulletin, 130, 617- 1602 629

Lehmann, J. (2015). Ammonite Biostratigraphy of the Cretaceous—An Overview. DOI: 10.1007/978-94-017-9633-0_15

Lehrmann, D., Ramezani, J., Bowring, S., Martin, M., Montgomery, P., Enos, P., Payne, J., Orchard, M., Hongmei, W., Jiayong, W. (2006). Timing of recovery from the end-Permian extinction: Geochronologic and biostratigraphi constraints from south China. Geology. 34. DOI: 10.1130/G22827A.1.

Leng, M.J., Marshall, J. D. (2004). Paleoclimate interpretation of stable isotope data from lake sediment archives. Quaternary Science Reviews. Vol 23. Issue 7-8. Pages 811-831. DOI: 10.1016/j.quascirev.2003.06.012

Li M, Zhu L, Wang J, Ju J, Liu C, Ma Q, Xu T, Qiao B and Wang X (2021) Holocene Lake Evolution and Glacial Fluctuations Indicated by Carbonate Minerals and Their Isotopic Compositions in the Sediments of a Glacial Melt Recharge Lake on the Northwestern Tibetan Plateau. Front. Earth Sci. 9:656281. doi: 10.3389/feart.2021.656281

Li, Q., Parrish, R. R., Horstwood, M. S. A., McArthur, J. M. (2014). U–Pb dating of cements in Mesozoic ammonites. Chem. Geo. 376, 7683. DOI:10.1016/j.chemgeo.2014.03.020.

Liivamägi, S., Środoń, J., Bojanowski, M.J. , Gerdes,A., Stanek, J.J., Williams, L., Szczerba, M., (2018). Paleosols on the Ediacaran basalts of the East European Craton: A unique record of paleoweathering with minimum diagenetic overprint, Precambrian Research,316,66-82. DOI:10.1016/j.precamres.2018.07.020.

Looser, N. Madritsch, H. Guillong, M., Laurent O., Wohlwend, S. (2021). Absolute Age and Temperature Constraints on Deformation Along the Basal Décollement of the Jura Fold and Thrust Belt From Carbonate U-Pb Dating and Clumped Isotopes Tectonics. Vol 40 (3). DOI: 10.1029/2020TC006439.

Lougheed, B. C., Obrochta, S. P. (2019). A Rapid, Deterministic Age-Depth Modeling Routine for Geological Sequences with Inherent Depth Uncertainty. Paleoceanography and paleoclimatology. 34 (1) 122-133. DOI: 10.1029/2018PA003457.

Lowe, D.J., (2011). Tephrochronology and its application: A review. Quaternary geochronology. Vol 6. Issue 2. Page 107-153). DOI: 10.1016/j.quageo.2010.08.003.

Lucas, S. G. (2018). The GSSP Method of Chronostratigraphy: A Critical Review. Frontiers in Earth Science. Vol 8, Page 191. DOI=10.3389/feart.2018.00191.

Lucas, S. G. (2021). Biostratigraphy in Encyclopedia of Geology (Second Edition) 2021, Pages 89-95. https://doi.org/10.1016/B978-0-08-102908-4.00076-XGet ri

Ludwig, K. R. (2012). User's Manual for Isoplot Version 3.75–4.15: a Geochronological Toolkit for Microsoft Excel Berkeley Geochronological Center Special Publication, 5 (2012).

Lukoczki, G., Haas, J., Gregg, J.M., Machel, H.G., Kele, S., and John, C.M., (2019). Multi-phase dolomitization and recrystallization of Middle Triassic shallow marine–peritidal carbonates from the Mecsek Mts. (SW Hungary), as inferred from petrography, carbon, oxygen, strontium and clumped isotope data: Marineand Petroleum Geology, 101, 440–458. DOI:10.1016/j.marpetgeo.2018.12.004.

Ma P., Wang, L., Wang, C., Wu, X., Wei, Y. (2015). Organic-matter accumulation of the lacustrine Lunpola oil shale, central Tibetan Plateau: Controlled by the paleoclimate, provenance, and drainage system. International

Journal of Coal Geology. 147-148, 58-70. DOI: 10.1016/j.coal.2015.06.011

MacDonald, J. M., Faithfull, J. W., Roberts, N. M. W., Davies, A. J., Holdsworth, C. M., Newton, M., Williamson, S., Boyce, A., John, C. M. 2019. Clumped-isotope palaeothermometry and LA-ICP-MS U–Pb dating of lava-pile hydrothermal calcite veins. Contrib Mineral Petrol, 174, 63. https://doi.org/10.1007/s00410-019-1599-x.

Machel, H.G. (1997). Recrystallization versus neomorphism, and the concept of 'significant recrystallization' in dolomite research, Sedimentary Geology,113, 3–4,161-168, DOI: 10.1016/S0037-0738(97)00078-X

Mädel F., (1984). Estratigrafıa del tramo inferior del pozo descubridor Palmar Largo x-1. YPF Bol Inf Petrol 1–2:109.

Mángano, M. G., Buatois, L. A. (2021). Cambrian Explosion, Editor(s): David Alderton, Scott A. Elias, Encyclopedia of Geology (Second Edition), Academic Press, Pages 583-602, DOI:10.1016/B978-0-08-102908-4.00142-9.

Mangenot, X., Gasparrini, M., Gerdes, A., Bonifacie M., Rouchon V. (2018). An emerging thermochronometer for carbonate-bearing rocks: Δ_{47}/(U-Pb). Geology. 46 (12), 1067-1070. DOI:10.1130/G45196.1.

Mangenot, X. (2017). Pairing ∆47 geothermometry and U/Pb geochronometry to reconstruct the diagenetic, thermal and fluid-flow histories of carbonate rocks in sedimentary basins. PhD thesis. DOI: 10.13140/RG.2.2.21283.71200.

Marquillas R.A. (1985). Estratigrafıa, sedimentologıa y paleoambientes de la Formacion Yacoraite (Cretacico Superior) en el tramo austral de la cuenca, norte argentino. Tesis Doctoral, Universidad Nacional de Salta, 1–139.

Marquillas, R.A., del Papa, C.E., Sabino, I.F., (2005). Sedimentary aspects and paleoenvironmental evolution of a rift basin: Salta Group (Cretaceous-Paleogene), northwestern Argentina. International Journal of Earth Sciences 54 94-113.

Marquillas, R.A., del Papa, C., Sabino, I., and Heredia, J., (2003). Prospección del límite K/T en la cuenca del Noroeste, Argentina: Revista de la

Marquillas, R.A., Sabino, I., Sial, N.A., Del Papa, C., Ferreira, V., Matthews, S. (2007). Carbon and oxygen isotopes of Maastrichtian-Danian shallow marine carbonates: Yacoraite Formation, northwestern Argentina: Journal of South American Earth Sciences, 23, 4, 304-320. DOI: 10.1016/j.jsames.2007.02.009.

Marquillas, R.A., Salfity, J.A., Matthews, S.J., Matteini, M., Dantas, E., (2011). U-Pb zircon age of the Yacoraite Formation and its significance to the Cretaceous-Tertiary boundary in the Salta Basin, Argentina. In: Salfity, J.A., Marquillas, R.A. (Eds.), Cenezoic Geology of the Central Andes of Argentina. SCS Publisher, pp. 227–246.

Marquillas, R.A., Salfity, J.A., (1989). Distribución regional de los miembros de la Formación Yacoraite (Cretácico Superior) en el noroeste argentino. Contribuciones de los Simposios sobre Cretácico de América Latina, Parte A, Eventos y Registro Sedimentario 253-272. Buenos Aires.

Mason, A. J., Henderson, G. M., Vaks, A. 2016. An Acetic Acid-Based Extraction Protocol for the Recovery of U, Th and Pb from Calcium Carbonates for U-(Th)-Pb Geochronology. Geostand. Geoanalytical Res, 37 (3), 261-275. DOI:10.1111/j.1751-908X.2013.00219.x.

Matys Grygar, T., Hošek, M., Mach, K., Schnabl, P., & Martinez, M. (2017). Climatic instability before the Miocene Climatic Optimum reflected in a Central European lacustrine record from the Most Basin in the Czech Republic. *Palaeogeography, palaeoclimatology, palaeoecology, 485,* 930-945. Doi: 10.1016/j.palaeo.2017.08.011

McArthur, J.M. Howarth, R.J. Shields, G.A. Zhou, Y. (2020). Chapter 7 - Strontium Isotope Stratigraphy, Editor(s): Felix M. Gradstein, James G. Ogg, Mark D. Schmitz, Gabi M. Ogg, Geologic Time Scale 2020, Elsevier, Pages 211-238, DOI: 10.1016/B978-0-12-824360-2.00007-3.

McCormack, J., Kwiecien (2021). Coeval primary and diagenetic carbonates in lacustrine sediments challenge palaeoclimate interpretations. Sci Rep 11, 7935 (2021). DOI: 10.1038/s41598-021-86872-1.

McInerney, F. A., & Wing, S. L. (2011). The Paleocene-Eocene Thermal Maximum: A perturbation of carbon cycle, climate, and biosphere with implications for the future. Annual Review of Earth and Planetary Sciences, 39, 489-516. DOI: 10.1146/annurev-earth-040610-133431

McManus J, Berelson, W.M., Severmann, S., Poulson, R.L., Hammond, D.E., Klinkhammer, G.P., Holm, C. (2006). Molybdenum and uranium geochemistry in continental margin sediments: paleoproxy potential. Geochimica et Cosmochimica Acta. 70:4643–4662.

Meinhold, G., Roberts, N. Arslan, A., Jensen, S., Ebbestad, J., Högström, A., Taylor, W. (2020). U–Pb dating of calcite in ancient carbonates for age estimates of syn- to post-depositional processes: a case study from the upper Ediacaran strata of Finnmark, Arctic Norway Geol. Mag., 157, 1367-1372. DOI: 10.1017/S0016756820000564

Milankovitch, M. (1920). Mathematical Theory of Heat Phenomena Produced by Solar Radiation (Gauthier-Villars, 1920).

Milankovitch, M. (1941). Canon of Insolation and the Ice-age Problem (Königlich Serbische Akademie, 1941).

Miyajima, Y. Saito, A., Kagi, H., Yokoyama, T., Takahashi, Y., Hirata, T. (2020). Incorporation of U, Pb and Rare Earth Elements in Calcite through Crystallisation from Amorphous Calcium Carbonate: Simple Preparation of Reference Materials for Microanalysis. Geostandards and Geoanalytical Research. 45(1). Pages 189-205. DOI: 10.1111/ggr.12367.

Miller, J. S., Matzel, J. E. P., Miller, C. F., Burgess, S. D., Miller, R.B. (2007). Zircon growth and recycling during the assembly of large, composite arc plutons, Journal of Volcanology and Geothermal Research, Volume 167, Issues 1–4, DOI:10.1016/j.jvolgeores.2007.04.019.

Meinhold, G., Roberts, N., Arslan, A., Jensen, S., Ebbestad, J., Högström, A. Høyberget, M., Agić, H., Palacios, T., Taylor, W. L. (2020). U–Pb dating of calcite in ancient carbonates for age estimates of syn- to post-depositional processes: A case study from the upper Ediacaran strata of Finnmark, Arctic Norway. Geological Magazine, 157(8), 1367-1372. Doi:10.1017/S0016756820000564.

Methner K., Mulch A., Fiebig J., Wacker U., Gerdes A., Graham S.A., Chamberlain C.P. (2016). Rapid Middle Eocene temperature change in western North America. Earth Planet Sci Lett 450:132–139.

Montanez, I.P., Read, F.J. (1992). Fluid-rock interaction history during stabilization of early dolomites, Upper Knox Group (Lower Ordovician) U.S. Appalachians. J. Sed. Petrol., 62, 735-778.

Montano D., Gasparrini M., Gerdes A., Albert R., Della Porta, G. (2021). In-situ U-Pb dating of Ries Crater lacustrine carbonates (Miocene, South-West Germany): implications for continental carbonate chronostratigraphy. Earth and Planetary Science Letters 568 (1):117011. DOI: 10.1016/j.epsl.2021.117011

Moorbath S., Taylor P. N., Orpen J. L., Treloar P., Wilson J. F. (1987). First direct radiometric dating of Archaean stromatolite limestone. Nature 326:865–867. DOI: 10.1038/326865a0.

Molina, E., Arenillas, J., Arz, J.A. (1998). Mass extinction in planktic foraminifera at the Cretaceous/Tertiary boundary in subtropical and temperate latitudes. Bulletin de la Societe Geologique de France 169(3):351-363.

Mon, R., Salfity, J. (1995). Tectonic Evolution of the Andes of Northern Argentina. Chapter from: M 62: Petroleum Basins of South America. Edited by A. J. Tankard, R. Suarez Soruco, and H. J. Welsink.

Monaldi, C.R., Salfity, J.A., Kley, J. (2008). Preserved extensional structures in an inverted Cretaceous rift basin, northwestern Argentina: Outcrop examples and implications for fault reactivation. Tectonics 27 (1). DOI: 10.1029/2006TC001993.

Moreno J.A. (1970). Estratigrafía y paleogeografía del Cretácico superior en la cuenca del noroeste argentino, con especial mención de los Subgrupos Balbuena y Santa Bárbara. Rev Asoc Geol Arg 24:9–44.

Moroni, A.M. (1982). Correlación palinológica en la Formaciones Olmedo y Yacoraite. Cuenca del Noroeste Argentino. 3o Congreso Geológico Chileno (Concepción), Actas, 340-349.

Moroni, A. M. (1984). Mtchedlishvilia saltenia n. sp. en sedimentitasdel Grupo Salta, provincia de Salta, in Actas, Congreso Ar-gentino de Paleontología y Bioestratigrafía, 3th, Corrien-tes: Buenos Aires, Asociación Paleontológica Argentina, 129-139.

Morrison, J.O. & Brand, U. (1988). An evaluation of diagenesis and chemostratigraphy of upper Cretaceous molluscs from the Canadian Interior Seaway. Chemical Geology Isotope Geoscience section. Vol. 72(3), pp. 235-248.

Mottram, C.M., Kellett, D.A., Barresi, T., Zwingmann, H., Friend, M., Todd, A., Percival, J.B. (2020). Syncing fault rock clocks: Direct comparison of U-Pb carbonate and K-Ar illite fault dating methods. Geology. 48 (12), 1179–1183. DOI: 10.1130/G47778.1.

Muttik, N., Kirsimäe, K., Newsom, H. E., Williams, L. B. 2011. Boron isotope composition of secondary smectite in suevites at the Ries crater, Germany: Boron fractionation in weathering and hydrothermal processes. Earth and Planetary Science Letters, 310, 244–251. DOI: 10.1016/j.epsl.2011.08.028.

Nakashima, S., Yoko K., Norio K., Motoko I., and Natsuki M. (2018). "Geochemistry and the Origin of Life: From Extraterrestrial Processes, Chemical Evolution on Earth, Fossilized Life’s Records, to Natures of the Extant Life" *Life* 8, no. 4: 39. DOI: 0.3390/life8040039

Neiva, A.M.R., Carvalho, P.C.S., Antunes, I.M.H.R., Albuquerque, M.T.D., Santos, A.C.S., Cunha, P.P., Henriques, S.B.A. (2019). Assessment of metal and metalloid contamination in the waters and stream sediments around the abandoned uranium mine area from Mortórios, central Portugal, Journal of Geochemical Exploration, Volume 202. Pages 35-48. DOI: 10.1016/j.gexplo.2019.03.020.

Nicholson, S. L., Pike, A. W., Hosfield, R., Roberts, N. M. W., Sahy, D., Woodhead, J., Cheng, H., Edwards, R. L., Affolter, S., Leuenberger, M., and Burns, S. J. (2020). Pluvial periods in Southern Arabia over the last 1.1 million-years, Quaternary Sci. Rev., 229, 106112, DOI: 10.1016/j.quascirev.2019.106112.

Noronha-D'Mello, C.A.A., Nair, B.S. Mahesh, A.K. Warrier, Rahul Mohan (2021). Siby Kurian. Glacial-Holocene climate-driven shifts in lacustrine and terrestrial environments: Rock magnetic and geochemical evidence from East Antarctic Mochou Lake, Palaeogeography, Palaeoclimatology, Palaeoecology, Volume 576. DOI:10.1016/j.palaeo.2021.110505.

Nuriel P., Weinberger, R., Kylander-Clark, A.R.C., Hacker, B.R., Craddock, J.P. (2017). The onset of the Dead Sea transform based on calcite age-strain analyses. The Geological society of America.

Nuriel, P., Craddock, J., Kylander-Clark, A. R., Uysal, T., Karabacak, V., Dirik, R. K., Hacker, B. R. and Weinberger, R. (2019). Reactivation history of the North Anatolian fault zone based on calcite age-strain analyses. Geology, 47, 465-469. https:// doi.org/10.1130/G45727.1.

Nuriel, P., Wotzlaw, J., Ovtcharova, M., Vaks, A., Stremtan, C., Šala, M., Roberts, N. M. W., Kylander-Clark, A.R.C., (2021). The use of ASH-15 flowstone as a matrix-matched reference material for laser-ablation U − Pb geochronology of calcite. Geochronology, 3, 35–47, DOI: 10.5194/gchron-3-35-2021

O’Brien, G. W., Goldie Divko LM, Tingate P, et al. (2011). Basin resource management frameworks: 4D geoscience information, modelling and knowledge systems to allow the informed assessment and management of earth resources. Energy Procedia 2011; 4: 3865–3872.

Omarini, R.H., Salfity, J.A., Linares, E., Viramonte, J.G., Gorustovich, S.A., (1989). Petrologia geoquimica y edad de un filon lamproitico en el Subgrupo Pirgua (Alemania-Salta). Revista del Instituto de Geologia y Mineria 7 (Universidad Nacional de Jujuy).

Opdyke, N.D., Channell, J.E.T., 1996. Magnetic Stratigraphy. San Diego, CA: Academic Press, page 346.

Osinski, G.R., Cockell, C.S., Pontefract, A. Sapers., H.M. (2020). The Role of Meteorite Impacts in the Origin of Life. Astrobiology. Vol 20. No.9. DOI: 10.1089/ast.2019.2203.

Pache, M., Reitner, J., Arp, G., 2001. Geochemical evidence for the formation of a large Miocene "travertine" mound at a sublacustrine spring in a soda lake (Wallerstein Castle Rock, Nördlinger Ries, Germany). Facies. 45 (1), 211-230. DOI:/10.1007/BF02668114.

Pagel, M., Bonifacie, M., Schneider, D.A., Gautheron, C., Brigaud, B., Calmels, D., Cros, A., Saint-Bezar, B., Landrein, P., Sutcliffe, C. and Davis, D. (2018). Improving paleohydrological and diagenetic reconstructions in calcite veins and breccia of a sedimentary basin by combining Δ47 temperature, δ18Owater and U-Pb age. ChemicalGeology, 481, 1-17.

Palma, R., (1986). Procesos diageneticos en las rocas calcfireas de la Formaci6n Yacoraite. Cretacico Superior. Noroeste de Argentina. Primera Reuni6n Argentina de Sedimentologia. Reslimenes expandidos, 236-238.

Pancost, R. (2017) Climate change narratives. Nature Geosci 10, 466–468. DOI: 10.1038/ngeo2981.

Paquette, J.L., Barbosa, J., Rohais, S., Cruz, S., Goncalves, P., Peucat, J., Leal, A., Santos-Pinto, M., Martin, H. (2015). The geological roots of South America: 4.1Ga and 3.7Ga zircon crystals discovered in N.E. Brazil and N.W. Argentina. Precambrian Research. 271. 49-55. DOI: 10.1016/j.precamres.2015.09.027.

Parrish, R.R., Parrish, C.M. and Lasalle, S. (2018). Vein calcite dating reveals Pyrenean orogen as cause of Paleogene deformation in southern England, Journal of the Geological Society, 175, 425-442.

Parrish, J.T., Rasbury, E.T., Chan, A., Hasiotis, S.T. (2019). Earliest Jurassic U-Pb ages from carbonate deposits in the Navajo Sandstone, southeastern Utah, USA. Geology 2019; 47 (11): 1015–1019. doi: 10.1130/G46338.1

Petrus, J. A., Chew, D. M., Leybourne, M. I., and Kamber, B. S. (2017). A new approach to laser-ablation inductively-coupled-plasma mass spectrometry (LA-ICP-MS) using the flexible map interrogation tool 'Monocle', CHEMICAL GEOLOGY, 463, 76–93, DOI: 10.1016/j.chemgeo.2017.04.027.

Patterson C., Brown H., Tilton G. and Inghram M. (1953). Concentration of Uranium and Lead and the Isotopic Composition of Lead in Meteoritic Material. Phys. Rev. 92, 1234-1235.

Pimentel, M., Carmo, I.O. and Terra, G.J.S. (2012). U-Pb age of tuffs from the Balbuena Group, Salta Basin, NW Argentina. In: VIII Simposio Sudamericano de Geologia Isotopica, Medellın. Resumos. Medellın: Universidad Nacional de Colombia.

Pohl, V. J. (1977). Paläomagnetische und gesteinsmagnetische Untersuchungen an den Kernen der Forschungsbohrung Nördlingen 1973. Geologica Bavarica 75, 328-348.

Pohl, J., Poschlod, K., Reimold, W. U., Meyer, C., Jacob, J., (2010). Ries crater, Germany: The Enkingen magnetic anomaly and associated drill core SUBO 18. In: Roger, L., Gibson, L., Reimold, W. U. (Eds.), Large Meteorite Impacts and Planetary Evolution IV, DOI:10.1130/2010.2465(10).

Pupin, J. P. (1976). Signification des caractères morphologiques du zircon commun des roches en pétrologie. Base de la méthode typologique.

Applications. (Thèse d'État), Université de Nice. 394 p.

Quattrocchio. M (2006). PALYNOLOGY AND PALAEOCOMMUNITIES OF THE PALEOGENE OF ARGENTINA. Revista Brasileira de Paleontologia 9 (1), 101-108, by the Sociedade Brasileira de Paleontologia**.**

Quattrocchio. M., Volkheimer, W. (2000). Palynological zonation of the Paleogene of the Colorado and Salta Group basin, Argentina. Rev Espanola Micropaleont 32:61–78.

Quattrocchio, M., Volkheimer, W., Marquillas, R., Salfity, J. (2005). Palynostratigraphy, palaeobiogeography and evolutionary significance of the Late Senonian and Early Palaeogene palynofloras of the Salta Group, northern Argentina. Revista Española de Micropaleontología. 37

Raine J.I., Beu A.G., Boyes A.F., Campbell H.J., Cooper R.A., Crampton J .S., Crundwell, M.P. Hollis, J.H., Morgans, H.E. (2015). Revised calibration of the New Zealand Geological Timescale: NZGT2015/1. GNS Science Report 2012/39. Lower Hutt, GNS Science.

Raup, D. M, Sepkoski, J.J. Jr. (1982). Mass extinctions in the marine fossil record. Science. Mar 19;215(4539):1501-3. doi: 10.1126/science.215.4539.1501.

Rasbury, E. T. and Cole, J. M., (2009). Directly dating geologic events: U-Pb dating of carbonates. Rev. Geophys. 47 (3). DOI: 10.1029/2007RG000246.

Rasbury, E.T., Present, T.M., Northrup, P., Tappero, R.V., Lanzirotti, A., Cole, J.M., Wooton, K.M., Hatton K. (2021). Tools for uranium characterization in carbonate samples: case studies of natural U–Pb geochronology reference materials. Geochronology, 3, 103–122, 2021. DOI: 10.5194/gchron-3-103-2021.

Raskovsky, M.A., (1968). Relevamiento geológico del sector sur delyacimiento Los Berthos [Seminario II]: Salta, UniversidadNacional de Tucumán, Facultad de Ciencias Naturales, 41 p.

Reeder, R.J., Nugent, M., Tait, C.D., Morris, D. E., Heald, S. M., Beck, K.M., W. P., Hess, Lanzirotti, A. (2001). Coprecipitation of Uranium(VI) with Calcite: XAFS, micro-XAS, and luminescence characterization, Geochimica et Cosmochimica Acta, Volume 65, Issue 20, Pages 3491-3503,
DOI: 10.1016/S0016-7037(01)00647-0.

Renne, P.R., Deino, A.L., Hilgen, F.J., Kuiper, K.F., Mark, D.F., Mitchell, W.S., Mor-gan, L.E., Mundil, R., Smit, J., (2013). Time scales of critical events around the Cretaceous–Paleogene boundary. Science339, 684–687.
.

Reyes, F.C., (1972) Correlaciones en el Cretácico de la cuenca andinade Bolivia, Perú y Chile: La Paz, Revista Técnica de Yaci-mientos Petrolíferos Fiscales Bolivianos, v. 1, p.101-144.

Reyes, F.C., Salfity, J.A. (1973). Consideraciones sobre la estratigrafía del Cretácico (Subgrupo Pirgua) del noroeste argentino. Actas 5th Congr Geol Arg 3:355–385.

Reyes, F.C., Salfity, J.A., Viramonte, J.G., Gutierrez, W. (1976). Consideraciones sobre el vulcanismo del Subgrupo Pirgua (Cretacico) en el norte argentino. Actas 6th Congr Geol Arg 1:205–223.

Resentini, A. Andò, S. Garzanti, E., Malusà, M.G., Pastore, G., Vermeesch, P., Chanvry, E., Dall'Asta, M. (2020). Zircon as a provenance tracer: Coupling Raman spectroscopy and UPb geochronology in source-to-sink studies, Chemical Geology, Volume 555, DOI:10.1016/j.chemgeo.2020.119828.

Riding, R., 1979. Origin and diagenesis of lacustrine algal bioherms at the margin of the Ries crater, Upper Miocene, southern Germany. Sedimentology. 26 (5), 645-680. DOI:10.1111/j.1365-3091.1979.tb00936.x.

Rihs, S. Sturchio, N. Orlandini, K. Cheng, L. Teng, H. Fenter, P. Bedzyk, M. (2004).

Interaction of uranyl with calcite in the presence of EDTA. Environ. Sci. Technol., 38, pp. 5078-5086.

Ring, U., Gerdes, A. (2016). Kinematics of the Alpenrhein - Bodensee graben system in the Central Alps: Oligocene/Miocene transtension due to formation of the Western Alps arc. Tectonics. 35. DOI: 10.1002/2015TC004085.

Roberts, N., Drost, K., Horstwood, M., Condon, D. J., Chew, D., Drake, H., Milodowski, A. E., McLean, N. M., Smye, A., Walker, R. J., Haslam, R., Hodson, K., Imber, J. Beaudoin, N. (2020a). LA-ICP-MS U-Pb carbonate geochronology: strategies, progress, and application to fracture-fill calcite. Geochronology Discussion, Copernicus Gesellschaft mbH. https://doi.org/ 10.5194/gchron-2019-15. In press, 2020.

Roberts, N. M. W., Lee, J.K., Holdsworth, R.E., Jeans, C., Farrant, A.F., Haslam, R. (2020b). Near-surface Palaeocene fluid flow, mineralisation and faulting at Flamborough Head, UK: new field observations and U–Pb calcite dating constraints Solid Earth. 11, 1931–1945, 2020 DOI: 10.5194/se-11-1931-2020

Roberts, N. M. W., Rasbury, T., Parrish, R. R., Smith, C. J. M., Horstwood, M. S. A., Condon, B. J., (2017). A calcite reference material for LA-ICP-MS U-Pb geochronology. Geochem. Geophys. 18 (7), 2807-2814. https://doi.org/ 10.1002/2016GC006784.

Roberts, N.M.W., Walker, R.J., (2016), U-Pb geochronology of calcite-mineralized faults: Absolute timing of rift-related fault events on the northeast Atlantic margin: Geology, v. 44, p. 531–534, DOI:10 .1130 /G37868 .1.

Roberts, N.M.W., Žák, J., Vacek, F., Sláma, J. (2021). No more blind dates with calcite: Fluid-flow vs. fault-slip along the Očkov thrust, Prague Basin, Geoscience Frontiers, Volume 12, Issue 4. DOI: 10.1016/j.gsf.2021.101143

Rocholl, A., Böhme, M., Gilg, H. A., Pohl J., Schaltegger, U., Wijbrans, J. (2018). Comment on ‘‘A high-precision ^{40}Ar/^{39}Ar age for the Nördlinger Ries impact crater, Germany, and implications for the accurate dating of terrestrial impact events” by Schmieder et al. (Geochim. et Cosmochim. Acta 220 (2018) 146–157). Geochim. et Cosmochim. Acta. 238, 599–601. DOI:10.1016/j.gca.2018.05.018.

Rocholl, A., Schaltegger, U., Gilg, H. A., Wijbrans, J., Böhme, M., (2017). The age of volcanic tuffs from the Upper Freshwater Molasse (North Alpine Foreland Basin) and their possible use for tephrostratigraphic correlations across Europe for the Middle Miocene. Int. J. Earth Sci. 107 (2), 387-407. DOI.10.1007/s00531-017-1499-0.

Roemers, E., Fernandes, L.A., Freire, E.B., Simões, L.S. (2015). Microbial filaments in stromatolites and laminites of Balbuena III Sequence (Maastrichtian/Danian) of Yacoraite Formation in Metán-Alemania Sub-basin, Salta region, Argentina, and its palaeoenvironmental significance. Brazilian Journal of Geology. 45 (3). Pages 399-413. DOI: 10.1590/2317-488920150030255.

Rohais S., Hamon Y., Deschamps, R., Gasparrini, M, Beaumont, V., Kolher E., Barbier M. (2012). Advancement report: Phases I&II. Cretaceous outcrop analog from Argentina for microbial pre-salt Atlantic series: JIP COMPAS – year 2. Confidential IFP Report 65621.

Rohais, S., Hamon, Y., Deschamps, R., Gasparrini, M., Beaumont, V., Kohler, E., Barbier, M., Doligez, B. (2014). Final report: Phases III – Cretaceous Outcrop analog from Argentina for Microbial Pre-salt Atlantic Series: JIP COMPAS – YEAR 3. IFPEN Report 65622.

Rohais, S., Hamon, Y., Deschamps, R., Beaumont, V., Gasparrini, M., Pillot, D., Romero-Sarmiento, M. F. 2019. Patterns of organic carbon enrichment in a lacustrine system across the K-T boundary: Insight from a multi-proxy analysis of the Yacoraite Formation, Salta rift basin, Argentina. International Journal of Coal Geology. 210. DOI: 10.1016/j.coal.2019.05.015.

Romanchuk A.Y., Vlasova I. E., Kalmykov S. N. (2020). Speciation of Uranium and Plutonium from Nuclear Legacy Sites to the Environment: A Mini

Review. Frontiers in Chemistry. Vol 8. Pag 630. DOI=10.3389/fchem.2020.00630.

Romaniello, S. J., Herrmann, A. D., & Anbar, A. D. (2013). Uranium concentrations and (super 238) / (super 235) U isotope ratios in modern carbonates from the Bahamas; assessing a novel paleoredox proxy. Chemical Geology, 362:305-316.

Rossignol, C., Hallot, E., Bourquin, S., Poujol, M., Jolivet, M., Pellenard, P., Ducassou, C., Nalpas, T., Heilbronn, G., Yu, J., Dabard, M. (2019). Using volcaniclastic rocks to constrain sedimentation ages: To what extent are volcanism and sedimentation synchronous? Sed. Geo. 381, 46-64 DOI: 10.1016/j.sedgeo.2018.12.010

Rouff, A. A., E. J. Elzinga, R. J. Reeder, and N. S. Fisher (2004). X-ray absorption spectroscopic evidence for the formation of Pb (II) inner-sphere adsorption complexes and precipitates at the calcite-water interface, Environ. Sci. Technol., 38, 1700– 1707. DOI: 10.1021/es0345625

Sabino, I.F. (2002). Geologıa del Subgrupo Pirgua (Cretacico) del noroeste argentino. Tesis Doctoral, Universidad Nacional de Salta, pp 1–260**.**

Sadler, P. M. 1981. Sediment accumulation rates and the completeness of stratigraphic sections." The Journal of Geology. 569–584. DOI: 10.1086/628623.

Saller, A., Rushton, S., Buambua, L., Inman, K., McNeil, R., Dickson, J. A. D. T. (2016). Presalt stratigraphy and depositional systems in the Kwanza Basin, offshore Angola. AAPG Bulletin. 100 (7), 1135–1164. Doi: 10.1306/02111615216

Salfity, J.A. (1979). Paleogeologıa de la cuenca del Grupo Salta (Cretacico-Eogenico) del norte de Argentina. Actas. 7th Congr Geol Arg 1:505–515.

Salfity, J.A (1980). Estratigrafıa de la Formacion Lecho (Cretacico) en la Cuenca Andina del Norte Argentino. Tesis 1, Universidad Nacional de Salta, Publicacion Especial, pp 1–91

Salfity, J. A. (1982). Evolucion paleogeogra fica del Grupo Salta (Cretacico-Eogenico), Argentina. Actas 5th Congr Latinoam Geol, Buenos Aires 1:11–26.

Salfity J.A., Marquillas, R.A. (1994). Tectonic and sedimentary evolution of the Cretaceous-Eocene Salta Group Basin, Argentina. In: Salfity JA (ed). Cretaceous Tectonics of the Andes. Earth Evolution Sciences, Friedr. Vieweg & Sohn, 266–315. DOI: 10.1007/978-3-322-85472-8_6

Santos, M. M., Lana, C., Scholz, R., Buick, I., Schmitz, M. D., Kamo, S. L., Gerdes, A., Corfu, F., Tapster, S., Lancaster, P., Storey, C. D., Basei, M. A. S., Tohver, E., Alkmim, A., Nalini, H., Krambrock, K., Fantini, C., & Wiedenbeck, M. (2017). A new appraisal of Sri Lankan BB zircon as a reference material for LA-ICP-MS U-Pb geochronology and Lu-Hf isotope tracing. Geostandards and Geoanalytical Research, 41(3), 335-358. DOI: 10.1111/ggr.12167

Scardia, G., Parenti, F., Miggins, D. P., Gerdes, A., Araujo, A. G., and Neves, W. A. 2019. Chronologic constraints on hominin dispersal outside Africa since 2.48 Ma from the Zarqa Valley, Jordan, Quaternary Sci. Rev., 219, 1–19. DOI:10.1016/j.quascirev.2019.06.007.

Scholz, C.A., Johnson, T.C., Cohen, A.S., Kinge, J.W., Peck, J.A., Overpeck, J.T., Talbot, M.R., Brown, E.T., Kalindekafe, L., Amoako, P.Y.O., Lyons, RP., Shanahan, T.M., Castan˜eda, I.S., Heil, C.W., Forman, S.L., McHargue, L.R., Beuning, K.R., Gomez, J., Pierson, J., 2007. East African megadroughts between 135 and 75 thousand years ago and bearing on early-modern human origins. Proceedings of the National Academy of Sciences 104, 16416–16421.

Scheller, E. L., Swindle, C., Grotzinger, J., Barnhart, H., Bhattacharjee, S., Ehlmann, B. L., et al. (2021). Formation of magnesium carbonates on Earth and implications for Mars. Journal of Geophysical Research: Planets, 126, e2021JE006828. DOI: 10.1029/2021JE006828

Schoene, B. (2014). U-Th-Pb Geochronology. Refererence Module in Earth Systems and Enviromental Sciences in ‘Treatise on Geochemistry’, Second edition. Editor(s): Heinrich D. Holland, Karl K. Turekian, Elsevier.Vol 4.

Pages 341-378. DOI: 10.1016/B978-0-08-095975-7.00310-7.

Schoene, B., Samperton, K. M., Eddy, M. P., Keller, G., Adatte, T., Bowring, S.A., Khadri, S.,F. R., Gertsch, B. (2015). U-Pb geochronology of the Deccan Traps and relation to the end Cretaceous mass extinction. Science. 347 (6218), 182-184. DOI: 10.1126/science.aaa0118

Schoene, B., Eddy, M.P., Samperton K.M., Keller, Keller, C.B., G., Adatte, T., Khadri, S.F.R. (2019). U-Pb constraints on pulsed eruption of the Deccan Traps across the end-Cretaceous mass extinction. Science. DOI: 10.1126/science.aau2422.

Schmieder, M., Kennedy, T., Jourdan, F., Buchner, E., Reimold, W.U., 2018a. A high-precision ^{40}Ar/^{39}Ar age for the Nördlinger Ries impact crater, Germany, and implications for the accurate dating of terrestrial impact events. Geochim. Cosmochim. Acta. 220, 46-157. https://doi.org/10.1016/j.gca.2017.09.036.

Schmieder, M., Kennedy, T., Jourdan, F., Buchner, E., Reimold, W. U., 2018b. Comment on "A high-precision ^{40}Ar/^{39}Ar age for the Nördlinger Ries impact crater, Germany, and implications for the accurate dating of terrestrial impact events." By Schmieder et al. (Geochim. Cosmochim. Acta. 2018). 238, 599-601. DOI:10.1016/j.gca.2018.05.018.

Schumer, R. Jerolmack, D.J. (2009). Real and apparent changes in sediment deposition rates through time. J. Geophys. Res., 114. DOI: 10.1029/2009JF001266

Schwab, K. (1984). Contribucion al conocimiento del sector occidental de la cuenca sedimentaria del Grupo Salta (Cretacico-Eogenico) en el noroeste argentino. Actas 9th Congr Geol Arg 1:586–604

Schwarz, H. W., Hanel, M., Trieloffet, M. 2020. U-Pb dating of zircons from an impact melt of the Nördlinger Ries crater. . Meteoritics & Planetary Science 55, Nr 2, 312–325. https://doi.org/ 10.1111/maps.13437.

Seder-Colomina, M, Mangeret, A, Stetten, L, Merrot, P, Diez, O, Julien, A, Barker, E, Thouvenot, A, Bargar, J, Cazala, C, Morin, G. (2018). Carbonate Facilitated Mobilization of Uranium from Lacustrine Sediments under Anoxic Conditions. Environ Sci Technol. 2018 Sep 4;52(17):9615-9624. DOI: 10.1021/acs.est.8b01255.

Shannon, R. D. (1976). Revised effective ionic radii and systematic studies of interatomic distances in halides and chalcogenides, Acta Crystallogr., Sect. A Cryst. Phys. Diffr. Theor. Gen. Crystallogr., 32, 751– 767.

Sharman, G. R., Malkowski, M. (2020). Needles in a haystack: Detrital zircon Usingle bondPb ages and the maximum depositional age of modern global sediment. Earth-science Reviews. Vol 203, 103109. DOI: 10.1016/j.earscirev.2020.103109.

Sial, A., Ferreira, V., Frei, R., Marquillas, R., Barbosa, J., Gaucher, C. C., Windmöller, Natan. N.,S. (2013). Mercury as a proxy for volcanic activity during extreme environmental turnover: The Cretaceous-Paleogene transition. Palaeogeography Palaeoclimatology Palaeoecology. 387. 153-164. 10.1016/j.palaeo.2013.07.019.

Sial, A.N. Gaucher C., Ferreira, V.P., Pereira, N.S., Cezario, W.S., Chiglino, L., Lima, H.M. (2015). Chapter 2 - Isotope and Elemental Chemostratigraphy, Editor(s): Mu. Ramkumar, Chemostratigraphy, Elsevier, Pages 23-64, https://doi.org/10.1016/B978-0-12-419968-2.00002-9.

Sial, A. Ferreira, V., Toselli, A., Parada, M., Aceñolaza, F., Pimentel, M. Alonso, R. (2001). Carbon and Oxygen Isotope Compositions of Some Upper Cretaceous–Paleocene Sequences in Argentina and Chile. International Geology Review. 43. 892-909. DOI: 10.1080/00206810109465054.

Sibley, D. F., Gregg, J. M., (1987). Classification of Dolomite Rock Texture. Journal of Sedimentary Research. 57 (6). Pages 967-975.

Shoemaker, M. C., and Chao, E. 1961. New evidence for the impact origin of the Ries basin, Bavaria, Germany. J. Geophys. Res. 66 (10), 3371-3378. DOI:10.1029/JZ066i010p03371.

Shuman, N, B (2021). Approaches to Paleoclimate Reconstruction, Editor(s): David Alderton, Scott A. Elias, Encyclopedia of Geology (Second Edition), Academic Press, Pages 299-308, DOI:10.1016/B978-0-08-102908 4.00174-0.

Sláma, J., Košler, J., Condon, D.J., Crowley, J.L., Gerdes, A., Hanchar, J.M., Horstwood, M.S.A., Morris, G.A., Nasdala, L., Norberg, N., Schaltegger, U., Schoene, B., Tubrett, M.N., Whitehouse, M.J. (2008). Plešovice zircon — A new natural reference material for U–Pb and Hf isotopic microanalysis. Chemical Geology, 249, (1–2), 1-35. DOI: 10.1016/j.chemgeo.2007.11.005.

Smeraglia, L., Looser, N., Fabbri, O., Choulet, F., Guillong, M., and Bernasconi, S. M. (in review). U-Pb dating of middle Eocene-middle Pleistocene multiple tectonic pulses in the Alpine foreland, Solid Earth Discuss. [preprint], https://doi.org/10.5194/se-2021-2, in review, 2021.

Smeraglia, L., Looser, N., Fabbri, O., Choulet, F., Guillong, M., Bernasconi, S. M. (2019). U-Pb dating of middle Eocene-middle Pleistocene multiple tectonic pulses in the Alpine foreland. Solid Earth Discuss. DOI: 10.5194/se-2021-2.

Smit, J. Hertogen, J. (1980). An extraterrestrial event at the Cretaceous–Tertiary boundary. Nature 285, 198–200.

Smith P.E., Farquhar R.M. (1989). Direct dating of Phanerozoic sediments by the 238U single bond 206Pb method. Nature, 341. 518-521. DOI: 10.1038/341518a0.

Smith, P. E., U. Brand, R. M. Farquhar. (1994). U-Pb systematics and alteration trends of Pennsylvanianaged aragonite and calcite. Geochim. Cosmochim. Acta. Vol. 58, pp. 313–322.

Song, H., Kemp, D.B., Tian, L. et al. (2021). Thresholds of temperature change for mass extinctions. Nat Commun 12, 4694 (2021). DOI: 10.1038/s41467-021-25019-2.

Sprain, C.J., Renne, P.R., Clemens, W.A., and Wilson, G.P. (2018). Calibration of chron C29r: New high-precision geochronologic and paleomagnetic constraints from the Hell Creek region, Montana: GSA Bulletin, Doi: 10.1130/B31890.1.

Stacey, J.S., Krammers, J.D (1975). Approximation of terrestrial lead isotope evolution by a two-stage mode. EPSL, Vol 26. Issue 2, pages 207-221.

Starck, D. (2011) Cuenca Cretácica-Paleógena del Noroeste Argentino. VIII Congreso de Exploración y Desarrollo de Hidrocarburos. Simposio de Cuencas Argentinas: visión actual, Mar del Plata, pp. 407–453

Stöffler, D., Artemieva, N. A., Wünnemann K., Reimold, W. U., Jacob, J., Hansen B. K., Summerson, I. A. T., (2013). Ries crater and suevite revisited—Observations and modeling Part II: Modeling. *Meteorit. Planet. Sci.* 48 (4), 590-627. DOI:10.1111/maps.12086.

Stokke, E. W., Jones, M. T., Riber, L., Haflidason, H., Midtkandal, I., Schultz, B. P., and Svensen, H. H. (2021). Rapid and sustained environmental responses to global warming: the Paleocene–Eocene Thermal Maximum in the eastern North Sea, Clim. Past, 17, 1989–2013, https://doi.org/10.5194/cp-17-1989-2021.

Sturchio, N.C., Antonio, M.R., Sederholm, L. Sutton, S.R., Brannon, J.C. (1998). Tetravalent Uranium in Calcite. Science. Vol 281 (5379) 971-3. DOI: 10.1126/science.281.5379.971.

Suarez-Gonzalez, P. Benito, M.I., Quijada, I.E., Mas. R., Campos-Soto, S. (2019). 'Trapping and binding': A review of the factors controlling the development of fossil agglutinated microbialites and their distribution in space and time. Earth-Science Reviews. Vol 194, Pages 182-215.

Suzuki, Y., Mukai, H., Ishimura, T. et al. Formation and Geological Sequestration of Uranium Nanoparticles in Deep Granitic Aquifer. (2016). Sci Rep 6, 22701. https://doi.org/10.1038/srep22701

Svensson, M. J. O., Osinski, G. R., Goudge, T. A., Longstaffe, F. J., (2021). Terrestrial Analogs 2021 (LPI Contrib. No. 2595).

Swart, P. K., 2015. The geochemistry of carbonate diagenesis: The past, present and future. *Sedimentology,* 62, 1233-1304. https://doi.org/10.1111/sed.12205.

Tao, M., Peng, L., Longwei, Q., Yongshi, M., Yali, L., Hongmei, L. Fuq, C. Changsheng, Q. (2017). Formation and distribution of the high quality reservoirs in a deep saline lacustrine basin: A case study from the upper part of the 4th member of Paleogene Shahejie Formation in Bonan sag, Jiyang depression, Bohai Bay Basin, East China. PETROL. EXPLOR. DEVELOP., 2017, 44(6): 948–959. DOI: 10.1016/S1876-3804(17)30107-6.

Talbot, M.R. (1990). A review of the palaeohydrological interpretation of carbon and oxygen isotopic ratios in primary lacustrine carbonates. Chemical Geology: Isotope Geoscience section. Vol 8, issue 4 page 261-279. DOI: 10.1016/0168-9622(90)90009-2.

Thompson, D.L, Stilwell, J.D., Hall M. (2015) Lacustrine carbonate reservoirs from Early Cretaceous rift lakes of Western Gondwana: Pre-Salt coquinas of Brazil and west Africa Gondwana Res., 28 (1), 26-51. DOI: 10.1016/j.gr.2014.12.005

Tribovillard, N., Algeo, T. J., Lyons, T., & Riboulleau, A. (2006). Trace metals as paleoredox and paleoproductivity proxies; an update. Chemical Geology, 232(1-2):12-32.

Veizer, J., Ala, D., Azmy, K., Bruckschen, P., Buhl, D., Bruhn, F., Carden, G.A., Diener, A., Ebneth, S., Godderis, Y. and Jasper, T., 1999. ^{87}Sr/^{86}Sr, δ^{13}C and δ^{18}O evolution of Phanerozoic seawater. Chemical geology. 161 (13), 59-88.

Valais, S., Cónsole-Gonella, C. (2019). An Updated Review of the Avian Footprint Record from the Yacoraite Formation (Maastrichtian-Danian), Northwestern Argentina. Ichnos. 26. 224-241. DOI: 10.1080/10420940.2018.1538982.

Valencio, D.A., Giudice, A., Mendıa, J.E., Oliver, G.J. (1976). Paleomagnetismo y edades K/Ar del Subgrupo Pirgua, provincia de Salta, Repu´ blica Argentina. Actas 6th Congr Geol Arg 1:527–542.

Van Wagoner, J. C., Mitchum, R. M., Campion, K. M., Rahmanian, V. D. (1990). Siliciclastic Sequence stratigraphy in Well Logs, Cores and Outcrops: Concepts for High-Resolution Correlation of Time and Facies, 55. DOI: 10.1306/Mth7510.

Van Wagoner JC, Posamentier HW, Mitchum RM, Vail PR, Sarg JF, Loutit TS, Hardenbol J, (1988) An overview of the fundamentals of sequence stratigraphy and key definitions. In: Wilgus CK, Hastings BS, Kendall CGSC, Posamentier HW, Ross CA, Van Wagoner JC (eds) Sea-level changes: an integrated approach, vol 42. Society for Sedimentology Geology, Special Publication, pp 39–45.

Vellekoop, J., Esmeray-Senlet, S., Miller, K.G., Browning, J.V., Slujis, A., Van de Schootbrugge B., Damstè, J.S., Brinkhuis, H., (2016). Evidence for Cretaceous-Paleogene boundary bolide “impact winter” conditions from New Jersey, USA. GEOLOGY, v. 44; no. 8; p. 619–622. DOI: 10.1130/G37961.1

Vermeesch, P. (2021). Maximum depositional age estimation revisited. Geoscience Frontiers. Vol 12. Issue 2, pages 843-850. DOI. 10.1016/j.gsf.2020.08.008.

Viramontes J. G., Kay S. M., Becchio R., Escayola M., Novitski I. (1999). Cretaceous rift related magmatism in central-western South America. Journal of South-American Earth Sciences, 12, 109-121.

Volkheimer, Wolfgang & Novara, Martín & Narváez, Paula & Marquillas, Rosa. (2006). Palynology and paleoenvironmental significance of the Tunal Formation (Danian) at its type locality, El Chorro creek (Salta, Argentina). AMEGHINIANA (Rev. Asoc. Paleontol. Argent.) - 43 (3): 567-584.

Walter, B. F., Gerdes, A., Kleinhanns, I. C., Dunkl, I., Eynatten, H. V., Kreissl, S.,

Markl, G., (2018). The connection between hydrothermal fluids, mineralization, tectonics and magmatism in a continental rift setting: Fluorite Sm-Nd and hematite and carbonates U-Pb geochronology from the Rhinegraben in SW Germany. Geochimica et Cosmochimica Acta, 240, (11-42). DOI: 10.1016/j.gca.2018.08.012.

Watson, E., Swindles, G., Lawson, I., Savov, I., Wastegård, S. (2017). The presence of Holocene cryptotephra in Wales and southern England: HOLOCENE CRYPTOTEPHRA IN WALES AND SOUTHERN ENGLAND. Journal of Quaternary Science. DOI: 10.1002/jqs.2942.

Wainman, C.C., McCabe, P.J., Crowley, J.L. (2018); Solving a tuff problem: Defining a chronostratigraphic framework for Middle to Upper Jurassic nonmarine strata in eastern Australia using uranium–lead chemical abrasion–thermal ionization mass spectrometry zircon dates. AAPG Bulletin. 102 (6), 1141–1168. DOI: 10.1306/07261717140.

Weishampel, D.B., Barret. P.M., Coria, R.A., Le Loeuff, J., Xing X., Xijin X., Sahni, A., Gomani, E.M.P., Noto, C.R. (2004). Dinosaur Distribution. In book: In book: The DinosauriaEdition: 2nd editionChapter: Dinosaur DistributionPublisher: University of California PressEditors: D.B. Weishampel, P. Dodson, H. Osmolska. DOI: 10.1525/california/9780520242098.003.0027.

Weyer, S., Anbar, A. D., Gerdes, A., Gordon, G. W., Algeo, T. J., & Boyle, E. A. (2008). Natural fractionation of $^{238}U/^{235}U$. Geochimica et Cosmochimica Acta, 72(2):345-359.

Wendt I. Carl C. (1991). The statistical distribution of the mean squared weighted deviation. Chemical Geology (Isotope Geoscience Section), 86, 275–285.

Westerhold, T., Röhl, U., Wilkens, R. H., Gingerich, P. D., Clyde, W. C., Wing, S. L., Bowen, G. J., and Kraus, M. J. (2018). Synchronizing early Eocene deep-sea and continental records – cyclostratigraphic age models for the Bighorn Basin Coring Project drill cores, Climate of the Past, 14, 303-319. DOI. 10.5194/cp-14-303- 1115.

Wetherill, G.W. (1956). Discordant uranium lead ages. Trans. Amer. Geophys. Union 37, 320-326.

White, T., Del Papa, C., Andrews, E. (2018). Chronostratigraphy of Paleogene strata, Salta Basin, northwestern Argentina: A reply to Hyland and Sheldon's comment. Palaeogeography, Palaeoclimatology, Palaeoecology. 511. Pages 643-645.

Wiedenbeck, M., Allé, P., Corfu, F., Griffin, W. L., Meier, M., Oberli, F., Quadt, A. V., Roddick, J. C, Spiegel, W. (1995). Three natural zircons standards for U-Th-Pb, Lu-Hf, Trace element and REE analyses. Geostandards Newsletter. 19 (1) 1-23. DOI: 10.1111/j.1751-908X.1995.tb00147.x

Williams, I. S., & Claesson, S. (1987). Isotopic evidence for the Precambrian provenance and Caledonian metamorphism of high grade paragneisses from the Seve Nappes, Scandinavian Caledonides. II: Ion microprobe zircon U-Th-Pb. Contribution to Mineralogy and Petrology, 97, 205-217**.**

Winkelstern, I., Lohmann, K. (2016). Shallow burial alteration of dolomite and limestone clumped isotope geochemistry. Geology. 44. DOI:10.1130/G37809.1.

Witts, J.D., Newton, R.J., Mills, B.J.W., Wignall, P.B., Bottrell, S.H., Hall, J.L.O., Francis, J.E., Crame, J.A. (2018). The impact of the Cretaceous–Paleogene (K–Pg) mass extinction event on the global sulfur cycle: Evidence from Seymour Island, Antarctica. Geochimica et Cosmochimica Acta 230 17–45. DOI: 10.1016/j.gca.2018.02.037.

Woodhead, J., Petrus, J. A. (2019). Exploring the advantages and limitations of in situ U-Pb carbonate geochronology using speleothems. Geochronology 1(1):69-84. DOI: 10.5194/gchron-1-69-2019

Wotzlaw, J. Hüsing, S., Hilgen, F., Schaltegger, U. (2014). High-precision zircon U–Pb geochronology of astronomically dated volcanic ash beds from the Mediterranean Miocene. Earth and Planetary Science Letters. DOI: 407. 19-34. 10.1016/j.epsl.2014.09.025.

Wray, Christopher Michael (2018). "Investigating Uranium incorporation in modern carbonates by sequential extraction: Applied to the Permian - Triassic boundary in Lung Cam, Vietnam" (2018). LSU Master's Theses. 4712.

Zachos, J. C., Dickens, G. R., & Zeebe, R. E. (2008). An early Cenozoic perspective on greenhouse warming and carbon-cycle dynamics. Nature, 451(7176), 279-283. DOI: 10.1038/nature06588.

Zeebe, R.E., Ridgwell, A., Zachos, C. (2016). Anthropogenic carbon release rate unprecedented during the past 66 million years. Nature Geoscience. 9. 325-329. DOI: 10.1038/ngeo2681.

Zeebe, R.E, Lourens, L.J., (2019). Solar System chaos and the Paleocene-Eocene boundary age constrained by geology and astronomy. Science. 365 (6456). Pages 926-929. DOI: 10.1126/science.aax0612.

Zhang, W., Ming, Q., Shi, Z., Chen, G., Niu, J., Lei, G., Chang, F. and Zhang, H. (2014) Lake Sediment Records on climate change and human activities in the Xingyun Lake catchment, SW China. PLOS ONE., v.9, pp.1-10. DOI: 10.1371/journal.pone.0102167

Zimicz, A.N., Fernández, M., Bond, M., Chornogubsky, L., Arnal, M., Gárdenas, M., Fernicola, J.C. (2020). Archaeogaia macachaae gen. et sp. nov., one of the oldest Notoungulata Roth, 1903 from the early-middle Paleocene Mealla Formation (Central Andes, Argentina) with insights into the Paleocene-Eocene south American biochronology. Journal of South American Earth Sciences 103. 102772. DOI: 10.1016/j.jsames.2020.102772

11 SUPPLEMENTARY DATA

m £	Seq. ©	Carbonate facies	Sample name	Carb. phase	δ^{13}C*	δ^{18}0*	LA session	Age** (Ma)	$2\sigma_{int}^{\#}$ (Ma)	$2\sigma_{exp}^{\$}$ (Ma)	$2\sigma_{exp}$ (%)	N "	MSWD †	y-int "	rej ¶
151		grastropods rudstone-packstone	UJ53	MIC-C	-1.71	-1.80									
			UJ53	EC	-1.41	-13.12									
149		oolitic grainstone with peloids	UJ52												
147		stromatolite boundstone	UJ51	MIC-C	0.98	1.89	27/02/2019	64.86	2.04	2.30	3.55	33	1.2	0.822±0.008	0
146		oolitic grainstone	UJ50	OC	1.20	1.72	27/02/2019	66.67	3.04	3.20	4.80	31	0.7	0.817±0.001	0
			UJ50	MIC-C	0.73	1.56	27/02/2019	64.55	3.00	3.20	4.96	26	1.1	0.817±0.001	5
145		stromatolite boundstone	UJ49	MIC-D	1.35	2.51									
			UJ49	MIC-C	1.48	2.43									
140		oolitic grainstone	UJ48	OC	1.18	1.08									
139		stromatolitic boundstone	UJ47	MIC-C	0.96	2.02									
136		fine grained stromatolite	JUR25	MIC-C			14/08/2016	64.31	2.64	2.81	4.37	29	0.7	0.826±0.003	0
			JUR25	MIC-D	1.22	1.22	14/08/2016	63.62	3.98	4.09	6.43	22	1.6	0.834±0.005	0
135		stromatolitic boundstone	UJ46												
134		stromatolite domal boundstone	UJ45	MIC-D	1.91	-0.29									
			UJ45	MIC-C	2.16	3.44									
131		oolitic grainstone	UJ44	OM	1.83	-0.20									
127		mustache stromatolite boundstone	UJ43	MIC-D	1.92	4.92	28/02/2019								
			UJ43	MIC-C	2.19	2.76	28/02/2019	62.30	1.20	1.50	2.41	28	1.3	0.820±0.002	3
125		oolitic grainstone	UJ42	EC			17/06/2019	64.09	0.76	1.22	1.90	45	1.5	0.836±0.003	1
	2		UJ42	OC	1.88	2.90	16/10/2018	65.20	1.40	1.70	2.61		1.5	0.819±0.002	2
			UJ42	MIC-C			16/10/2018								
123		stromatolite boundstone	UJ41												
122		oolitic grainstone	UJ40	OC	1.95	-0.07									
			UJ40	MIC-D	2.63	4.28									
120		oolitic grainstone	UJ39	OC	1.98	0.80	27/02/2019	65.31	1.49	1.80	2.76	33	1.2	0.821±0.001	0
			UJ39	EC			27/02/2019								
		oolitic grainstone	UJ38	OC	1.72	2.20									
114		stromatolite boundstone	UJ37b												
113		stromatolite boundstone	UJ37a												
105		oolitic grainstone	UJ36	OD	2.96	2.47									
102		oolitic grainstone	UJ35												
100		gastropods rudstone/grainstone	UJ34												
99		oolitic grainstone	UJ33	OC	2.37	1.50									
			UJ33	EC			16/10/2018								
			UJ33	MIC-C	1.72	2.40	16/10/2018	77.00	30.00			16	4.3	0.833±0.009	11
98.5		stromatolite boundstone	UJ33A	MIC-C			16/10/2018								
96		stromatolite boundstone	UJ32	MIC-C	1.80	0.91									
91		oolitic grainstone	UJ31	OM	2.75	5.07									
88.5		stromatolite boundstone	UJ30B												
88		oolitic grainstone	UJ30A	OD	3.25	3.62									
86		oolitic grainstone	UJ29												
85	1	oolitic grainstone to packstone with gastropos and mudclasts	UJ28												
80		Agglutinated, dendriform stromatolite boundstone	UJ27												
79		oolitic grainstone	UJ26	OD	3.45	4.70									
74		trombolite boundstone	UJ25												

£ stratigraphic height along the Juramento section in metres

© Stratigraphic sequence according to Rohais et al. (2019) and Deschamps et al. (2020)

* δ13C and δ18O values expressed as relative to V-PDB (Vienna Pee Dee Belemnite) standard.

** Tera-Wasserburg diagram U-Pb lower intercept ages

Absolute internal uncertainty (excluding long-term excess of variance of 1.5%).

$ Absolute expanded uncertainty (including ong-term excess of variance of 1.5%).

" Number of LA-ICPMS spot analyses.

† Mean Squared Weighted Deviates

" Y-axis intercept =initial Pb/Pb ratio.

¶ rejected datapoints

Table Supplementary data 4. Results Juramento section sequences 1 and 2

m £	Seq. ©	Carbonate facies	Sample name	Carb. phase	δ^{13}C*	δ^{18}0*	LA session	Age** (Ma)	$2\sigma_{int}$ # (Ma)	$2\sigma_{exp}$ $ (Ma)	$2\sigma_{exp}$ (%)	N "	MSWD †	y-int "	rej ¶
238		oolitic grainstone	UJ78	OC	-1.83	-6.18	16/10/2018	60.00	17.00			22	3.7	0.818±0.003	0
238			UJ78	MIC-C			16/10/2018								
237		stromatolite boundstone	UJ77	MIC-C	-1.37	-5.86									
236		oolitic grainstone	UJ76	OC	-0.66	-5.67									
233.5		oolitic grainstone	UJ75b	MIC-C	0.14	-4.17									
			UJ75b	OC	-0.02	-6.85	27/02/2019	61.38	6.17	6.20	10.10	30	1.0	0.818±0.001	0
233		stromatolite boundstone	UJ75a	MIC-D	0.51	-1.23	28/02/2019								
			UJ75a	MIC-C	0.93	-1.42	28/02/2019	75.00	15.00	15.04	20.00	13	5.6	0.815±0.004	0
230		oolitic grainstone	UJ74	OC	-0.01	-3.24	16/10/2018	61.70	1.80	2.00	3.24	23	0.8	0.817±0.002	4
229		grapestone-ooid grainstone to packstone	JURD9	OC			14/08/2016								
			JURD9	MIC-M			14/08/2016								
227			UJ72	MIC-C	-0.17	-4.82	17/04/2019	65.69	0.57	1.13	1.70	32	1.4	0.828± 0.002	2
			UJ73	MIC-C	-0.17	-4.82	17/06/2019	63.72	0.66	1.20		28	0.7	0.832±0.002	0
			UJ73	MIC-C	-0.17	-4.82	16/10/2018	64.13	0.67	1.20	1.87	25	1.5	0.826±0.002	0
			UJ73	MIC-C	-0.17	-4.82	28/02/2019	64.74	0.97	1.30	2.10	35	0.7	0.826±0.002	1
			UJ73	MIC-C	-0.17	-4.82	27/02/2019	64.40	0.68	1.20	1.86	31	1.3	0.824±0.001	1
227			UJ73	MIC-D			17/04/2019	63.70	2.12	2.30	3.61	16	2.2	0.818±0.003	
218	4	siltstone with algal laminae	UJ72	MIC-C	0.55	-1.03									
217		fine grained stromatolite	JURD3	MIC-D	1.08	1.45	14/08/2016	62.58	2.05	2.26	3.61	18	0.8	0.824±0.003	0
			JURD3	MIC-C	1.40	0.58	14/08/2016	63.44	1.53	1.80	2.84	40	1.8	0.820±0.001	0
216		oolitic grainstone	UJ71	OC	1.54	1.25	27/02/2019	62.31	4.50	4.60	7.38	13	0.9	0.820±0.002	
			UJ71	EC			27/02/2019								
			UJ71	MIC-C	0.02	-0.54	27/02/2019								4
211		fine grained stromatolite	JURC10	MIC-D			14/08/2016	63.66	1.44	1.73	2.72	19	0.8	0.825±0.004	0
			JURC10	MIC-C	0.54	1.15	14/08/2016	66.81	11.15	11.20	16.76	13	0.6	0.826±0.007	0
210		oolitic grainstone	UJ70	OC	1.07	0.00									
208		stromatolite boundstone	UJ69	MIC-D	1.03	1.91	16/10/2018								
			UJ69	MIC-C	1.51	1.73	16/10/2018	62.70	1.20	1.80	2.87	25	1.3	0.816±0.002	0
206		oolitic grainstone with pel	UJ68	OM	1.18	1.03									
203		oolitic grapestone with microbial intraclasts	UJ67	OM	1.42	1.87									
198		oolitic grainstone	UJ66b	OC	0.75	1.10									
197		stromatolite breccia	UJ66a	MIC-D	0.26	1.69									
			UJ66a	MIC-C	1.19	1.32									
194		oolitic grainstone with gastropods and	UJ65	OC	0.08	1.27									
			UJ65	MIC-C	0.36	1.69									
192		oolitic grainstone	UJ64	OC	-0.95	0.84	16/10/2018	64.70	2.00	2.20	3.40	25	1.0	0.821±0.002	0
			UJ64	MIC-C			16/10/2018								
191		stromatolite boundstone	UJ63	MIC-C	0.13	1.67	27/02/2019								
185		oolitic grainstone	JURC6	OC	0.20	1.29	14/08/2016	64.25	2.48	2.66	4.14	24	0.7	0.823±0.004	0
			JURC6	EC			14/08/2016	64.51	1.73	1.98	3.07	16	1.0	0.810±0.001	0
184.5		oolitic grainstone	UJ62a	EC			17/06/2019	64.30	1.10	1.50	2.33	30	1.7	0.820±0.003	1
			UJ62a	OM	-0.17	-0.98	28/02/2019	57.10	4.00	4.10	7.10	22	1.8	0.835±0.008	6
180		oolitic grainstone	UJ61												
175	3	domal stromatolite and trombolite boundstone	UJ60	MIC-C	-0.90	2.42	27/02/2019	64.99	1.64	1.90	2.92	31	1.0	0.823±0.002	0
171		laminated stromatolite bo	UJ59	MIC-C	-2.25	2.94									
170		oolitic grainstone	UJ58	EC			17/06/2019	65.62	0.85	1.30	1.98	28	1.1	0.819±0.003	3
169		oolitic grainstone	UJ57	OC			16/10/2018	64.60	1.10	1.50	2.32	30	1.2	0.819±0.002	0
			UJ57	MIC-C			16/10/2018	-							
160		carbonate mudstone	UJ56	OD			16/10/2018	-							
			UJ56	MIC-D	1.87	1.55	16/10/2018	-							
			UJ56	MIC-C	1.46	1.78	16/10/2018	64.30	2.20	2.40	3.73	27	1.3	0.822±0.030	0
158		siltstone	UJ55	LC			17/04/2019								
156.5		carbonate mudstone	UJ54a												
156		carbonate mudstone	UJ54	MIC-C	-1.06	-1.84									

£ stratigraphic height along the Juramento section in metres

© Stratigraphic sequence according to Rohais et al. (2019) and Deschamps et al. (2020)

* δ13C and δ18O values expressed as relative to V-PDB (Vienna Pee Dee Belemnite) standard.

** Tera-Wasserburg diagram U-Pb lower intercept ages

Absolute internal uncertainty (excluding long-term excess of variance of 1.5%).

$ Absolute expanded uncertainty (including ong-term excess of variance of 1.5%).

" Number of LA-ICPMS spot analyses.

† Mean Squared Weighted Deviates

" Y-axis intercept =initial Pb/Pb ratio.

¶ rejected datapoints

Table supplementary data 5. Results from Juramento section sequences 3 and 4.

m £	Seq. ©	Carbonate facies	Sample name	Carb. phase	δ^{13}C*	δ^{18}0*	LA session	Age** (Ma)	2σ $_{int}$ # (Ma)	2σ $_{exp}$ $ (Ma)	MSWD	N	MSWD †	y-int "	rej ¶
72		stromatolite boundstone	UJ24B	EC			17/06/2019	65.80	1.00	1.40	2.13	2	19.0	0.770±0.004	9
			UJ24B	OM	3.28	2.05	27/02/2019	59.20	4.90	5.00	8.45	11	31.0	0.774±0.004	0
			UJ24B	MIC-M	3.52	4.03	27/02/2019								
			UJ24B	MIC-C			27/02/2019	78.00	13.00	13.00	16.67	24	31.0	0.809±0.035	6
71.5		oolitic grainstone	UJ24a	OC	3.75	6.27									
71		oolitic grainstone	JUR8	OM	2.5	1.33	14/08/2016	65.11	3.27	3.41	5.24	1	20.0	0.821±0.002	0
			JUR8	EC			14/08/2016	66.45	1.22	1.58	2.38	2	15.0	0.813±0.010	0
69		oolitic grainstone	UJ23	OM			27/02/2019	67.37	5.28	5.40	8.02	1	25.0	0.816±0.003	5
			UJ23	EC			17/06/2019	65.13	0.58	1.10	1.69	1	27.0	0.827±0.003	5
68		oolitic grainstone	JUB7	OD			14/08/2016	65.52	2.06	2.29	3.50	1	25.0	0.822±0.015	0
			JUB7	EC			14/08/2016	67.32	1.63	1.92	2.85	1	21.0	0.828±0.002	0
67		oolitic grainstone	UJ22												
66.5		oolitic grainstone	UJ21	EC	2.69	1.74									
66.2			CH1	OND	3.51	6.26	14/08/2016	65.49	1.47	1.77	2.70	1	27.0	0.820±0.002	0
			CH1	EC			14/08/2016	61.90	2.14	2.33	3.76	2	14.0	0.816±0.0027	0
65		oncoidal rudstone	JUB6	OND			14/08/2016	58.88	2.43	2.58	4.38	1	33.0	0.818±0.002	0
			JUB6	EC			14/08/2016	64.73	0.96	1.37	2.12	1	27.0	0.830±0.003	0
64.8		oncoidal rudstone	UJ20	EC	3.01	4.38									
			UJ20	OND	4.19	6.05									
64.5		oncoidal rudstone	JUB5	EC			14/08/2016	65.99	0.94	1.37	2.08	1	15.0	0.817±0.004	0
			JUB5	EC			17/06/2019	64.78	0.51	1.10	1.70	1	42.0	0.831±0.006	3
			JUB5	OND			14/08/2016	65.42	2.60	2.78	4.25	1	20.0	0.818±0.003	0
63		oolitic grainstone	UJ19	OND	3.98	5.01									
59		trombolite boundstone inside and oolitic grainstone	UJ18	MIC-C	4.44	8.67									
57.5		oolitic grainstone	UJ17	OD	3.44	5.09	17/06/2019								
		oolitic grainstone and microbial boundstone	UJ17	EC			17/06/2019	65.20	1.70	1.90	2.91	2	29.0	0.825±0.008	2
57			UJ16	OC	2.73	3.77									
			UJ16	MIC-D	3.47	4.18									
56.5		oolitic grainstone	JUB1	OM			14/08/2016	65.08	3.66	3.79	5.82	2	29.0	0.819±0.005	0
55.8	1	oolitic grainstone	UJ15	OC	2.22	3.40	16/10/2018	66.30	1.30	1.60	2.41	1	30.0	0.815±0.004	0
			UJ14	MIC-C			16/10/2018								
55		oolitic grainstone	UJ14	OC	2.33	2.56	16/10/2018	66.90	1.60	2.00	2.99	1	28.0	0.802±0.001	0
42.5		planar stromatolite boundstone	UJ13	MD	1.87	2.72									
			UJ12	EC			27/02/2019								
			UJ12	MIC-C			27/02/2019								
42		oolitic grainstone	UJ12	OC			27/02/2019	66.94	1.60	1.90	2.84	1	30.0	0.820±0.001	0
32.5		medium grained sandstone and stromatolite boundstone	UJ11	MC	1.65	0.31									
31.5		oolitic grainstone	UJ10	OC	2.25	3.61									
30.5		mustache stromatolite boundstone	UJ9	MIC-C	2.15	0.97									
28		oolitic grainstone	UJ8	OC	1.94	2.07									
26.3		peloid oolitic grainstone to packstone	UJ7	EC			17/06/2019	65.84	0.41	1.10	1.67	2	31.0	0.821±0.004	2
25.5		trombolite to planar stromatolite boundstone	UJ6a	MIC-D	2.42	3.72									
				MIC-C	1.93	1.98	16/10/2018	67.74	0.58	1.20	1.77	1	31.0	0.815±0.002	0
24		sandy oolitic grainstone	UJ6												
18		sandy oolitic grainstone	UJ5												
5.5		sandy oolitic grainstone	UJ4												
5		sandy oolitic grainstone	JUR1	OC			14/08/2016								
4		sandy oolitic grainstone	UJ3	OC			27/02/2019								
2.5		medium grained sandstone with carbonate algal mats and ostracods	UJ2												
2		silty to fine-grained sandstone with carbonate algal mats and ostracods	UJ1												

£ stratigraphic height along the Juramento section in metres

© Stratigraphic sequence according to Rohais et al. (2019) and Deschamps et al. (2020)

* δ13C and δ18O values expressed as relative to V-PDB (Vienna Pee Dee Belemnite) standard.

** Tera-Wasserburg diagram U-Pb lower intercept ages

Absolute internal uncertainty (excluding long-term excess of variance of 1.5%).

$ Absolute expanded uncertainty (including ong-term excess of variance of 1.5%).

" Number of LA-ICPMS spot analyses.

† Mean Squared Weighted Deviates

" Y-axis intercept =initial Pb/Pb ratio.

¶ rejected datapoints

Table Supplementary data 6. Results Juramento section sequence 1

m £	Seq.©	Sample name	Carb. phase	δ13C*	δ180*	LA session	Age** (Ma)	2σ int # (Ma)	2σ exp $ (Ma)	2σ exp (%)	N "	MSWD †	y-int "	rej ¶
160	4	CPP74	OC	-3.50	-5.48									
159		CPP72	OC	-2.75	-4.23									
158		CPP69	OC	-2.38	-4.13									
156		CPP63	MIC-C	-2.17	-3.10									
155		CPP58	OC	-0.12	-5.04									
154		CPP55	MIC-C	0.38	1.69									
153.5		CPP47	OC	-2.29	-4.15									
151		CPP39	OC	-1.24	-2.65									
150.5		CPP37	OC	-2.20	-6.01									
150		CPP35	OC	-1.47	-0.98									
143		CPP26	OC	-2.59	-0.48									
143		CPP26	MIC-C	-2.30	-1.25									
142		UC37	OC	-2.15	-6.08	28/02/2019	58.50	2.30	2.40	4.20	31	5.6	0.802±0.007	0
140		UC36	MIC-D	-3.29	0.67									
140		UC36	MIC-C	-3.03	-1.66									
139		CPP21	MIC-C	-2.96	-1.15									
139		CPP21	MIC-D	-2.35	2.14									
138		CPP20		-2.52	-4.06									
133.5		CPP5	OC	-4.16	-4.88									
132	3	CPP1		-3.32	-4.08									
126		UC34	OD			28/02/2019	62.00	36.00	36.01	58.00	18	38.0	0.825±0.030	0
112		UC33	OC	0.24	0.31	17/04/2019	63.28	1.85	2.00	3.20	26	1.4	0.817±0.001	0
110		UC32	MIC-D	-0.24	-2.14									
108		UC31	MIC-D	1.54	4.42									
108			MIC-C	1.28	1.61									
105		UC30	MIC-C	1.04	1.38	28/02/2019	66.90	1.43	1.70	2.60	43	0.9	0.838±0.002	0
104.5			MIC-D	1.10	3.00	28/02/2019	62.50	1.80	2.00	3.40	35	1.5	0.830±0.003	0
97		UC28	MIC-C	0.70	1.15	17/06/2019	66.21	1.60	1.90	2.80	13	0.8	0.834±0.001	0
97		UC28	MIC-D	0.56	0.33									
93		UC26	MIC-C	-0.95	-1.98									
91		UC25	OD			16/04/2019	54.20	16.43						
90		UC24	MIC-C	1.19	0.86									
90		UC24	MIC-D	0.22	4.28									
90		UC24	OD	1.08	1.63									
88		UC23	OC	0.37	-1.34	17/06/2019					3			3
88		UC23	OC			17/04/2019					6			6
84	2	UC22												
81		UC21	OC	0.13	1.06									
80		UC20	EC	-0.05	-11.48									
80		UC20	MIC-C	0.10	-0.55									
80		UC20	MIC-C	-0.56	-0.68									
74		UC20	LC	2.51	4.63	28/02/2019	64.60	2.70	2.80	4.40	27	1.8	0.835±0.008	0
66		UC19	EC	0.03	-8.82									
66		UC19	MIC-C	1.67	2.18									
66		UC19	OC	1.78	2.17	28/02/2019	65.90	3.80	3.90	5.90	35	1.7	0.832±0.003	2
62.5	1	UC18	MIC-D	3.64	6.84									
62.5		UC18	OD	2.14	0.67									
60		UC17	MIC-C	2.84	5.61									
56		UC15	OD	2.48	6.59	17/04/2019	64.50	4.50	4.60	7.10	23	11.2	0.792±0.007	2
56		UC15	MIC-C	1.33	3.34									
51		UC14	OD	2.35	4.45									
51		UC14	EC	0.91	-9.79	17/06/2019	63.06	0.45	1.00	1.66	31	1.2	0.853±0.004	0
41		UC11	EC			17/04/2019								
41		UC11	MIC-D	1.97	2.07	17/04/2019								
41		UC11	MIC-C	1.69	1.61									
41		UC11	OD			16/04/2019	66.99	1.92						
39		UC10	EC			17/06/2019	60.50	1.70	1.90	3.20	30	10.0	0.840±0.023	1
		UC10	LC			16/04/2019	59.70	2.50						
37		UC9b	LC			17/04/2019	61.82	1.39	1.70	2.70	28	4.5	0.815±0.004	4
36.5		UC9b	OD	1.87	1.46	17/04/2019	62.90	8.20	8.30	13.00	3	0.7	0.813±0.006	2
34.5		UC9	MIC-D	2.08	5.13	17/04/2019	85.38	5.23	5.40	6.30	21	3.0	0.859±0.004	0
34		UC9	MIC-C			17/04/2019	70.43	1.50	1.80	2.50	33	4.2	0.838± 0.002	1
27		UC7	OD?				76.20	4.50						
25		UC6	MIC-D	-0.39	3.83									
20		UC5	OC?			28/02/2019	64.30	2.10	2.30	3.60	28	0.6	0.814±0.003	0
18		UC4	MIC-D	1.25	5.61									
16		UC3	MIC-C			28/02/2019	66.10	2.90	3.06	3.24	22	1.6	0.812±0.004	0

£ stratigraphic height along the Juramento section in metres

© Stratigraphic sequence according to Rohais et al. (2019) and Deschamps et al. (2020)

* δ13C and δ18O values expressed as relative to V-PDB (Vienna Pee Dee Belemnite) standard.

** Tera-Wasserburg diagram U-Pb lower intercept ages

Absolute internal uncertainty (excluding long-term excess of variance of 1.5%).

$ Absolute expanded uncertainty (including ong-term excess of variance of 1.5%).

" Number of LA-ICPMS spot analyses.

† Mean Squared Weighted Deviates

" Y-axis intercept =initial Pb/Pb ratio.

¶ rejected datapoints

Table Supplementary data 7. Results Cachipampa section

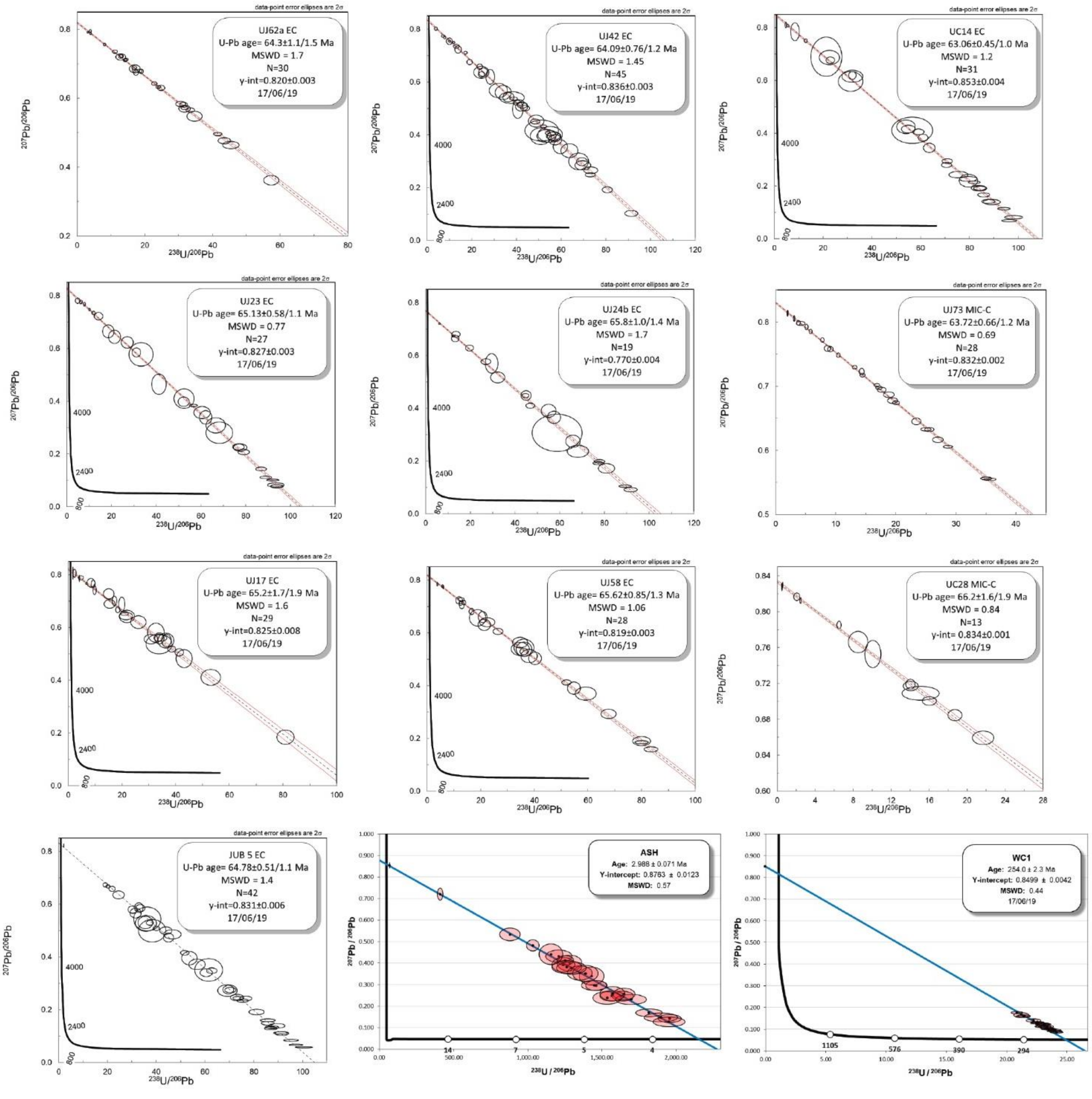

Tera supplementary data 8. Wasserburg diagrams from the LAcarb session done on 17/06/19

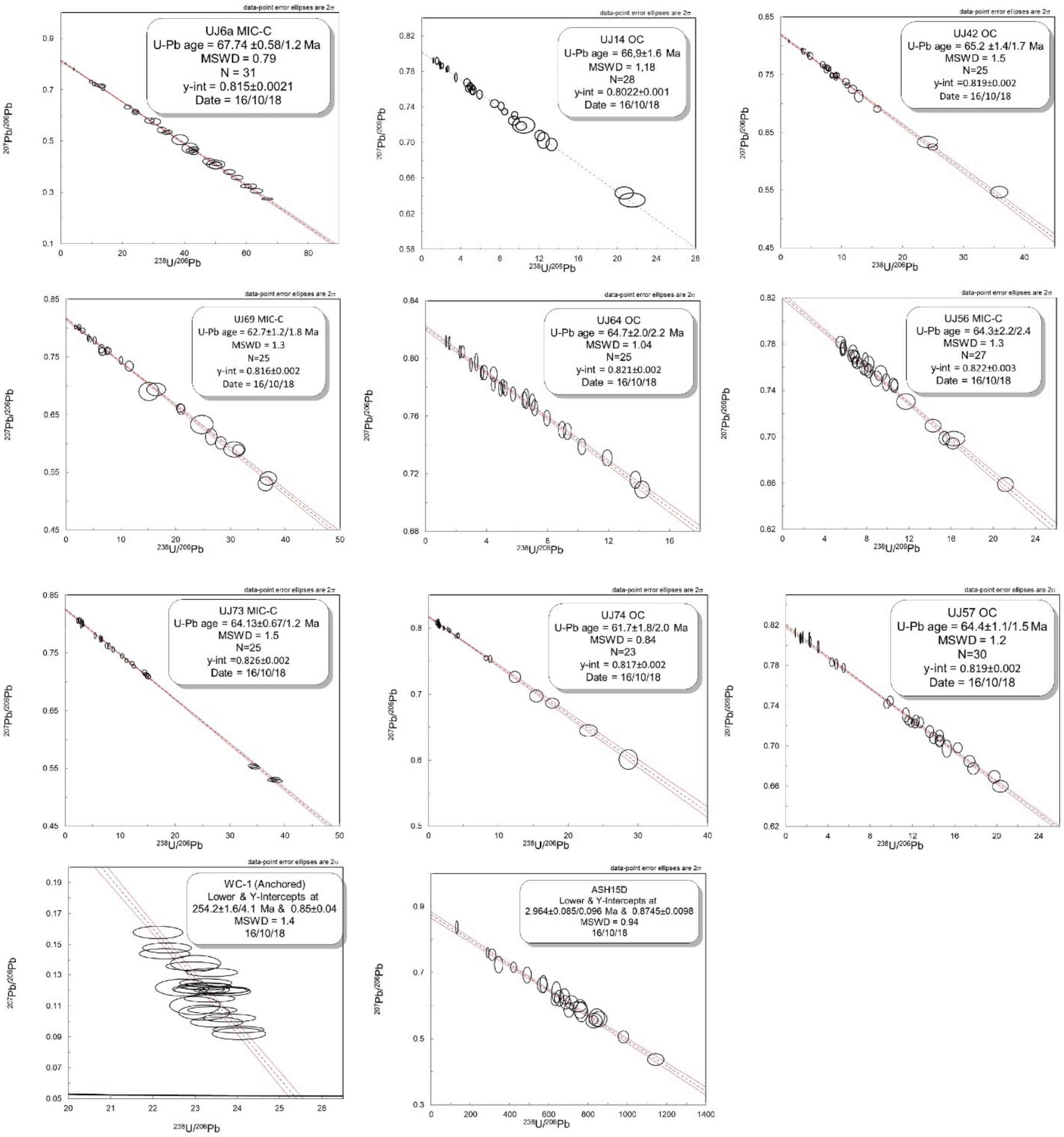

Table supplementary data 9. Tera Wasserburg diagrams from the LAcarb session done on 16/10/18

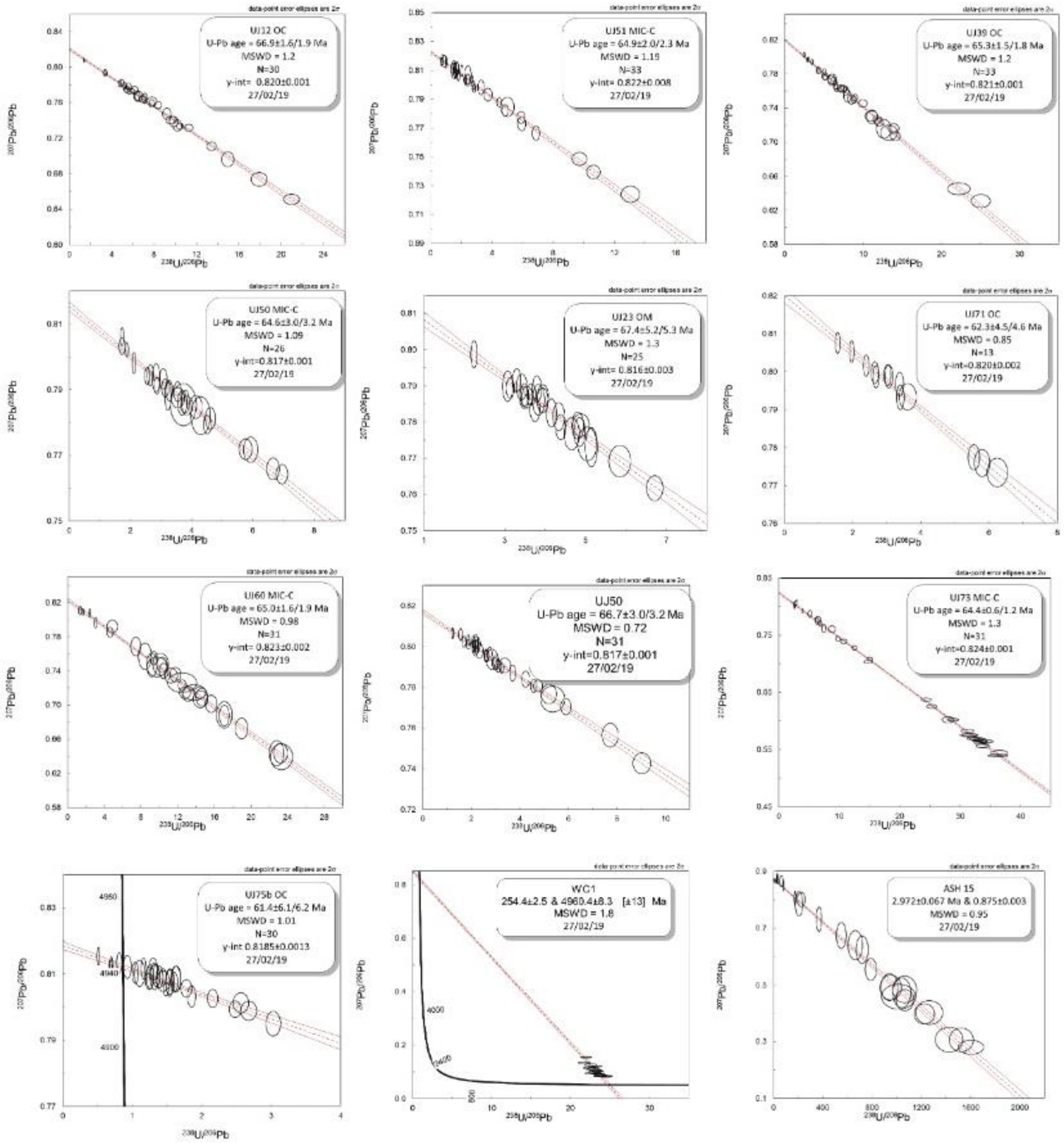

Table supplementary data 10. Tera Wasserburg diagrams from the LAcarb session done on 27/02/19

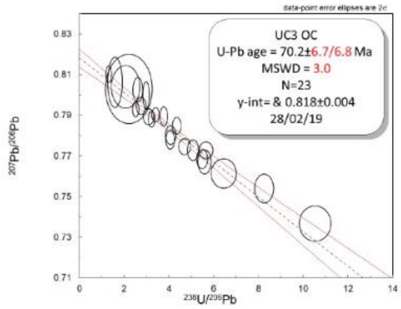

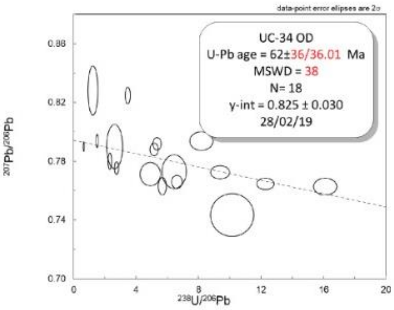

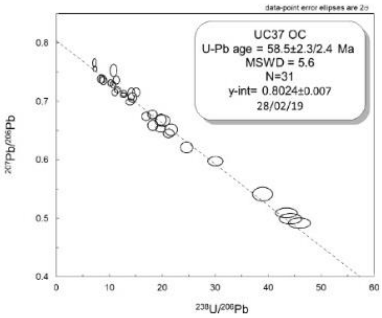

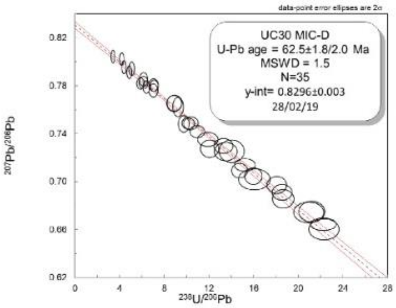

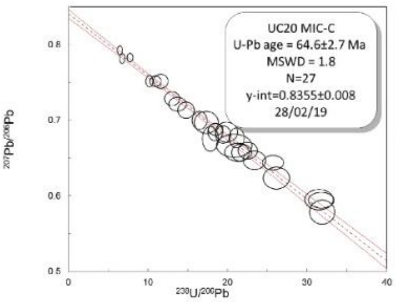

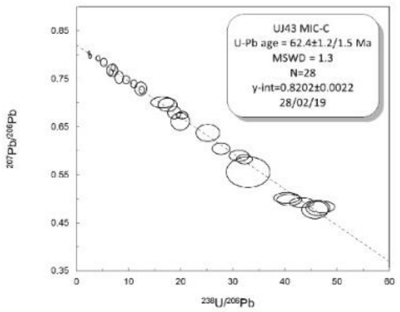

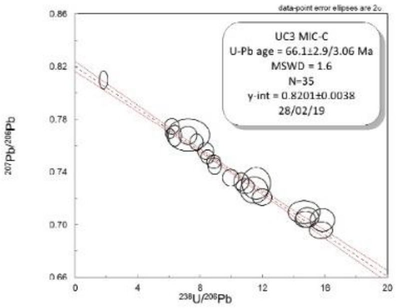

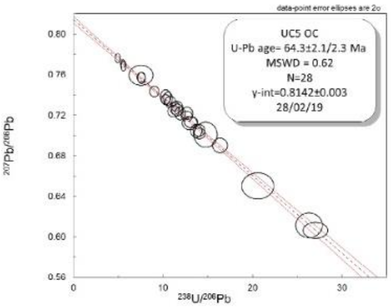

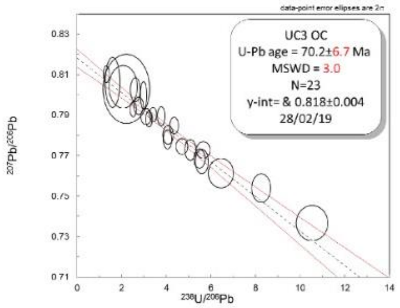

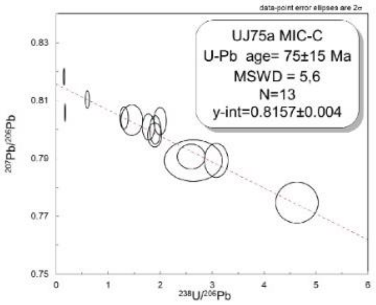

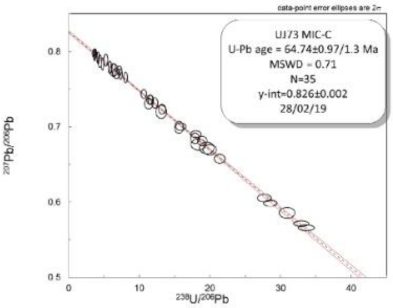

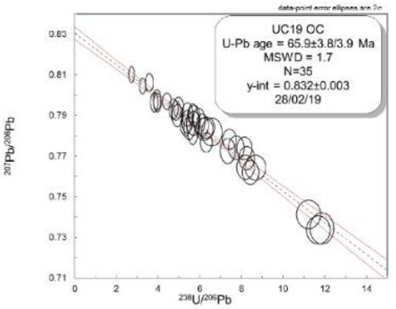

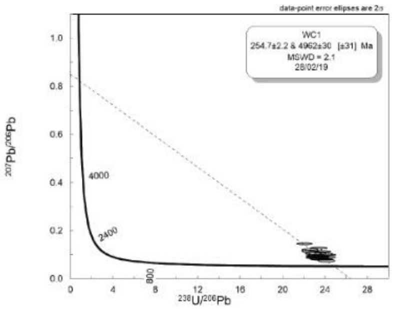

Table supplementary data 11. Tera Wasserburg diagrams from the LAcarb session done on 28/02/19

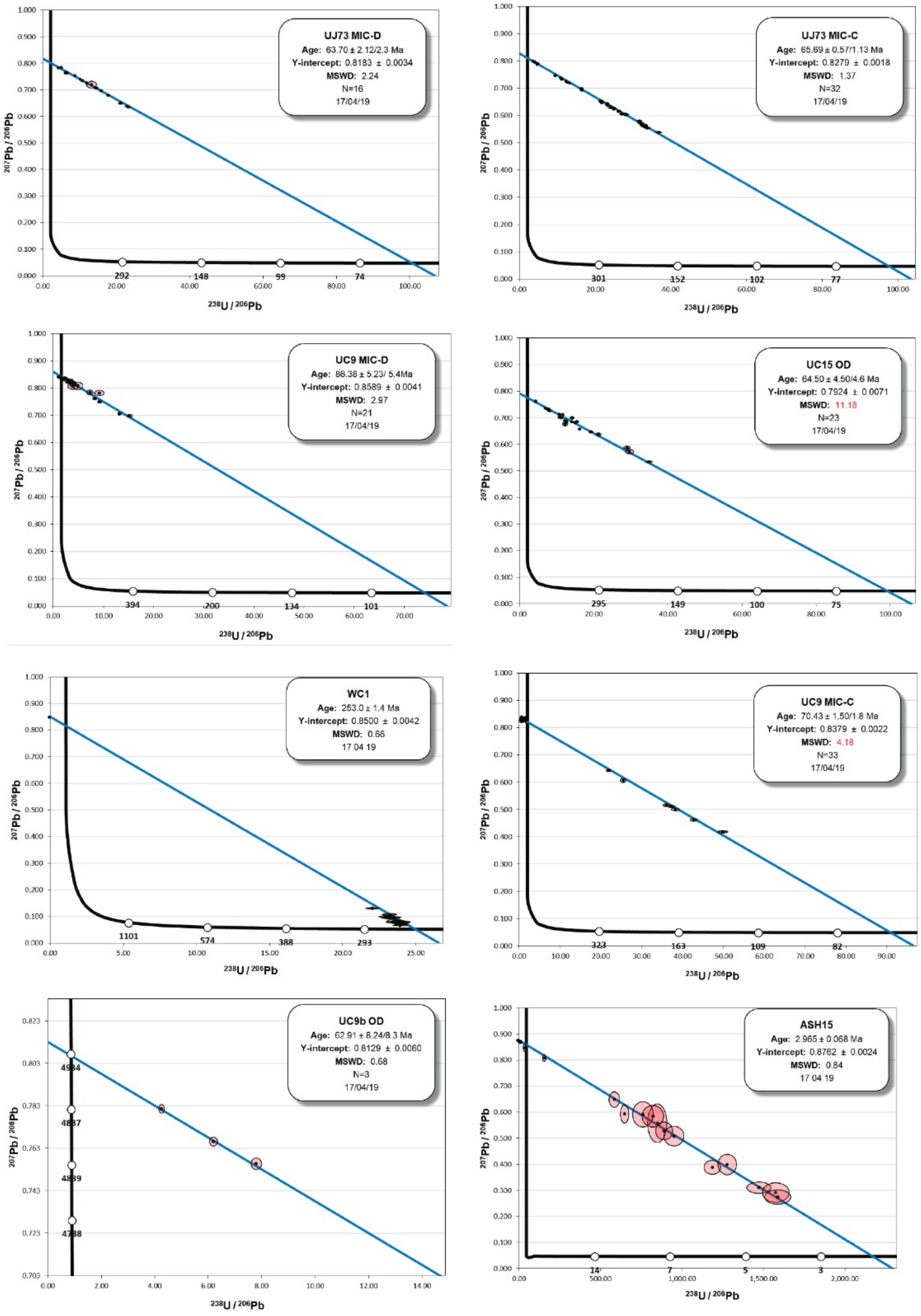

Table supplementary data 12. Tera Wasserburg diagrams from the LAcarb session done on 17/04/19

Supplementary data 13

Excel file SUPPLEMENTARY DATA 13. Settings of the Laser and of the ICP-MS instrument and raw data for zircon and carbonate dating sessions.